

University of Southampton Research Repository ePrints Soton

Copyright © and Moral Rights for this thesis are retained by the author and/or other copyright owners. A copy can be downloaded for personal non-commercial research or study, without prior permission or charge. This thesis cannot be reproduced or quoted extensively from without first obtaining permission in writing from the copyright holder/s. The content must not be changed in any way or sold commercially in any format or medium without the formal permission of the copyright holders.

When referring to this work, full bibliographic details including the author, title, awarding institution and date of the thesis must be given e.g.

AUTHOR (year of submission) "Full thesis title", University of Southampton, name of the University School or Department, PhD Thesis, pagination

UNIVERSITY OF SOUTHAMPTON

FACULTY OF ENGINEERING AND THE ENVIRONMENT

School of Chemistry

A Study of Acoustic Cavitation and Hydrogen Production

by

Thomas Mark Foley

Thesis submitted for the degree of Doctor of Engineering

October 2014

UNIVERSITY OF SOUTHAMPTON

ABSTRACT

FACULTY OF ENGINEERING AND THE ENVIRONMENT

School of Chemistry

Doctor of Engineering

A STUDY OF ACOUSTIC CAVITATION AND HYDROGEN PRODUCTION

by Thomas Mark Foley

This thesis presents a study of acoustic cavitation generated in an ultrasonic reactor, with the particular aim of enhancing hydrogen gas production and release.

The stabilisation of cavitation clusters formed in a set of ultrasonic reactors is demonstrated. The highly stable cluster is induced by the positioning of a rod at the antinode of the sound field employed. These sound fields were characterised with a new technique based on particle imaging. Here adding rheoscopic particles within such reactors revealed a novel and useful method for the characterisation of standing wave fields. This observation was supported by pressure measurements using a hydrophone. In addition the stabilised cluster was investigated using an electrochemical method to monitor the erosion of the surface directly above the cluster, at short (10's of μ s) and long (100's of s) timescales. Both timescales indicate changes in the stability and nature of the cluster, which in turn is dependent on the local surface conditions (roughness) of the rod/electrode assembly.

Low light level imaging of the stabilised cavitation cluster demonstrates the occurrence of sonoluminescence (SCL). It is shown that the spatial extent of light emitted via SCL is correlated with the pressure amplitude of the sound field. A visual 'shimmer' effect is also shown to be emanating from stabilised cavitation clusters. This is attributed to local heating which in turn induces refractive index changes, which are enhanced through the use of Schlieren imaging. This local cluster induced-heating of the liquid is quantified using a variety of physical measurements.

Investigation into the ultrasonic enhancement of the production of molecular hydrogen from aluminium corrosion is made. This study showed that the sonochemical enhancement was insignificant compared to local heating effects associated with the sound field.

Analysis of the performance of an electrolysis system, designed and manufactured by the project sponsors (HTOGO Ltd.), is reported. Measurement of the hydrogen gas produced by the system highlights a low Faradaic efficiency and long response time for gas release. An innovative method for the rapid release of gas via ultrasonic outgassing of a liquid reservoir, containing hydrogen and oxygen gas bubbles, is demonstrated.

A novel optically isolated Coulter counter system for the *in-situ* determination of the size distribution of bubbles in a bubbly liquid reservoir is reported. This thesis illustrates the underpinning principles of this technique and the determination of the best calculation method for successful calibration and accurate measurement of the bubble size distributions generated in an electrochemical reactor.

The knowledge gained and the new technology developed in this project is expected to accelerate and improve the development of the use of electrolytic hydrogen for internal combustion engine applications.

Contents

ABSTRACT	i
Contents	i
DECLARATION OF AUTHORSHIP	v
Acknowledgements.....	vii
Definitions and Abbreviations.....	viii
Chapter 1: Introduction.....	xi
1.1 Motivation and summary	xi
1.2 GANTT Chart	xiii
1.3 Hydrogen.....	1
1.3.1 Hydrogen as an energy carrier	1
1.3.2 Hydrogen and internal combustion engines.....	4
1.4 Metal recycling as a hydrogen source	5
1.5 Aluminium.....	6
1.5.1 Aluminium reactions in alkaline conditions	7
1.5.2 Aluminium reactions in neutral conditions.....	8
1.6 Cavitation	9
1.6.1 Cavitation clusters and erosion	13
1.6.2 Sonoluminescence	17
1.6.3 Characterisation of acoustic cavitation	19
Chapter 2: Experimental	21
2.1 General experimental methods	21
2.1.1 Chemicals	21
2.1.2 Vessels and reactors.....	22
2.1.3 Pressure measurements.....	24
2.1.4 Temperature measurements.....	24
2.1.5 Imaging techniques.....	24
2.1.5.1 High-speed imaging.....	24
2.1.5.2 Sonoluminescence and Schlieren imaging.....	25
2.1.6 Aluminium electrode/erosion sensor.....	25
2.1.7 HTOGO Electrolysis Device.....	26
2.1.8 Hydrogen detection and measurement.....	28
2.1.9 AC-modulation technique	32

Chapter 3: Cavitation bubble clusters.....	33
3.1 Ultrasonic reactor characterisation.....	33
3.2 Erosion sensor.....	40
3.2.1 High-speed imaging	40
3.2.2 Cavitation erosion and surface pre-treatment	46
3.3 Luminescence.....	56
3.4 Shimmer visualisation/Schlieren imaging.....	59
3.5 Enhancement of hydrogen production from aluminium.....	68
3.6 Conclusions	71
Chapter 4: Ultrasound assisted gas release	73
4.1 Electrolysis device characterisation.....	73
4.1.1 Experimental setup.....	73
4.1.2 Hydrogen measurement.....	75
4.1.2.1 Sensor calibration.....	75
4.1.2.2 Electrolysis system	75
4.1.3 Uncompensated resistance measurement	82
4.1.3.1 Dummy cell calibration and method validation.....	85
4.1.3.2 Measurement of R_u in the electrolysis system	86
4.1.3.3 Modular cell for AC-modulation determination of R_u	90
4.2 Ultrasound assisted gas release.....	93
4.2.1 Ultrasonic field characterisation	93
4.2.2 Gas release	98
4.2.2.1 Outgassing mechanism.....	105
4.3 Gas void fraction calculation	107
4.4 Heating effects	109
4.5 Conclusions	113
Chapter 5: Bubble populations	115
5.1 Coulter counter	115
5.1.1 Theory.....	116
5.1.2 Experimental details.....	122
5.1.2.1 μ -channel fabrication.....	122
5.1.2.2 Measuring the resistance across the channel	126
5.1.2.3 Opto-isolation.....	128
5.1.3 Calibration and validation	128
5.1.3.1 Polarisation curve.....	129
5.1.3.2 Particle calibration	129
5.1.3.2.1 Particle translocation example	130

5.1.3.2.2	Multiple particle translocations	132
5.1.3.3	Bubble calibration	145
5.1.3.3.1	Bubble translocation example	147
5.1.3.3.2	Multiple bubble translocations.....	148
5.1.4	Measurement of the bubble size distribution.....	151
5.1.4.1	Results	152
5.1.4.1.1	40 μm channel.....	153
5.1.4.1.2	64 μm channel.....	154
5.1.4.1.3	100 μm channel.....	160
5.1.4.2	Comparison of distributions	164
5.2	Conclusions and discussion	167
Chapter 6:	Conclusions and further work.....	169
Appendices	173
Appendix 1.	316L grade steel composition.....	175
Appendix 2.	CO sensor and aluminium casing	176
Appendix 3.	CO sensor calibration to hydrogen.....	177
Appendix 4.	SEM images of rheoscopic particles.....	178
Appendix 5a.	Conductivity data for 0.1 M NaOH.....	179
Appendix 5b.	Experimental variables for Figure 4.25.....	181
Appendix 6.	Coulter counter theoretical function comparison	182
Appendix 7.	Vortex density coefficients	183
Appendix 8.	Optocoupler calibration details.....	184
Appendix 9.	Smythe model coefficients.....	185
Appendix 10:	Speed of sound measurements.....	186
Appendix 11:	Visual Basic Programs	187
List of References	209

DECLARATION OF AUTHORSHIP

I, Thomas Mark Foley

declare that the thesis entitled

A Study of Acoustic Cavitation and Hydrogen Production

and the work presented in the thesis are both my own, and have been generated by me as the result of my own original research. I confirm that:

- this work was done wholly or mainly while in candidature for a research degree at this University;
- where any part of this thesis has previously been submitted for a degree or any other qualification at this University or any other institution, this has been clearly stated;
- where I have consulted the published work of others, this is always clearly attributed;
- where I have quoted from the work of others, the source is always given. With the exception of such quotations, this thesis is entirely my own work;
- I have acknowledged all main sources of help;
- where the thesis is based on work done by myself jointly with others, I have made clear exactly what was done by others and what I have contributed myself;
- none of this work has been published before submission.

Signed:.....

Date:.....

Acknowledgements

I would like to thank the following people for their support, guidance, efforts and friendship throughout the course of my doctorate.

Pete, for your ability to strike the perfect balance between being a friend and supervisor, for your catchphrases (“What the hell?!”, “Thaaaaaamas!”, “Brace yourself”), for your enthusiasm and for making lab ‘work’ enjoyable. This time next year Rodney.

Doug, for your help with VB coding (“Doug, can I borrow you for a moment?”) and for your unparalleled authority when hailing taxis in times of need.

Maciek, Rob, Jack, Mike, Jake, Jimmy and the rest of the Friday night gang, thanks for making these four years more enjoyable.

Etch, Tris and the whole Soni/Download crew for much needed nights of scwn.

Ric and Drew, for your unquestioning friendship.

Laura, for your constant love and support.

Mum and Dad for your love and encouragement throughout my university career.

Definitions and Abbreviations

A	Electrode area (cm^2)
C	Concentration (mol dm^{-3})
c	Specific heat capacity (J K^{-1})
c_1	Speed of sound in bubble-free liquid (m s^{-1})
c_2	Speed of sound in bubble cloud (m s^{-1})
C_{DL}	Double layer capacitance (F)
d	Bubble diameter (m)
D	Channel diameter (m)
E	Electrode potential (V)
F	Faradays constant (C mol^{-1})
f	Gas void fraction
F_1	Deblois and Bean theoretically based correction function
F_2	Deblois and Bean empirically based correction function
F_3	Smythe correction function
f_0	Fundamental frequency (Hz)
f_{drive}	Driving frequency (Hz)
I_{sens}	Hydrogen sensor current (A)
K_c	Zero gas conductivity (S cm^{-1})
K_e	Reduced electrolyte conductivity (S cm^{-1})
L	Channel length (m)
P	Pressure (kPa)
P_0	Hydrostatic liquid pressure (kPa)
P_{atm}	Atmospheric pressure (kPa)
P_B	Blake pressure (kPa)
P_i	Incident pressure (kPa)
P_{opt}	Minimum applied pressure required for inertial cavitation (kPa)
P_r	Reflected pressure (kPa)
P_t	Transmitted pressure (kPa)
Q	Volumetric flow rate (m s^{-1})
r	Bubble radius (m)
R	Channel radius (m)
R_B	Blake radius – the threshold for R_0 in the Blake equation (m)
R_{max}	The maximum radius of the bubble (m)
R_0	Initial bubble radius (m)
R_{1-3}	Schmitt trigger resistors
R_F	Faradaic resistance (Ohm)
R_r	Resonant bubble radius (m)
R_u	Uncompensated resistance (Ohm)
t	Time (s)
T_{max}	Maximum temperature ($^{\circ}\text{C}$)
V_{cc}	Common collector voltage (V)
V_G	Gas volume (cm^3)
V_L	Liquid volume (cm^3)
V_{pp}	Peak to peak voltage (V)
V_{ref}	Schmitt trigger reference voltage (V)
V_{upper}	Upper Schmitt trigger threshold (V)

V_{lower}	Lower Schmitt trigger threshold (V)
Z	Impedance (Ohms)
θ	Phase angle (rad)
μ	Kinematic viscosity (Pa s)
ν_0	Linear resonance frequency for bubble pulsations (Hz)
ρ	Electrolyte resistivity (Ohm cm ⁻¹)
σ	Specific conductivity (S cm ⁻¹) or Surface tension (N m ⁻¹)
ω	Diameter (m)

AC	Alternating Current
ADC	Analogue to Digital Converter
CCD	Charged Coupled Device
CO	Carbon Monoxide
CPOX	Catalytic Partial OXidation
CSV	Comma Separated Values
DAQ	Data AQuisition
DC	Direct Current
EC	Electrochemistry
EDTA	EthyleneDiamineTetraAcetic acid
FFT	Fast Fourier Transform
FPS	Frames Per Second
HHV	Higher Heating Value
ICE	Internal Combustion Engine
LED	Light Emitting Diode
LHV	Lower Heating Value
MBSCL	MultiBubble SonochemiLuminescence
MBSL	MultiBubble SonoLuminescence
MBT	Maximum Break Torque
MMO	Mercury Mercury Oxide
N	Neutral (electrode)
NO _x	Nitrogen oxides
OA	Operational amplifier
ORR	Oxygen Reduction Reaction
PC	Personal Computer
PEC	PhotoElectroChemical
POX	Partial OXidation
PV	PhotoVoltaic
PMMA	PolyMethylMethAcrylate
PVC	PolyVinyl Chloride
R/C	Reference/Counter electrode
RICCS	Reactor Induced Cavitation Cluster Stabilisation
SHE	Standard Hydrogen Electrode
SMR	Steam Methane Reforming
SNR	Signal to Noise Ratio
US	Ultrasound
USB	Universal Serial Bus
VB6	Visual Basic 6

Chapter 1: Introduction

1.1 Motivation and summary

The Engineering Doctorate (EngD) is a four-year research programme in which the research direction is driven by the interest of a sponsoring company. HTOGO Ltd. is the sponsor for the work presented in this thesis.

HTOGO Ltd. design and manufacture water electrolysis devices for retro fit installation into vehicles. In their system hydrogen produced from the electrolysis cell feeds into the engine and mixes with the fuel and air in the cylinder, producing a quicker and more efficient burn at certain fuel-air-hydrogen ratios [1-6]. Investigation was aimed and conducted toward aiding their endeavours, utilising equipment and expertise that would otherwise be unavailable to them, whilst maintaining a novel research direction. Hence the research presented spans a broad range of experimental areas, all linked to the concept of controlling hydrogen gas production and release with particular focus on the manipulation of gas bubbles in liquids using ultrasound. An overview of each chapter is now presented.

Chapter 1 examines the relevant literature and contains a general overview of the subjects discussed and is geared to provide grounding for the research topics discussed thereafter. Theories and information relating to specific areas of research are discussed in the relevant chapters.

An overview of the experimental conditions is presented in chapter 2. This is combined with the exact conditions for each experiment which are also presented in each relevant chapter thereafter. This is written with the aim of providing enough information for independent recreation of the experiments.

Chapter 3 examines the subject of acoustic cavitation and its effects, in particular cavitation erosion produced from a hemispherical bubble cluster formed on the face of a downward pointing rod in an ultrasonic reactor. Investigation is made into and using the innovative erosion sensor developed by Birkin *et al.* [7, 8]. Exploration is also made into the concept of producing hydrogen gas via the erosion of aluminium with ultrasound. Furthermore study is also focussed on a novel application of Schlieren technique for the imaging of a shimmer effect; a refractive index change observed to be emanating from a cavitation cluster.

Chapter 1: Introduction

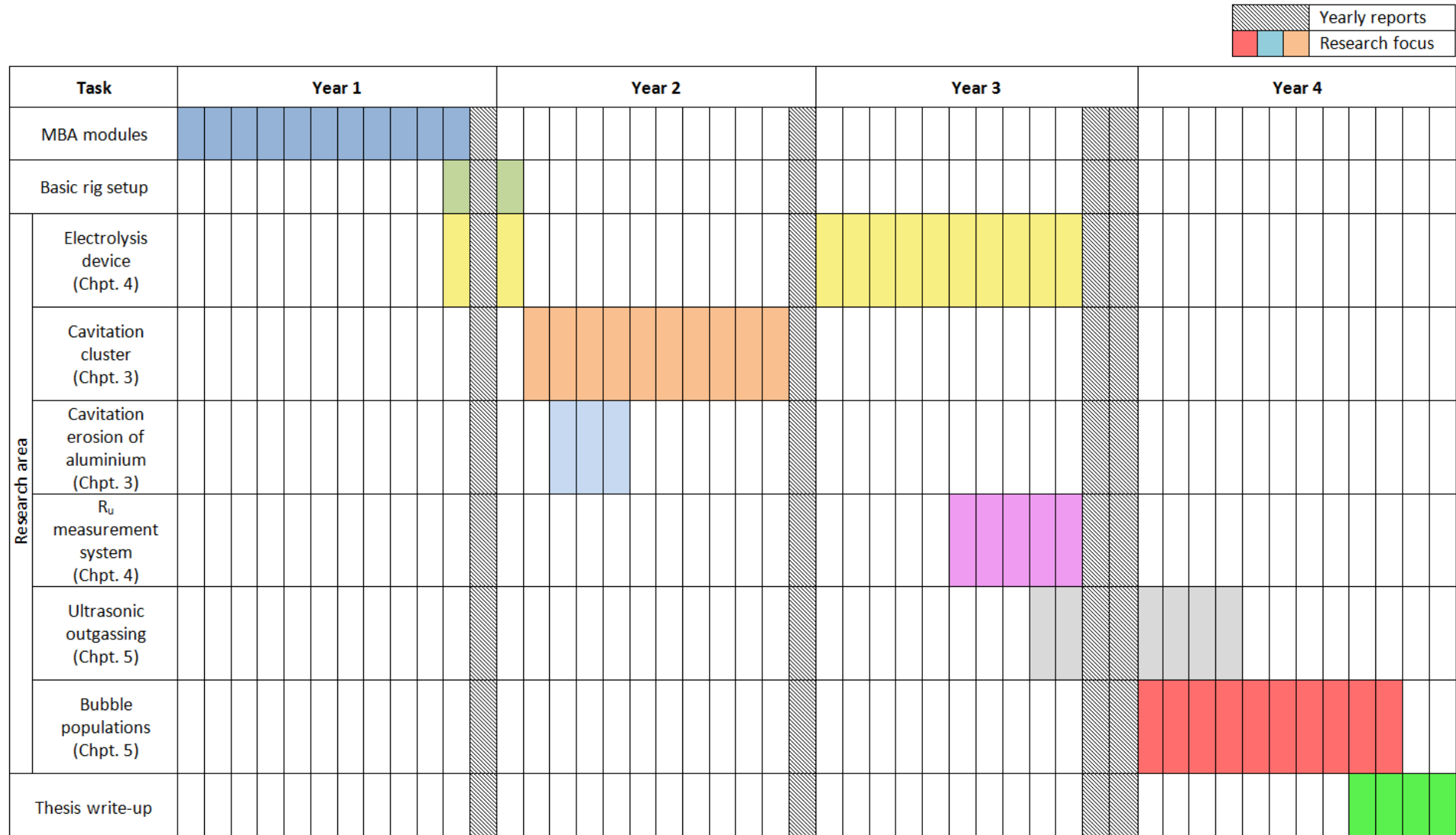
Chapter 4 focusses on the experiments conducted with an electrolysis cell (manufactured by HTOGO Ltd), which were aimed at providing characterisation of the performance of the device with demonstration of its limitations. The study introduces a novel interpretation for the uncompensated resistance between the electrolysis cell electrodes. This section also discusses an innovative method of controlling the hydrogen output by the outgassing of an electrolytically gas filled liquid using ultrasound.

Chapter 5 details the investigation into the quantification of bubble populations. This features the novel application of the Coulter counter technique for the estimation of the bubble size distribution of the population produced by an electrolysis cell.

Chapter 6 provides a summary of the work presented and gives recommendations for continuation of the research.

The next section provides an overview of the time spent on each research area in the form of a GANTT chart. This is followed by the background information section.

1.2 GANTT Chart



1.3 Hydrogen

1.3.1 Hydrogen as an energy carrier

There is an ever increasing need for a clean, renewable energy source. The production of fossil fuels is reaching peak rates and the depletion of these finite sources is of concern. A Governmental White Paper [9] and others [10-12] examine this energy challenge and focus on the vital importance of improving air quality by the cessation of polluting methods of energy production. Many believe that hydrogen as an alternative fuel has the potential to address these concerns [10-20]. In its purest form the combustion of hydrogen produces zero harmful emissions and production may use a variety of energy inputs, including renewable sources. Hydrogen can also be fed into an appropriate fuel cell or added to a conventional internal combustion engine (ICE) for increased fuel economy and reduced emissions. Thus if generated through renewable or nuclear sources, green energy based hydrogen systems can be one of the best solutions for accelerating and ensuring a transition to global energy stability and sustainability.

Dunn [10] and Hefner [21] have examined this global energy systems transition. When exploring the world's energy history in terms of the physical states of matter of the fuel a transition to gaseous hydrogen becomes a logical progression. Since the 19th century the world has been slowly shifting from one form of energy to another; from solids to liquids to gases, as illustrated by Hefner (see Figure 1.1).

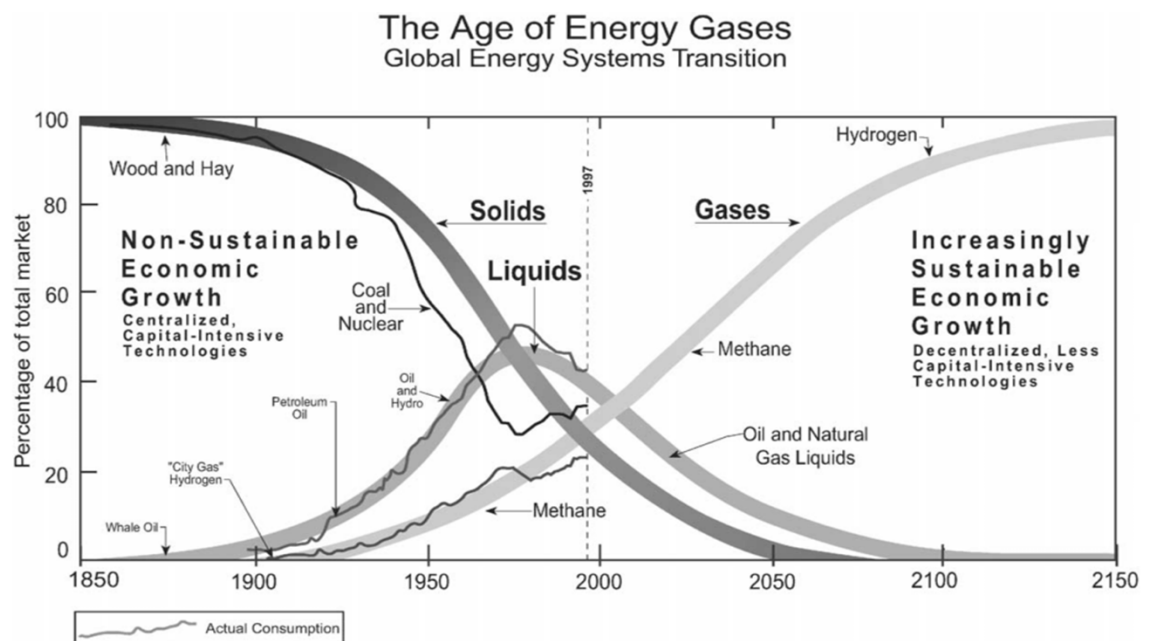


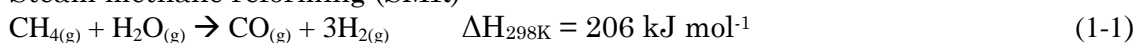
Figure 1.1 Global energy systems transition taken from Hefner [21]

Chapter 1: Introduction

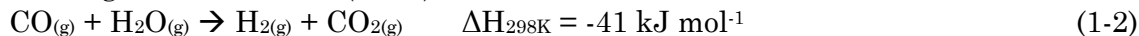
Johnston *et al.* [12] outline a roadmap to sustainability with hydrogen, exploring five problems that are slowing the adoption of hydrogen; production, storage, distribution, safety and public perception. The work presented in this report is mainly concerned with the storage of hydrogen, be it temporarily in gas form in a liquid reservoir to enable enhanced control of its release.

Bartels *et al.* [20] amongst others [10, 12-15, 22, 23] demonstrate how hydrogen can be generated from a variety of sources. Wang [23] duly summarizes the current state of hydrogen production, explaining that due to the low conversion efficiencies of biological systems as well as the high cost of water electrolysis, chemical methods dominate the market for commercial hydrogen production. Natural gas and coal are currently the two main feed-stocks used for hydrogen production. Hydrogen generated from natural gas occurs mainly via the well-established process of methane steam reforming, as described in equations (1-1) and (1-2) [24, 25].

Steam methane reforming (SMR)



Water gas shift reaction (WGS)



Partial oxidation (POX) and catalytic partial oxidation (CPOX) of hydrocarbons also offer methods for hydrogen production via natural gas. This process involves the reaction of hydrocarbons (natural gas) with oxygen to produce carbon monoxide and hydrogen. The non-catalytic partial oxidation of hydrocarbons typically occurs with flame temperatures of 1200–1500 °C to ensure complete conversion and to reduce carbon or soot formation. Catalysts can be added to the partial oxidation system to lower the operating temperatures [26]. The other main feedstock for hydrogen production, coal, is utilised by a gasification process in which coal and oxygen are heated with steam to produce hydrogen and carbon monoxide [27]. This can also additionally incorporate the water gas shift reaction (eq. 2) to increase the hydrogen output. The issues with these production methods are the same as if the fuels were used directly for energy production; they are non-renewable and dirty fuels with heavy carbon footprints that do not provide long-term energy security. As such, the cost of fossil fuels is rapidly increasing while many other alternative sources of energy are decreasing in cost as technologies improve and economies of scale are achieved [20].

Alternative sources for hydrogen production include biomass [14, 28], water photolysis [29] and electrolysis [30], which can be powered by other sources such as nuclear [22], solar [31, 32], and wind energy [33, 34]. Restricted by the low hydrogen and energy yield, and its questionable carbon neutrality, the reforming of biomass as a sustainable hydrogen source is still under review [14, 35]. Water photolysis using photoactive electrodes is a promising renewable hydrogen source, however it is still at the early stages of development and technical difficulties mean that industrial scale up will be a significant problem [29, 36].

The expense of electricity compared to direct fossil fuel use is the major hurdle to water electrolysis as a hydrogen source, however improvements in electrolysis device efficiency through on-going research are driving down the cost [37]. Table 1-1 presents a summary of the efficiencies of some of the relevant hydrogen production methods.

<i>Technology</i>	<i>Feed stock</i>	<i>Efficiency</i>	<i>Maturity</i>	<i>References</i>
Steam reforming	Hydrocarbons	65-85 % ^a	Commercial	[38-40]
Partial oxidation	Hydrocarbons	60-90 % ^a	Commercial	[38, 40, 41]
Alkaline electrolysis	Water + electricity	50-75 % ^a	Commercial	[36, 37, 42]
PEM electrolysis	Water + electricity	55-70 % ^a	Near term	[36, 37]
Photolysis	Water + sunlight	5-30%	Long term	[36]

Table 1-1 Hydrogen generation technology summary

^a Total system efficiency based on the lower heating value (LHV)

In order to obtain the goal of a carbon-free hydrogen economy, electrolysis powered by nuclear power is an attractive alternative, offering a lower cost option in terms of large scale electricity production, and additional efficiency improvements using steam generation. However, most of the literature is focused on hydrogen production powered through renewable means, with continuing improvements in these methods making the idea a more credible concept. Until one or several of these methods progress to become sustainable for large scale hydrogen production, other transitional technologies are needed. The addition of hydrogen gas to internal combustion engines presents a possible stepping stone toward a hydrogen economy.

Chapter 1: Introduction

1.3.2 Hydrogen and internal combustion engines

There is increasing concern over how vehicle emissions are affecting the environment and human and animal health. Coupled with the diminishing supply of conventional fuels, this is driving research to focus on steps aimed toward a renewable energy future. An example of this is seen with research into the use of hydrogen as an additive to vehicle fuels. The potential advantages to using hydrogen as a fuel are made obvious with comparison of its properties to other common fuels (see Table 1-2).

<i>Properties</i>	<i>Hydrogen</i>	<i>Methane</i>	<i>Propane</i>	<i>Gasoline (iso-octane)</i>
Chemical formula	H ₂	CH ₄	C ₃ H ₈	(C ₈ H ₁₈)
Min. ignition energy / mJ	0.02	0.29	0.26	0.24
Flame speed / cm s ⁻¹	237	42	46	41.5
Diffusion coef. / cm ² s ⁻¹	0.61	0.16	0.12	0.05
Quenching gap / cm	0.06	0.2	0.2	0.2
Higher heating value / MJ kg ⁻¹	142	55	50.4	(47.3)
Molecular mass / g mol ⁻¹	2.02	16.04	44.10	(114)

Table 1-2 Comparison of the various properties of hydrogen, methane, propane and gasoline fuels. Data taken from [43].

The addition of hydrogen to conventional internal combustion engines (ICE's) can be enacted through either a pure hydrogen burn or as part of a mix of fuels within the engine (dual fuel) [1-5, 44-46]. It is the latter approach that HTOGO Ltd., the sponsoring company take. The electrolysis devices produced by HTOGO Ltd. are retro-fitted into vehicles. Once the ignition is engaged the device is initiated at a constant voltage (powered by the vehicle battery) and produces hydrogen and oxygen gas via electrolysis (details in experimental section 2.1.7). The hydrogen gas mixture feeds into the engine and mixes with the fuel and air in the cylinder.

Two major benefits have been reported in the literature from the addition of hydrogen to an ICE; decreased emission levels and increased fuel efficiency. Improved emission performance has been reported with respect to carbon monoxide

and unburned hydrocarbons [1, 5, 43]. In some cases, depending on specific alterations to the engine spark timings, NO_x emission reductions have also been reported [1, 43, 44, 47, 48]. However, at the spark timings giving the maximum break torque (MBT) and the best fuel efficiencies, the NO_x emission levels were not improved [49]. Improved fuel efficiency has been reported in several papers [5, 43, 44, 46-48, 50, 51] and is associated with an altered flame speed for an optimised burn. With the increasing cost of oil and the growing concern for the deterioration in air quality, the advantages of hydrogen addition to ICE's are very appealing, even more so as an intermediate step towards a full carbon-free hydrogen economy. However, the technology of the addition of hydrogen to the ICE is yet to reach the mainstream industry and requires precise control of the component ratio in hydrogen/air/fuel mixture [1, 52, 53]. Chapters 4 and 5 make investigation into the controlled release of hydrogen gas from the HTOGO electrolysis system with this precise control in mind. While this electrolysis system will be investigated further in this report, hydrogen production through metal digestion will also be studied.

1.4 Metal recycling as a hydrogen source

An alternative source for hydrogen production is found through the use of metals. Chemical displacement reactions occur between certain reactive metals, such as aluminium or magnesium, and hydrogen sources, such as water or hydrocarbons, releasing hydrogen gas [13, 35, 54]. In certain reactions, a violent release of hydrogen can occur very soon after contact, even in mild conditions. Hence this concept has the potential to address cost (depending on the metal abundance) and safety problems associated with hydrogen; real time production is possible via indirect storage of hydrogen in aqueous solutions or hydrocarbon mixtures. Furthermore the storage and transportation issues normally associated with hydrogen, in gas or liquid form, are potentially avoided. It is also worth noting that pure liquid hydrogen contains less hydrogen per unit volume (71 kg m⁻³) than potential sources for these reaction such as water (111 kg m⁻³) and gasoline (84 kg m⁻³) [14]. So far, Aluminium, zinc and magnesium have been used in this way [13, 23, 35].

An alternative and elegant adaptation of this source of hydrogen is found in metal recycling. This idea is based on the generation of clean energy starting with waste materials. Metals such as aluminium are used in many consumable products and

Chapter 1: Introduction

considerable quantities of waste are produced; such as aluminium cans, electrical wire, industrial scraps and aluminium foil. This waste can be utilized to produce clean energy in the form of hydrogen through reaction with hydrogen containing sources [14, 23]. Aluminium shows considerable promise for hydrogen generation via this method [55] and therefore will be discussed further.

1.5 Aluminium

Aluminium possesses a wide range of valuable properties for this application. It has a high energy density (29 MJ kg^{-1}), is abundant, and is considered a waste material (millions of tons of municipal waste alone produced annually [56]). The metal is relatively inexpensive and light in weight, with a density of 2700 kg m^{-3} [57], potentially helping to lead to significant reduction in the weight of an aluminium based system. Furthermore it has highly negative standard electrode potential (-1.66 V) which makes it, in principle, an excellent reducing agent, capable of producing hydrogen gas upon contact with aqueous solutions. All of this helps make aluminium one of the most viable metals for sustainable energy production in the future.

However, the problem with using aluminium is regarding its passive layer. This passive oxide layer forms on the surface of aluminium due to its strong affinity for oxygen. Hence aluminium has a strong corrosion resistance, with the protective layer preventing any further oxidation. In any other circumstances this can be a great advantage, however it becomes a major hurdle when trying to realize continuous and controllable hydrogen generation through aluminium corrosion [23]. Figure 1.2 displays the Pourbaix diagram for aluminium devised by Delmon and Pourbaix [58]. This diagram indicates the theoretical circumstances in which aluminium should show corrosion (forming Al^{3+} at low pH and AlO_2^- at high pH values) and passivity due to hydrargillite ($\text{Al}_2\text{O}_3 \cdot 3\text{H}_2\text{O}$ at near-neutral pH values) and immunity at high negative potentials. These reactions are relevant in the proceeding sections, with a view towards hydrogen production.

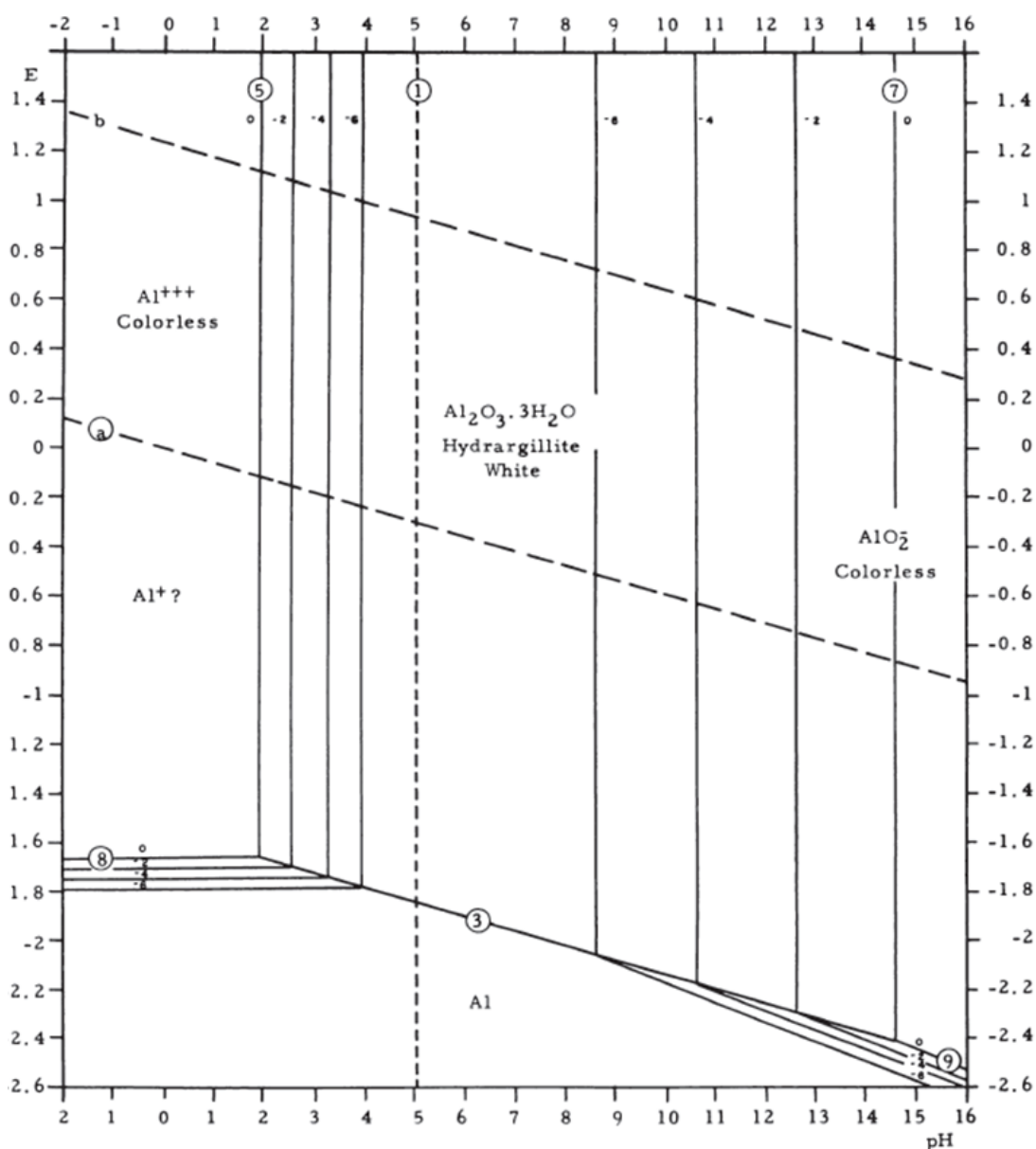


Figure 1.2 Potential–pH diagram (Pourbaix diagram) for aluminium–water system at 25 °C, taken from Deltombe and Pourbaix [58]

1.5.1 Aluminium reactions in alkaline conditions

In strongly alkaline conditions the passive oxide layer on the surface of the aluminium is destroyed by hydroxide ions. Without this protective layer the aluminium reacts and hydrogen production results even at room temperature. Sodium hydroxide (NaOH) is one of the most commonly encountered alkalis, reacting as shown in equations (1-3) to (1-5) [59].

Chapter 1: Introduction



Overall:



The steps shown in equations (1-3) to (1-5) were suggested to be involved in this hydrogen generation process [18, 19]. Sodium hydroxide depleted for the hydrogen evolution in equation (1-3) will be regenerated through the decomposition of $NaAl(OH)_4$ in equation (1-4). Therefore only water is consumed during the overall reaction, summarized in equation (1-5). Note, this is a well-known parasitic reaction, which is undesirable in aluminium–air batteries [60]. Several studies have been conducted into hydrogen generation based on this reaction [19, 57]. An unfortunate property of sodium hydroxide is its high corrosiveness, which can prove problematic for application in vehicles or power systems [61]. Clearly the reactions demonstrate the potential for hydrogen gas generation via reaction of aluminium in alkaline conditions; however it does not offer an obvious method for controlling or rapidly ceasing the gas release. If we instead consider the activation of aluminium from neutral conditions a greater degree of control can be acquired for the production and release of hydrogen gas.

1.5.2 Aluminium reactions in neutral conditions

In neutral conditions, bare (un-passivated) aluminium reacts with water to produce hydrogen as shown in equation (1-6).



However, penetration of the oxide layer does not occur so readily in neutral conditions, hence affecting the metal activity to significantly decrease. Removing this passivating oxide layer is the major boundary to hydrogen production here. Thus, the improvement and exploration of methods of exposing the metal surface and improving the activity of aluminium is of great interest. Recent experimentation [61-65] has focussed on the milling, cutting, drilling or grinding of aluminium to depassivate the surface, resulting in increased amounts of hydrogen generation. However, for continuous gas evolution, non-stop mechanical action is required due to the rapid repassivation of the metal surface under these conditions

[66]. Alternatively, a novel concept proposed here focuses on the use of acoustic cavitation erosion to depassivate the aluminium surface. To fully comprehend this notion, it is important to understand the theoretical background of cavitation and its effects and this is the topic for discussion in the next section.

1.6 Cavitation

Cavitation is a broad term covering a myriad of physical and chemical phenomena. It can be described as the nucleation, growth and collapse of bubbles in a liquid by appropriate physical forces. Some of the common cavitation inception techniques are as follows and are duly summarised by Leighton [67], Young [68] and Lauterborn [69].

- Hydrodynamic cavitation produced by pressure variations in a flowing liquid [70-72].
- Optical cavitation produced by photons from a high intensity laser causing local heating, liquid breakdown and bubble formation [69, 73-75].
- Particle cavitation produced by elementary particles creating local heating in the liquid [68, 76].
- Spark discharge causing vapour gases to evaporate into the cavity from the surrounding medium [77-79].
- Acoustic cavitation produced by sound waves in a liquid [67, 68].

It is the last technique that the research presented here is concerned with; specifically, cavitation generated by ultrasound (US), meaning a cyclic sound pressure wave with a frequency above that of human hearing ($> ca. 18$ kHz). When a sound wave is passed through a solution it is subjected to compression and rarefaction cycles. The response of a cavity is dependent on the amplitude and frequency of the pressure wave, in addition to many other factors including the size and location of the cavity, and the liquid properties and ambient experimental conditions. A brief summary of bubbles dynamics regarding acoustic cavitation is subsequently presented and the reader is directed to the literature for more detailed descriptions and reviews [67, 68, 80].

Chapter 1: Introduction

Acoustic cavitation can generally be divided into two subclasses; inertial and non-inertial, depending on the lifetime and termination of each individual bubble.

Inertial cavitation is the term given to the process in which this isothermal growth of a bubble is followed by an adiabatic collapse. Non-inertial cavitation is the process in which the bubble oscillates in the presence of the acoustic field with the pressure within the gas phase preventing bubble collapse.

When a bubble expands and contracts it is considered to do work and have work done on it respectively. For rapid bubble growth to occur then the tension in the liquid must exceed a threshold; the Blake pressure (P_B) [67, 81]. This is named after Francis Blake who devised a model for calculating this pressure threshold for quasi-static pressure changes (see equation (1-7)).

$$P_B = P_0 + \frac{8\sigma}{9} \sqrt{\frac{3\sigma}{2R_B^3(P_0 + (2\sigma/R_B))}} \quad \text{for} \quad R_0 \ll R_r \quad (1-7)$$

Here R_0 is the equilibrium bubble radius which is termed R_B in the above equation; R_r is the radius of a bubble that would be in pulsation resonance with the incident sound field; P_B is the minimum acoustic pressure in which a gas bubble of radius R_B will explosively grow; P_0 is the hydrostatic liquid pressure outside of the bubble and σ is the surface tension. It is important to note that this equation neglects viscosity and inertial effects and hence can only be applied when the surface tension dominates and in quasi-static pressure changes (applied frequency must be lower than resonance frequency of the bubble; $R_0 \ll R_r$).

With the continuation of bubble expansion, the pressure in the liquid increases, exceeding the threshold value due to inertia effects. At a point the bubble growth can no longer be maintained and halts, and then begins to reduce in size. For a bubble collapse to be inertial, it must first grow explosively, and second collapse in such a way that the energy transferred to the bubble from the liquid is significantly concentrated, leading to the breaking up of the bubble. Non-inertial

Inertial

Figure 1.3 shows a schematic of the bubble radius as a function of time during inertial (right) and non-inertial collapse (left).

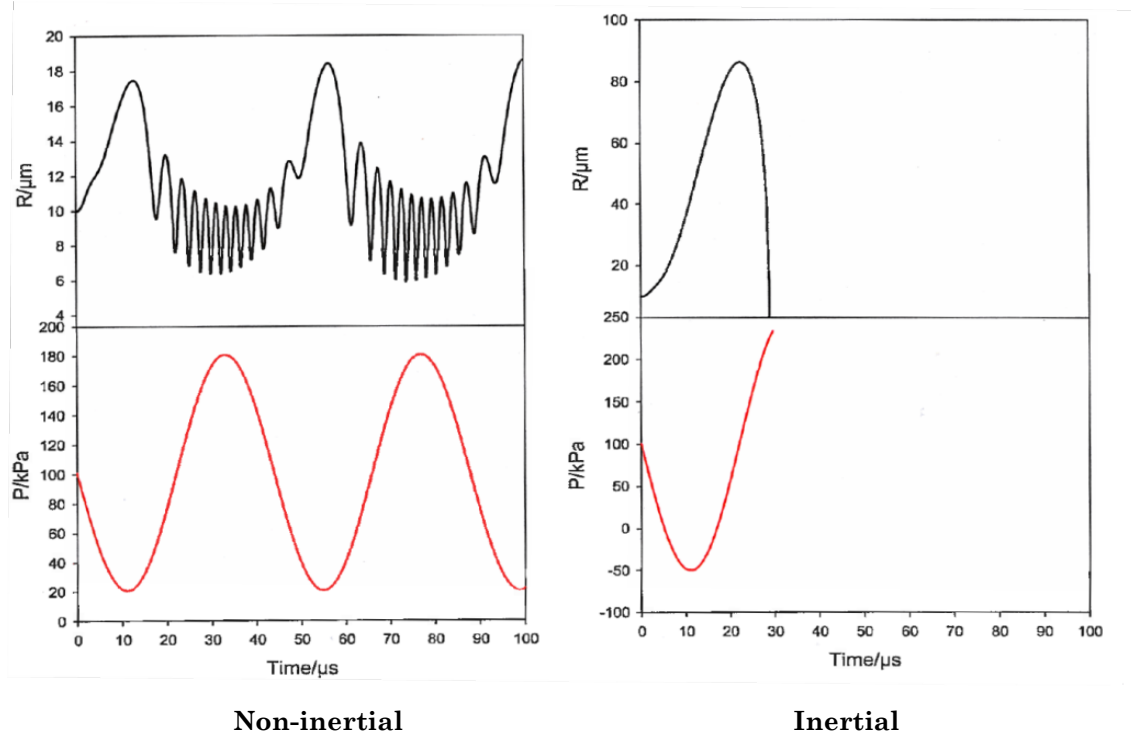


Figure 1.3 Plots showing the radius of a bubble (R) as a function of time under the action of a pressure wave. The bubble has an initial radius of $10\text{ }\mu\text{m}$ and is subjected to a sound field of 160 kPa peak to peak (left) or 300 kPa peak to peak (right). The right hand bubble undergoes an inertial collapse whereas the right hand bubble exhibits a repetitive oscillation. Taken from Vian [82].

The conditions that result in inertial cavitation are not only reliant on the acoustic pressure exceeding the Blake threshold and as such it does not explain whether the cavitation will be inertial or non-inertial. In order to ascertain the type of cavitation that will occur, Apfel manipulated models developed by Rayleigh [83] and Noltingk and Neppiras [84] to obtain an energy equation with respect to the bubble wall velocity [85]. By setting the maximum bubble wall velocity equal to the speed of sound in the liquid, the expansive threshold, $R_{max}/R_0 = 2.3$ is obtained, where R_{max} is the maximum bubble radius and R_0 the initial bubble radius. Hence according to Apfel's model the bubble must expand to at least 2.3 times its initial radius if the subsequent collapse is to be classified as inertial. This is known as the expansive threshold.

Flynn [86, 87] also derived an expansive threshold, of $R_{max}/R_0 = 2$. This was based on the limit at which the energy supplied to the liquid during bubble growth outweighs the dissipation effects during collapse, resulting in a sufficient concentration of energy for collapse. Here the bubble must expand to twice its size for inertial collapse to ensue, hence in good agreement with the Apfel expansive threshold.

Chapter 1: Introduction

Furthermore, Holland and Apfel [88] introduced a model based on the temperature generated within the bubble. Assuming adiabatic collapse, it is possible to calculate the maximum temperature (T_{max}) generated within a bubble exposed to a pressure field. Based on experimental data by Suslick *et al.* [89], an inertial event can be defined as one in which $T_{max} > 5000$ K. It should be noted that other temperatures have been used in the range 960 to 5000 K [90].

Figure 1.4 shows a plot of the described cavitation thresholds for an air bubble in water at an applied drive frequency of 23 kHz. The Blake threshold is shown to compare the limit for explosive growth of a bubble. The temperature threshold is derived from the Apfel and Holland model and the expansive threshold from the Apfel model.

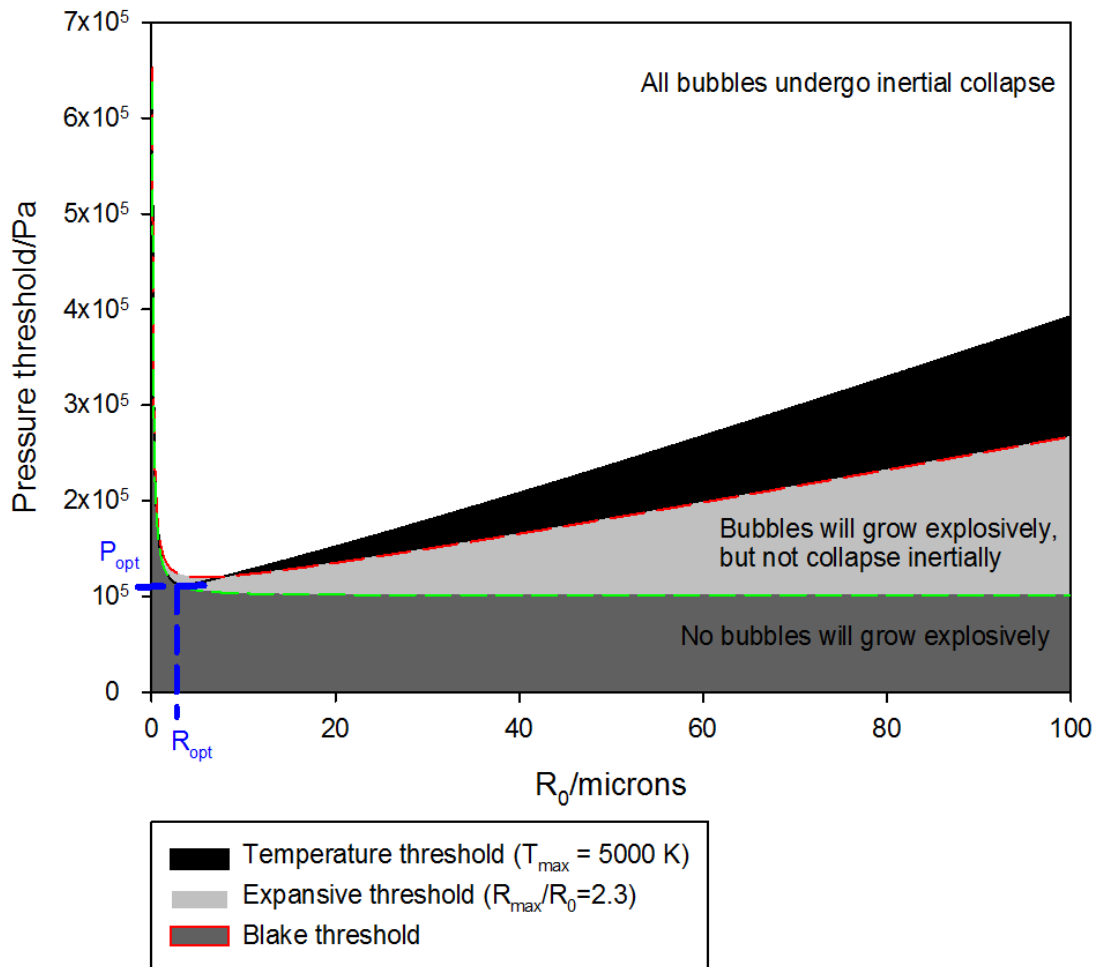


Figure 1.4 Plot showing the thresholds associated with the cavitation of an air bubble in water at an applied drive frequency of 23 kHz and hydrostatic pressure of 101325 Pa (1 atm). The temperature threshold is based on model developed by Holland and Apfel, where the maximum temperature in an inertially collapsing bubble is 5000 K. The expansive threshold is based on the criterion that $R_{max}/R_0 = 2.3$. For comparison the Blake threshold for explosive growth is also shown. Figure taken from Hanumanthu [91], based on the output from a program developed by Power [92].

The plot shows the variation in these thresholds as a function of initial bubble radius and drive pressure. Bubbles with initial conditions above the expansive and temperature thresholds can be classed as inertial depending on the chosen criterion. At the pressure corresponding to P_{opt} , only bubbles of radius R_{opt} will exhibit inertial collapse. At pressures greater than P_{opt} a range of bubbles larger than R_{opt} will undergo inertial cavitation.

It is important to note that the discussed thresholds for rapid growth and inertial collapse are used in an illustrative manner, due to the limitations and assumption of individual models. In reality, the inertial/non-inertial threshold is relatively blurred.

The bubble collapse associated with inertial cavitation leads to the extreme conditions which are known to generate the exotic phenomena associated with these events (acoustic emissions [93], the emission of light [94, 95], the destruction of organic material, chemical change [96, 97], and the erosion of a surface local to the cavitation source [98-100]). It is the erosive effects of inertial cavitation that are of interest for the activation of aluminium for hydrogen production. So far this situation has only been considered for a single bubble; however, much of the focus of the work presented in this thesis is on the effects bubble-bubble interactions within bubbles clusters. This is the topic discussed in the next section.

1.6.1 Cavitation clusters and erosion

The mechanisms by which cavitation causes erosion have been previously studied [7, 67, 100, 101]. The proposed processes responsible for erosion of surfaces during cavitation are shockwave and microjet impact onto the surface as a result of transient bubble collapse close to the solid/liquid interface [93, 98, 102, 103]. Here the erosive effect of multi-bubble structures is of interest.

A recent overview of bubble dynamics and the effects of multi-bubble interactions was presented by Lauterborn and Kurz [104]. They include a study on the types of multi-bubble structures that may form depending on the experimental conditions employed. The terms used by the authors to describe multi-bubble environments are listed in Table 1-3.

Chapter 1: Introduction

<i>Term</i>	<i>Description</i>	<i>References</i>
Cluster	Small group of bubbles	[105-107]
Cloud	Large group of bubbles	[104]
Bubble web	Filaments set up in a standing wave field	[67, 108-114]
Cone-like	Structure at a piston-like emitter (PLE) vibrating at high amplitude	[115]
Jelly-fish	Hemispherical cluster and streamers	[106]
Spherical	(and hemispherical)	[116, 117]

Table 1-3 Types of multi-bubble structures as detailed by Lauterborn and Kurz [116]

These multi-bubble structures are composed of bubbles of different radii and varied inter-bubble distances. In turn this affects the forces experienced by an individual bubble. The work presented here is primarily concerned with (hemispherical) bubble clusters formed on a downward pointing rod in an ultrasonic reactor.

The principle forces acting on bubbles arise from the liquid pressure as a result of the external sound field applied to instigate cavitation, as discussed in section 1.6. There are also forces which affect the translational motion of the bubble. A common method of addressing these forces is in terms of the time-averaged translational behaviour of bubbles, as described by Leighton [67], Doinikov [118] and others [116, 119-121]. This approach is based on the theory of acoustic radiation forces. It is well known that gas bubbles (and solid particles, liquid drops, etc.) suspended in an acoustically driven fluid undergo steady, time-averaged, hydrodynamic forces that make them travel, cluster and interact with one another. These acoustic radiation forces on gas bubbles are typically referred to as Bjerknes forces, named after C.A. Bjerknes and his son V.F.K. Bjerknes, who were the first to report on such forces [122]. The literature generally divides these forces into two types; primary and secondary Bjerknes forces. Primary Bjerknes forces are the forces experienced by single bubbles and cause them to migrate in an acoustic field or to gather in certain areas, such as pressure nodes or antinodes of standing sound waves. Secondary

Bjerknes forces are responsible for bubble-bubble interactions causing them to attract or repel each other, and can lead to stable bubble structures (such as detailed in Table 1-3) under certain conditions. Mathematically the Bjerknes force is calculated as the time average of a specified expression, which is the instantaneous force exerted on a bubble by the surrounding (acoustically excited) liquid. Accordingly, the sign of the Bjerknes force shows the resultant direction of the bubble translation in an acoustic field [123]. The reader is directed to the literature for comprehensive mathematical descriptions of Bjerknes forces [110, 118, 119].

The concept of the erosion of a surface caused by the collapse of a cloud of bubbles has been described by Hansson *et al.* [98, 124]. The energy associated with the collapse of a bubble (or shell of bubbles in a cluster) at the edge of a cluster is transferred to its neighbours. Highly energetic collapses at the centre of a cluster can result, due to the inward concentration of energy. The ensuing violent microjet and shock wave impacts are still attributable to individual bubbles, but the magnitude of the effect is magnified by the cluster collapse.

The advantages of the described erosive nature of cavitation are exploited in a number of heterogeneous electrochemical processes. In particular, the application of ultrasonically generated cavitation has been employed to produce erosive effects for electrode depassivation in electrosynthetic [125, 126] and electroanalytical [127-129] processes. This principle is also utilised in an erosion sensor developed by Birkin *et al.* [7, 8]. The design and application of the erosion sensor system to electrochemically detect erosion generated by acoustic cavitation is well documented in the literature [7, 130-135].

The erosion sensor is essentially a disk electrode consisting of an aluminium wire supported by epoxy resin within a stainless steel encasing which is used as the counter/reference electrode (see experimental section 2.1.6 for fabrication details). In this two-electrode electrochemical technique, the aluminium working electrode is held under potential control in a 'passive' state to form an insulating oxide layer. In the absence of any erosion mechanisms no current is observed. Inertial cavitation in the environment local to the electrode surface can induce erosion of the passive layer, rendering the exposed material electrochemically active. This depassivation is then followed by reformation of the passive oxide layer. The current that passes through the electrode to oxidise the material at the surface is

Chapter 1: Introduction

recorded as a function of time. It is the repassivation under electrochemical control that is the observed current *vs.* time signal.

Figure 1.5 (taken from Birkin *et al.* [130]) illustrates the erosion/corrosion of a passivated electrode interface by a single cavitation event and the time periods associated with each respective step. An example current time transient generated from an erosion event (taken from Vian *et al.* [136]) is shown in Figure 1.6.

Investigation into the erosive effects of cavitation clusters was performed, utilising the described erosion sensor principle. As discussed, other products of inertial cavitation include the generation of heat, the emission of light and the cause of chemical change. These effects can be measured and are used to investigate and characterise inertial cavitation. Information on these effects is presented in the next section.

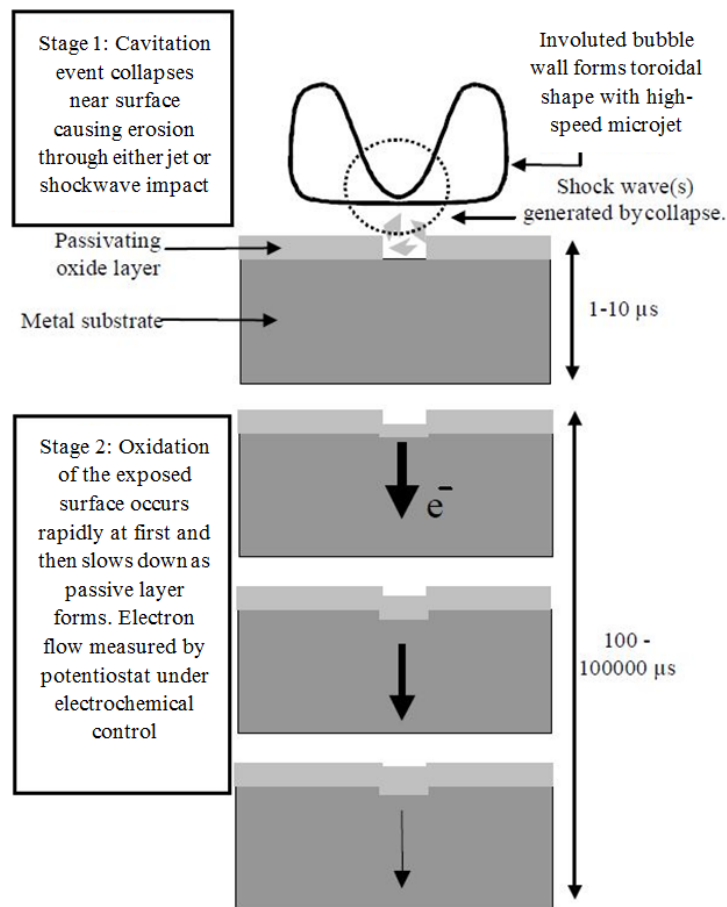


Figure 1.5 Schematic illustrating the erosion of a passivated interface by a single cavitation bubble, taken from Birkin *et al.* [130].

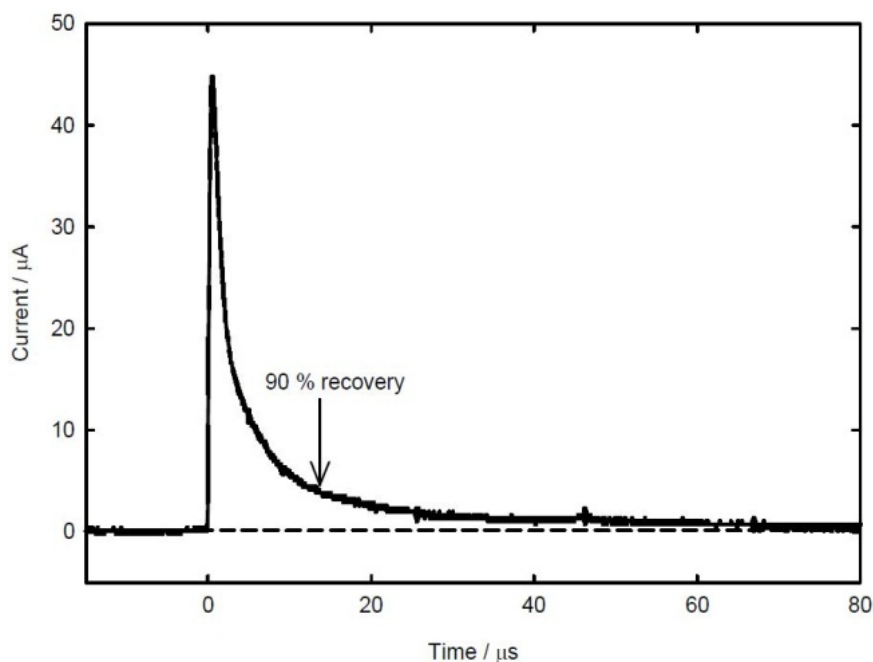


Figure 1.6 Plot showing a typical current time transient recorded for a surface event on an aluminium electrode (\varnothing 250 μm). The ultrasonic drive frequency was 23.17 kHz and the voltage amplitude to the transducer was 100 V (zero to peak) corresponding to a power of $56 \pm 5 \text{ W cm}^{-2}$ [131]. The electrode was positioned 0.5 mm from the tip of an ultrasonic horn. Plot taken from Vian[136]

1.6.2 Sonoluminescence

The bubble collapse associated with inertial cavitation leads to extreme conditions which are known to generate a range of exotic phenomena. One of these phenomena is the emission of light [67, 94]; a process termed sonoluminescence (SL). The literature postulates a variety of different mechanisms for sonoluminescence, including thermal [84, 137], mechano-chemical [138, 139] and electrical [140, 141] processes, to name only a few of the large number of relevant publications in this intensively debated and complex subject. However the majority of recent works attribute the observed effects to sonochemical processes involving reactive species (free radicals and electronically excited molecules) which may occur as a result of high temperatures generated within the collapsing bubble [67].

Sonoluminescence can occur as a result of single or multi-bubble collapse. Single bubble sonoluminescence (SBSL) can ensue the collapse of a single bubble which has formed at the anti-node of a standing wave caused by ultrasonic irradiation of liquid in a cell. Under optimum conditions, SBSL can take place as a sequence of flashes which occur periodically and simultaneously with the bubble collapse. This was demonstrated by Gaitan *et al.* [142] as shown in Figure 1.7.

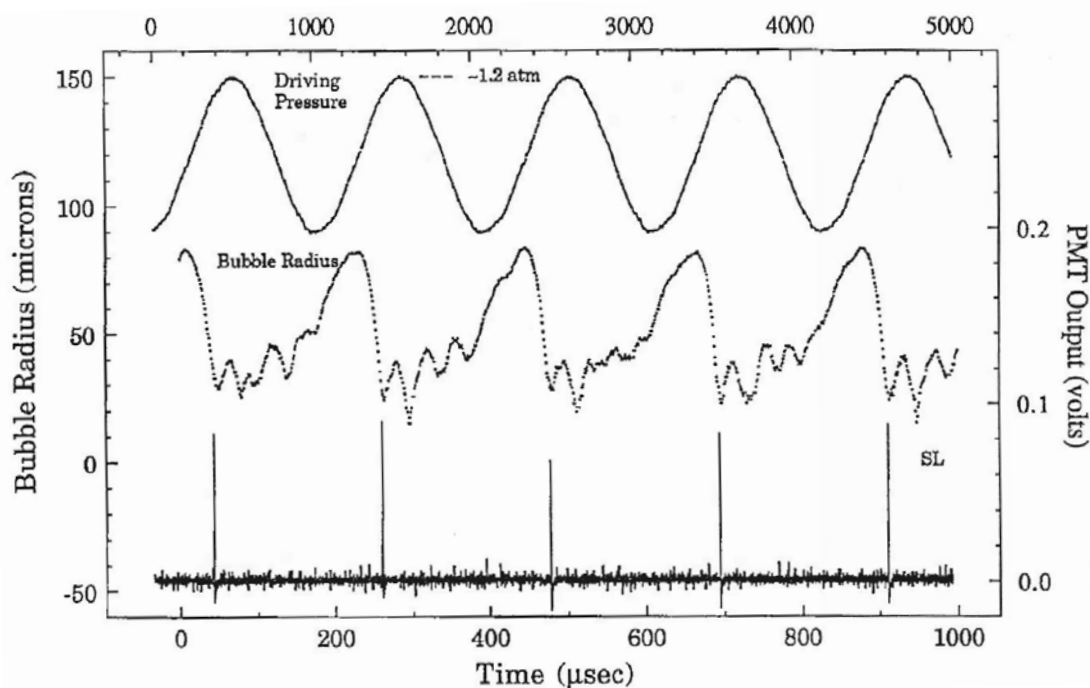


Figure 1.7 Simultaneous plots of the sound field (top, no y-axis), bubble radius (middle, left y-axis) and photomultiplier output (bottom, right y-axis). The cell contained glycerine and was driven at $P_A = 1.2$ atm and $\nu = 22.3$ kHz in glycerine (21% wt. in pure water). Experiment conducted by Gaitan *et al.* [142].

Multi-bubble sonoluminescence (MBSL) is the emission of light from a cluster of cavitating bubbles. The bubbles within the cluster are subjected to differing pressures depending on their spatial location and as such it is likely that only a proportion of the bubbles with the cluster actually emit SL.

Light generation can also be achieved indirectly through coupled chemical reactions (e.g. sonochemiluminescence (SCL)). This phenomenon can be defined as the emission of light as a result of a chemical reaction triggered by acoustic cavitation. Luminol is used in the work presented here as it is well known to emit light when exposed to ultrasound of sufficient intensity to produce inertial cavitation.

The mechanism of sonochemiluminescence has been investigated by a number of authors [143, 144], determined as shown in Figure 1.8. The reaction involves initial oxidation as a result of the generation of the hydroxyl radical species, $\text{OH}\cdot$. Note, the mechanism also suggests $\text{O}_2\cdot$ is important in the overall reaction.

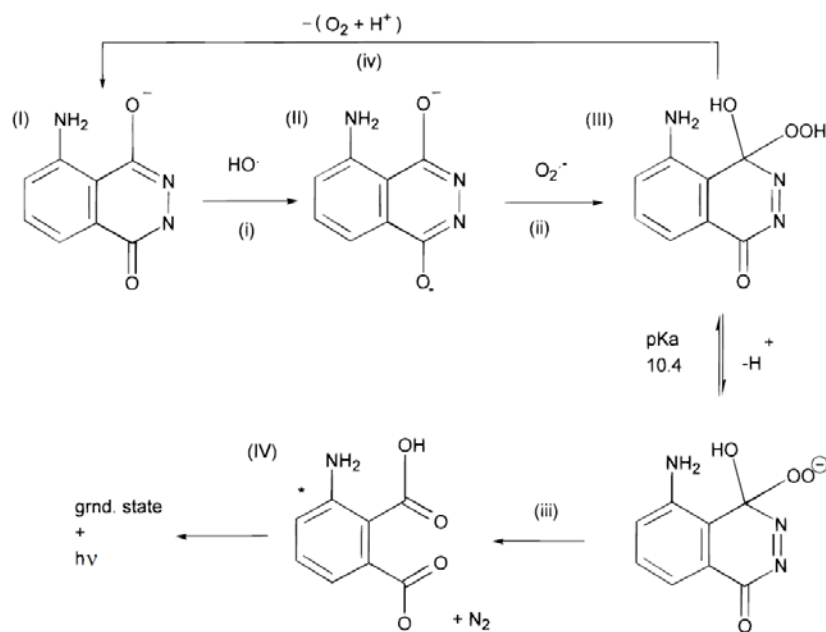


Figure 1.8 Mechanism of sonochemiluminescence of luminol proposed by McMurray *et al.*[143]

This mechanism indicates strong pH dependence with alkaline solutions being more effective. H_2O_2 concentration also has a significant effect on the level of light emission [143, 145]. Furthermore, the addition of EDTA prevents the possibility of any artificial signal generation, by chelating any contaminant metal ions that might otherwise catalyse the decomposition of H_2O_2 to OH^\bullet [92].

In previous studies, SCL of luminol has been used to visualize the spatial distribution of cavitation in solution [143, 145, 146]. It should be noted that the level of light generated by sonochemiluminescence is significantly greater than that recorded for sonoluminescence (SL) in isolation, a process in which light is emitted from the cavitation alone. Birkin *et al.* [145] and Offin [131] have shown that there is good correlation between sonoluminescence, of which the light is directly attributable to the inertial cavitation, and sonochemiluminescence. However, SCL can be falsely directly attributed to cavitation due to forced convection attributed to acoustic streaming effects [131], which may carry reaction products away from the cavitation source. As such care must be taken when drawing conclusions on the spatial distribution of cavitation through the interpretation of SCL measurements.

1.6.3 Characterisation of acoustic cavitation

Investigation of acoustic cavitation was primarily undertaken in the work presented here through study of the discussed erosion, sonochemiluminescence and

Chapter 1: Introduction

temperature effects. These measurements can be complementary and provide a greater understanding of the complex cavitation environment. However of course these are not the only effects or measures of cavitation that can be examined. Indeed, despite the extensive application range of high power ultrasound and acoustic cavitation, there is no recognised and agreed standardised measure of cavitation. A study in 1996 compiled and analysed the views of almost 70 experts in the field and demonstrated the significant need for standardisation [147, 148], comprised of a stated medium, sound field, and detector, plus a scale or end point. For a detailed description of different techniques used to measure cavitation, the user is directed to the report [148].

Subsequently, research into the production of a reference cavitation source [149-151] and the feasibility of a reference cavitation medium [152] was conducted. This led to the formation of a project to investigate the attributes of a range of sensors, with a view to illuminating the aspects of possible future ‘standard sensors’, entitled “Characterisation Of Measures Of Reference Acoustic Cavitation” (COMORAC) [153]. The study utilised the developed reference cavitation source [149] and tested a range of sensors based on sonoluminescence, sonochemiluminescence [145], sonochemical sensors including the Weissler reaction [154, 155], Fricke [156] and terephthalic acid [157] dosimetry, calorimetry, erosion sensors based on polymer degradation [158], electrochemical techniques [7] and foil erosion [159], and acoustic sensors including a broadband passive sensor [160, 161], a focussed bowl passive sensor [162, 163] and a subharmonic activity indicator [164]. The study compared the techniques and highlighted the advantages and disadvantages of their use in limited ‘real-world’ conditions, *i.e.* away from the ideal laboratory testing environment. The report concluded that further COMORAC studies were required, in which iterative development of the reference cavitation source and measures of cavitation should be made.

Further research into the characterisation of cavitation has been conducted with single [165] and multi-frequency [166] reference cavitation vessels. The experts in this field continue to work towards the ultimate aim of producing a recognised standard source and measure of acoustic cavitation in water.

The details of the experimental setup and conditions for the cavitation investigation experiments, and of those experiments discussed in the proceeding chapters, are discussed in the following chapter.

Chapter 2: Experimental

This chapter provides a guide and reference point for the experimental research conducted during the course of the EngD, the results of which are discussed in the proceeding chapters. An overview of the general experimental conditions is presented first, which includes details of the chemicals, equipment and fabrication processes. This is followed by the details of each individual experiment.

2.1 General experimental methods

In all experiments, any water used was first processed using a water purification system (Pur1te select™ by ONDEO, conductivity: $< 0.07 \mu\text{S cm}^{-1}$). All glassware was immersed in decon90 surfactant solution (*ca.* 3%) for a minimum of 3 hours and then rinsed with purified water and the relevant experimental solution prior to use when possible. All chemicals were used as received and without further purification. Table 2-1 presents a list of the chemicals used with the supplier and purity.

2.1.1 Chemicals

<i>Chemical</i>	<i>Supplier</i>	<i>Purity</i>
Aluminium grit	Merck Millipore	>99.0 %
Aluminium oxide (0.3 + 1 μm)	Struers	Unknown
Aluminium oxide (25 μm)	Buehler	Unknown
Aluminium pellets	Sigma Aldrich	>99.9 %
Ceric oxide	Fluka	>99.9 %
EDTA	Fisher Scientific	>99.0 %
Hydrogen peroxide	Timstar Laboratories	>99.8 %
Iron (III) chloride	Sigma Aldrich	>96 %
Luminol	Sigma Aldrich	>97.0 %
Potassium ferricyanide	Sigma Aldrich	>99.0 %
Potassium ferrocyanide	Fisher Scientific	>99.9 %
Sodium carbonate	Fisher Scientific	>99.5 %
Sodium chloride	Fisher Scientific	>99.9 %
Sodium hydroxide	Fisher Scientific	>99.9 %
Sodium sulphate	Sigma Aldrich	>99.0 %
Strontium nitrate	Sigma Aldrich	>99.0 %

Table 2-1 List of chemicals used

Chapter 2: Experimental

2.1.2 Vessels and reactors

Investigation within the Birkin research group at Southampton has previously been focussed on two methods of generating ultrasound; the use of an ultrasonic horn or the application of an ultrasonic transducer, typically fixed to the underside of a cell to make a reactor. This investigation primarily makes use of the latter.

Throughout this thesis, various combinations of cells and transducers were used to make construct ultrasonic reactors. For ease of reference, they are labelled as follows.

Reactor 1: A cylindrical quartz glass cell, dimensions as shown in Figure 2.1(a).

Reactor 2: A modified borosilicate glass Dreschel bottle with dimensions as shown in Figure 2.1(b). Note the transducer was later added for the outgassing experimentation as discussed in Chapter 4.

Reactor 3: A modified borosilicate glass Dreschel bottle with dimensions as shown in Figure 2.1(c) and SQ13 threaded ports. The base of the bottle was replaced with a thinner piece of glass than normal.

Reactor 4: A cuboidal PMMA cell, dimensions as shown in Figure 2.1(d).

The reactors employed commercially available piezoelectric transducers (reactors 1, 2 and 4: MP Interconsulting, transducer type MPI-C-28, reactor 3: Beijing Chengcheng Weiye Science and Technology Co. Ltd., transducer type CCH-4535D-28ZBPZT-4). Both transducer types have a resonant frequency of 28 kHz. The transducers were affixed to the cells using quick-set epoxy resin (Araldite). Unless otherwise stated, a function generator (Thurlby TTI TG101) was used to generate the signal, which was amplified using a power amplifier (Brüel&Kjaer type 2713). BNC connectors were soldered on to the transducer contacts so that a BNC cable could be used to connect the transducers to the power amplifier. Details of the settings used to generate the signal are detailed in each relevant figure caption.

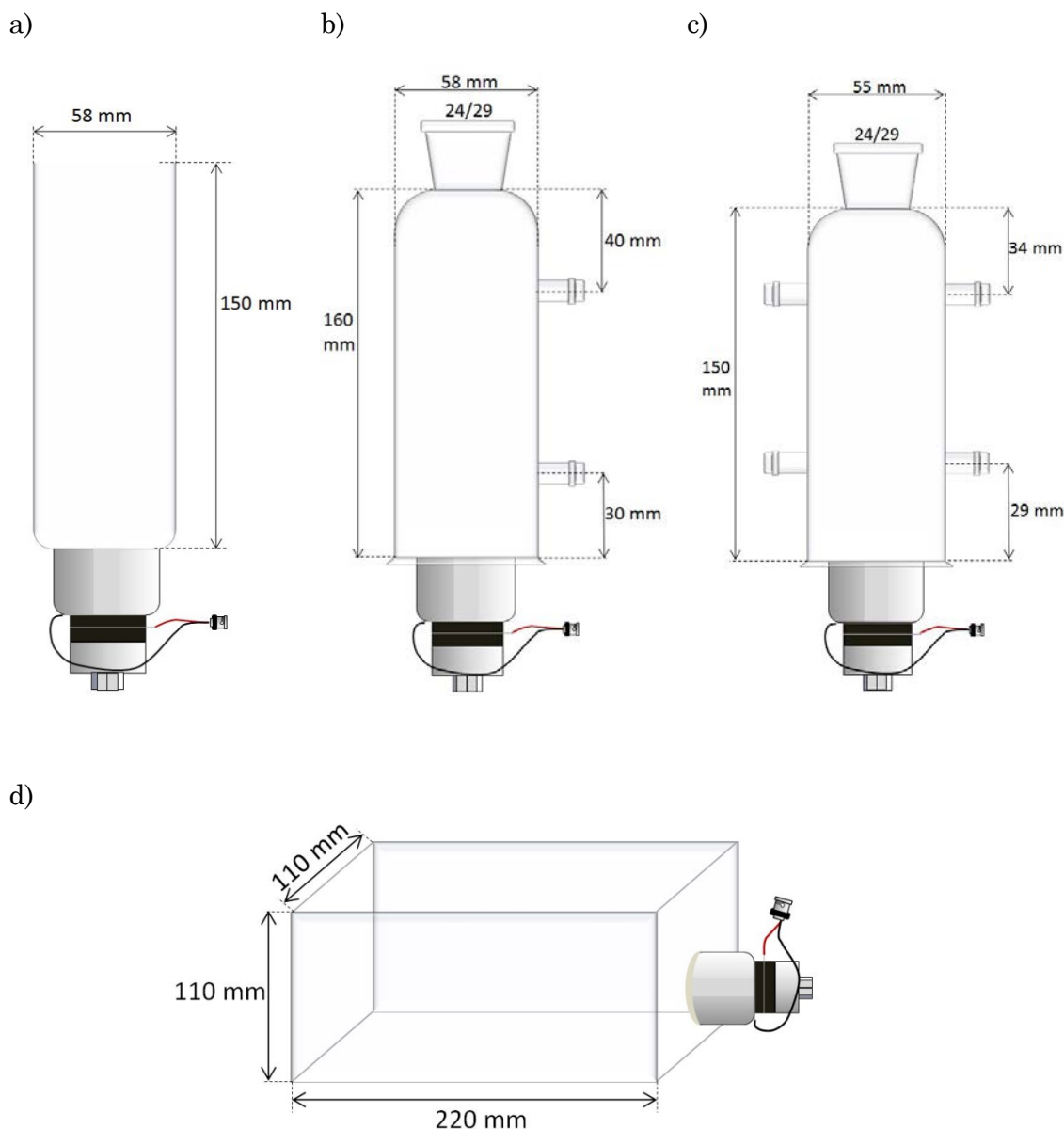


Figure 2.1 Schematic drawings of ultrasonic reactors: a) Reactor 1, a cylindrical quartz glass cell, b) Reactor 2, a modified borosilicate glass Dreschel bottle, c) Reactor 3, a modified borosilicate glass Dreschel bottle with SQ13 threaded ports, d) Reactor 4, a cuboidal PMMA cell. Reactors 1, 2 and 4 consist of transducers from MP Interconsulting (*type MPI-C-28*) and reactor 3 has a transducer from Beijing Chengcheng Weiye Science and Technology Co. Ltd. (*CCH-4535D-28ZBPZT-4*). Both of these transducer types are resonant at 28 kHz.

Chapter 2: Experimental

2.1.3 Pressure measurements

The pressure fields and cavitation noise generated in the reactors were measured through the use of hydrophones placed within the liquid. Two types of hydrophone were employed (TC4013 and TC4038, Teledyne Reson) and the hydrophone output was monitored on oscilloscopes (Owon SDS-7102V or Gould DSO465) and transferred to a PC. In-house written software (appendix 11: FFT oscilloscope.vbp) was used to process the data by performing an FFT analysis of the signal with comparison of the input and output signals.

2.1.4 Temperature measurements

Real-time temperature measurements were acquired using a K-type thermocouple (Pico Technology), positioned in the relevant cell or liquid flow. The thermocouple was interfaced to a computer via a thermocouple data logger (USB TC-08, Pico Technology). In-house written software (appendix 11: HTOGO FFT.vbp) or software supplied with the data logger (PicoLog, Pico Technology) was used to monitor and save the temperature data.

2.1.5 Imaging techniques

2.1.5.1 High-speed imaging

High-speed imaging was utilised in numerous experiments in order to investigate processes occurring at millisecond and microsecond timescales. A high-speed camera (Photron APX-RS was used in combination with different lenses, which are detailed in each individual experimental description). The camera is capable of capturing frames at 250,000 fps with exposure times as low as 1 microsecond, however at the cost of reduced resolution. The frame rate and exposure times are stated in the description of each experiment and in each relevant figure legend. The camera was connected to a computer via a FireWire cable and commercial software (Photron FASTCAM Viewer 3.0) was used to control the camera and transfer and save the data.

2.1.5.2 Sonoluminescence and Schlieren imaging

Images for the sonoluminescence experiments were acquired using an intensified CCD camera (DS-800, Photonic Science) connected to a frame grabber. In order to detect a low level of light, SL experiments were performed in blackout conditions.

The Schlieren experimentation utilised the high-speed camera with a 12x adjustable zoom lens (Navitar). The camera was positioned on an XY stage (Manfrotto) in order to provide the fine adjustment required in the Schlieren experiments.

Further details of the setup for each individual experiment are detailed in each relevant section.

2.1.6 Aluminium electrode/erosion sensor

Aluminium electrodes were constructed to be used as erosion sensors in the relevant experimentation. These were fabricated by encasing aluminium wire (Advent research materials, 250 μm \varnothing , purity: 99.98%) in stainless steel tubing (6 mm O.D., 4 mm I.D.), sealed with slow set epoxy resin (Struers). The diameter of the electrode was chosen as it provides a compromise between the ease of fabrication, the shape of the resultant current time transient produced by erosion, and its relative size with respect to the erosive event produced by ultrasound in the environments in question [82, 131, 132]. Shielded cable (1 m length, RS components) was used to connect the electrode to the potentiostat via two connectors; an SMA crimp plug and a BNC connector (both RS components). Unless otherwise stated, the electrode surfaces were pre-treated by polishing in a figure of eight motion with silicon carbide paper and successive grades of alumina slurry (1 μm and 0.3 μm Al_2O_3 , Struers) supported on polishing pads (MicroCloth by Buehler). Inspection of the surface was performed using a camera (CV-S3200, Jai) with macro-lens (12 x zoom, Navitar) to confirm a smooth reproducible surface.

The aluminium electrode was held at 0 V *vs.* the stainless steel encasing reference/counter in order to simplify the apparatus employed. The sensor was used in conjunction with an electrical device (constructed in-house) consisting of a current follower to amplify the signal and optocoupler as shown in Figure 2.2.

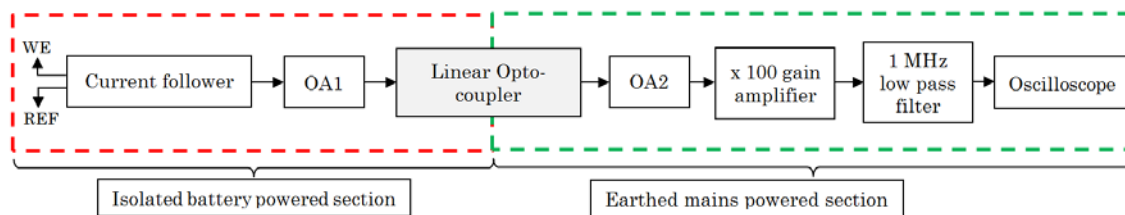


Figure 2.2 Schematic showing the opto-isolation apparatus, the electrochemical cell, and recording equipment. The isolated battery powered (— —) and mains powered (— —) sections are highlighted. OA1 and OA2 refer to appropriate op-amps employed in the system. Schematic adapted from Vian *et al.* [129].

The circuit was designed such that the only connection between the electrochemical circuit and the earthed environment was through an optically isolating linear opto-coupler (IL300). This is highlighted in Figure 2.2. The employed linear opto-coupler consisted of an efficient AlGaAs LED emitter coupled to two independent PIN photodiodes. In addition to one of the photodiodes transferring the signal from the electrochemical circuit, the second photodiode ensured the linearity of the output using a simple feedback circuit [132]. This arrangement was adapted from the comprehensive application notes provided by the manufacturer [167]. An oscilloscope (Gould DSO 465) was used to monitor the current output.

Experiments which monitored the long term effects (see section 3.2.2) of erosion employed a Schmitt trigger counting system (detailed in section 3.2.2), the output of which was interfaced to a PC using a USB data acquisition module (Cole Parmer, WZ-18200-10) and in-house written software (appendix 11: Cavitation sensor.vbp).

2.1.7 HTOGO Electrolysis Device

Several areas of the research presented in this thesis involve the study of gas produced from an electrolysis device, the details of which are now given. The device employed in these experiments was designed and constructed by the sponsoring company, HTOGO Ltd. Figure 2.3 shows a schematic of the design and a photograph of the device. The bipolar cell stack consists of eleven stainless steel plates (thickness = 1.0 mm, separation = 1.0 mm, 316L grade – for steel elemental composition see appendix 1) which form ten electrochemical cells in series. The outer two plates were connected to the negative terminal (cathodes) of the power supply (ISO-TECH IPS-1820D) and the centre plate to the positive terminal (anode), as labelled in Figure 2.3. The four plates in between each anode and cathode are not directly connected to the power supply and are denoted with an ‘N’ to highlight this. Nevertheless the plates are electrochemically active and will act

as *de facto* anodes and cathodes, with alternating polarity either side of each plate in the series. The power supply was always operated in constant current mode and a switch unit (built in-house) was used to connect and disconnect the power supply from the electrolysis device.

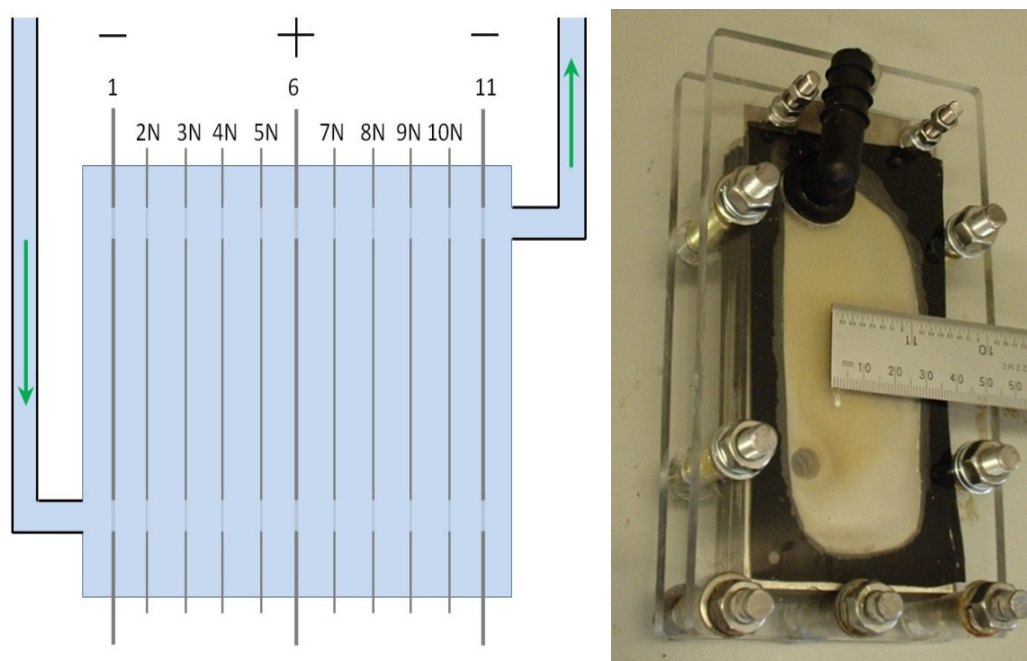
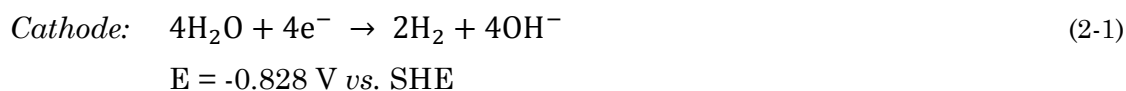


Figure 2.3 Electrolysis device designed and constructed by HTOGO Ltd. The green arrows show the direction of the liquid flow. The plates are numbered for reference. Plates denoted with an 'N' for 'Neutral' are plates that are not directly connected to the power supply.

During the process of water electrolysis, water is consumed at the cathode and reduced to produce hydrogen gas and hydroxide ions. At the anode, hydroxide ions are oxidised to produce oxygen gas and water. The half reactions and equilibrium potentials (obtained from the Nernst equation) for the production of hydrogen and oxygen gas in alkaline conditions can be written as shown in eqs. (2-1) and (2-2).



Chapter 2: Experimental

Hence the overall reaction of water electrolysis can be written as shown in equation (2-3) and the equilibrium cell voltage for the overall cell reaction is 1.229 V at 298 K, which relates to a Gibbs free energy change of 237.2 kJ. This is the minimum amount of electrical energy required drive the reaction. However in practice it is essential to apply a higher potential to enhance the rate of electron transfer processes to drive the current to overcome ohmic losses inherent in the system.

2.1.8 Hydrogen detection and measurement

Several of the conducted experiments required the ability to detect and measure the concentration of hydrogen gas, either produced from an electrolysis cell or via reaction of aluminium with aqueous solutions. A commercial carbon monoxide (CO) sensor (Alphasense, CO-BF) was used for this purpose. The device exhibits a suitable hydrogen cross sensitivity of 65% compared to carbon monoxide at 400 ppm with a maximum working limit of *ca.* 3% H₂ [168]. The sensor is essentially a conventional three electrode system and was controlled by a potentiostat (made in-house by T.W.Young). The output signal was sent to a data acquisition card (Cole Parmer 18200-10) connected via USB to a computer. A machined aluminium casing was designed and fabricated to hold and seal the sensor in position to allow gas to pass over the surface (see appendix 2). Copper piping was used to channel the gas flow from the source to the sensor and finally evacuate it from the system. An air compressor pump (Clarke Wiz Air) was used to flow air through the cell and over the sensor, which was positioned downstream of the apparatus as demonstrated in Figure 2.4. The gas flow was regulated by an airflow controller (GEC-Elliott Process Instruments) and monitored with an airflow sensor (Honeywell, AWM43300V). The airflow sensor output was interfaced to a PC using a data acquisition card (Cole Parmer 18200-20. All of the sensor connected to the PC were interfaced using in-house written software (appendix 11: HTOGO FFT.vbp), which processed and saved the data.

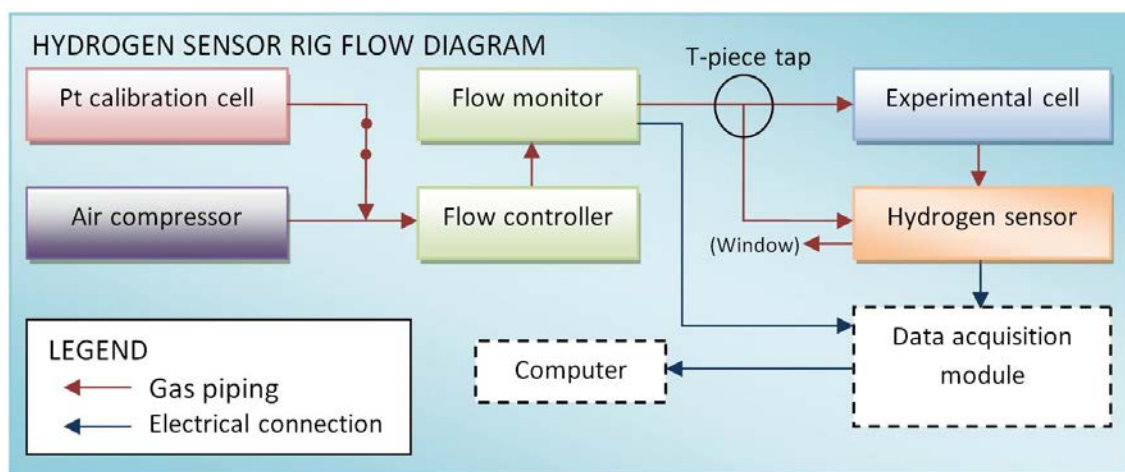


Figure 2.4 Schematic showing the gas flow system for the hydrogen sensor, used in several of the experimental setups

In order to calibrate the sensor response to a known amount of hydrogen gas, a small electrolysis cell was designed and constructed. The dual compartment glass cell (depicted in Figure 2.5) housed two lengths of platinum wire ($\varnothing = 500 \mu\text{m}$, Goodfellow, 99.99 % purity) separated by a glass frit. The cell was filled with H_2SO_4 (0.1 M) solution and a potential difference was applied across the two wires with a DC power supply (ISO-TECH IPS-1820D) in constant current mode. The current and air flow were varied in a series of experiments whilst recording the applied current, the airflow and the gas sensor response. The oxygen gas produced at the anode was evacuated from the system whilst the hydrogen gas produced at the cathode entered the air flow which was channelled to flow over the gas sensor. Table 2-2 shows the values used for the experimental variables, chosen to give a range of hydrogen concentrations. The amount of hydrogen generated is proportional to the current passed and so the sensor response was calibrated to the varying steady state concentrations of hydrogen.

Chapter 2: Experimental

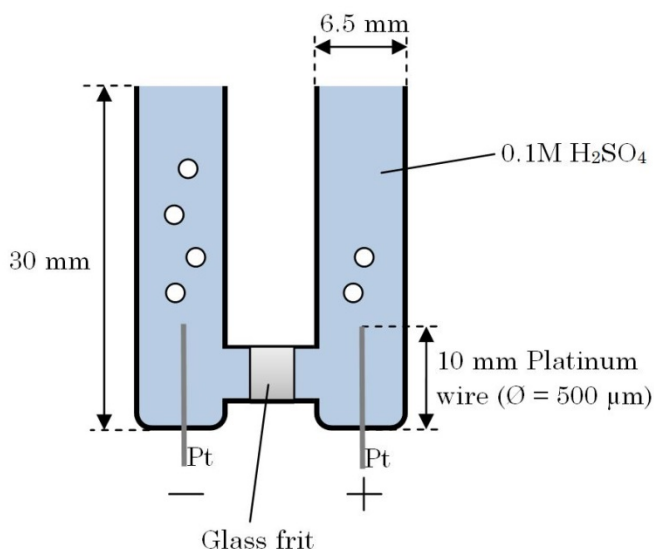


Figure 2.5 Drawing of electrolysis cell consisting of two platinum electrodes ($\varnothing = 500 \mu\text{m}$) used to calibrate the CO-BF sensor for hydrogen gas

<i>Airflow</i> <i>/cm³ min⁻¹</i>	<i>Applied current</i> <i>/μA</i>	<i>Theoretical H₂</i> <i>flow</i> <i>/cm³ min⁻¹</i>	<i>Theoretical H₂</i> <i>percentage</i> <i>/%</i>
630.31	15.10	0.12	0.01830
768.14	15.10	0.12	0.01500
399.14	15.10	0.12	0.02890
151.62	15.10	0.12	0.07610
151.54	15.10	0.12	0.07610
308.07	15.10	0.12	0.03740
308.54	15.10	0.12	0.03740
308.72	9.09	0.07	0.02250
158.89	9.09	0.07	0.04360
500.19	9.09	0.07	0.01390
124.16	9.09	0.07	0.05580
743.25	9.09	0.07	0.00933
327.86	9.09	0.07	0.02110
487.74	9.09	0.07	0.01420

Table 2-2. Range of values tested for the hydrogen sensor calibration experiments. Details of the airflow and applied electrolysis current are given with corresponding hydrogen gas generation rate and concentration.

Results from the calibration experiments are presented in Figure 2.6, which shows the current output from the sensor for known concentrations of hydrogen generated by the platinum electrolysis cell.

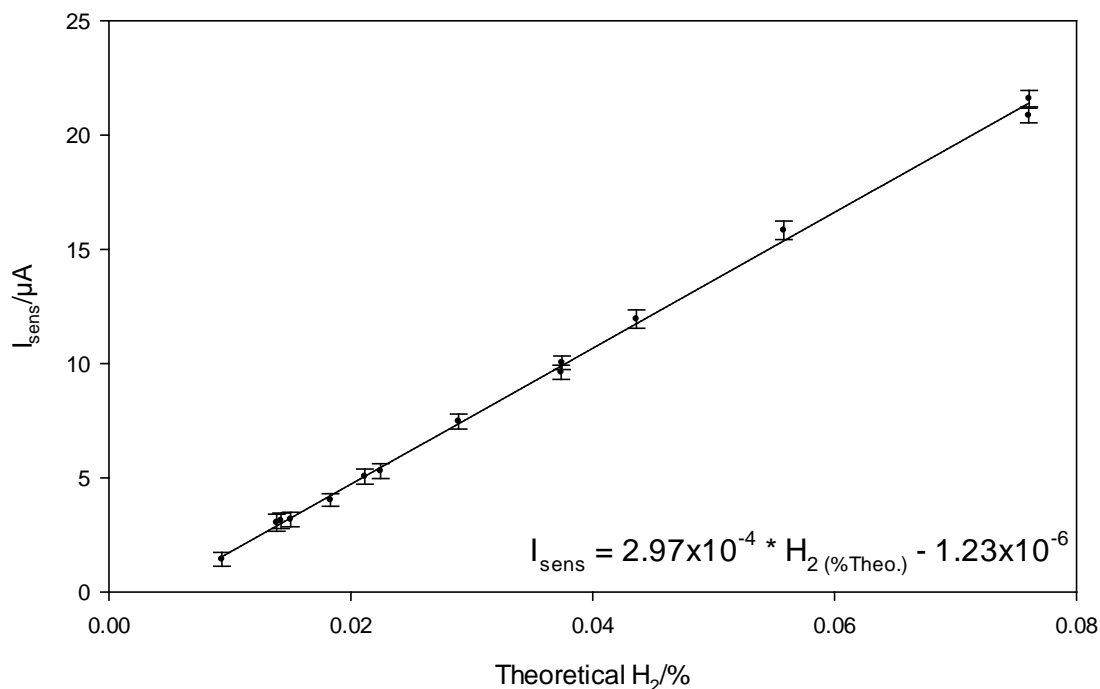


Figure 2.6 Plot showing the current response of the sensor versus the theoretical amount of hydrogen, across the tested range of applied currents and airflows. Each point represents an average of the steady state current at each concentration with the standard deviation represented with error bars. A linear regression was performed and the resulting relationship as given in the plot was used to convert the sensor signal into a concentration of hydrogen gas.

The airflow and current range details are disclosed in Table 2-2. As expected from the product literature, the sensor exhibits a linear response across the range of concentrations tested. The equation of the best fit polynomial line was used to convert the sensor signal to a hydrogen percentage and this was programmed into the visual basic program (appendix 11: HTOGO fft.vbp). The r-squared value is very close to 1 and hence shows that the linear regression is sufficiently accurate to use as a calibration.

Furthermore tests of the sensor response at higher hydrogen gas concentrations showed that the experimental results produced from the electrolysis cell are valid. The highest calibrated concentration of 2 % hydrogen in air produced a sensor response of 6 mA. This fits with the linear regression produced from the lower concentrations.

The hydrogen calibration was also validated by a separate experiment in which a comparison of the volume of hydrogen collected in a gas syringe and the theoretical amount was made. The total charge passed was 15.31 coulombs, which equates to

Chapter 2: Experimental

1.95 cm³ of hydrogen, calculated using Faraday's Law. The syringe contained 2 cm³ (± 0.1 cm³) of gas which compares well to the theoretical amount. Therefore the calibration of the CO response against the theoretical amount is validated. Details of this calibration are shown in appendix 3.

In order to validate the assumption that the electrolysis process is performing at a Faradaic efficiency of 100 % and that the concentration calculations are therefore correct, an experiment was conducted to volumetrically measure the hydrogen gas being produced. A gas syringe (5 cm³ \pm 0.1 cm³, SA-CO) was used to collect the hydrogen from the cell whilst monitoring the applied current. The charge was calculated and the volume of gas collected was compared to theoretical amount.

2.1.9 AC-modulation technique

A system was designed and developed to measure the uncompensated resistance in experiments in which the electrolysis cell was employed. By successfully measuring and monitoring the uncompensated resistance of the electrolyte during device operation, a greater understanding of the system was reached and reasoned improvements were more easily applied. Initial experiments made measurement of the uncompensated resistance across two of the neutral plates in the electrolysis cell (labelled with the suffix 'N' in Figure 2.3). This evolved into a separate resistance measurement module positioned at the outlet of the reactor. Both of these systems are discussed further in the relevant sections, 4.1.3 and 4.1.3.3 respectively.

In both systems, a function generator (TiePie Handyscope HS3) was used to apply a sinusoidal wave (16 kHz, 100 mV_{pp}) across the plates, through the liquid. The return signal was sampled via an ADC (Cole Parmer 18200-20) card interfaced to a PC. A Fourier transform was performed on the data, giving signal amplitude data across the frequency spectrum. The resistance was calculated according to *Ohm's Law*, with the calculated amplitude from the Fourier transform at the input frequency (converted to current using the gain employed) and the amplitude of the input signal. The interfacing of the card to the PC and all of the data analysis was completed using in house written software on Microsoft Visual Basic 6 (appendix 11: HTOGO FFT.vbp).

Chapter 3: Cavitation bubble clusters

This chapter reports a study of bubble clusters produced on the face of a downward pointing rod immersed in an ultrasonic reactor. These bubble clusters are normally investigated on the tip of an operating piston-like emitter [169-171]. However, as will be shown here, stable clusters can be produced on a stationary cylinder or rod placed with a suitable sound field. The cluster that forms is then characterised with techniques associated with the investigation of inertial cavitation. This approach was adopted as it allows the unusual physical [93-95, 171, 172] and chemical [96, 97, 172, 173]) conditions generated by inertial cavitation to be studied during this stable cluster collapse. In particular surface erosion [7, 98-100, 133, 174-177], chemical activity [135, 145, 177-180] and local temperature effects [181, 182] were investigated. Finally the utilisation of the cluster for the production of molecular hydrogen is presented.

3.1 Ultrasonic reactor characterisation

Investigation into the nature and effects of cavitation clusters was conducted primarily with ultrasonic reactor 1 (section 2.1.2 for details). Characterisation of the sound field in this reactor was undertaken using hydrophones to measure the pressure under varying conditions. Furthermore rheoscopic (literally “flow showing” [183]) particles were employed to aid the visualisation of the standing wave structure in the generated sound fields. These highly reflective and thin plates are widely used as a tool to visualize liquid flow behaviour (typically 10’s to 100’s μm^2 in area x 0.07 μm thickness - see appendix 4 for SEM image of particles) [183-186]. Here they are used to visualise the standing wave patterns associated with different acoustic modes generated within the reactor.

Figure 3.1 shows an image of reactor 1 overlaid with the measured pressure as a function of hydrophone-to-base distance. The reactor was filled with purified water (230 cm^3) containing rheoscopic particles (0.025 g, PM-01 tracers, Kalliroscope) and irradiated with ultrasound (28 kHz, 3 V_{pp} from amplifier monitor). The images obtained showed that the observed particle distribution was unchanging over time under these conditions. Two different hydrophones were used to measure the acoustic pressure field (TC4013 and TC4038, Reson) at varying distances from the base of the reactor to the acoustic centre of each hydrophone (as detailed in the

Chapter 3: Cavitation bubble clusters

associated product literature). For each measurement the hydrophone output was sampled for 1 s at 1 MHz using an oscilloscope (Owon SDS-7102V). In-house written software (appendix 11: FFT Owon Oscilloscope.vbp) was used to process the data by performing an FFT analysis of the signal, extracting the component at 28 kHz, followed by calibration according to the manufacturers hydrophone sensitivity data.

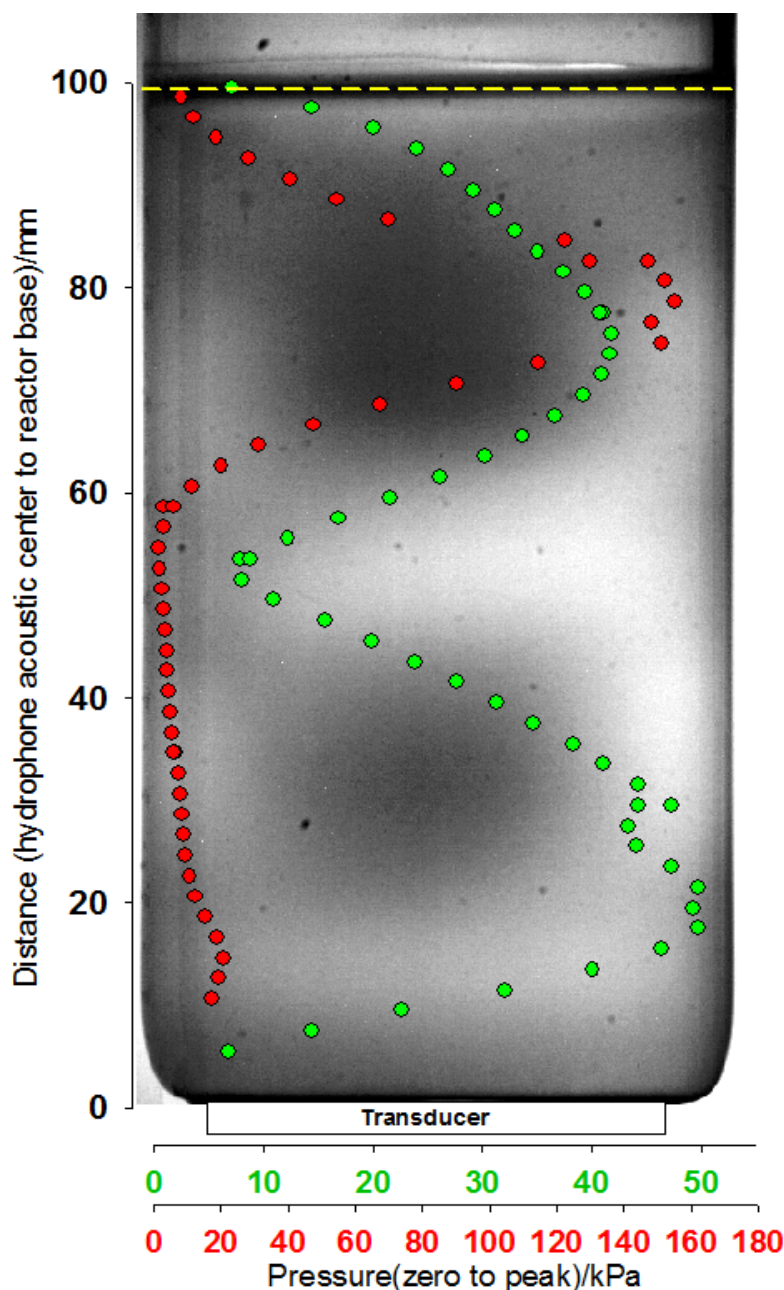


Figure 3.1 Image of ultrasonic reactor 1 filled with purified water (230 cm³) containing rheoscopic particles (0.025 g). The image is overlaid with the pressure measured by two hydrophones; the red data points (•) were measured with a Reson TC4013 and the green points (•) with a smaller Reson TC4038 hydrophone. For both types, the hydrophones were positioned centrally in the reactor at varied distances from the base. The transducer was driven at 28 kHz, 3 V_{pp}. The dashed yellow line (—) highlights the liquid-air interface. The original image contrast was adjusted to highlight the light and dark regions.

Chapter 3: Cavitation bubble clusters

The image in Figure 3.1 shows that the particles appear to interact with the sound field and scatter light according to the pressure field present. The exact mechanism is unknown and requires further investigation. A possible theory for this may be that the particles are forced to adopt specific orientations at different positions in the pressure field, for example at the antinodes (pressure maxima). If these particles were aligned normal to the camera, then the light travelling from behind the reactor would be blocked and the image would appear darker in certain regions. The unaligned particles would not block the light as much and would appear relatively lighter, generating the observed effect. Another possibility may be that the pressure field affects the concentration of the particles. This relocation is attributed to radiation forces, which can cause particles to travel toward either the node (pressure minimum) or antinode (pressure maximum) of the field depending on the relative density of the fluid and particles [187]. Irrespective of the mechanism, this shows for the first time that these particles and imaging are useful in characterising a standing wave field within reactors of this type.

The pressures measured by the TC4038 hydrophone (green points, •) under the same conditions correlate with these regions, exhibiting higher pressures (40 and 50 kPa) at the darker regions. The pressure measured by the larger TC4013 hydrophone correlates with the TC4038 data at *ca.* 80 mm above the base, with a relatively large increase in pressure (*ca.* 150 kPa); however with only a relatively small pressure increase (*ca.* 20 kPa) for 10 to 30 mm. A likely reason for the difference is that the hydrophone (and the displaced volumes involved) has a significant effect on the sound field. The interaction of the invasive hydrophones with the sound field and the displacement of liquid may significantly alter the conditions upon which the mode is dependent.

This effect is exhibited in Figure 3.2, which shows images of the reactor as the hydrophone (TC4013) measurements presented in Figure 3.1 were taken. It is clear that the particle localisation varies according to the position of the hydrophone. In image a) there are faint lines showing collection of the particles in bands across the cell. As the hydrophone is positioned deeper into the liquid through images b) to d), these lines become darker exhibiting the excitation of a mode as more particles are driven into position. Images e) and f) show the hydrophone positioned even further into the cell and exhibit the detuning of the mode as no particle localisation is evident.

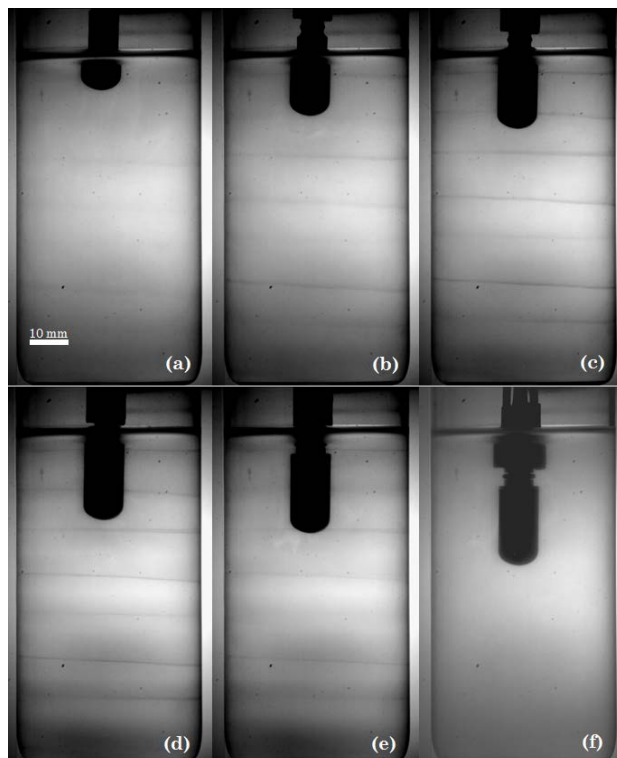


Figure 3.2 Images of the reactor and hydrophone (TC4013) taken during the acquisition of the pressure measurements as presented in Figure 3.1. The hydrophone acoustic centre was positioned at: a) 99 mm, b) 91 mm, c) 87 mm, d) 83 mm, e) 79 mm and f) 69 mm from the base of the reactor. The experimental conditions are stated in the Figure 3.1 caption.

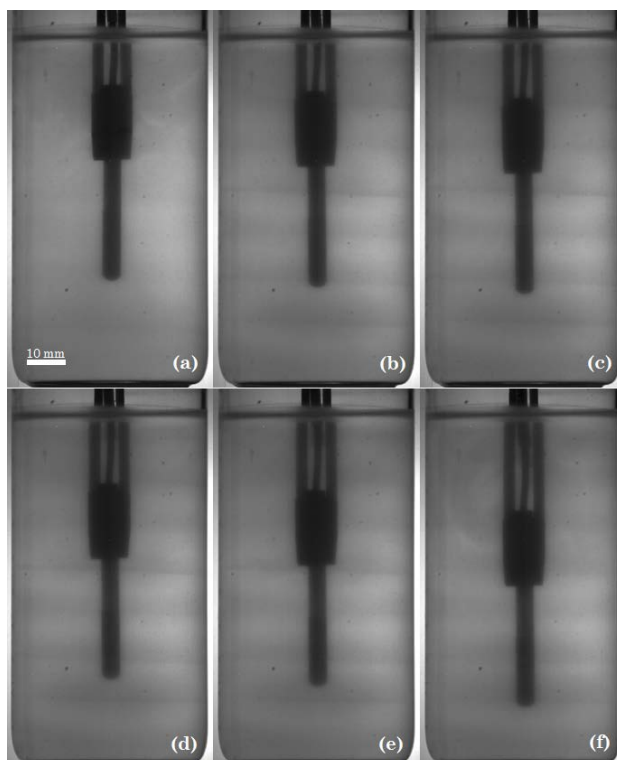


Figure 3.3 Images of the reactor and hydrophone (TC4038) taken during the acquisition of the pressure measurements as presented in Figure 3.1. The hydrophone acoustic centre was positioned at: a) 31 mm, b) 29 mm, c) 27 mm, d) 25 mm, e) 23 mm and f) 17 mm from the base of the reactor. The experimental conditions are stated in the Figure 3.1 caption.

Chapter 3: Cavitation bubble clusters

Hence the hydrophones change the sound field within the reactor dependant on its position. Figure 3.3 shows a similar effect with the TC4038 hydrophone, however with more subtle particle banding effect occurring deeper in the reactor. The TC4013 hydrophone therefore has different influence on the sound field than the TC4038. This change in behaviour is attributed to the difference in sizes involved. This provides an explanation the variation in the patterns and magnitudes of the recorded pressure exhibited in Figure 3.1.

In a further set of experiments the transducer drive signal was varied and tuned to different modes, exhibited by varied standing wave patterns highlighted by the rheoscopic particles. Figure 3.4 shows images obtained at varied standing wave fields produced by altering the drive conditions for the reactor. The arrows (→) highlight the regularity of the banding effects observed in these images. As discussed, the mechanism of interaction of the particles with the pressure field is unconfirmed and requires further investigation. However, it is shown that the by varying the transducer drive conditions, varied modes can be excited to produce the spatial variation of the sound field within the cylinder and this is highlighted by the particles. The reactor in image a) was not irradiated with ultrasound and hence there are no observed patterns. Images b), d) and e) show similar banding effects caused by modes with different axial symmetry. Image c) exhibits a comparable pattern to that observed Figure 3.1 (the frequency was the same for both experiments) with two relatively large dark regions evident. Image f) demonstrates that a much higher frequency produces a standing wave with closer axial banding, which correlates with the shorter associated wavelength.

The pressure field measurements and the particle imaging have demonstrated that ultrasonic reactor (1) can be excited to produce non-moving spatial pressure variations or modes in the liquid. This characterisation was achieved using relatively low excitation amplitudes of the reactor with the intension of avoiding inertial cavitation effects. However as the drive amplitude to the transducer was increased it caused cavitation to occur, which manifested as bubble filaments or clusters due to radiation forces.

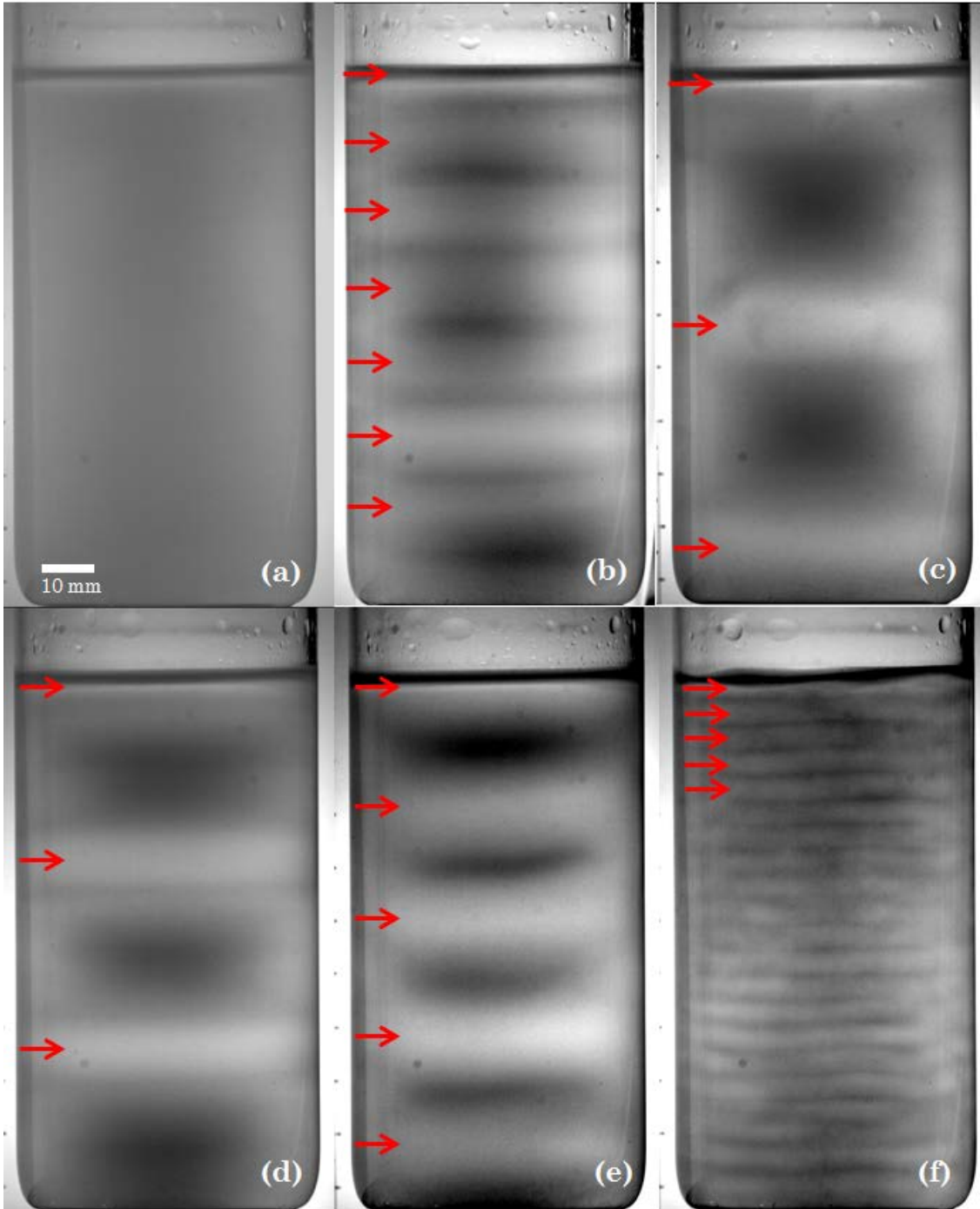


Figure 3.4 Images of reactor 1 containing rheoscopic particles (0.025 g) in purified water (230 cm³), irradiated with varied ultrasonic fields.: a) no ultrasound, b) 25.63 kHz, 19.3 V_{pp}, c) 28 kHz, 27.2 V_{pp}, d) 30.38 kHz 9 V_{pp}, e) 39.62 kHz, 19.3 V_{pp}, f) 138.87 kHz, 14.8 V_{pp}. The red arrows (→) highlight the standing wave patterns.

More specifically, primary and secondary Bjerknes forces are the cause these effects. Primary forces cause bubbles to migrate in an acoustic field or to gather in certain areas, such as pressure nodes or antinodes of such standing sound waves. The secondary forces make them attract or repel each other, and can also lead to stable bubble structures under certain conditions. In a vessel such as reactor 1, the

Chapter 3: Cavitation bubble clusters

formed cavitation clusters tend to exhibit poor spatial stability, usually as a bubble web consisting of a central cluster with interconnecting filaments (also called acoustic streamers). This is not ideal for investigation and can be overcome by placing a hard rod at the antinode of the pressure wave. Under these circumstances with a sufficiently high pressure field, a stable hemi-spherical cluster can form on the face of the downward pointing rod. Figure 3.5 shows an example of such a cluster localised at the end of a rigid rod positioned in an ultrasonic reactor (1). The rod is positioned with the downward pointing face at a distance of 77 mm from base. This is at the antinode as shown by pressure measurements (see Figure 3.1). This localisation of the cluster is due to Bjerknes forces between the cluster and the wall of the rod face (discussed in section 1.6.1), which provides stabilisation for the cluster and hence a more suitable subject for investigation.

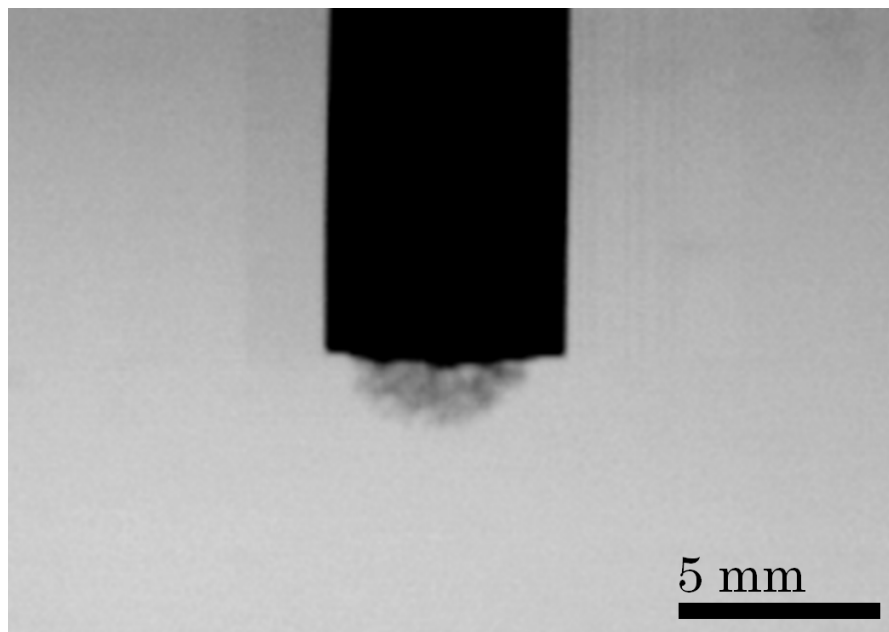


Figure 3.5 Image showing an example of a hemi-spherical cavitation cluster formed on the face of a downward pointing steel rod (O.D. = 6mm) positioned centrally, 77 mm from the base of reactor 1 filled with purified water (230 cm³). The transducer was driven at 27.27 kHz, 20 V_{pp}, 32 dB. The high-speed camera recorded frames at 1000 fps with an exposure time of 1/7000 s.

This novel approach of reactor induced cavitation cluster stabilisation (RICCS) is applied for study of the erosive effects of the cavitation cluster formed on the face of the erosion sensor rod in the next section.

3.2 Erosion sensor

The erosion sensor system (detailed in sections 1.6.1 and 2.1.6) was used to probe the environment within ultrasonic reactors (reactors 1 and 4 shown in Figure 2.1) and investigate cavitation clusters formed on the surface of the downward pointing erosion sensor via RICCS. Here the stabilisation of cluster is induced by the positioning of the sensor body and the conditions employed. The erosion sensor system has been previously shown to be a good electrochemical detector of erosion events generated by ultrasonic cavitation clusters [7, 136, 177]. Here the erosion sensor was used to focus on short timescale (100's of μs) phenomena (section 3.2.1) in combination with high-speed imaging, and also longer timescale (100's of s) occurrences using an erosion event counting system (section 3.2.2).

3.2.1 High-speed imaging

The conditions required to generate the stable cluster were investigated. The transducer drive signal was varied and tuned so that a stable bubble cluster was formed during each experiment. The drive signal details are presented in Table 3-1 with each associated pressure, measured by a hydrophone (TC4013, Reson) positioned in place of the erosion sensor¹.

<i>Experiment</i>	<i>Frequency / kHz</i>	<i>Amplitude / V_{pp}</i>	<i>Amplification / dB</i>	<i>Pressure (zero to peak) / kPa</i>
1	27.420	20	29.0	84.4 ± 6.5
2	30.125	20	26.5	92.8 ± 12.1
3	28.466	20	30.0	67.4 ± 3.9

Table 3-1 Drive signal details for the ultrasonic transducer used in high-speed imaging experimentation. The pressure was measured by a hydrophone (TC4013) positioned in place of the electrode. The presented pressures are the average of five measurements and the error is the standard deviation across these values.

High-speed imaging of the cluster formed at the end an erosion sensor was performed. Images were recorded simultaneously with the current *vs.* time response from the erosion sensor system, using an oscilloscope (Gould DSO465) to capture the current *vs.* time history.

Figure 3.6 shows an individual image of the cavitation cluster formed on the rod captured using a high-speed camera. Here the erosion sensor body is outlined by

¹ Note this is an estimate as the absence of the rod and hydrophone may alter the pressure.

Chapter 3: Cavitation bubble clusters

the blue dotted line (---). The cavitation cluster was commonly observed to exhibit a double shell structure in which a smaller and darker cluster was surrounded by a larger and sparser hemisphere. For future reference these are labelled C1 and C2 as highlighted by the yellow (---) and red (---) dotted lines respectively. The C1 cluster may be darker due to either smaller bubbles packed more densely or fewer larger bubbles. It should be noted that the other features of the image including the light and dark areas in the background are artefacts of the backlighting method and are not produced by the ultrasound.

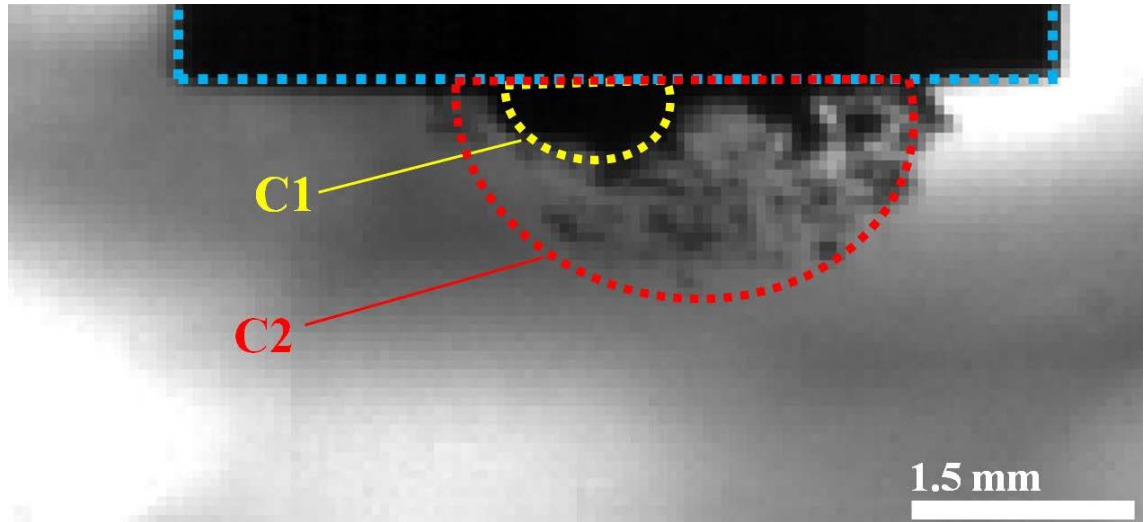


Figure 3.6 Image (frame 16 from Figure 3.9) of a cavitation cluster formed on the end of an erosion sensor electrode (O.D. = 6 mm). The blue dotted line (---) highlights the edge of the erosion sensor body. The experimental details are presented in the caption for Figure 3.8. The double shell structure of the bubble cluster is highlighted by the yellow dotted line (---) for the smaller and denser cluster and the red dotted line (---) for the larger and sparser cluster. The light and dark areas outside of these regions are an artefact of the uneven backlighting and are not produced from the cavitation environment.

The results from the high-speed imaging experiments can be seen in Figures 3.6 to 3.8. In each case, the blue line (—) is the current *vs.* time signal from the aluminium electrode (erosion sensor). The results shown are 200 μ s snapshots from each experiment, selected to exhibit a typical response from the dataset with a resolution high enough to resolve individual erosion events. The high-speed images are 10 μ s apart with an exposure time of 6.7 μ s per image, and are arranged in sequence above each graph, positioned with the centre of each image at the corresponding time on the x-axis.

Figure 3.6 shows an example where the erosion transients were observed to have the same periodicity as the ultrasonic pressure cycle (here 27.42 kHz), as demonstrated by the scale bar. The periodicity of the sound wave also coincides

Chapter 3: Cavitation bubble clusters

with the cavitation cluster cycle, with a cluster forming and collapsing once per cycle. These results suggest that the cluster collapse is the cause of the erosion of the electrode with each event occurring during the same frame as a cluster collapse ($\pm 10 \mu\text{s}$), highlighted by the red outlined frames. The double shell structure as described in Figure 3.6 is evident to some degree with a small darker region (C1) observed, particularly in the frame before or during each cluster collapse. Note that at this shutter speed there is a degree of averaging in each frame, meaning that the moment of cluster collapse cannot be determined to as high a time resolution as the erosion events. This is exhibited in frames 7, 11 and 18 which show that the cluster has not completely collapsed, compared to frames 4 and 15 in which the cluster has disappeared. The identical periodicities of the sound cycle, cluster collapse and erosion events demonstrates the concept of the erosion of a surface caused by the concerted collapse of a cloud of bubbles, as described by Hansson *et al.* [98, 124].

The results presented in Figures 3.7 and 3.8 are from experiments similar to Figure 3.6, however in which the acoustic drive settings were varied (30.125 kHz, 20 Vpp, 26.5 dB and 28.466 kHz, 20 Vpp, 30 dB respectively). The measured pressures under these conditions are reported in each relevant caption.

Contrary to Figure 3.6, the graphs in Figures 3.7 and 3.8 demonstrate erosion events that occur once every two sound cycles. This is shown by the sound period scale bar which comprises half of the time in between erosion events. The high-speed images in both Figures 3.7 and 3.8 also show a different pattern to that observed in Figure 3.6. The larger C2 cluster appears to form and collapse with the same frequency as the drive signal (as in Figure 3.6), however the smaller and darker C1 cluster persists for longer, only collapsing every two sound cycles. Hence the formation and collapse cycle of this darker region of bubbles, C1, occurs with the same frequency as the erosion events. It is evident that there are occasions when the larger cloud collapses and disappears from visual observation, yet the smaller inner cloud remains. In these instances, such as images 5, 11 and 18 in Figure 3.7 and images 3, 10 and 17 in Figure 3.8, there are no erosion events. Consequently it can be inferred that it is the collapse of the inner C1 cluster responsible for the erosion of the surface in these examples. The observed difference in periodicity of the inertial collapse is attributed to the size and bubble population within the cluster.

Chapter 3: Cavitation bubble clusters

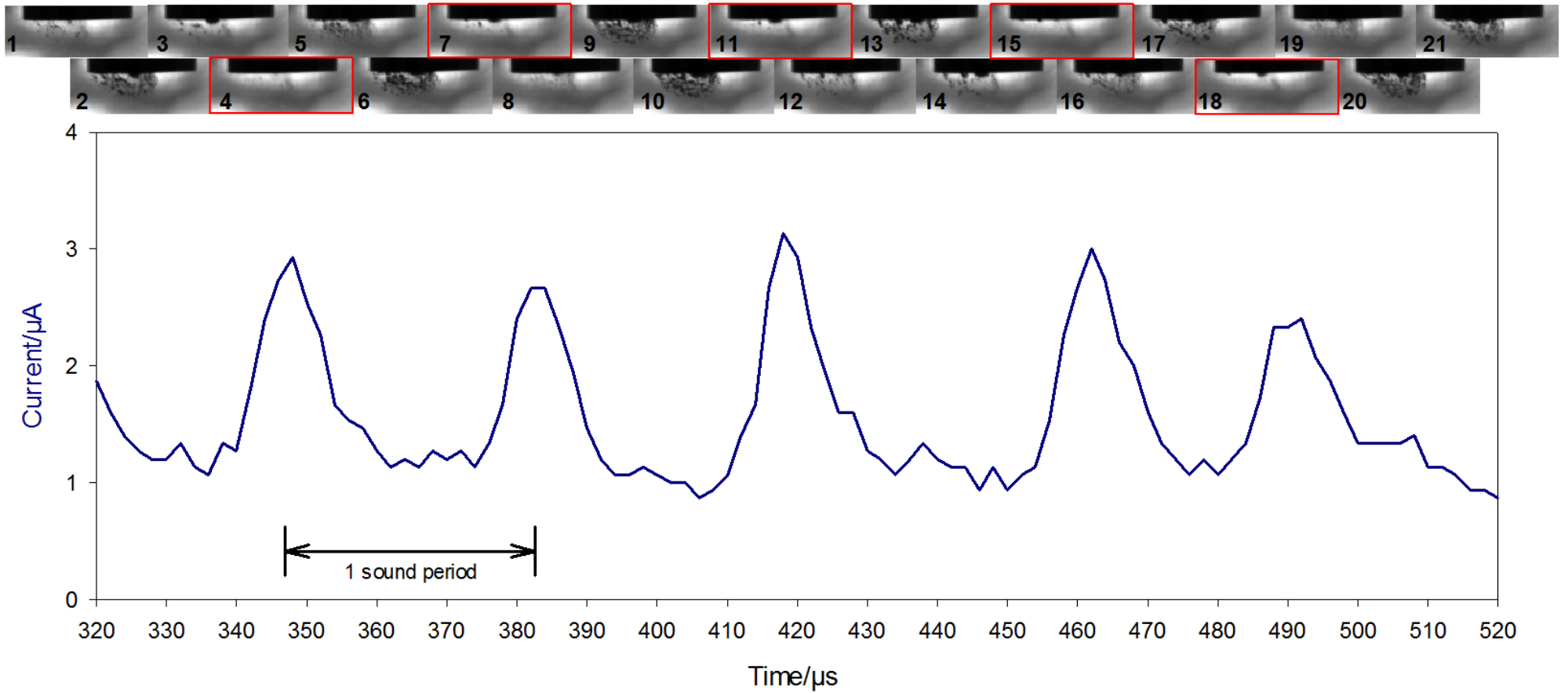


Figure 3.7 Plot showing the current vs. time signal from an erosion sensor held at 0 V vs. steel submitted to ultrasonic cavitation with simultaneously recorded high-speed images. The oscilloscope sampled the data at 500 kHz. The camera frame rate was 100000 fps with an exposure time of 6.71 μs. The transducer was driven at 27.420 kHz, 20 V_{pp}, 29 dB. The pressure measured by the hydrophone in these conditions was 84.4 kPa ± 6.5 kPa (zero to peak). The sensor was positioned 77 mm from the base of reactor 1 (centrally) containing 0.1 M Na₂SO₄ (230 cm³). The images shown above the graph are separated by 10 μs, with the centre of each image corresponding to the time that it was taken on the x axis. The red boxes (—) highlight the images that coincide with the peaks shown in the current vs. time trace.

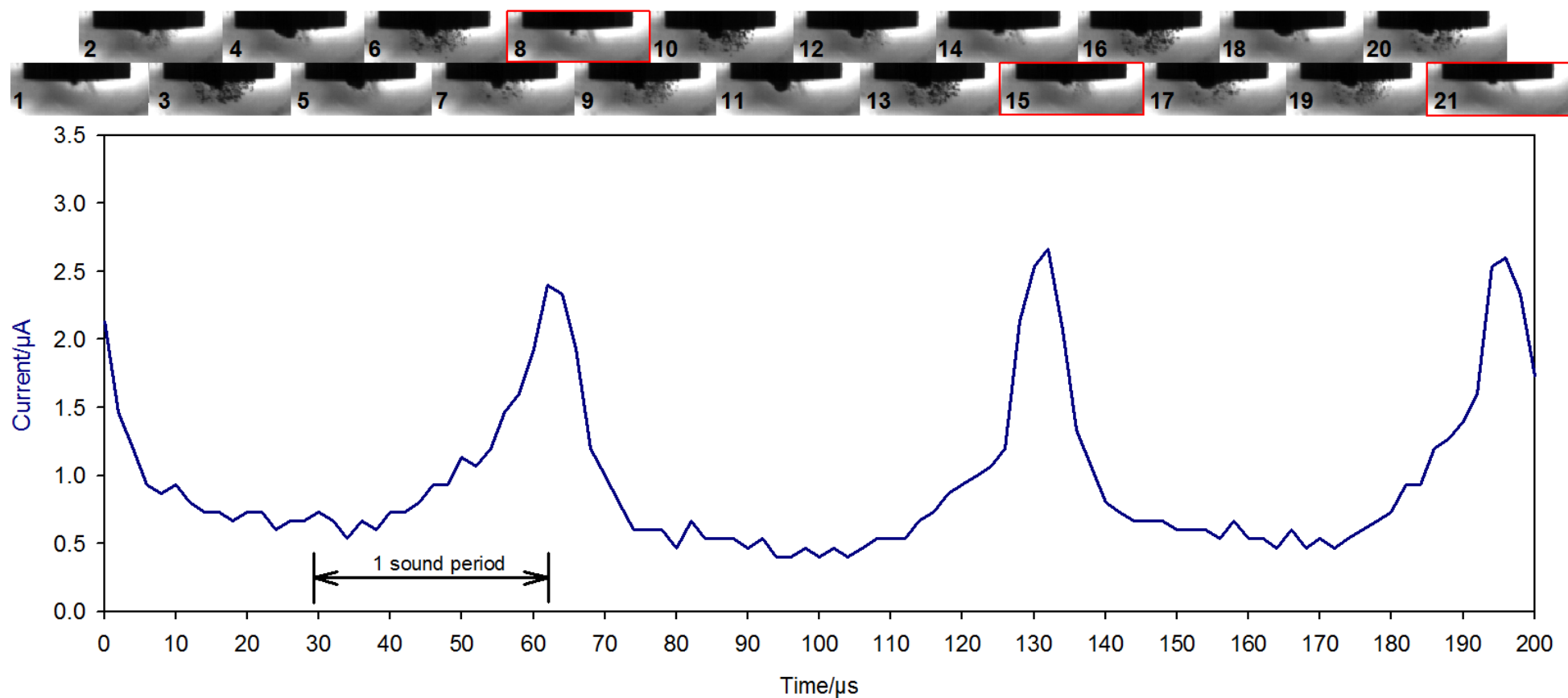


Figure 3.8 Plot showing the current vs. time signal from an erosion sensor held at 0 V vs. steel submitted to ultrasonic cavitation with simultaneously recorded high-speed images. The oscilloscope sampled the data at 500 kHz. The camera frame rate was 100000 fps with an exposure time of 6.71 μ s. The transducer was driven at 30.125 kHz, 20 Vpp, 26.5 dB. The pressure measured by the hydrophone in these conditions was $92.8 \text{ kPa} \pm 12.1 \text{ kPa}$ (zero to peak). The sensor was positioned 77 mm from the base of reactor 1 (centrally) containing 0.1 M Na_2SO_4 (230 cm^3). The images shown above the graph are separated by 10 μ s, with the centre of each image corresponding to the time that it was taken on the x axis. The red boxes (—) highlight the images that coincide with the peaks shown in the current vs. time trace.

Chapter 3: Cavitation bubble clusters

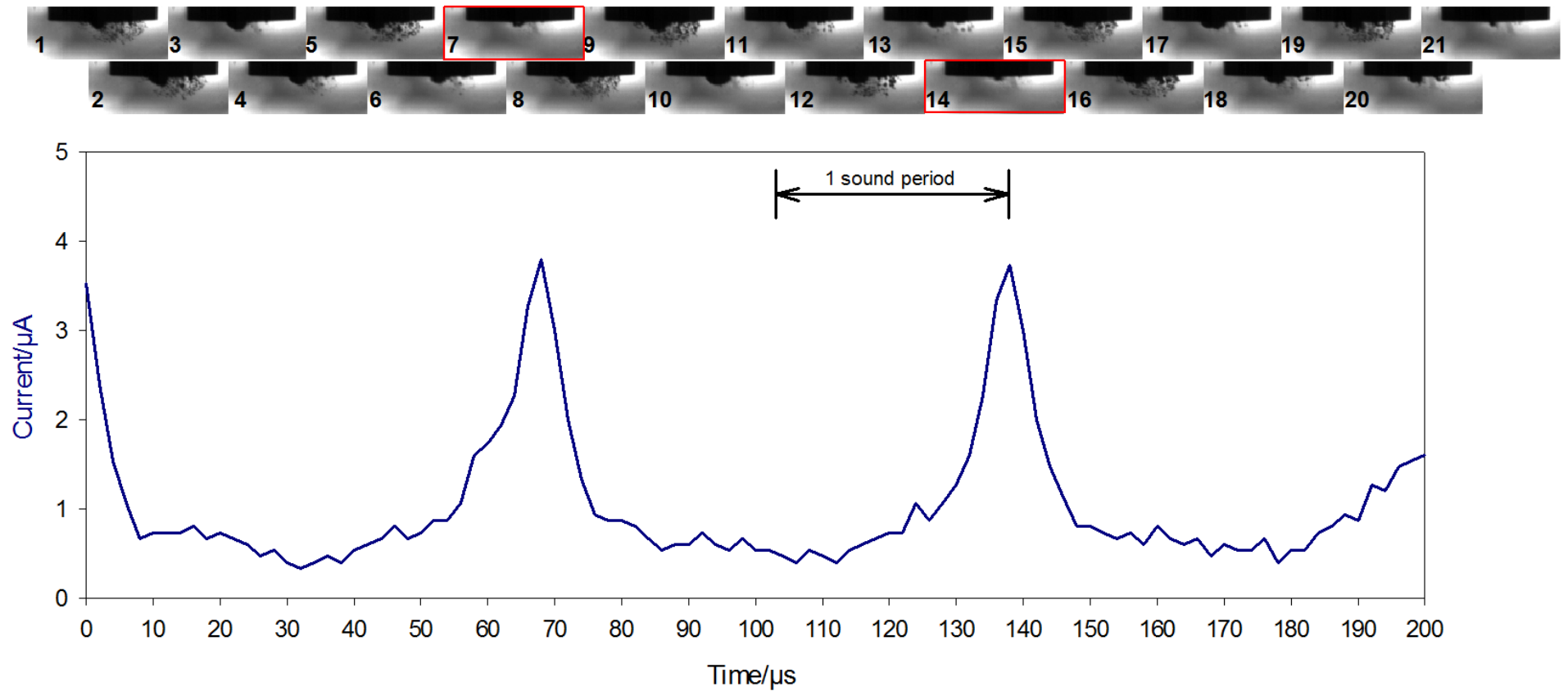


Figure 3.9 Plot showing the current vs. time signal from an erosion sensor held at 0 V vs. steel submitted to ultrasonic cavitation with simultaneously recorded high-speed images. The oscilloscope sampled the data at 500 kHz. The camera frame rate was 100000 fps with an exposure time of 6.71 μs . The transducer was driven at 28.466 kHz, 20 Vpp, 30 dB. The pressure measured by the hydrophone in these conditions was $67.4 \text{ kPa} \pm 3.9 \text{ kPa}$ (zero to peak). The sensor was positioned 77 mm from the base of reactor 1 (centrally) containing 0.1 M Na_2SO_4 (230 cm^3). The images shown above the graph are separated by 10 μs , with the centre of each image corresponding to the time that it was taken on the x axis. The red boxes (—) highlight the images that coincide with the peaks shown in the current vs. time trace.

Chapter 3: Cavitation bubble clusters

In summary it has been shown that the formation of a cavitation cluster at the end of a downward facing rod in an ultrasonic reactor can result in the erosion of an aluminium electrode, which can be monitored to enable the counting of individual ‘erosion events’ associated with each cluster collapse. The nature of the cavitation cycle depends on the conditions and the excitation sound wave, which can result in erosion occurring at different moments in the cluster collapse; every one or two cycles. It has been shown that the bubbles in the ‘inner cluster’ closest to the electrode surface are primarily responsible for the dramatic erosive effect. The longer term consequences of the cavitation cluster and the response with the erosion sensor will now be examined.

3.2.2 Cavitation erosion and surface pre-treatment

The results presented in previous section have shown the effects generated by cavitation cluster phenomena on surface erosion over a 200 μ s time window. However, the long term (10’s of minutes) erosive effects relating to cluster stability and performance of the erosion sensor are unknown in such an environment. Hence a set of experiments designed to investigate longer timescales and the ageing of the sensor, with focus on the influence of surface pre-treatment, were undertaken.

In order to monitor erosion events over relatively long periods of time (the events are usually $< 100 \mu$ s timescale and hence require sample rates of the order of 1 MHz to fully resolve), a system was developed to automatically count the number of erosion events. This system primarily consists of a current follower which feeds into a Schmitt trigger followed by a counting system.

The Schmitt trigger is a comparator which switches its polarity when the input passes upward through a positive reference voltage (denoted V_{upper} in Figure 3.10). In addition the output resets to its initial state when the input signal returns below a second lower reference voltage (denoted V_{lower} in Figure 3.10). This allows for events to be registered and avoids ‘noise’ on a signal, triggering a false event. Hence this is ideal for counting transients generated by cavitation induced erosion/corrosion. The trigger system uses a positive feedback loop to ensure that the input signal has to pass through the lower threshold voltage, thus preventing multiple triggering and switching against from a singular erosion event or noise. A complete schematic demonstration of the Schmitt trigger action is demonstrated in

Figure 3.10. Variation of resistor values within the Schmitt trigger circuit allows the threshold levels, V_{upper} and V_{lower} , to be controlled as shown by Vandenstein [188]. These were set to appropriate values according to the current *vs.* time transients generated by the sensor system in response to erosion events. A variable resistor was used so that the Schmitt trigger levels could be adjusted during experimentation, details of which are demonstrated in Figure 3.11.

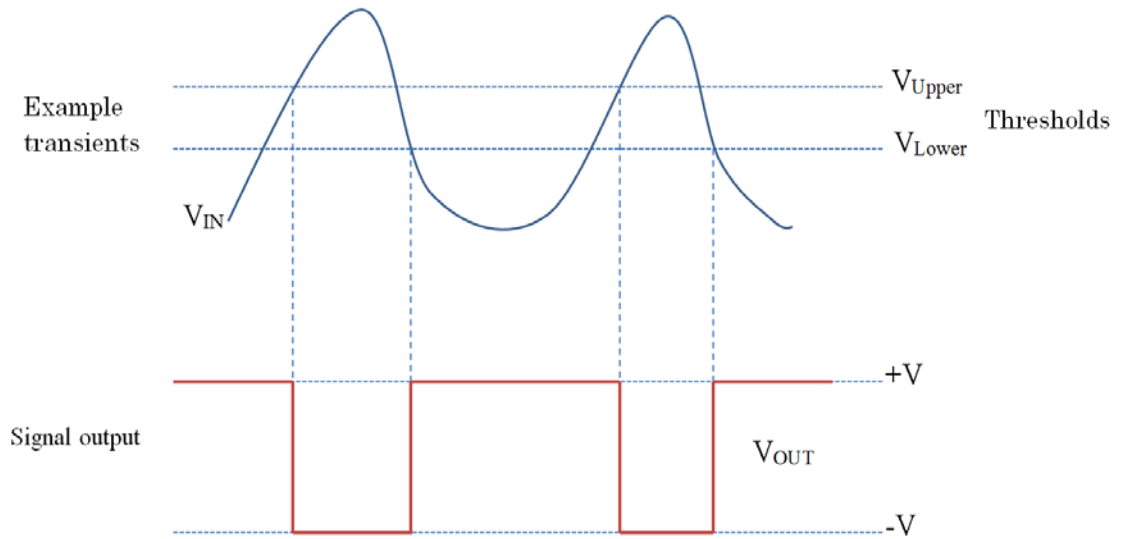


Figure 3.10 Schematic demonstrating the use of a Schmitt trigger system to count individual erosion/corrosion events.

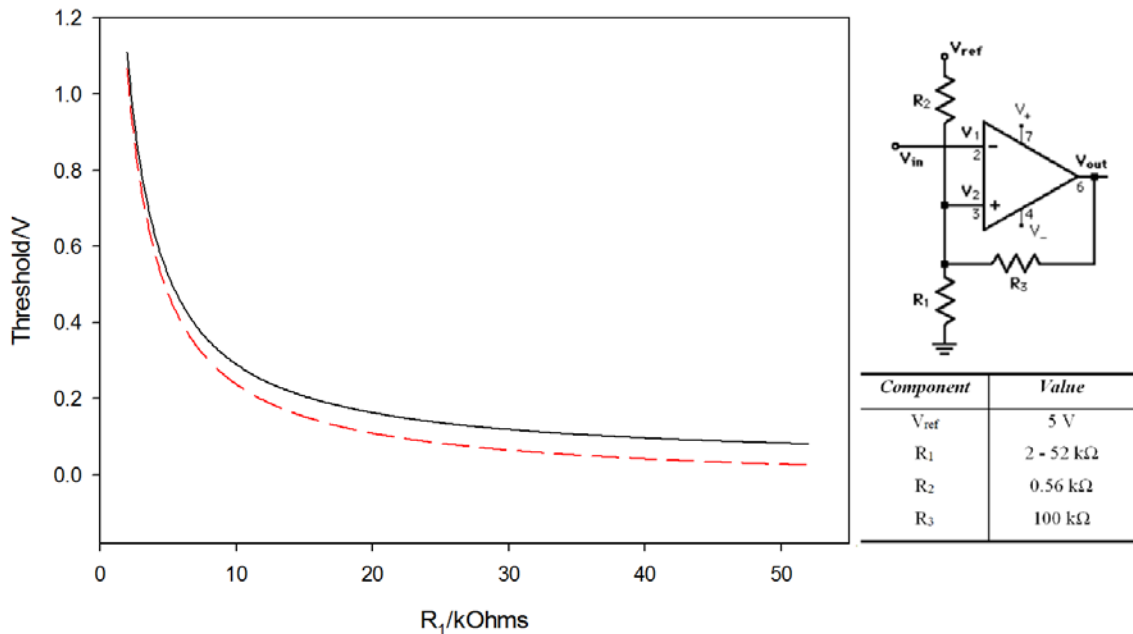


Figure 3.11 Plot showing the range of potentials that the Schmitt trigger thresholds cover ($-V_{upper}$, $-V_{lower}$), changed by adjusting the R_1 value between 2 kOhms at setting '0' to 52 kOhms at setting '10' on the instrumentation employed. There is a linear relationship of dial setting to resistance within these bounds. The Schmitt trigger circuit layout is also shown (from product literature) with the associated component values.

Chapter 3: Cavitation bubble clusters

In order to determine the number of events the signal output of the Schmitt trigger was routed to the counter input of a data acquisition module (Cole Parmer 18200-10) which connected to a PC via USB. This system design enabled the counting of individual erosion events above a pre-set threshold over long periods of time, ideal for study of the erosion sensor surface and its dependence on pre-treatment.

Figure 3.12 demonstrates the setup used for the varied pre-treatment experiments. For each experiment, reactor 1 (see Figure 2.1 for details) was filled with fresh Na_2SO_4 solution (0.1 M, 230 cm^3) and the erosion sensor was positioned centrally in the cell with the electrode face 77 mm from the base of the reactor. The transducer was pulsed, 3 seconds on, 3 seconds off at a drive signal of 27.08 kHz, 20 V_{pp} , 31 dB (tuned to resonance to produce a stable cluster). In order to measure the pressure under these conditions, a hydrophone (Reson, TC4013) was positioned in place of the electrode after erosion experimentation was complete. The measured zero-to-peak pressure is reported in the appropriate figure legend.

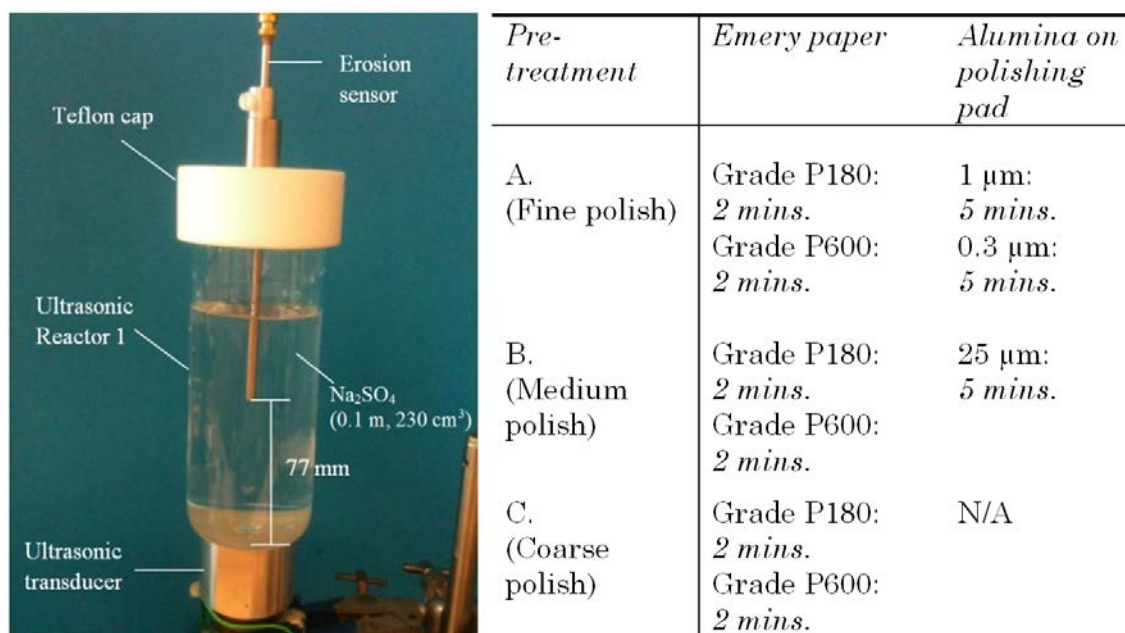


Figure 3.12 Image (left) of the experimental setup for the pre-treatment experiments with table (right) demonstrating the pre-treatment details for each experiment (A, B and C).

The pre-treatment of the electrode surface was varied as detailed in Figure 3.12. In each case after the electrode had been pre-treated it was subjected to the ultrasonic cavitation cluster and the erosion count was measured and recorded using in house software (appendix 11: Cavitation sensor.vbp). Each experiment was terminated at the point at which the erosion count had diminished to

relatively negligible amounts, the electrode inspected then returned to its original state prior to repeats.

For each type of pre-treatment experiment, a short calibration was conducted in which the Schmitt thresholds were varied after every 3 second pulse, across the Schmitt range selected. The threshold levels that gave the largest count were then selected for the following erosion count experiment. This ensured that the majority of the erosion events would be counted and not missed due to suboptimal Schmitt threshold levels. The calibration graphs are presented in Figure 3.13 and the Schmitt levels chosen for each experiment is detailed in each relevant legend.

Chapter 3: Cavitation bubble clusters

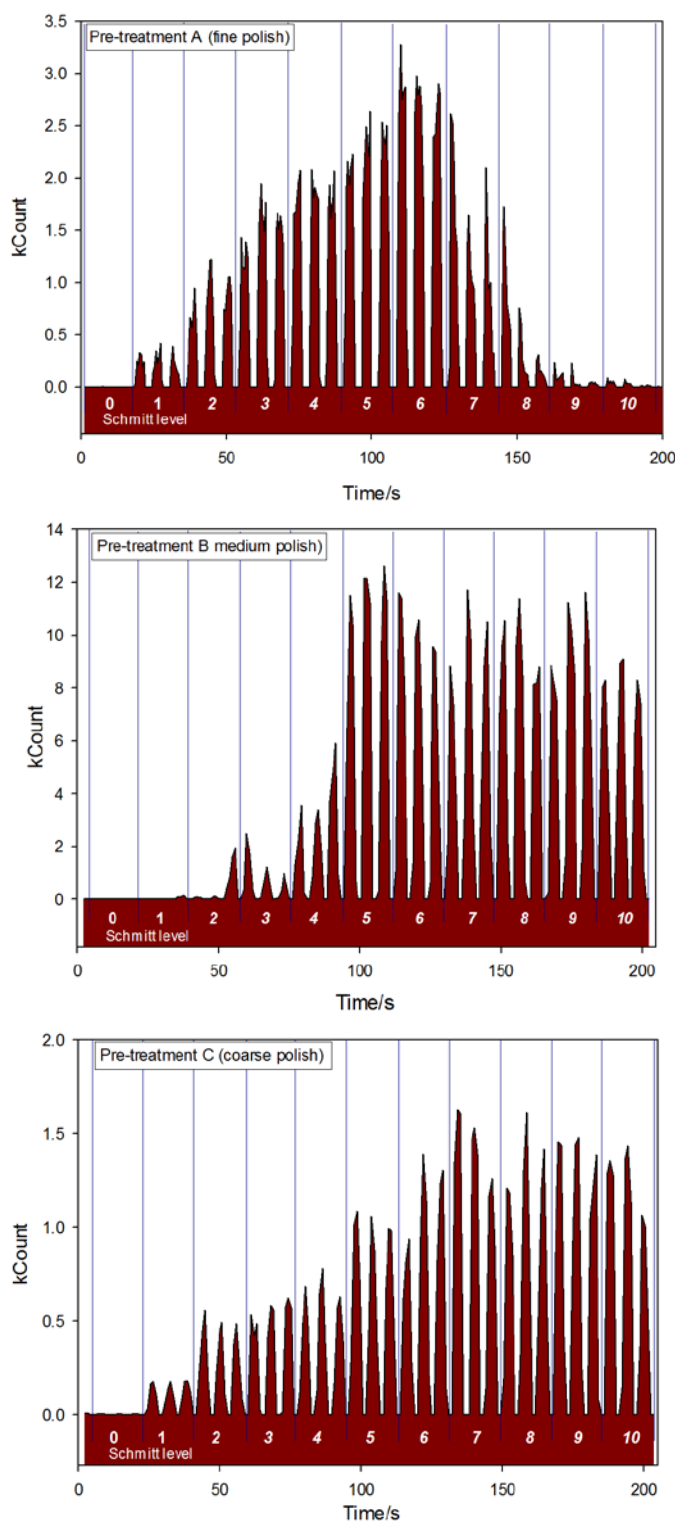


Figure 3.13 Plots showing the data used for calibration of the Schmitt trigger levels. In each experiment the erosion sensor was exposed to three bursts of ultrasound (27.08 kHz, 20 Vpp, 31 dB \equiv 60.3 kPa (zero-to-peak), 3 s duration each) per Schmitt trigger setting between 0 and 10 inclusively, as labelled on the plots separated by blue lines (—). The electrode was positioned with its face 77 mm from the base of reactor 1 which contained Na₂SO₄ (0.1 M, 230 cm³). Plot A (top) demonstrates the results corresponding to pre-treatment A (fine polish), plot B (middle) for pre-treatment B (medium polish) and plot C (bottom) for pre-treatment C (coarse polish). Schmitt levels 6, 5 and 7 were chosen for A, B and C respectively.

Figure 3.14 to Figure 3.16 show the measured erosion count as a function of time for the cluster collapse/aluminium erosion system for the three different pre-treatment regimes employed. In these figures, the erosion count during each 3 s window (above a set current threshold determined by the Schmitt setting detailed in the caption) is shown in black (—), and the cumulative count in red.

The results obtained for the pre-treatment ‘A’ (Figure 3.14, fine polish) experiments exhibit differences in the total erosion count and poor reproducibility. However, as predominantly shown by the cumulative count (—) there are similarities wherein three zones of different rates of erosion exist. During the first zone (labelled zone 1) the erosion rate is low compared to the subsequent region. This is more prominent in the results from pre-treatment A2 (bottom graph in Figure 3.14), where the region lasts for *ca.* 1500 seconds and exhibits a linear rate in the cumulative plot. During this period it was noted that the bubble cluster exhibited a degree of instability. Here the cluster was focussed at different positions around the electrode surface and the shape of the cluster varied between hemispherical and irregular forms. Once the polished electrode surface had been exposed to the sound field for some time (varied between several and 10’s of minutes), the cavitation cluster exhibited a greater degree of stability and appeared to ‘lock on’ about a specific point on the electrode surface, forming a stable hemispherical bubble cluster. This coincided with a region of higher erosion rate (zone 2) in which the accumulative count also exhibits a linear trend, with a steeper gradient. This was succeeded by a final region (zone 3) in which the rate of erosion is very low. During this region the cluster appeared to decrease in size and in some circumstances disappeared into the recesses that had been created through erosion.

The results obtained for the pre-treatment ‘B’ (Figure 3.15, medium polish) both exhibit a very similar trend to the top graph in Figure 3.14 (fine polish). As before, three separate regions of differing erosion rate exist, highlighted by the change in the gradient of the cumulative count. An initial region (zone 1) where low erosion counts are observed progresses into a region of increased but steady rate of erosion (zone 2). The erosion rate then decreases in the final region (zone 3). Similar bubble cluster patterns were observed as described for the experiments with pre-treatment ‘A’.

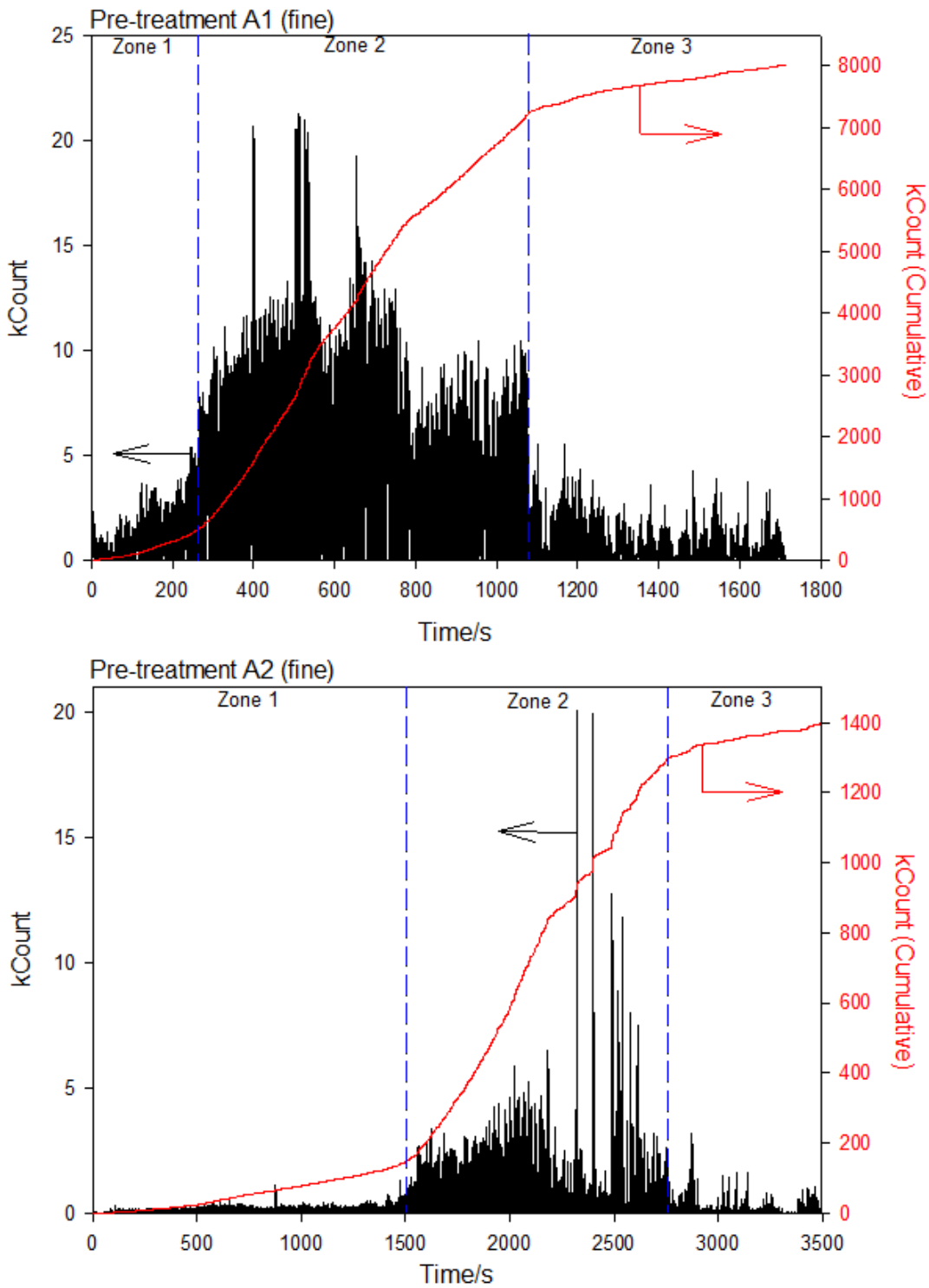


Figure 3.14 Plots showing erosion count *vs.* time (--- black line, left axis) and cumulative count (--- red line, right axis) for experiments in which the erosion sensor was subject to pre-treatment ‘A’ (fine polish, see Figure 3.12). The transducer was pulsed, 3 seconds on, 3 seconds with a drive signal of 27.08 kHz, 20 V_{pp}, 31 dB. The measured pressure under these conditions was 60.3 kPa (zero-to-peak). The ‘zones’ separating the different stages of erosion are separated by blue dashed lines (---).

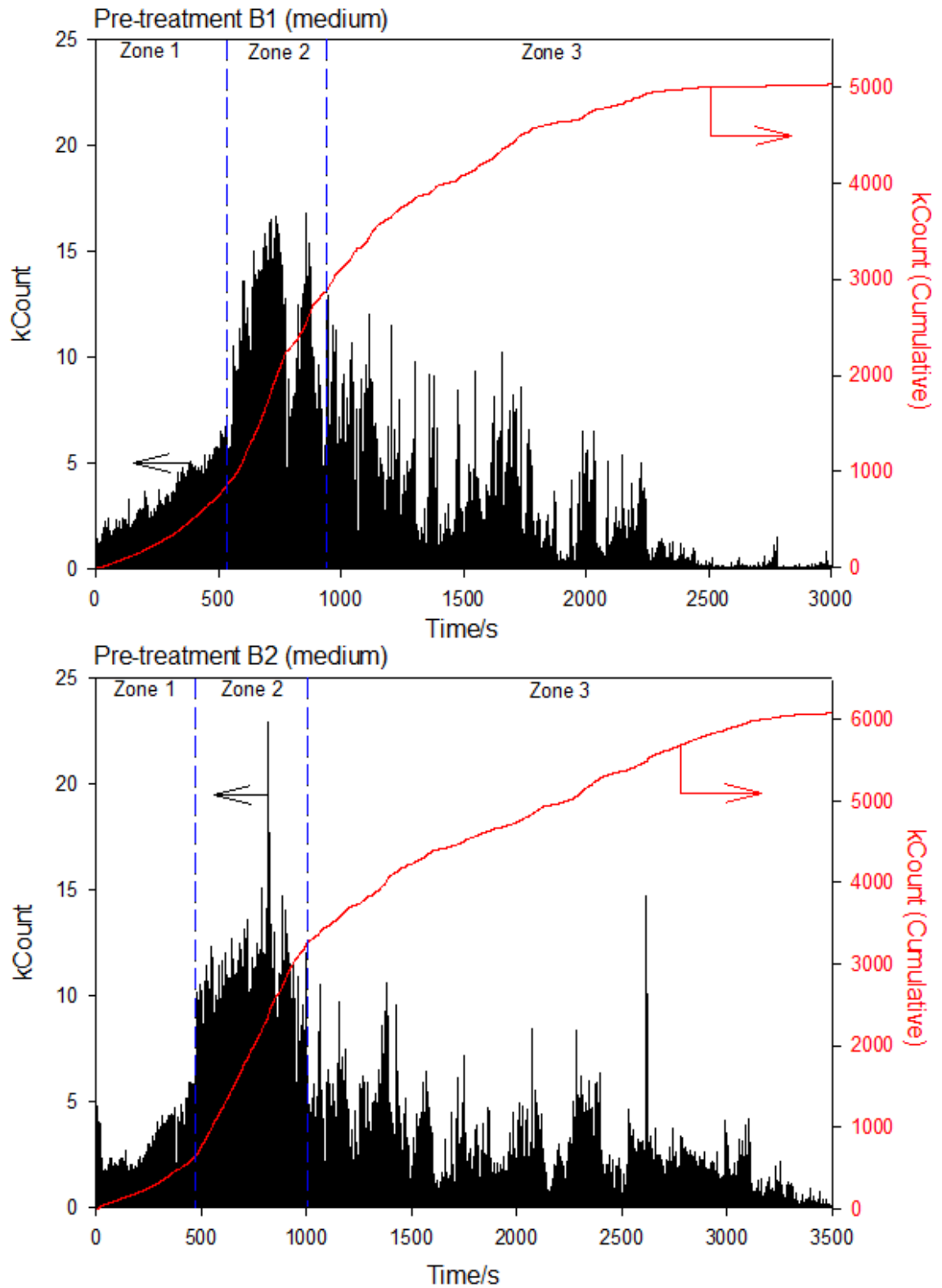


Figure 3.15 Plots showing erosion count *vs.* time (— black line, left axis) and cumulative count (— red line, right axis) for experiments in which the erosion sensor was subject to pre-treatment ‘B’ (medium polish, see Figure 3.12) The transducer was pulsed, 3 seconds on, 3 seconds with a drive signal of 27.08 kHz, 20 V_{pp}, 31 dB. The measured pressure under these conditions was 60.3 kPa (zero-to-peak). The ‘zones’ separating the different stages of erosion are separated by blue dashed lines (---).

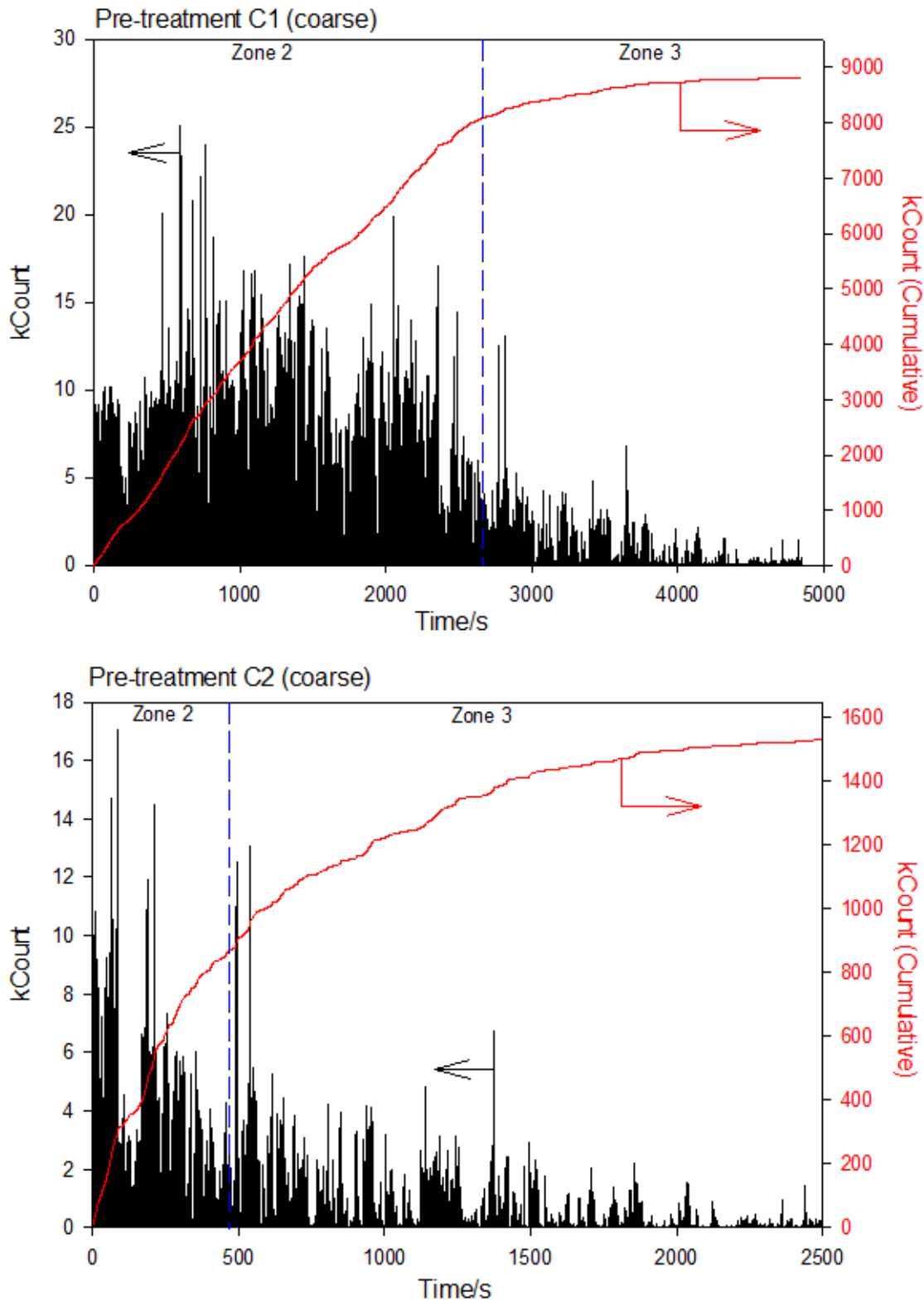


Figure 3.16 Plots showing erosion count *vs.* time (--- black line, left axis) and cumulative count (--- red line, right axis) for experiments in which the erosion sensor was subject to pre-treatment ‘C’ (coarse polish, see Figure 3.12) The transducer was pulsed, 3 seconds on, 3 seconds with a drive signal of 27.08 kHz, 20 V_{pp}, 31 dB. The measured pressure under these conditions was 60.3 kPa (zero-to-peak). The ‘zones’ separating the different stages of erosion are separated by blue dashed lines (---).

The results obtained for the pre-treatment 'C' (Figure 3.16, coarse polish) demonstrate a different trend to that observed with pre-treatments 'A' and 'B'. Here the initial rate of erosion is highest and is steady showing a linear progression in the cumulative count. This is succeeded by a final region in which the erosion rate decreases to negligible amounts. These regions are very similar to the zone 2 and zone 3 regions from pre-treatments 'A' and 'B' and as such they are labelled as so. Furthermore it was observed that the rougher surface exhibited a very stable cluster from the offset of ultrasonic irradiation, again in hemispherical form residing at one position on the electrode surface. Towards the end of the experiment, the cluster appeared decrease in size and in some circumstances disappeared into the recesses that it had created. There is disparity between the two graphs for pre-treatment 'C' with experiment 1 (top graph, Figure 3.16) exhibiting much larger total erosion count than experiment 2 (bottom graph).

The results and experimental observations suggest that three discernible stages in the lifetime of the erosion sensor exposed to an ultrasonically produced cavitation cluster exist. In summary these are as follows.

- Initial stage (zone 1): The highly polished surface provides very few nucleation points for cavitation bubbles and the cluster demonstrates instability or is not spatially locked to the electrode. In turn this causes relatively few erosion events. Progression is made onto the next stage once the surface becomes partially roughened.
- Main stage (zone 2): Area of steady erosion rate in which most of the erosion occurs. This is caused by a stable hemispherical bubble cluster formed on the face of the downward pointing electrode. The stability is enhanced through stabilised nucleation on the partially roughened surface that can be formed through either pre-treatment or cavitation erosion. The erosion continues until the electrode surface has become severely damaged.
- Final stage (zone 3): Plateau region in which the erosion rate is very low. Here the cavitation cluster is decreased in size and may enter the recesses created in zone 2.

Chapter 3: Cavitation bubble clusters

Once roughened, mechanically or through cavitation erosion, the cluster exhibits a greater stability and causes more erosive damage. This occurs for a period until the surface becomes more severely distorted and recessed, at which point the count decreases.

Clearly although the cluster produces a reproducible event within the cylindrical cell, this is limited by the surface conditions of the rod/electrode assembly. In addition while the erosion sensor is useful in characterising cavitation it is also limited to a finite number of 'events' when used in the manner described. This is in agreement with Vian who investigated erosion produced with an operating piston-like emitter [82, 176].

3.3 Luminescence

While erosion is inherently linked to inertial collapse, one of the most interesting effects of inertial cavitation is the generation of light directly (e.g. sonoluminescence (SL)) or through coupled chemical reactions (e.g. sonochemiluminescence (SCL)). Hence an investigation was made into these effects as it is of interest to the basic understanding of the cluster itself and to the assessment of local chemical activity within the system (see introduction for a description of the mechanism for light generation from luminol). Initial experimentation attempted to detect sonoluminescence (not SCL) emission, conducted with an intensified CCD camera under 'dark room' conditions using reactor 1 to generate a cluster at the face of the erosion sensor as previously described. However, the cavitation cluster did not emit a measurable amount of light with the CCD employed. Therefore sonochemiluminescence experiments were undertaken.

A similar experimental set up to that described previously in this chapter was employed, with the electrode positioned with its face 77 mm from the base of the reactor 1 containing a solution (230 cm³) comprised of luminol (5 μ M), Na₂CO₃ (0.1 M), H₂O₂ (0.1 mM), and EDTA (100 μ M) [92]. The transducer was driven at a 27.541 kHz (tuned to resonance to produce a stable cluster) across a range of amplification settings (15-35 dB, step 4 dB). A hydrophone was positioned in the cell (containing pure water, 230 cm³) with the element in place of the electrode and the pressure was recorded for each amplification setting. Images were acquired

using an intensified CCD camera (Photonic Science) connected to a frame grabber. The data was processed using commercial image analysis software (Tabaware ImageStacker) which enabled the averaging and stacking of the intensified sonochemiluminescence images with normal daylight images of the cell. Control experiments without the electrode in place were also performed.

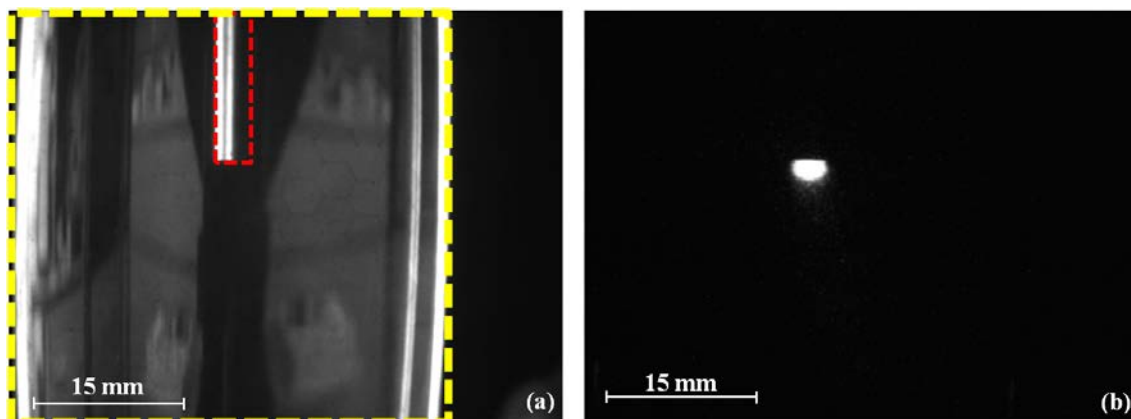


Figure 3.17 Examples of un-stacked images: a) the un-intensified background image of the electrode (highlighted by red dashed line — —) and reactor (highlighted by yellow dashed line — —) taken in the daylight and b) an intensified image of sonochemiluminescent activity occurring at the end of the electrode taken in dark room conditions. These images were stacked to obtain a composite image (picture e) in Figure 3.18). The brighter areas in image a) are reflections from the reactor wall and the electrode and are not a product of the ultrasonic irradiation.

Figure 3.17 shows images of the region surrounding the tip of the rod/electrode assembly under the conditions described. Each intensified image is a composite of many pictures averaged together to remove background noise, which can be problematic with intensified imaging. In addition, un-intensified background images of the cell and electrode were taken and compiled with each intensified image. An example of this is shown in Figure 3.17, which demonstrates the individual cell (a) yellow line) and electrode (a) red line) background image and the intensified SCL image (b). It is important to note that the background image (a) contains brighter areas which are merely unavoidable reflections under normal illumination conditions and are not related to the SCL phenomenon.

These images demonstrate that the only observable sonochemiluminescence occurring under these conditions was at the face of the electrode (i.e. where the cluster is located). Control experiments in the absence of the electrode/rod assembly (not shown) indicated no SCL activity occurring under the same intensifier settings, producing blank images.

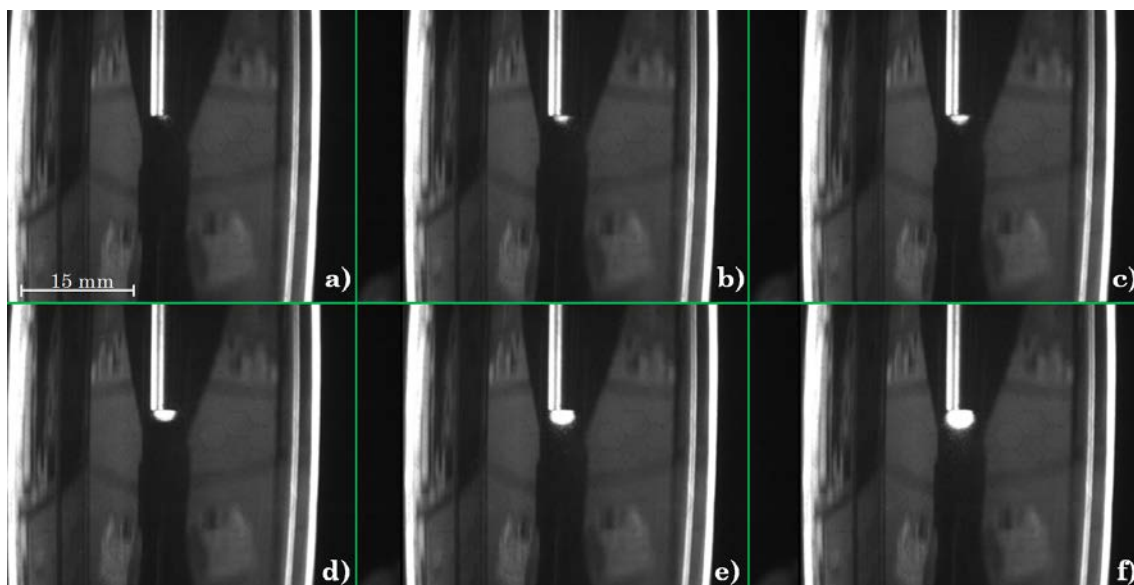


Figure 3.18 Composite images of the erosion sensor in reactor 1 containing 5 μM luminol, 0.1 M Na_2CO_3 , 0.1 mM H_2O_2 and 100 μM EDTA taken with an intensified digital CCD camera (Photonic Science). The transducer drive power increases through images a) to f). The transducer was driven at 27.541 kHz, 20 V_{pp} , with incrementally increasing gain: a) 15 dB, b) 19 dB, c) 23 dB, d) 27 dB, e) 31 dB, f) 35 dB, with associated zero to peak pressures measured by the hydrophone (TC4013) in place of the electrode: a) 13 kPa, b) 25 kPa, c) 28 kPa, d) 33 kPa, e) 35 kPa, f) 35 kPa. Each image was taken with the same exposure and intensity gain.

Figure 3.18 displays images of the hemispherical cavitation cluster undergoing sonochemiluminescence with increasing transducer drive power from a) to f) (corresponding pressures measured by TC4013 hydrophone ~ 13 to 35 kPa). It is clear that the size of the cluster increases with the drive power as the amount of sonochemiluminescence increases. The apparent non-linear increase in recorded pressure with increasing drive gain is again assumed to be due to the invasive nature of the hydrophone. An inherent non-linearity in the amplifier may also provide an explanation; however it appears that cluster increases in size, even when the measured pressure is constant (between e and f). Birkin *et al.* [145] have shown that there is good correlation between sonoluminescence processes, in which the light is directly attributable to the inertial cavitation, and sonochemiluminescence processes, in which the light emission is indirectly attributable. The correlation is not perfect as SCL can be falsely attributed to cavitation if rapid streaming effects occur [131]. This is attributed to the large amount of forced convection generated by the streaming, which may carry reaction products away from the cavitation source. Therefore the spatial distribution of the cavitation cluster cannot be exactly determined. However, these are assumed negligible effects on the observed trend that the size of the cluster and hence the

amount of sonochemiluminescence activity, both increase with acoustic pressure amplitude. Here the higher pressure variations cause larger clusters to be observed with the concomitant increase in luminescent output. This is in agreement with observation made by Hanumanthu [91] who demonstrated that the size of the cavitation cluster formed under an ultrasonic horn was correlated with the drive amplitude.

3.4 Shimmer visualisation/Schlieren imaging

Observations of a ‘shimmer effect’ emanating from a cavitation cluster were made during the initial erosion experiments. In order to investigate the effect further (which was barely visible by the naked eye) a set of experiment were undertaken. Preliminary experimentation utilised a basic shadowgraph technique in which laser light was shone through the cluster and surrounding area onto a plain surface. Although this was successful in showing changes in the liquid surrounding the cluster, it lacked the resolution to produce an enhanced visualisation of the system. Another approach involved the use of rheoscopic particles. The particles (PM-01 tracers, Kalliroscope) aided visualisation of the flow near the wall of the reactor, however at high concentrations the particles blocked the light reflecting off of the cluster and at low concentrations did not provide any improvement. Hence in order to investigate the shimmer effect further, Schlieren imaging was employed. This technique is designed to highlight, through judicious choice of optics, the refractive index changes that occur as a result of heating, pressure or concentration changes within a suitable fluid. There are many types of Schlieren setup of varying complexity resulting in differing sensitivities and fields of view. In the system a single-mirror, off axis system was employed. This allows a straightforward setup, permitted by the small test area of the cavitation cluster, to be developed. The setup for the Schlieren experimentation is shown in Figure 3.19 and was constructed using literature sources [189] and websites [190, 191]. To avoid distortion of the images through curved surfaces, an ultrasonic reactor with flat surfaces was employed (reactor 4, see Figure 2.1).

The system uses a point light source (LED shone through a pin hole) directed at a concave mirror ($\varnothing = 150$ mm, focal length, $f = 300$ mm) at 600 mm separation or twice the focal length of the mirror. The light is focussed by the mirror to a point close to the light source. The light path includes the cell and the bubble cluster as

Chapter 3: Cavitation bubble clusters

required. An imaging device, for example a high-speed camera, is used to capture an image of the object selected.

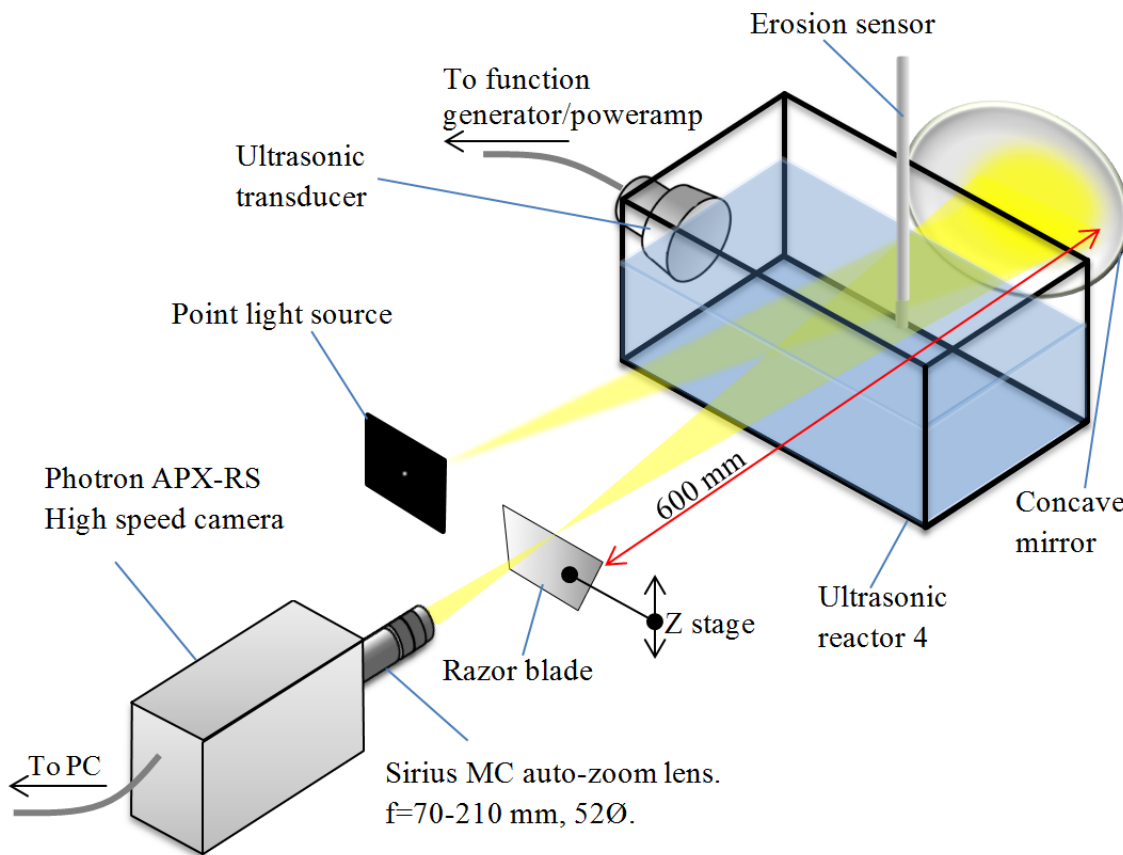


Figure 3.19 Schematic of the experimental setup used in the Schlieren imaging experiments

In the observed image the erosion sensor body appeared very dark as the light was blocked as with normal shadowgraph technique. The cavitation cluster scattered the light and hence also appeared darker. However, the area around the cavitation cluster did not appear darker using normal visualisation. In order to visualise a change in the index of refraction by eye (by density variation) a large refraction is needed; the observed shimmer is barely visible by eye and hence enhancement is clearly required. This can be achieved through the use of a fine edge of a razor blade to cut off some of the light reaching the camera lens in the system employed. In an image area of uniform density this will simply make the whole image darker. However, in an area with refractive index variations, the distorted beam focuses imperfectly and the image will appear darker in certain places and lighter in others. This is demonstrated in Figure 3.20 where the refractive index variation causes some of the light to bend. The resulting image is comprised of light which is undisturbed and uniform, with lighter and darker areas corresponding to the areas

where light that has been refocused onto the blocking edge (green arrow) or onto other areas of the lens (red arrow). Hence in the Schlieren system, the overall image appears darker; however, the contrast between the disturbed light and the undisturbed light in the area of interest is enhanced. Therefore a refractive index change will be visually enhanced by the introduction of the blocking edge.

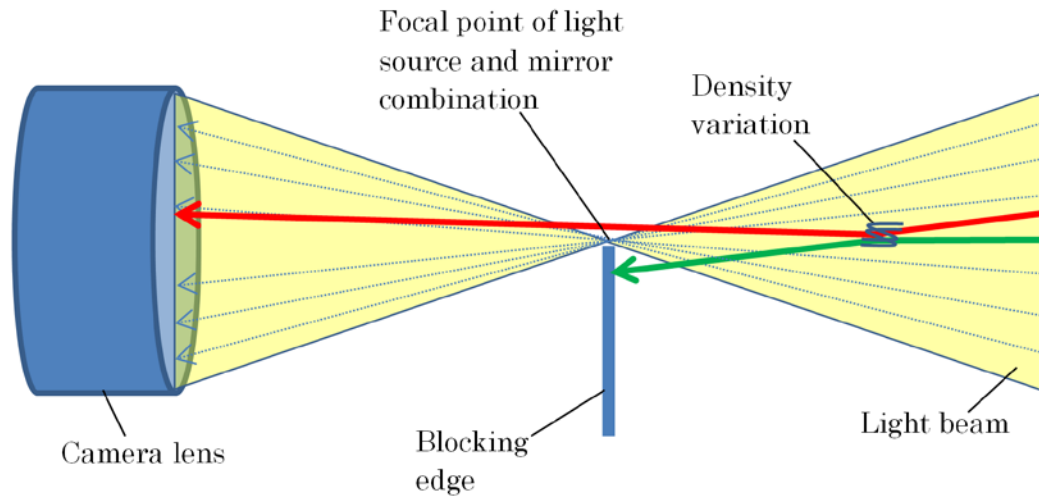


Figure 3.20 Schematic showing how a density variation causes refraction of the light and how this is blocked (— green arrow) by the razor blade edge resulting in darker areas and refracted to a different area on the lens (— red arrow) resulting in lighter areas.

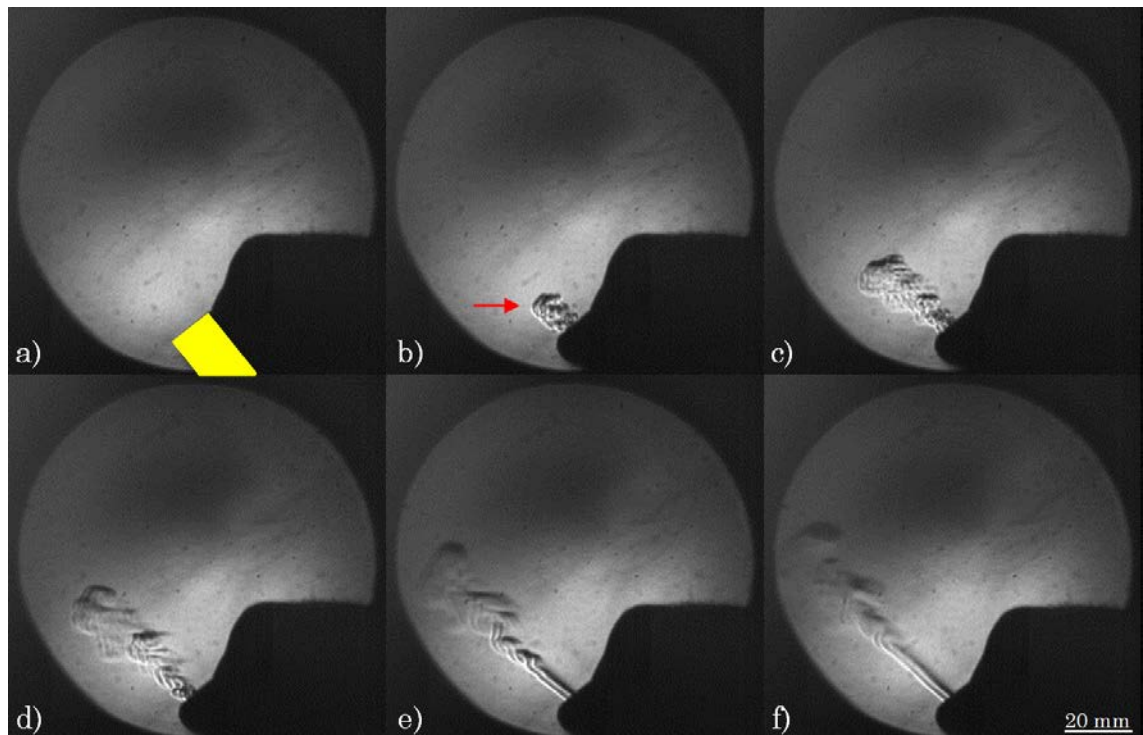


Figure 3.21 Sequence of images taken using the Schlieren technique (frame rate = 500 fps, exposure time = 1/4000 s). Frame a) was taken at $t = 0$ s, b) 8 ms, c) 24 ms, d) 46 ms, e) 84 ms and f) 118 ms. The yellow area (■) in frame a) shows the position of the lighter (behind the thumb) and the red arrow (→) in frame b) highlights the butane gas being expelled from the lighter.

Chapter 3: Cavitation bubble clusters

Figure 3.21 shows an illustrative example of this form of photography, conducted using a lighter to produce a refractive index change via a stream of butane injected into the air. The mirror is shown by the light circle comprising most of each frame. In frame a) the gas is yet to be released by the lighter (shown in yellow). Frame b) shows the first release of the gas (red arrow) and demonstrates the enhancement of the gas stream. The subsequent frames show the further release of the butane gas, also demonstrating the transition from turbulent to smooth flow at the outlet close to the lighter.

In order to test whether the Schlieren effect could enhance the cluster shimmer phenomenon, a test was conducted whilst observing a cavitation cluster at the end of the erosion sensor. The setup was as shown in Figure 3.19. The camera (Photron APX-RS) captured images at 60 fps with an exposure time of 1/60 seconds. The erosion sensor was positioned in the centre of reactor 4 (30 mm from the base) containing purified water (1 dm^{-3}).

Figure 3.22 demonstrates selected images from experiments in which the position of the razor blade edge was varied in order to determine the attainable range of contrast. The shadows cast by the erosion sensor and cluster are highlighted by the dashed yellow line (frame a) and red hemisphere (frame b) respectively. At this relatively long exposure time (compared to the cluster collapse high-speed images in section 3.2.1) the cavitation cluster appears as a constant dark hemisphere. This is because the cluster is collapsing many 100's of times per frame and the image is an average over this time. In frame a) there is no Schlieren effect occurring; all of the light is allowed to pass to the camera lens and as previously observed the shimmer was not observed. In b) and c) the razor edge at the focus has blocked some of the light and the shimmer is more evident. Images d) and e) exhibit the Schlieren effect to a much greater extent with darker and lighter regions enhancing the shimmer as plumes emanating from the cluster. Clearly the Schlieren technique is well-suited to provide an enhanced visualisation.

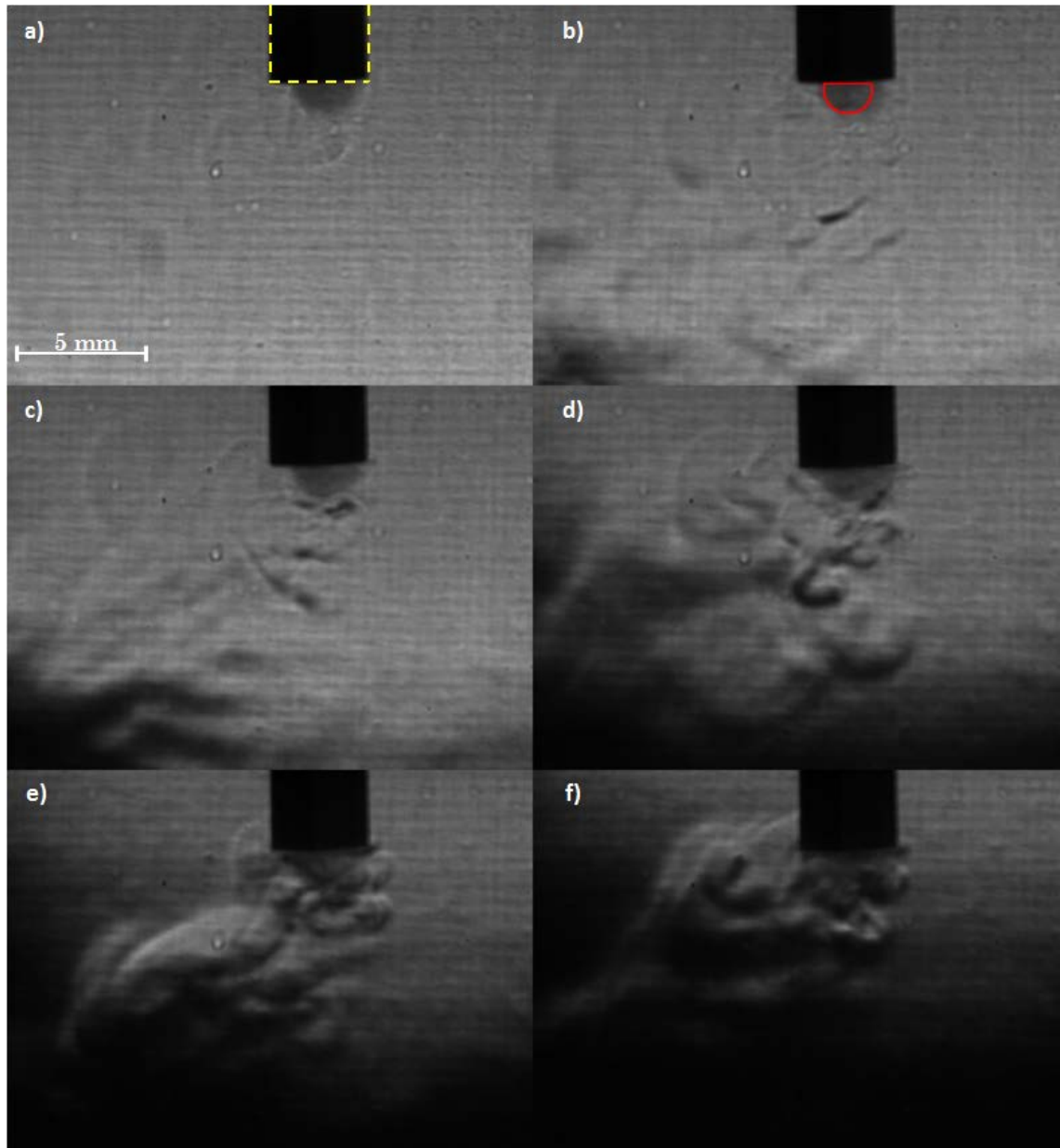




Figure 3.22 Schlieren images taken using a high-speed camera (60 fps, shutter: $1/f$ s). The height of the razor blade edge was gradually raised from a) a position where the light has an unobstructed path to f) where a considerable amount of light is blocked. The experiment was conducted with an erosion sensor (highlighted by the dashed yellow line ) positioned 30 mm from the base of reactor 4 filled with purified water (1 dm^3), with the transducer driven at 27.718 kHz, 20 V_{pp}, 35 dB. The hydrophone (TC4013) positioned in place of the erosion sensor under these conditions recorded a pressure 79.96 kPa (zero to peak). An outline of the resultant cavitation cluster is shown in frame b) by the red () semicircle.

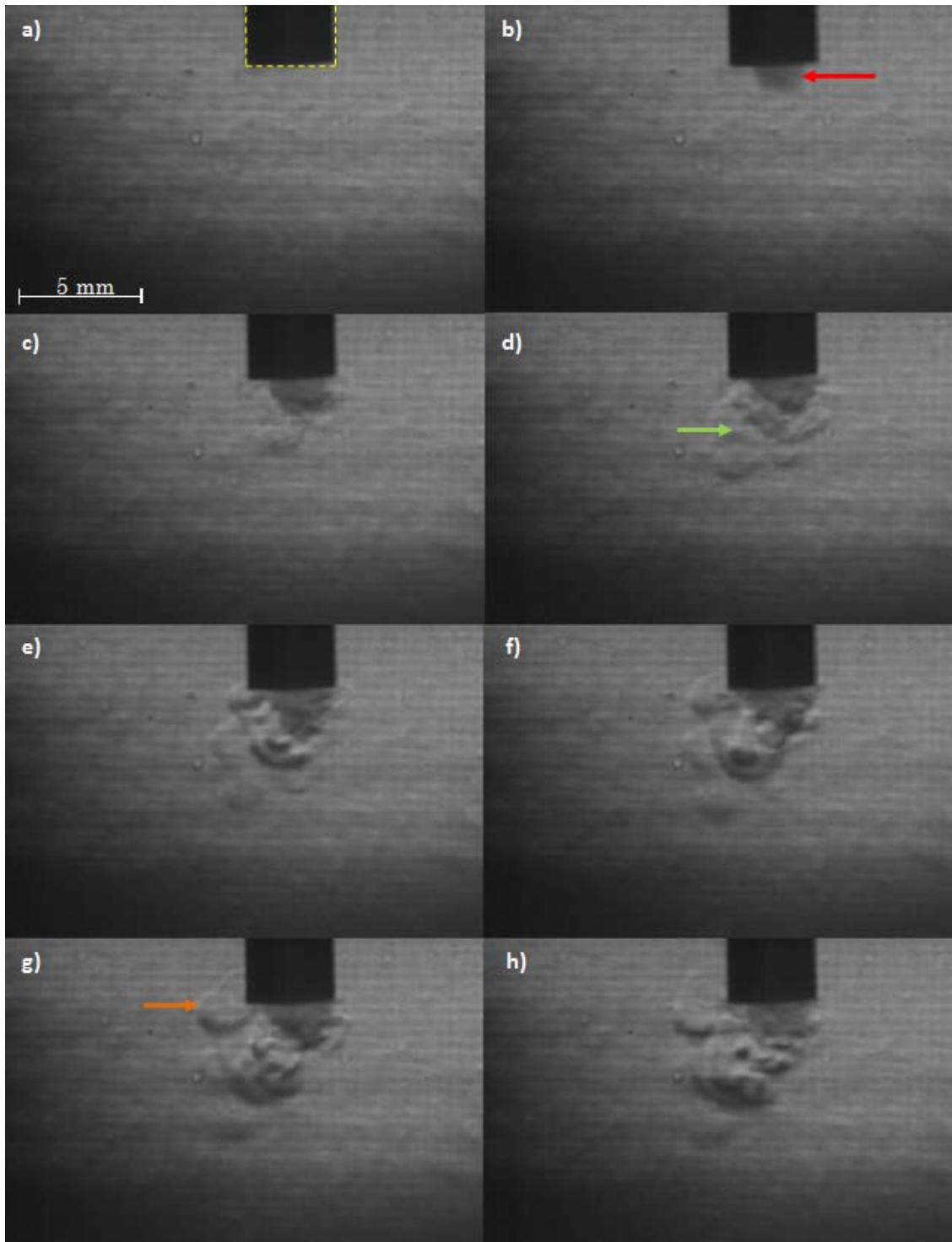
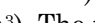
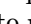
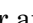



Figure 3.23 Schlieren images taken using high-speed camera (60 fps, shutter: $1/f$ s). Each image is 4 frames apart (6.67 ms). The erosion sensor (highlighted with dashed yellow line ) was positioned 30 mm from the base of reactor 3, filled with purified water (1 dm^3). The transducer was initiated simultaneously with frame a) and was driven at 27.718 kHz, 20 V_{pp}, 35 dB. The hydrophone (TC4013) positioned in place of the erosion sensor under these conditions recorded a pressure 79.96 kPa (zero to peak). The cavitation cluster is indicated with a red arrow () in frame b). The green arrow () shows the shimmer effect protruding beyond the cavitation cluster and the orange () arrow highlights the shimmer extending upwards around the sensor body.

Further experimentation was conducted by observing the area around the erosion sensor. The razor blade was mounted in position to cut out the optimal amount of light, information obtained from experiments documented in Figure 3.22. Figure 3.23 demonstrates the shimmer formation once the ultrasound was switched on and the cavitation cluster had formed. Frame a) shows the situation before the cluster or shimmer had appeared. Frame b) demonstrates that the cluster has formed (see arrow). However, no shimmer effective is apparent. The first appearance of the shimmer was made at *ca.* frame c) (which is 4 frames after b). This can only be seen by switching between frame b) and the next frame on a visual display unit, which demonstrates the shimmer appearing 16.7 ms (at most) after frame b). Hence it is clear that the presence of the cavitation cluster caused the refractive index change effect, and the effect forms quickly but not immediately after the cluster. After this the shimmer appeared to flow relatively slowly outwards from the cluster into the liquid in a stream like fashion. In the first *ca.* 50 ms the shimmer flow was observed to extend *ca.* 5 mm away from the cavitation cluster, therefore travelling at a speed of around 0.1 m/s. After this the flow decelerates and takes several seconds to reach the edge of the frame (*ca.* 15 mm away) as shown in Figure 3.24 image a). The effect was also observed to extend in different directions from the cluster, as shown by the red arrows in Figure 3.24 image a) which shows the situation *ca.* 4 s after that shown in Figure 3.23. The effect also extended upwards around the sensor body (see Figure 3.23 image g), for example).

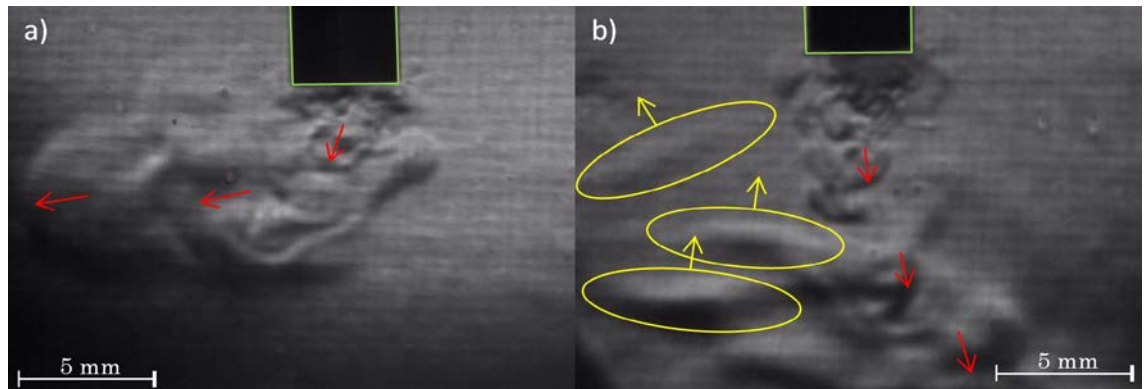


Figure 3.24 Schlieren images of cavitation clusters and surrounding areas. The erosion sensor (—) was positioned 30 mm from the base of reactor 4, filled with purified water (1 dm³). In image a) the conditions were the same as presented in Figure 3.23. The image was taken *ca.* 4 s after initiation of ultrasound. In image b) the transducer was driven at 28.75 kHz, 20 V_{pp}, 34 dB. The hydrophone (TC4013) positioned in place of the erosion sensor under these conditions recorded a pressure 65.24 kPa (zero to peak). The image was taken *ca.* 10 s after initiation of the ultrasound. The red (—) arrows demonstrate the direction of the flow. The yellow (—) circles demonstrate slower moving waves travelling in the opposite direction to the fast flow shown by the red arrows.

Chapter 3: Cavitation bubble clusters

Figure 3.24 also shows the presence of a series of slowly moving waves travelling in the opposite direction to the initially observed effect, only occurring many seconds after initiation of the cluster in a different example of the effect (see yellow highlights).

The most likely explanation for the observed shimmer is local heating, which causes refractive index changes through density variation. Other possibilities include local changes in concentration in the liquid or the scattering of light from micro- or nano-bubbles, which may be ejected from the cavitation cluster. The experiments were conducted in purified water ruling out the former. Nano-sized bubbles (where the diameter is smaller than or comparable to the wavelength of light) would only appear darker due to Rayleigh scattering of the light, producing time-averaged images without the generation of lighter areas that were observed. Micro-bubbles with diameters larger than the light wavelength would exhibit Mie scattering, in which the scattering angle is dependent on the bubble size [192]. This implies that the scattering angle would be changing in response to the applied sound field, which causes variation in the bubble sizes. Furthermore, radiation forces are expected to cause the rapid movement of bubbles and the relatively slow moving 'shimmer' does not respond to the sound field in this way. In addition there was no observed difference in the motion of the 'shimmer' before and after termination of the ultrasonic field. Hence the most likely cause of this refractive index change is local heating.

In order to gather further supporting evidence for a thermal effect associated with the stable cluster formation, experiments employed a thermocouple (K-type) embedded in epoxy in the centre of a steel tube. The tube was cut and polished so that the thermocouple junction was at the surface (see Figure 3.25). Figure 3.26 shows an example of the response from the thermocouple when exposed to ultrasound. The rod (shown in the images included in Figure 3.26) was positioned in the centre of reactor 1, 77 mm from the base and the ultrasound 'tuned' into resonance.

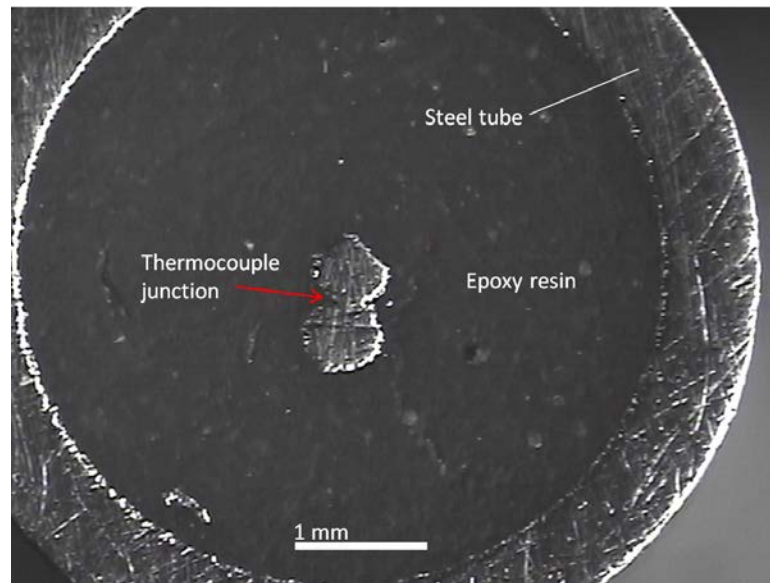


Figure 3.25 Image showing a K-type thermocouple embedded in epoxy resin (Struers) inside a steel tube (O.D. = 6 mm). The surface was polished with 25 μm Al_2O_3 on a polishing pad (Buehler).

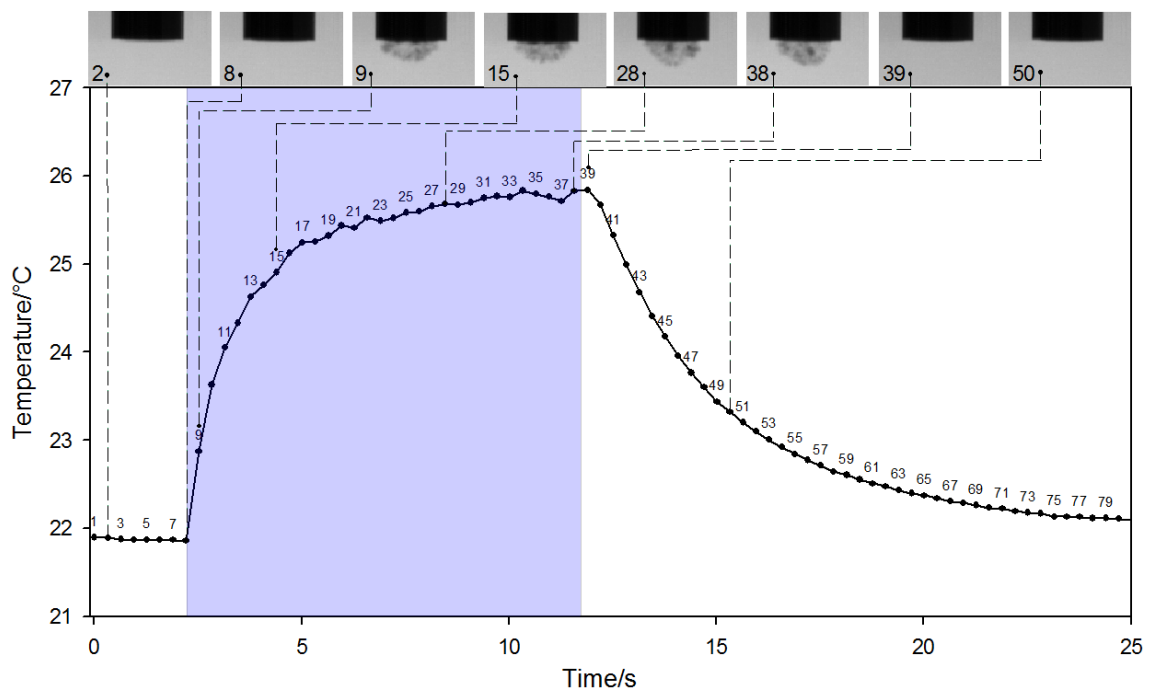


Figure 3.26 Plot showing the response from a thermocouple (K-type) embedded in epoxy resin (epofix) inside a steel tube (see Figure 3.25). The TC/tube was polished so that the TC was at the surface of the downward facing rod which was positioned 77 mm from the base of reactor 1 filled with purified water (230 cm^3). The time in which the ultrasonic irradiation (27.27 kHz, 20 V_{pp}, 32 dB) was initiated is shown by the shaded area. Selected high-speed images (exposure time of 1/7000 s) acquired simultaneously to the corresponding temperature data points (sample rate = *ca.* 3.2 Hz) are shown above the plot and are numbered and labelled accordingly.

Figure 3.26 shows that upon initiation of the ultrasound, a temperature rise is detected at the next sample, *ca.* 0.33 s later. The temperature increases further then appears to plateau < 10 s later. The plot indicates that local heating is of the

Chapter 3: Cavitation bubble clusters

order of *ca.* 4 °C with respect to the bulk fluid, in the short time in which the cell was irradiated. Although this is relatively modest, this is the first time such an effect has been observed in this environment and warrants further investigation in order to confirm whether the temperature variation is the cause of the observed refractive index change. Additional tests are also needed to assess reproducibility and for control experimentation to confirm the source of the heating effect.

It has therefore been shown that the stable cavitation clusters produced on the face of downward pointing rods in ultrasonic reactors produce effects usually associated with inertial cavitation. Attempts at using cavitation for the production of molecular hydrogen from aluminium were also made and this the focus in the next section.

3.5 Enhancement of hydrogen production from aluminium

Experimentation was also conducted with the aim of enhancing the production of hydrogen via the erosion of aluminium using cavitation. This was one of the initial aims of the project, based upon the theory as described in the introduction (see section 1.5.2). In these experiments aluminium rods and aluminium grit were subjected to ultrasound in a reactor filled with sodium hydroxide at varied concentrations.

Although many experiments were conducted, ultimately only a small enhancement in hydrogen production was ever achieved in one set of experiments. In these, the sodium hydroxide concentrations were selected to exhibit a range of rates of hydrogen production, via reaction with aluminium as detailed in section 1.5.

In each experiment, aluminium grit (*ca.* 12 mg) was introduced into the hydroxide solution through the top of a sealed container (reactor 2) in which air was flowed over the headspace through a Dreschel head. Downstream of this flow, the hydrogen level was detected by a calibrated hydrogen sensor as detailed in 2.1.8. This was performed with and without ultrasonic irradiation of the reactor.

Figure 3.27 demonstrates the rate of hydrogen production and temperature variation during the reaction of aluminium and sodium hydroxide (0.1 M). Upon simultaneous addition of aluminium and commencement of the ultrasound at *ca.*

260 s, the rate of hydrogen increased and reached a plateau at *ca.* $0.05 \text{ cm}^3 \text{ min}^{-1}$. During this time the temperature increased by *ca.* $3 \text{ }^\circ\text{C}$. Upon ceasing the ultrasound, the hydrogen production rate decreased and reached a plateau at *ca.* $0.035 \text{ cm}^3 \text{ min}^{-1}$. The temperature also inflects at this time, showing that the temperature rise was caused primarily by Joule heating from the transducer. Hence overall there was an apparent increase in the rate of hydrogen production when the ultrasound was commenced. However it is uncertain whether the increased production rate is caused by cavitation erosion or the temperature increase via enhanced reaction kinetics.

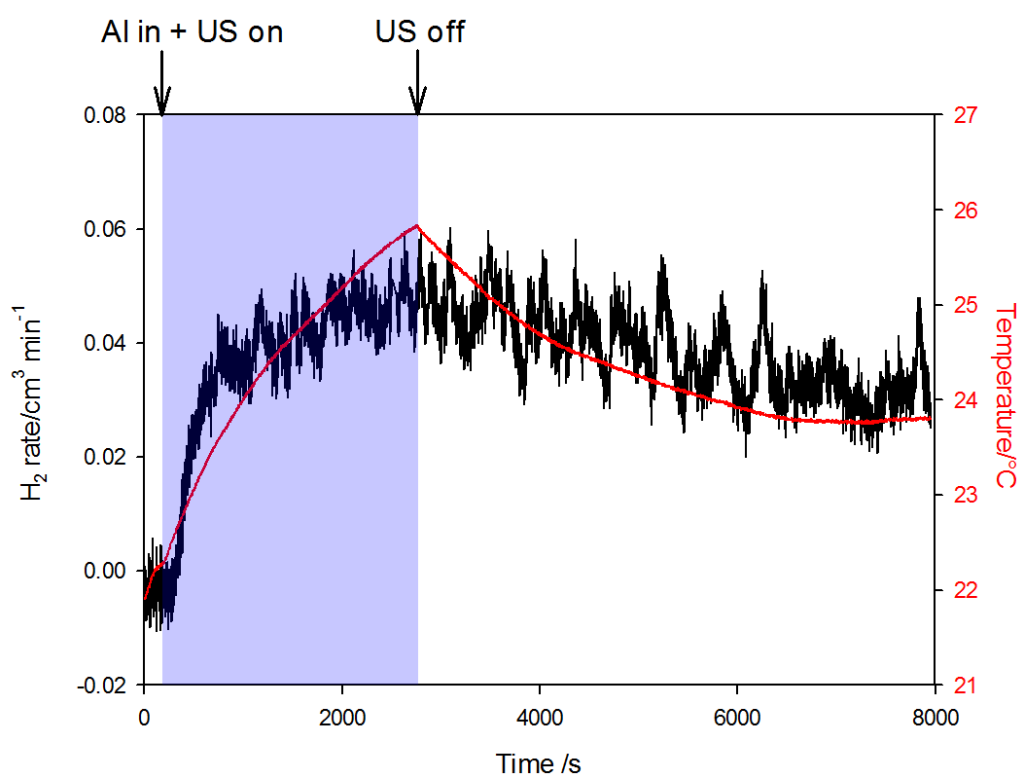


Figure 3.27 Plot showing the hydrogen production rate (—) and liquid temperature (—) produced from reaction aluminium grit (11.7 mg) with NaOH (250 cm³, 0.1 M) in reactor 2. The aluminium was added and the ultrasound initiated (28 kHz, 20 V_{pp}, 32 dB) simultaneously at *ca.* 260 s, highlighted by the arrow and shaded area on the plot. The airflow through head of the Dreschel flask was 305 cm³ min⁻¹ and the liquid flow 1.2 dm³ min⁻¹.

In order to assess the effect of ultrasound in different conditions, further similar experiments were conducted with varied hydroxide concentrations, and with and without ultrasound and temperature control of the liquid. Figure 3.28 shows the results from these experiments with the rate of hydrogen production shown as a function of pH (calculated from the varied sodium hydroxide concentrations of 0.02, 0.06, 0.1, 0.2 and 0.4 mol dm⁻³).

Chapter 3: Cavitation bubble clusters

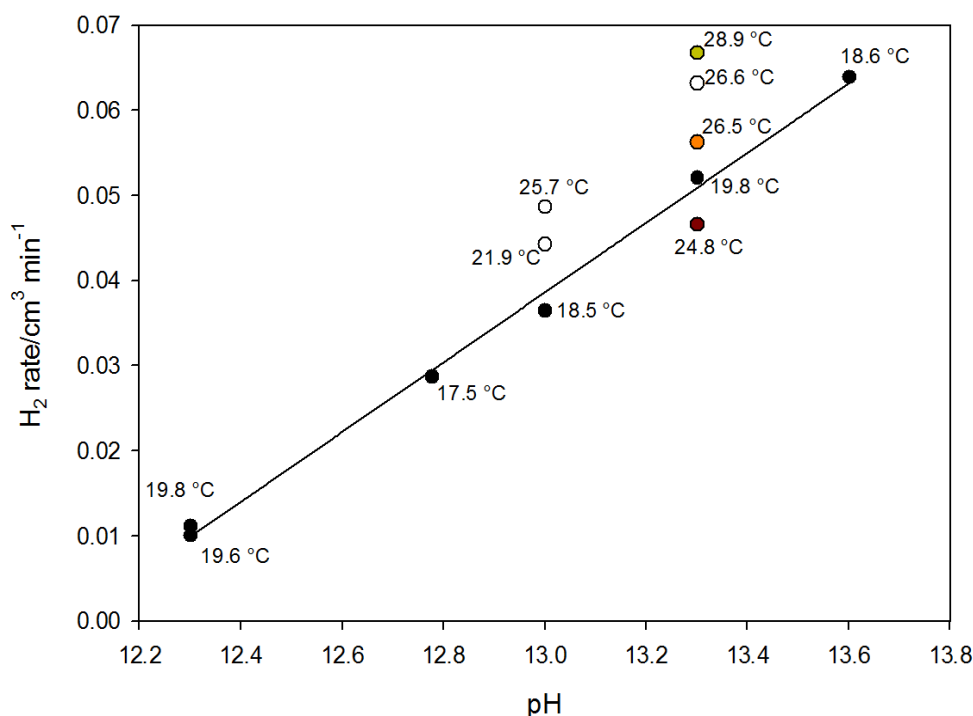


Figure 3.28 Plot showing the averaged steady state rates of hydrogen produced from aluminium grit (0.012 g) in sodium hydroxide solution at varied concentrations with (○) and without (●) ultrasonic irradiation. Results from three thermostatic experiments (●●●) are also shown.

Each data point on the figure represents the average level of hydrogen detected by the hydrogen sensor during the steady rate plateaus of hydrogen production achieved, as observed in Figure 3.27. The experiments conducted without ultrasound (●) show a linear increase in the rate of hydrogen production with increasing pH. The measured liquid temperatures are relatively constant in this range. The temperature controlled experiments (●●●) demonstrate an increase in rate with temperature within the set. However, these are lower than expected when compared to the experiments conducted without thermostatic control which had temperatures < 20 °C. It is assumed that this is due to errors in the measurements and calculation of the relatively low amounts of hydrogen generated. The experiments conducted with ultrasound (○) show an increased rate of hydrogen production when compared to those without (●). However, the increase is comparable to that shown by the increased temperature in the thermostatically controlled experiments. Hence it is unclear whether the relatively small increase is due to ultrasonic action or more likely as a result of the higher temperatures generated from calorific heating from the transducer.

A set of similar experiments were conducted using aluminium rods instead of aluminium grit. In these experiments, a cavitation cluster was formed on the rod

face, ensuring that cavitation erosion was occurring. However, similarly to the aluminium grit experiments, the hydrogen production rate did not significantly increase.

In conclusion, across all of the attempted experiments which employed the reaction of aluminium in alkaline conditions, including those with a hemispherical cavitation cluster formed on the face of an aluminium rod, there was never a clear and discernible enhancement in the generation of molecular hydrogen with ultrasound. For this reason, focus was diverted from trying to fulfil this aim and was instead focussed on the other topic areas presented.

3.6 Conclusions

The stabilisation of pseudo-hemispherical cavitation clusters formed in cylindrical ultrasonic reactors has been shown, induced by the positioning of a rigid rod according to the conditions employed. This has been termed reactor induced cavitation cluster stabilisation (RICCS). Pressure measurements have confirmed that this is at an antinode of a standing wave generated within the reactor.

The application of rheoscopic particles within ultrasonic reactors has revealed a novel and useful method for the characterisation of standing wave fields within reactors of this type. The mechanism of interaction between the particles and sound field is unclear and requires further investigation.

High-speed imaging has demonstrated the erosion of an aluminium electrode resulting from the collapse of bubble clusters formed on the electrode face in reactors. The studies also demonstrated that the collapse of the hemispherical cluster can result in erosion events occurring with varied periodicity; once or twice per sound wave cycle. This was linked to the appearance of a double shell structure in the hemispherical cluster wherein the inner cluster was observed to collapse once per sound wave cycle.

Intensified imaging of a cluster formed via RICCS in a luminol solution demonstrated the presence of sonochemiluminescence in the region of the hemispherical cluster. However, there was no detected sonoluminescence in the set-up employed, most likely because the level of light emitted was below the detection threshold. As the pressure amplitude increased, light was emitted

Chapter 3: Cavitation bubble clusters

through SCL in a larger spatial region, a result of the increasing spatial distribution of the cavitation cloud.

Experiments showed that three discernible regions of electrode (erosion sensor) degradation may exist, which are dependent on state (roughness) of the aluminium surface and the support. In turn, the stability of the cavitation cluster is affected, which exhibit varied erosive properties.

Investigation of a 'shimmer' effect emanating from clusters formed via RICCS have been shown to be the result of a refractive index change, which was enhanced through the use of Schlieren imaging. Local heating of the liquid was demonstrated and is most likely the cause of the observed effect.

Molecular hydrogen generation from aluminium in alkaline conditions has shown little or no enhancement upon irradiation with ultrasound. A small observed increase in the rate of gas evolution upon subjecting the reactor to ultrasound was most likely caused by the rise in temperature associated with calorific heating from the transducer.

Chapter 4: Ultrasound assisted gas release

This chapter discusses an investigation that was carried out with, and relates to, the electrolysis device manufactured by the sponsoring company, HTOGO Ltd. Analysis of the device performance is presented, including examination of the temporal response and efficiency analysis with consequential design enhancements suggested thereafter. The principally explored device improvement involves the novel concept of using ultrasound to control the release of gas from a bubbly liquid reservoir. This is investigated and analyses in the second half of the chapter.

The chapter begins with a discussion of the experimental setup and methods used to characterise the device performance.

4.1 Electrolysis device characterisation

4.1.1 Experimental setup

An experimental rig was designed and assembled in order to recreate the conditions in which the electrolysis device is utilised *in-situ* by HTOGO. This setup employed a modified Dreschel bottle (Reactor 2 in Figure 2.1 b) as a reservoir positioned above the electrolysis device so that the liquid (sodium hydroxide, 0.1 M) from the electrolysis cell, which was brought up as a bubble/electrolyte mix, was replenished by gravity induced flow from the outlet at the base of the bottle. A schematic of the rig is presented in Figure 4.1 which also shows the subsequently added pump and flow sensor. The outer two plates of the electrolysis device were connected to the negative terminals (cathodes) of the power supply (ISO-TECH IPS-1820D) and the centre plate to the positive terminal (anode), as labelled in Figure 4.1. The device was operated at a constant current controlled by the power supply employed. The current was monitored and noted in each experiment. Gases produced from the device were routed to the reservoir headspace where an air compressor (Clarke Wiz Air) generated a controlled airflow to direct the gas downstream to a hydrogen sensor. Hydrogen detection and measurement was achieved as detailed in section 2.1.8. A K-type thermocouple (TC) was held in place in a short section of polyvinylchloride (PVC) tube using quick set epoxy resin (Araldite), which was positioned in the flow as shown in the rig schematic. Temperature measurements were made using Pico Technology data logger (TC-08)

Chapter 4: Ultrasound assisted gas release

interfaced with a PC. In order to avoid electrical interference, the thermocouple was coated with a thin layer of clear nail varnish (Rimmel London).

All of the sensors were connected to a USB DAQ (Cole Parmer 18200-20) and interfaced to a PC using in-house written software (appendix 11, HTOGO FFT.vbp) which was programmed to provide ‘on-the-fly’ monitoring with routines to save and load data files as appropriate. Later amendments to the setup included the addition of a fluid pump (EHEIM Type 1105) and flow rate sensor (UCC Type DFC.9000). A mixture of silicon and PVC tubing was used to transfer the liquid between the cell and reservoir. Copper piping and PVC tubing was used to channel gas throughout the rig.

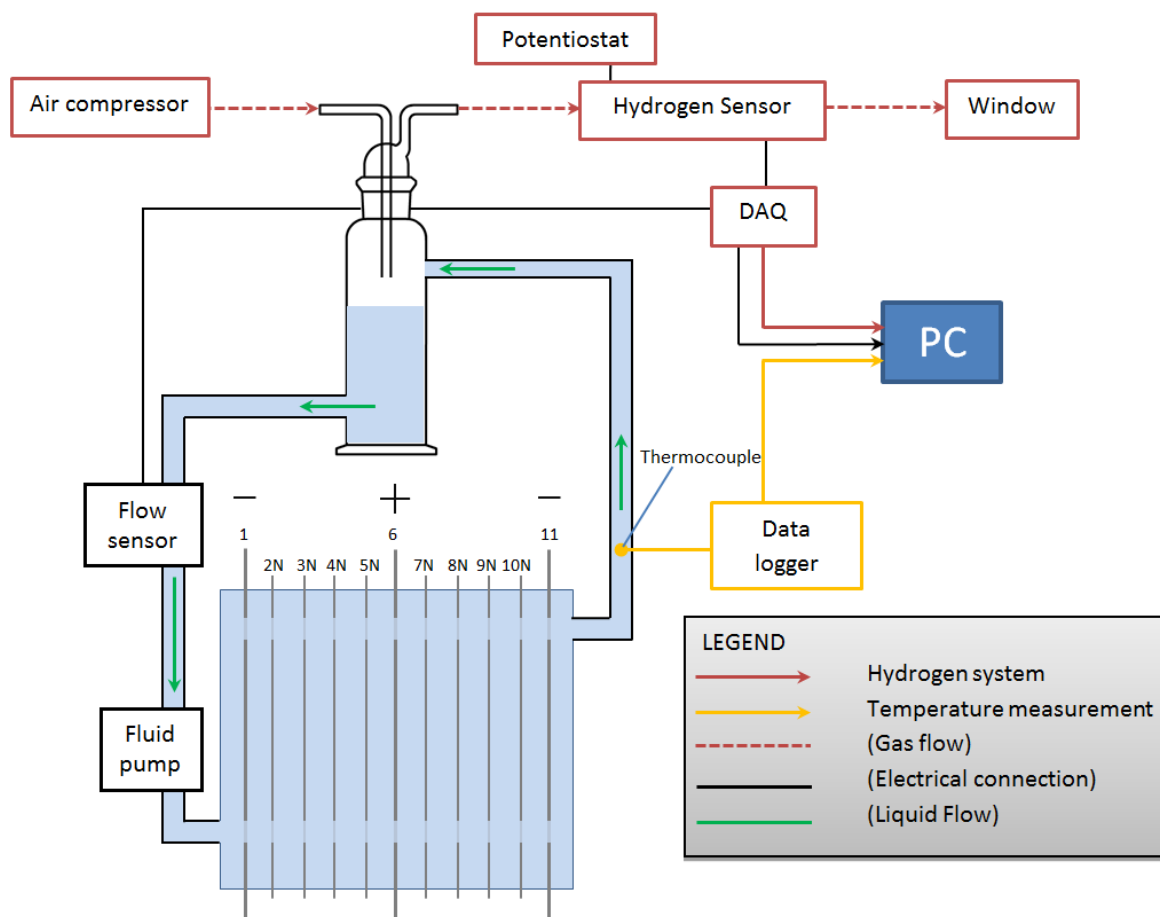


Figure 4.1 Schematic demonstrating the initial experimental setup with the subsequent addition of the liquid flow pump and flow sensor. Plates denoted with an ‘N’ for ‘Neutral’ are plates that are not directly connected to the power supply.

4.1.2 Hydrogen measurement

4.1.2.1 Sensor calibration

A carbon monoxide sensor (Alphasense, CO-BF) with cross-sensitivity for hydrogen gas was calibrated so that hydrogen generated from the electrolysis cell could be measured accurately and reproducibly (see Figure 2.6, page 31). Regular inspection of the sensors response were performed in the same manner as described in the experimental section in order to confirm that the operation of the sensor was not subject to deterioration in any way.

4.1.2.2 Electrolysis system

The HTOGO electrolysis device was initially tested by monitoring the hydrogen gas concentration and temperature as electrolysis was initiated. Figure 4.2 shows the response of the hydrogen sensor (—) and the temperature (—) during such an experiment. The blue shaded area shows the period in which the electrolysis device was on. The data shows that there was a considerable time delay from when the cell was powered on, shown by the dotted line, until any hydrogen is detected 70 seconds later. A further *ca.* 230 seconds is then required until the maximum level of hydrogen output was attained at the pseudo-plateau region from *ca.* 3400 s. Although the variation in this pseudo-plateau region is large, the time averaged level (over 100's of seconds) remains relatively constant. The time taken to reach 90 % of the maximum achieved level after switching the device on was *ca.* 250 s (maximum value taken as the average level between 3400 s and 4200 s).

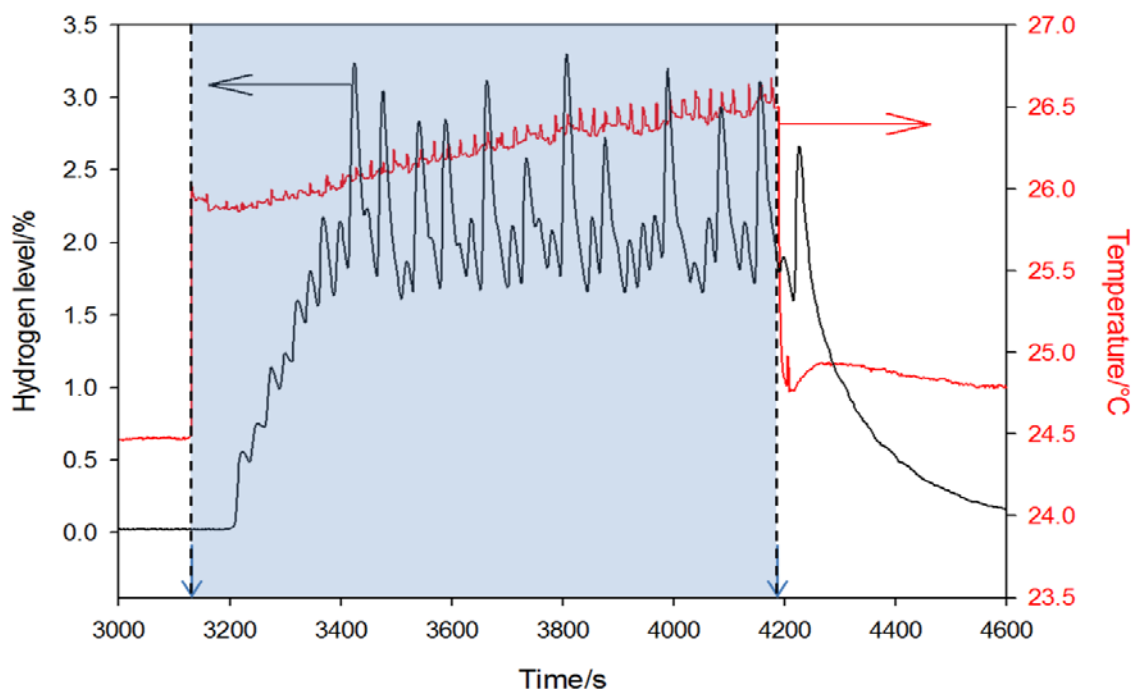


Figure 4.2 Response from the hydrogen sensor (black line —, left axis) and thermocouple (red line —, right axis). The electrolysis cell was turned on from 3130 s to 4190 s at a current of 250 mA. The air was flowed at $150 \text{ cm}^3 \text{ min}^{-1}$.

The hydrogen fluctuations were caused by the trapping of gas bubbles which need to build up in the device so that newly produced bubbles force the previously produced bubbles out of the cell and into the reservoir. In addition the initial 70 s delay was caused by the ‘gravity induced’ flow characteristics of the system. This is a severe limitation of an electrolysis cell operated with the flow driven by gas bubble production. Clearly a system such as this with a time constant of the order of 300 s for hydrogen production is non-ideal for input into an internal combustion engine (ICE), where the demand will vary over the driving cycle of the vehicle. Clearly a more rapid release of hydrogen is required that can be accurately controlled and incorporated into a vehicle and its associated engine management.

In addition, the large variation in hydrogen level shown by the peaks and troughs in the pseudo-plateau region between 3400 s and 4200 s is inadequate for a system in which precise control is needed [1, 6]. The variation was caused by small pockets of gas that were observed to be sporadically released at the outlet of the device. The gas produced was observed to build up in the top of the electrolysis device, creating a headspace of gas. This would continue until the gas was ejected as a ‘slug’ from the electrolysis cell. This repeatedly caused pockets of hydrogen gas to be released and detected by the hydrogen sensor (see Figure 4.2, *ca.* 3800 s). This effect was also detected by the temperature measurement (— Figure 4.2). Unfortunately

despite the electrical insulation layer on the thermocouple some cross talk from the cell was still noted. Hence the temperature jumps at *ca.* 3150 and 4200 s are not valid. However, the gas pocket ‘slug flow’ appear to be the cause of the regularly occurring small peaks in temperature. Note the gradual increase in temperature over the whole experiment shows a Joule heating effect associated with the electrolysis of the fluid in the cell.

It must be noted that these tests were performed using lower currents to power the electrolysis device than HTOGO employ. This was due to laboratory safety restrictions and hydrogen sensor working limits. As such a quantitative conclusion about the performance of the real device cannot be drawn. However, the principle remains that any build-up of gas in the cells should be avoided for precise control of the gas output. Furthermore it is advantageous to avoid parasitic reactions, (e.g. hydrogen gas oxidation or oxygen gas reduction) which reduce efficiency. In addition coverage of the electrode surfaces by gas bubbles directly adds to the electrical resistance between the plates. A liquid filled with more gas bubbles decreases the contact area between the electrodes and electrolyte, blocking electron transfer and increasing the ohmic loss, wasting energy via heat production.

Clearly the delayed and inconsistent hydrogen output is significantly detrimental for a system with aims of producing a steady rate of hydrogen to feed into an ICE in a controlled manner. In addition, analysis of the electrolysis cells performance could be made more accurately with a constant rate of gas release. Hence in attempts designed to address some of these limitations, a fluid pump to mechanically circulate the electrolyte through the device was added. Figure 4.3 demonstrates the response from the hydrogen sensor with electrolyte flowing at *ca.* $1 \text{ dm}^3 \text{ min}^{-1}$.

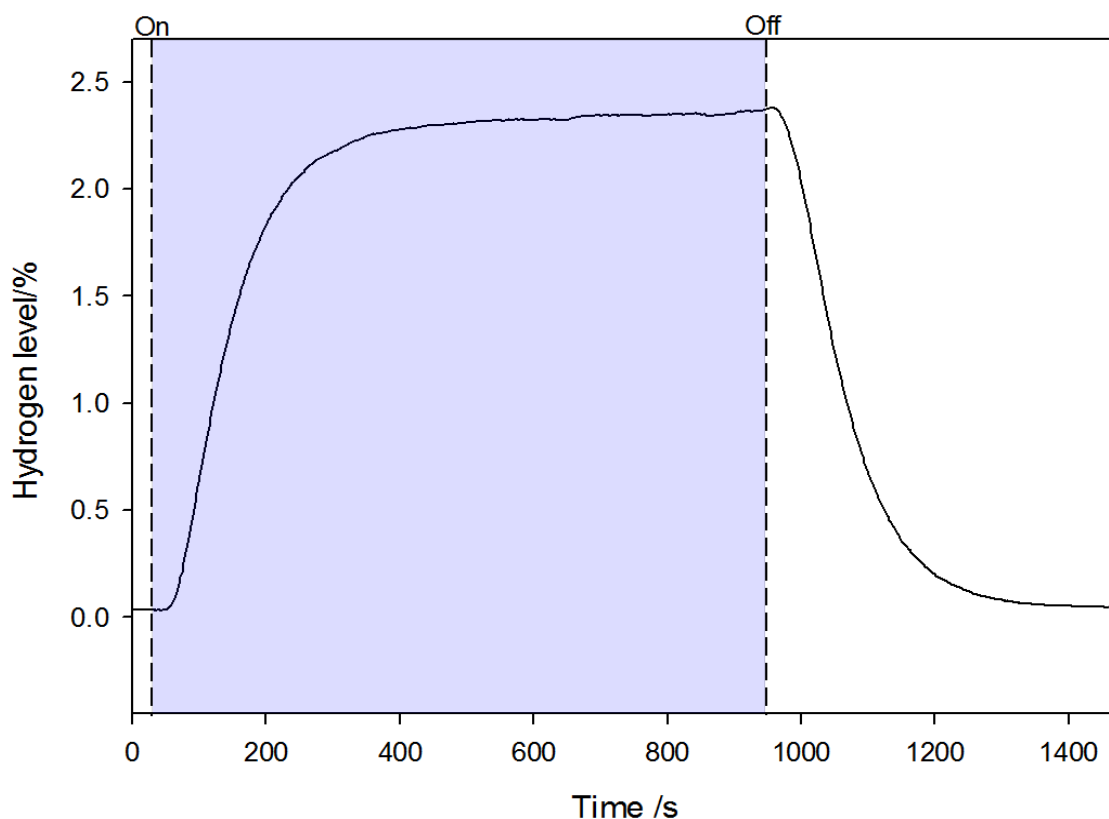


Figure 4.3 Plot showing the hydrogen production in the air stream from the apparatus. The electrolysis cell was turned on from 30 s to 945 s at 260 mA. The air was flowed through the Dreschel head at $150 \text{ cm}^3 \text{ min}^{-1}$. The electrolyte was pumped at $1.03 \text{ dm}^3 \text{ min}^{-1}$.

Figure 4.3 shows that the initial release of hydrogen from the system is quicker with forced liquid flow; the first sign of hydrogen gas is observed *ca.* 20 seconds after the electrolysis device was switched on (---). Although gas bubbles were observed to be produced and exit the electrolysis device almost immediately, it became apparent that the bubbles were transferred to the liquid reservoir and then recirculated through the device. These bubbles were noted to be smaller in size; presumably as a result of the faster fluid flow, inducing a faster detachment of the bubbles from the electrodes surface. Furthermore the flow hinders the collection and coalescence of bubbles in the headspace of the electrolysis cell. However the forced convection also resulted in the reservoir retaining more gas bubbles and hence more recirculation of gas bubbles ensued. Figure 4.3 demonstrates that the hydrogen level increases more smoothly and reaches a plateau (*ca.* 2.3 %), compared to experiments without forced convection. These traits demonstrate the observed cessation of the collection of large gas pockets at the output of the electrolysis device, resulting from the sporadic electrolyte flow. Perhaps counter-intuitively, the time taken to reach a stable concentration of hydrogen at the gas

sensor is actually longer with the flow pump; the 90 % response time is 270 s with electrolyte flow compared to *ca.* 250 s without. This is a consequence of the discussed effects, *i.e.* with the flow resulting in greater retention and recirculation of gas bubbles in the liquid reservoir. Therefore with the flow on, the electrolyte fills up with a greater number of smaller bubbles and turns an opaque milky white colour, only producing a steady rate of hydrogen output once the reservoir has been populated. Once this has occurred the rate of hydrogen produced by the electrolysis cell reaches equilibrium with the amount leaving the liquid reservoir. Without forced convection produced by the pump, the reservoir appears to contain less gas as the large slugs of gas that reach the reservoir are immediately ejected into the head space rather than recirculating through the system.

In order to assess the Faradaic efficiency of the electrolysis device, the hydrogen production rate was compared to the theoretical maximum for the current passed applying Faraday's Law. For example the results presented in Figure 4.3 were obtained at 260 mA, which if 100 % efficient (Faradaic efficiency) equates to a hydrogen production rate of $19.8 \text{ cm}^3 \text{ min}^{-1}$ from the ten cells in the device. The airflow is $150 \text{ cm}^3 \text{ min}^{-1}$ and so the theoretical maximum amount of hydrogen is 11.7 % for the given air flow rate. The sensor detects a maximum concentration of 2.3 % hydrogen in air in the plateau region. Hence when compared to the maximum theoretical value a current efficiency of only *ca.* 20 % is estimated.

This conversion rate is relatively low and further experiments were performed to explore the efficiency of the electrolysis system. Furthermore a set of supplementary experiments were conducted to go beyond the detection limits of the hydrogen sensor and give efficiency information at higher current values. Here the total gas output (hydrogen and oxygen) was measured volumetrically using a gas syringe (Weber Scientific B.S. 1263, 50 cm^3 , $\pm 2 \text{ cm}^3$) connected to the outlet of the Dreschel bottle, with a blocked inlet to give a closed system. These experiments were performed with and without induced electrolyte flow. The measured volume of gas was adjusted to give the volume of hydrogen gas produced, assuming a 2:1 ratio of hydrogen to oxygen. The adjusted value was then used in the comparison to the maximum theoretical amount for the charge passed to give the actual Faradaic efficiency of the system.

Chapter 4: Ultrasound assisted gas release

Figure 4.4 shows a compilation of the results, demonstrating the calculated Faradaic efficiency. Figure 4.4 shows that across all the experiments a positive correlation between the Faradaic efficiency and the electrolysis cell current was observed. The tests performed at lower currents (180 to 380 mA) measured with the electrochemical hydrogen sensor exhibit a linear correlation; with the Faradaic efficiency increasing from *ca.* 15 % to 30 % over the current range explored (~200 mA to 400 mA). The volumetric experiments measured using the gas syringe with electrolyte flow (red dots) are in close agreement with this, from *ca.* 300 to 400 mA, above which the trend gradually plateaus and appears to be levelling at around 35-40%.

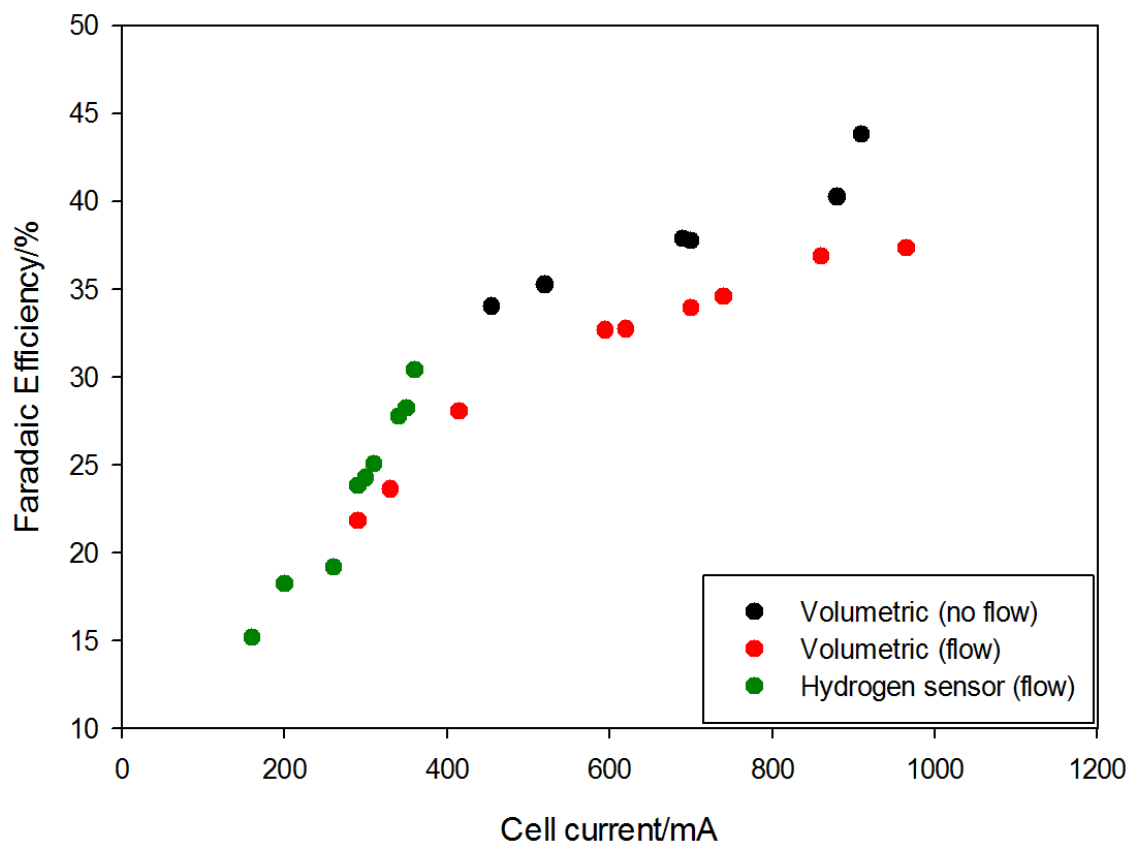


Figure 4.4 Plot showing the Faradaic efficiencies as a function of cell current for three sets of experiments; (•) = hydrogen concentration measured using gas sensor with an air flow of $150 \text{ cm}^3 \text{ min}^{-1}$ through the Dreschel head; (•) = measured gas volume output (gas syringe) with electrolyte flow ($1 \text{ dm}^3 \text{ min}^{-1}$); (•) = gas volume output (gas syringe) without electrolyte flow. All experiments used 0.1 M NaOH electrolyte.

The volumetric experiments measured using the gas syringe without electrolyte flow (black dots) exhibit a similar trend, however with a small offset above the other volumetric based values. The small difference between these volumetric tests

can be explained by considering that increased recirculation of gases induced by the electrolyte flow is to the detriment of the Faradaic efficiency. This is because more gas is available as reactants at the electrode surfaces for the parasitic back reactions; hydrogen oxidation and oxygen reduction. These back reactions waste energy converting the gaseous products back to water. Hence by increasing the flow rate through the cell, a greater proportion of the charge passed is consumed by these competing processes, resulting in a lower overall Faradaic efficiency.

Overall, the attained efficiency of the tested electrolysis device is relatively low (maximum of *ca.* 45 %) when compared with modern electrolysis devices, which exhibit Faradaic efficiencies close to 100 % [193, 194]. Possible reasoning for this can be found by considering the simplistic design of the electrolysis device. Although the uncomplicated design is ideal for cost minimization and ease of production, when compared to the more advanced devices a significant absence in the design of the device becomes apparent. This is the presence of an ionic membrane divider between the cells [40, 195]. The function of a membrane is to allow ions to pass through but minimise gas transfer. Hence such an addition would effectively help to obstruct the crossover of produced gases to the opposite electrodes and therefore prevent the unwanted reactions from occurring. Disadvantages of such a membrane can include the partial inhibition of ionic transfer (which would reduce energy efficiency) and produce an increase in the ohmic resistance.

The literature contains many examples of improvements of the device in terms of both Faradaic and overall energy efficiencies (Ursúa *et al.*, 2012 review, [196]). Some of these potential further enhancements include: the minimization of the electrode spacing to reduce ohmic losses; the development of effective membrane materials to hinder parasitic reactions; alteration of the working temperature to increase conductivity and reaction kinetics; and the use of more advanced electrocatalytic electrode materials to reduce the cell overpotential. Hence instead of focusing on the design of electrolysis device itself, the research in the rest of this chapter focussed on the study and enhancement of mechanism of hydrogen gas output from the system. By addressing this issue progression to the next generation of device can be initiated, where the demands of an ICE can be met in a more responsive and therefore more effective manner.

Chapter 4: Ultrasound assisted gas release

4.1.3 Uncompensated resistance measurement

The uncompensated resistance (R_u) is an inherent property arising from the electrode material, electrical leads or conductivity of the electrolyte. Myland [197] defines R_u as “the resistance between the working electrode and the entire equipotential surface that traverses the tip of the reference electrode”. Hence measurement of R_u in the described electrolysis system is useful, as changes in the gas population (and temperature) can be measured.

In order to assess the uncompensated resistance in the system employed, an AC-modulation method technique was applied. This is required (as opposed to DC) to avoid effects of polarisation at the electrode-electrolyte interface. In the technique, a sinusoidal voltage is applied to the cell and the sinusoidal current passing through the cell as a result is measured. The sinusoidal voltage and current can be defined as shown in eqs. (4-1) and (4-2) respectively.

$$E = \Delta E \sin \omega t \quad (4-1)$$

$$I = \Delta I \sin(\omega t + \theta) \quad (4-2)$$

Here E is the potential value, ΔE is the potential amplitude, I is the current, ΔI is the current amplitude, ω is the angular frequency (equal to $2\pi f$ where f is the sinusoidal frequency measured in Hz) and θ is the phase angle. The current that is measured may be in or out of phase with the applied sinusoid. A cell which behaves purely as a resistor will give a response with the current in phase with the potential ($\theta = 0^\circ$), following *Ohm's Law*. A cell which behaves purely as a capacitor will give a response with the current 90° ($\pi/2$ radians) out of phase with the potential. This follows from the definition of capacitance $q = CE$, where E is the potential across the plates and q is the charge.

The impedance, Z , can be defined analogously to the resistance of D.C. measurements as shown in eq. (4-3), where both the phase angle and the magnitude of the impedance are both functions of the applied frequency.

$$|Z| = \frac{|\Delta E|}{|\Delta I|} = |Z(\omega)| = \frac{|\Delta E(\omega)|}{|\Delta I(\omega)|} \quad (4-3)$$

Hence the impedance of a cell is defined as a vector quantity, having both magnitude and phase.

When determining the impedance of a cell, equivalent circuit models based on physical components are employed. Figure 4.5 demonstrates a simple equivalent circuit for an electrochemical cell.

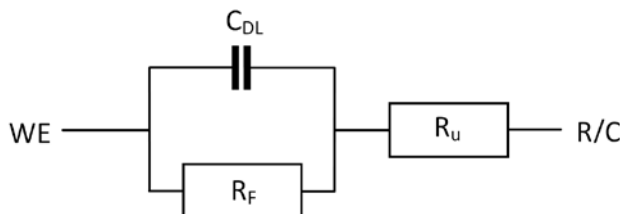


Figure 4.5 Schematic of a simple equivalent circuit of an electrochemical cell where *WE* is the working electrode, *R/C* is the reference/counter electrode, R_u is the uncompensated resistance, R_F is the Faradaic resistance and C_{DL} is the double layer capacitance.

Therefore by applying only a high frequency wave, the AC modulation technique isolates the uncompensated resistance from the Faradaic resistance (following the top route in the circuit in Figure 4.5). The amplitude of the applied high frequency signal provides a known voltage which can be used with the measured signal to calculate the resistance in the system using *Ohm's Law*.

The experimental details for this method are presented in section 2.1.9 (page 32). Figure 4.6 shows a schematic representation of the previous experimental setup with the added system for measuring the uncompensated resistance. The uncompensated resistance was measured at two locations: between the steel plate electrodes of the electrolysis device shown by connections labelled 'A' in Figure 4.6, and between two steel plate electrodes (detailed in section 4.1.3.3) positioned at the port connecting the reservoir to the electrolysis device, as shown by connections labelled 'B' in Figure 4.6.

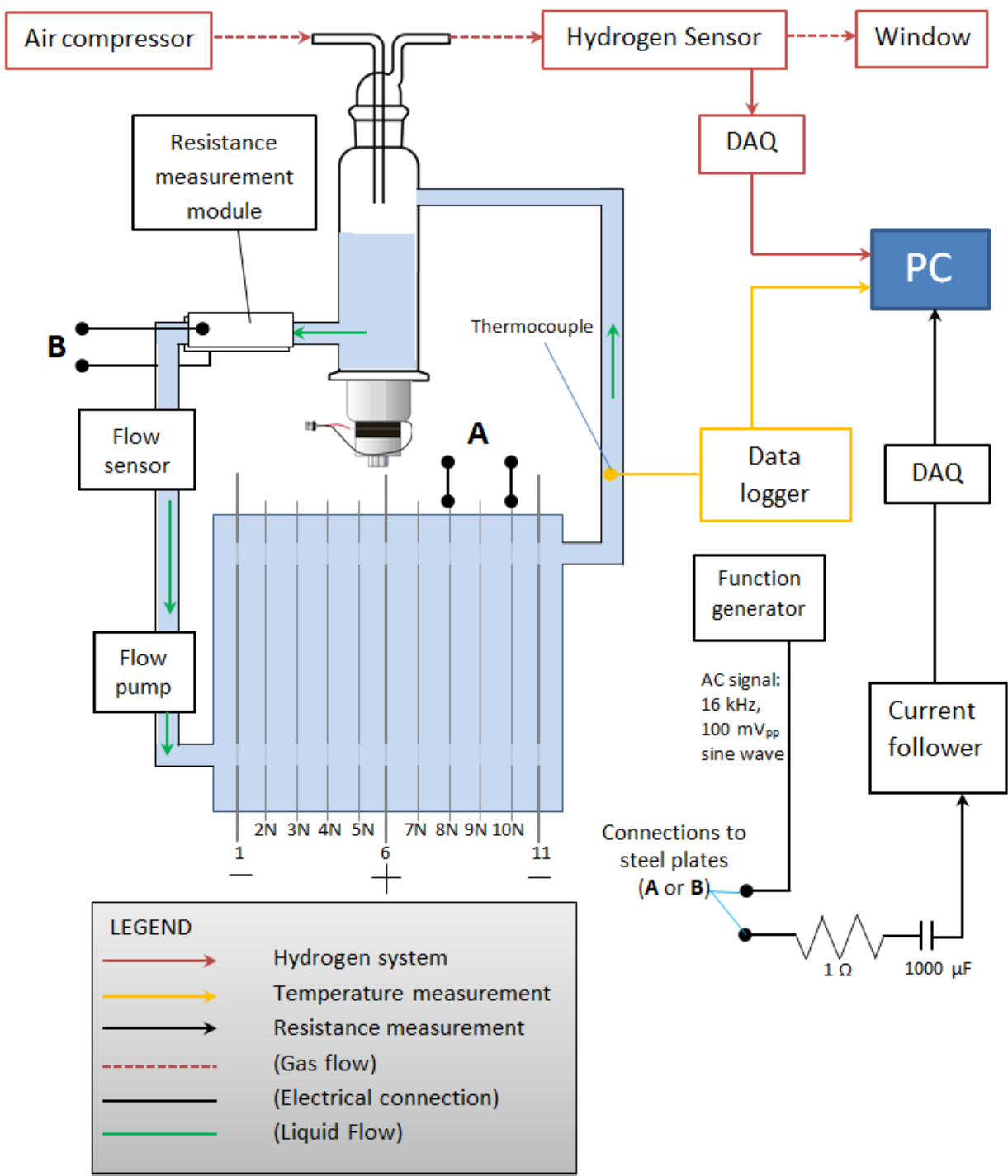


Figure 4.6 Schematic demonstrating the experimental setup with the equipment for measurement of the uncompensated resistance via the AC-modulation technique. The connections were made to the plate electrodes of the electrolysis device (labelled A) or to two steel plates of a modular flow-through section (detailed in section 4.1.3.3).

4.1.3.1 Dummy cell calibration and method validation

In order to validate the R_u measurement technique, a series of known value resistors were used as dummy cells and their values determined using the AC-modulation method as described in experimental section 2.1.9. Each dummy resistor was measured continuously for 15 seconds. This process was then repeated twice more and an average for each dummy cell value was calculated from the combined data. Figure 4.7 demonstrates the results from these experiments, with the black dots showing the resistance acquired via the AC measurement technique *vs.* the value of the resistor indicated by the coloured bands on the component (also checked with an ammeter). The black error bar values are 95 % confidence intervals from the data sets, which appear as line because the error is so small. The red dots demonstrate the 1:1 theoretical perfect response where the measured resistance equals the actual resistance.

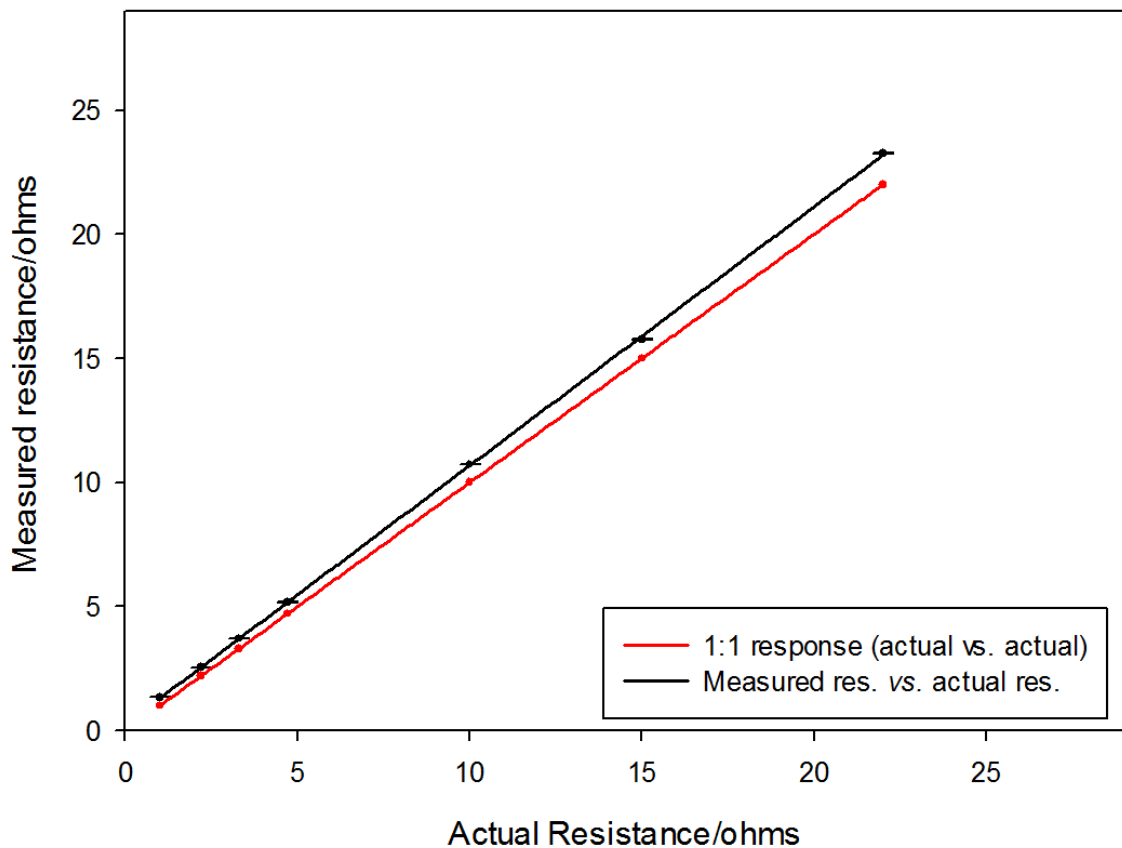


Figure 4.7 Graph showing the measured resistance values *vs.* the actual resistance values (black dots, •) of known value resistors. The red dots (•) demonstrates the perfect 1:1 response (actual resistance *vs.* actual resistance). Dummy resistor values: 1.0, 2.2, 3.3, 4.7, 10.0, 15.0 and 22.0 Ω . Drive signal = 16 kHz, 100 mV. Sample rate = 40 kHz. Polynomial fit for experimental data (black line —): $y=1.0423x + 0.2623$

Chapter 4: Ultrasound assisted gas release

The results show that AC-modulation approach is an excellent method for measuring the resistance of the dummy cell resistors, with experimental data that fits very well to the theoretical. A small systematic error is apparent in the measured values, shown by the increasing difference between the two lines. Although this can be considered negligible for the experiments conducted with the electrolysis system, any resistance measurement was calibrated using the relationship modelled by the best straight line fit (black line). Hence any quoted resistance value hereafter has been adjusted to cater for the small systematic error, an operation performed by the software (appendix 11: HTOGO FFT.vbp).

Note for any resistance measurement obtained on the electrolysis system, a 1 ohm resistor was added in series with the steel plates (shown in experimental schematic Figure 4.6). This ensures that the measured value is within the limits of the tested dummy cell range (this was the minimum resistance value tested in the calibration). Hence the software also corrects each resistance measurement by the subtraction of 1 ohm. Overall the precision and accuracy of the experimental approach are excellent. The system is capable of measuring resistances with $m\Omega$ resolution, demonstrated by the extremely small error and can be accurately determined on a sub second timescale, with a sample rate of 40 kHz.

4.1.3.2 Measurement of R_u in the electrolysis system

The AC-modulation technique was used in combination with the hydrogen sensor to investigate the production, build-up and outflow of gas within the electrolysis system.

Measurement across the electrolysis device was achieved between the electrodes labelled as 8N and 10N, as highlighted in Figure 4.6. In order to avoid interference from the DC potential applied to drive the electrolysis process, a large capacitor was connected in series with the electrodes to function as a DC block (see Figure 4.6).

Figure 4.8 shows a typical set of responses upon switching the electrolysis cell on and off. The shaded area bound by the dotted lines shows the period in which electrolysis was performed. The red line (—) shows the calibrated response from the hydrogen sensor as previously discussed, and the green line (—) shows the

uncompensated resistance between the device electrode plates, with a moving average of this data (—). Prior to electrolysis (0-30 s) a steady baseline resistance was observed in both the hydrogen level ($\sim 0\%$) and resistance measurement ($0.416\ \Omega$). Note that the moving average of the resistance appears to show a change before the cell is switched on at 30 s; however this was just an artefact of the way the moving average was calculated.

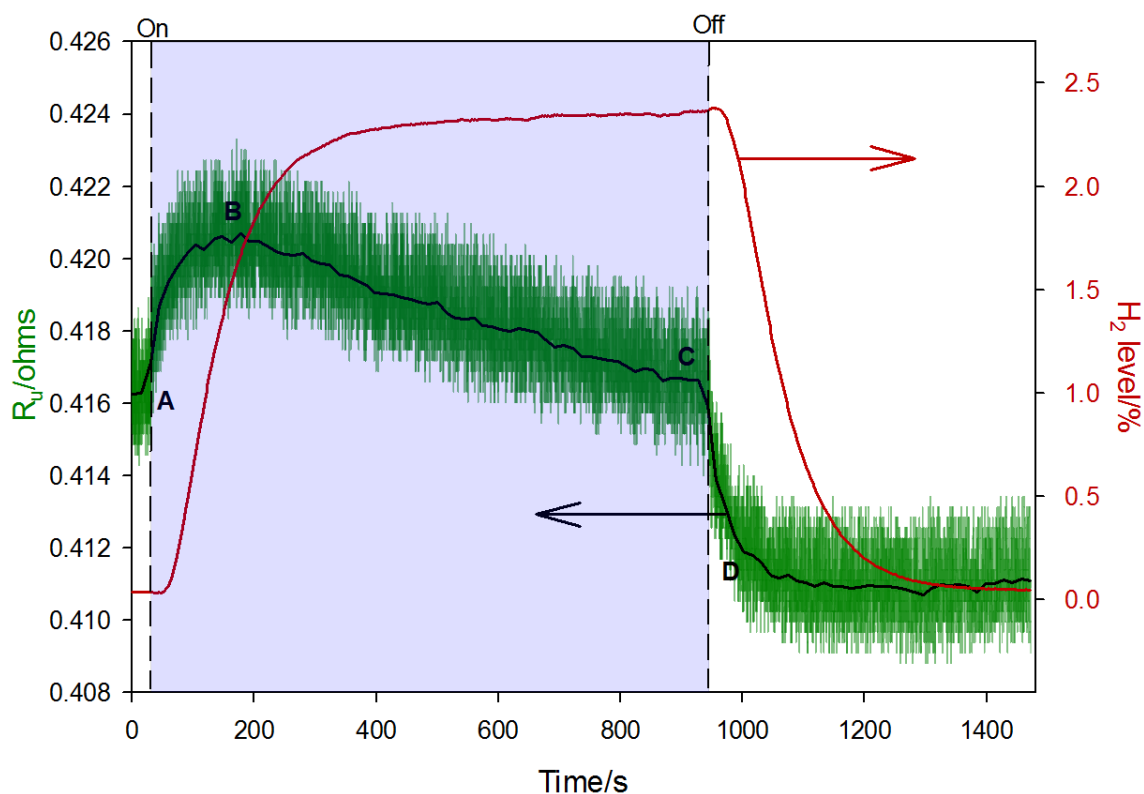


Figure 4.8 Plot showing the response from hydrogen sensor (—, right axis) and resistance measurement (—, left axis with moving average, —) upon turning the electrolysis device on at 30 s and off at 945 s at a current 260 mA using 0.1 M NaOH electrolyte. The airflow was set at $150\ \text{cm}^3\ \text{min}^{-1}$, and the liquid flow at $1.04\ \text{dm}^3\ \text{min}^{-1}$. Resistance measurement made between plates 8N and 10N as labelled in Figure 4.6.

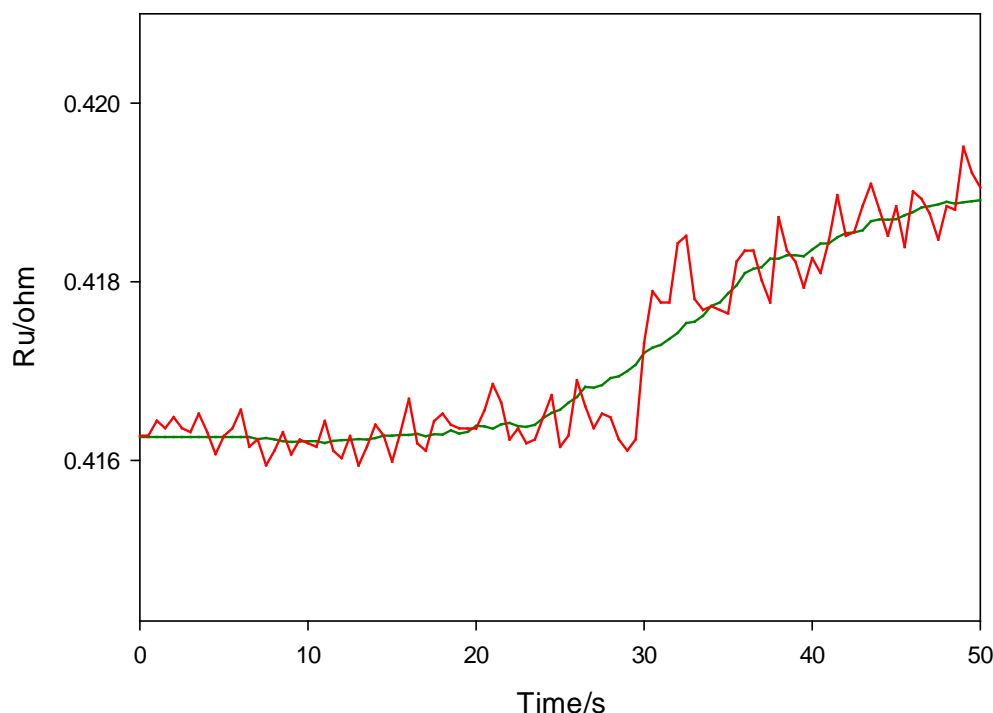


Figure 4.9 Plot showing the uncompensated resistance *vs.* time as the electrolysis cell is switched on a 30 s (same data as in figure 4.7 with shorter time window). R_u is represented by the raw data (—), coarse moving average (—) and fine moving average (—). The conditions are the same as given in Figure 4.8.

The green line in Figure 4.9 demonstrates a coarse moving average and exhibits a change in resistance before the electrolysis device is switched on, whereas the raw data (grey line) and the fine moving average (red line) demonstrate that this is misleading and a change is not observed until after the gas production is initiated.

Immediately after initiation of the gas generation at 30 s, an increase in the uncompensated resistance was observed for around 100 s. This proves that the delay in the response from the hydrogen sensor is due to the time taken for the bubbles to exit the system rather than a delay in the gas production. The trend then inflects and slowly decreases until the device was switched off at ~945 s. The uncompensated resistance within the cell then decreases and plateaus back to a steady value, which is actually below the initially observed baseline value.

The observed increase in uncompensated resistance upon turning on the electrolysis device (between ‘A’ and ‘B’ in figure 4.7) can be explained by considering the influence of the generated bubbles on the uncompensated resistance. As electrolysis progresses, hydrogen and oxygen bubbles are formed on the electrode surfaces and only detach upon reaching a critical volume, dependent

on the flow. Hence this effect continues adding to the resistance until the population of gas bubbles reaches equilibrium, where the same amount of gas being produced is leaving the system.

The decrease in resistance observed when the device is constantly on between points 'B' and 'C' in Figure 4.8 is attributed to the increase in electrolyte temperature as a result of joule heating of the electrolyte. The mobility of ions in a liquid increases as the temperature increases, and hence the conductivity increases and resistance decreases. This is investigated further and confirmed in section 4.3. Upon turning the device off the resistance immediately decreases and levels, returning to the situation where all of the gas bubbles have left the system. The difference in baseline values (points A and D) is attributed to the temperature change via Joule heating as discussed.

The difference in resistance observed between the baseline gas-free condition and bubble-populated electrolyte, at the start when the device is switched on (between A and B on figure 4.7) and at the end when the device is switched off (between C and D), is comparable; 4.9 m Ω and 5.0 m Ω respectively. This is a further indication that the resistance change between B and C is not related to the change in gas void fraction and that the gradual decline in resistance when the cell was powered is due to heating effects. As a control, other electrode plates spanning two cells (connected to electrodes 7N and 9N as labelled in Figure 4.6) were also investigated and the same resistance trend was observed.

Repeats of the experiment discussed above were conducted, keeping all conditions the same except the current passed through the electrolysis device. Experimentation was also performed with and without electrolyte flow. For each experiment, the measured difference of resistance between the gas-free condition and the steady state bubble-populated level was measured, before and after the electrolysis was initiated. For the example given above in Figure 4.8, this is an average of two values: the difference between points B and A, and the difference between points D and C. This value is termed ΔR_u in the subsequent discussion of the compiled results. For each resistance measurement, the data was sampled and averaged over several second time windows (between 3 and 10 s). The 95 % confidence interval was also individually calculated for each measurement based on each respective sample window.

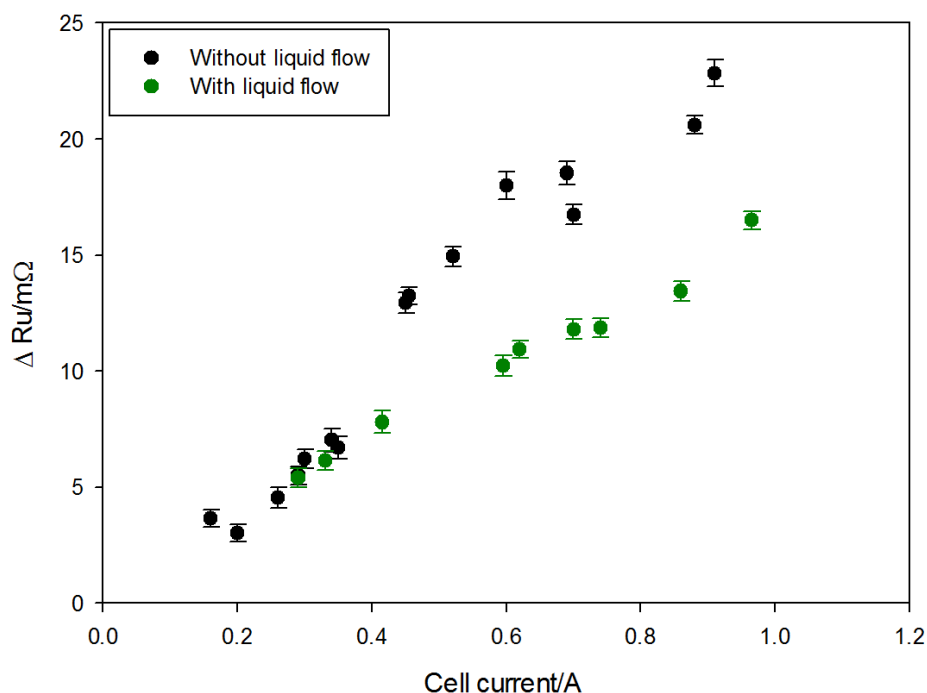


Figure 4.10 Graph shows the change in uncompensated resistance (R_u) between the conditions with and without gas generation *vs.* the electrolysis cell current. The results are for experiments with (•) and without (•) electrolyte flow. The electrolyte was 0.1 M NaOH, flowed at $1.04 \text{ dm}^3 \text{ min}^{-1}$. The airflow was $150 \text{ cm}^3 \text{ min}^{-1}$. Resistance measurements were made between plates 8N and 10N. The error bars are the 95 % confidence interval calculated from the variation in each 30 s sample.

Figure 4.10 shows the compiled ΔR_u as a function of cell current and flow conditions. The overall trend shows that the change in resistance increases with cell current, which correlates with the increase in gas void fraction with electrolysis current. It is apparent that the change in resistance ΔR_u , is generally smaller with the induced flow of electrolyte than without. This implies that the flow produces smaller bubbles which are retained in the fluid thus increasing the gas void fraction.

4.1.3.3 Modular cell for AC-modulation determination of R_u

In order to investigate the bubble population elsewhere in the electrolysis system, a modular cell was designed and constructed, through which the electrolyte could flow and be measured. This was designed so that it could be positioned in the path of the electrolyte between the reservoir and the electrolysis cell, as shown in Figure 4.6. The concept of measuring the resistance across the electrolysis device steel electrodes applies in the same way to the modular cell. The cell is shown in the schematic and picture in Figure 4.11. It consists of two small rectangular steel plates (grade 316L, 52 mm x 11 mm x 0.14 mm), separated by glass capillary tubes

(Ø 3 mm) and held in place with quick set epoxy resin (Araldite). Heat shrink was used to connect the PVC tubing to either end. Wires were connected to the outside of each plate with conductive silver paint (RS Components) and secured and insulated with epoxy resin.

The resistance module was placed at the exit of the reservoir (55 mm length of PVC tube separation between the reservoir and modular device) and the AC-modulation technique employed. As with the previously described measurement technique, the data was acquired and adjusted (appendix 11: HTOGO FFT.vbp) to output the calibrated uncompensated resistance as the electrolysis was initiated.

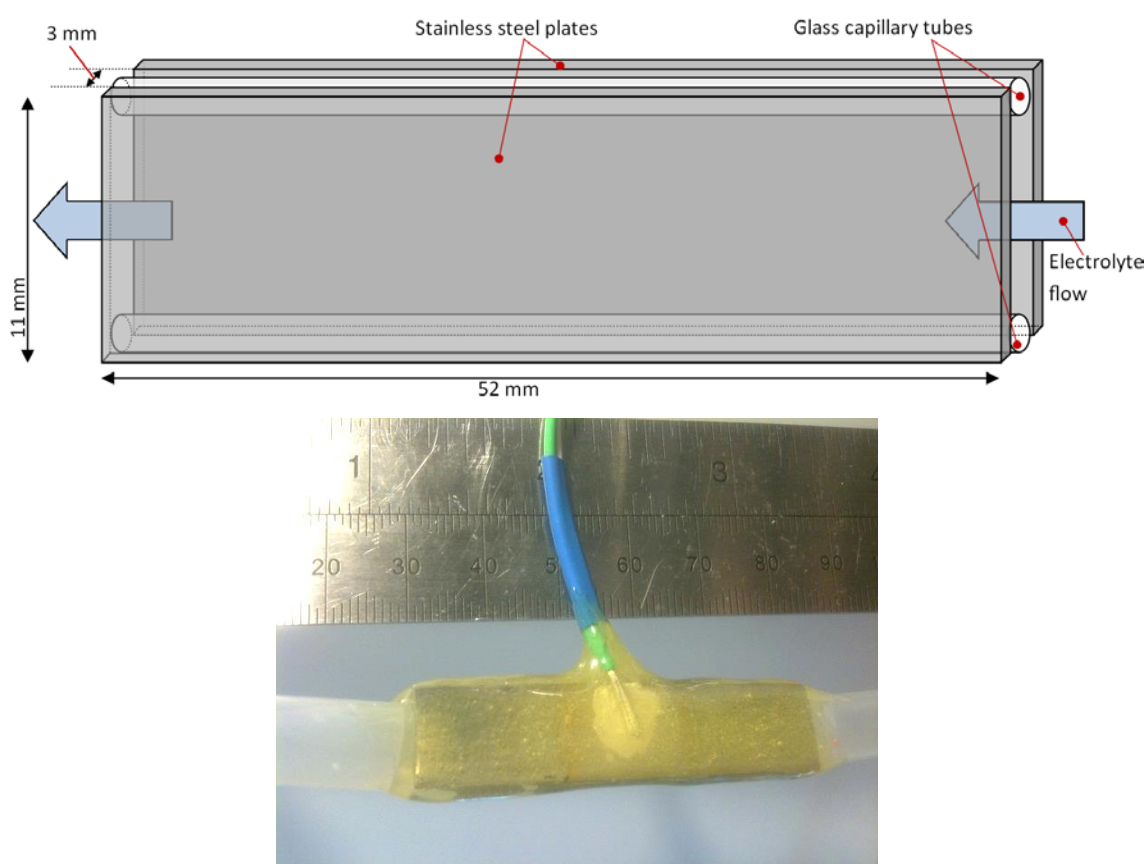


Figure 4.11 Schematic (top) and picture (bottom) of modular cell for measurement of the uncompensated resistance outside of the electrolysis device.

Figure 4.12 shows the uncompensated resistance (—) with a moving average (—) and hydrogen level (—) with the electrolysis cell ‘on’ time highlighted by the area shaded blue. The graph shows that the uncompensated resistance exhibits a similar trend to that observed within the electrolysis device plates. Initiating electrolysis, gas production causes an increase in the resistance (*ca.* 50 mΩ) as expected. However, this time there was a time delay of several seconds until the increase was detected. This is as expected due to the time taken for the liquid

Chapter 4: Ultrasound assisted gas release

carrying the bubbles to reach the module positioned downstream of the electrolysis device. The gas void fraction increases further as the gas population builds until a steady state value (*ca.* 4.09 Ω) was reached, again exhibiting the trend as observed in the electrolysis device. The measured resistance values and the corresponding change are an order of magnitude larger than those measured in across the electrolysis device electrodes. Here the resistance value difference between the gas-free and gas-filled conditions is *ca.* 50 m Ω , compared to *ca.* 5 m Ω for measurements made between electrodes of the electrolysis cell. This is because the smaller steel plates of the module provide less contact area to the electrolyte and the separation between the modular cell plates is larger than to the electrolysis device. Upon reaching the steady state, a small decline in the electrolyte resistance was observed and is again attributed to electrolyte (Joule) heating.

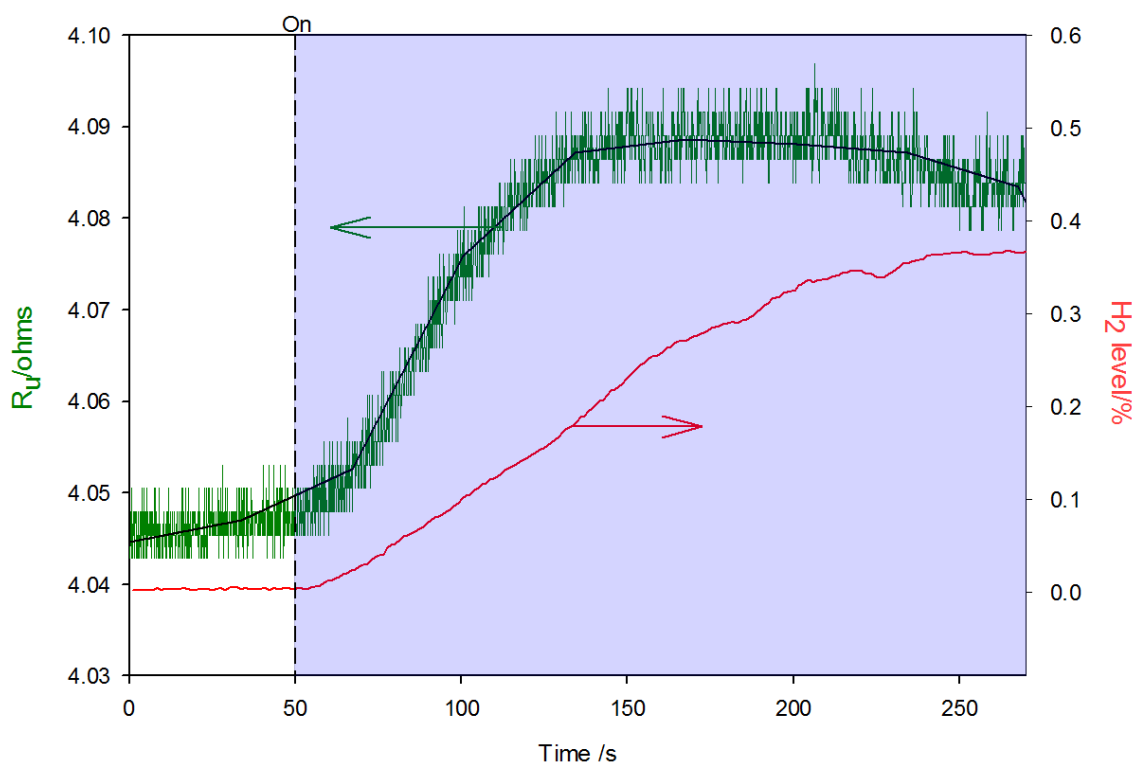


Figure 4.12 Graph showing the hydrogen level (—, right axis) and resistance change (—, left axis) across the module. The cell was turned on at 50 s for the entire duration at 325 mA. Airflow: 155 cm³ min⁻¹, liquid flow: 0.910 dm³ min⁻¹.

These results show that the AC-modulation technique can be applied to determine and monitor ‘on-the-fly’ the uncompensated resistance of a cell at the outlet of the reservoir. This capability is pivotal for the analysis and investigation of ultrasound assisted gas release from the reservoir, discussed in the next section.

4.2 Ultrasound assisted gas release

The previous results presented in this chapter suggest that gas release for the investigated electrolysis system occurs over a relatively long time period with a constant of the order of 100's of seconds. Clearly a more rapid and controllable release of hydrogen is desirable, particularly considering that the target application of this technology is for incorporation into a vehicle. Here the device must meet the variable demands of an ICE. In efforts to reduce the gas generation 'inertia' of these systems, an investigation of the integration of ultrasound, which is known to aid outgassing, will now be discussed in further detail.

4.2.1 Ultrasonic field characterisation

Initial experimentation was focussed on the design and characterisation of a reservoir suitable for use with the electrolysis system and the excitation of the containing fluid with power ultrasound. Hence modified Dreschel bottles (reactors 2 and 3 in section 2.1.2) were designed to meet the experimental requirements and were constructed by the department glassblower. The main features of the modifications include the addition of ports on the sides of the bottles. Sound field characterisation was achieved through the use of a calibrated hydrophone (Reson, TC4013) to measure the pressure in the liquid as a function of the conditions employed. Measurements were taken with the hydrophone on axis with respect to the cylindrical reactor and the drive frequency and amplitude were varied at different hydrophone positions in the z direction (vertically). Experiments were also conducted with and without liquid flow through the electrolysis system.

Figure 4.13 shows an example of a raw signal produced by the hydrophone. The sample is comprised of the main drive signal (blue shaded area) combined with noise emissions (above the shaded area) originating from the produced cavitation environment. Figure 4.14 shows the frequency components present in the data shown in Figure 4.13 (performed with in-house written software, see appendix 11: HTOGO FFT.vbp). As expected the largest peak can be seen at the fundamental drive frequency (f_0) at 27.6 kHz. Smaller frequency components corresponding to typical cavitation effects (sub and ultraharmonics for example) can also be seen. The amplitude of each measurement was adjusted according to the calibration data

Chapter 4: Ultrasound assisted gas release

(hydrophone manufacturer supplied) to account for the hydrophone's sensitivity and frequency dependency.

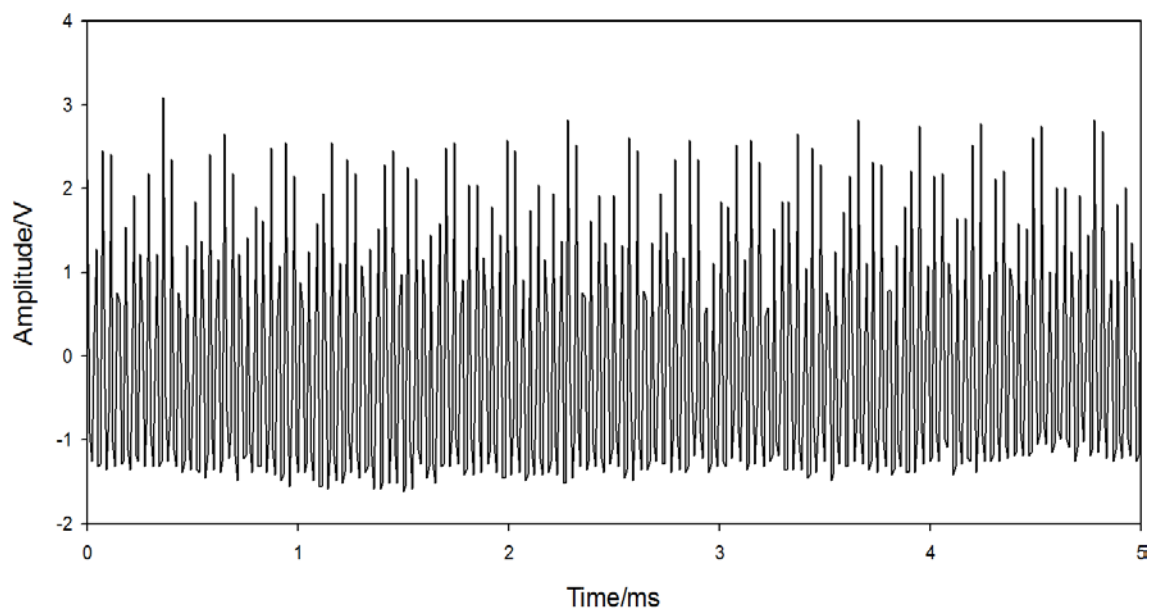


Figure 4.13 Example of a measured hydrophone signal before processing. The hydrophone was placed in the centre of reactor 2 with the tip of the hydrophone 46 mm from the base of the bottle. The liquid was purified water (165 cm^3 in the reactor), flowed at $0.910 \text{ dm}^3 \text{ min}^{-1}$. The transducer was powered at 27.6 kHz, 20 Vpp input signal to amplifier and a gain of 35 dB. The sample rate was 100 kHz.

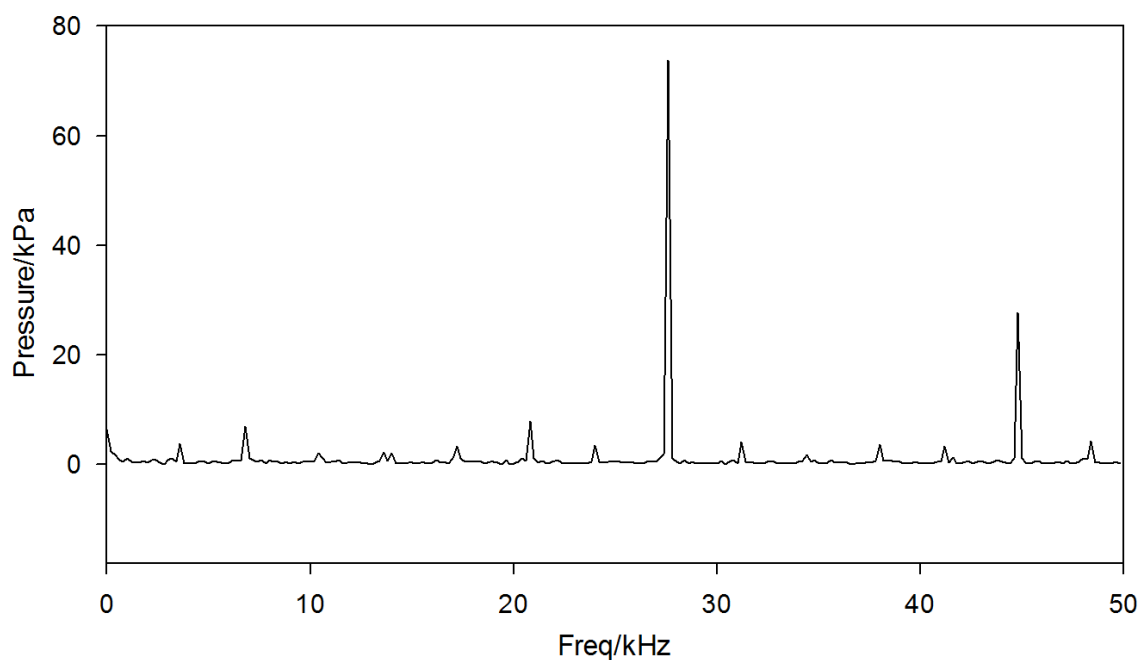


Figure 4.14 Plot showing the output from an FFT analysis of the hydrophone data (shown in Figure 4.13) processed by in-house written software (FFT oscilloscope.vbp). The excitation frequency (27.6 kHz) is shown to have an amplitude of *ca.* 74 kPa (zero to peak).

Figure 4.15 shows the results from pressure measurements recorded using the method described above. The black dots with error bars show the measured pressure *vs.* drive frequency with the hydrophone tip placed 46 mm from the base of the reactor. Here a frequency range of 27 to 30.5 kHz (step 100 Hz, 20V_{pp} input signal to amplifier, 30dB gain) was employed. Note the pressure measurements were made every 100 Hz over this range, in purified water (165 cm³ contained in reactor). In all cases the fluid was pumped at 0.91 dm³ min⁻¹. Each reading was taken three times and averaged, with standard deviations used as error bars. Further measurements were made under the same conditions at frequencies 27.6, 28.4 and 28.8 kHz with varied amplifier gain (10-35 dB, steps 5 dB).

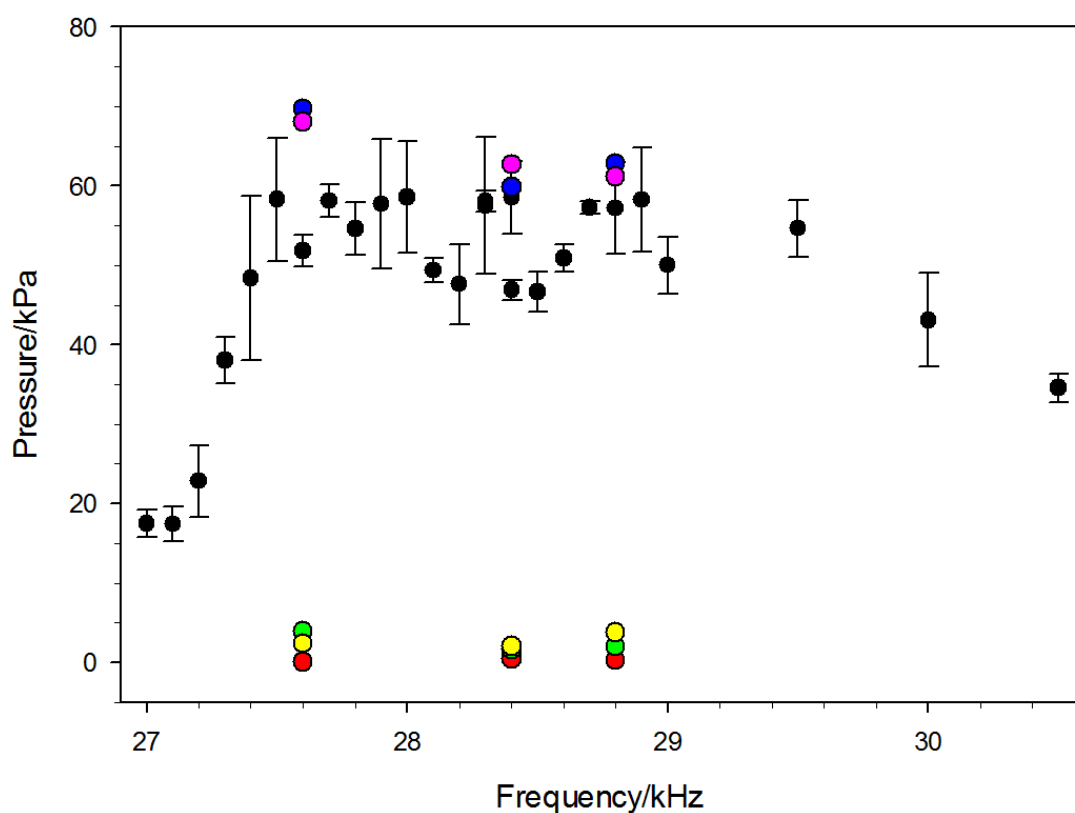


Figure 4.15 Plot showing the pressure *vs.* transducer drive frequency, measured with hydrophone (TC4013) tip positioned 46 mm from reactor base in reactor 2 containing purified water (165 cm³ contained in Dreschel bottle) flowing at 0.91 dm³ min⁻¹. The black dots (with error bars) show the response with the drive frequencies = 27 to 30.5 kHz, step 100 Hz, 20 V_{pp}, 30 dB. The coloured points show repeats at 27.6, 28.4 and 28.8 kHz, 20 V_{pp}, with varied amplification: • 10 dB, • 15 dB, • 20 dB, • 25 dB, • 30 dB, • 35 dB. The • 10 dB data sets are hidden behind the • 15 dB readings at *ca.* 0 kPa.

For the 30 dB amplification setting (•), the trend shows a steep increase in pressure from *ca.* 20 kPa (zero-to-peak) at 27 kHz to 50-60 kPa at 27.5 kHz to 29.5 kHz. A gradual decrease in pressure is observed between 29.5 to 30.5 kHz. The coloured

Chapter 4: Ultrasound assisted gas release

data points demonstrate that at each tested frequency, the pressure exhibits a sudden increase from *ca.* 0 Pa at 25 dB and below to *ca.* 60 kPa at 30 dB and above.

The pressure developed in a reactor will vary with the applied frequency and can be explained by considering resonance effects. Resonance is the tendency for a system to oscillate at greater amplitudes at certain frequencies. There are three primary systems to consider; the transducer, the cell and the effect of bubbles within the cell. The resonant frequency of the transducer is ~ 28 kHz, which is the frequency at which the mechanical displacement amplitude is expected to be at its maximum. However, the transfer of this motion to the sound field within the cell also depends on the cell itself. The sound field within the enclosed cylindrical cavity (similarly to the employed reactor) can be decomposed into its natural modes. These three dimensional modes of the reactor can be characterised axially (vertically), transversally (horizontally) and azimuthally (rotational symmetry about the axis). These modes combine to produce the spatial variation of the sound field within the cylinder. If the mechanical resonance of the transducer matches the mode frequency, the conditions required to generate the highest pressure amplitude within the liquid could be expected. While this is certainly true in the absence of a significant gas bubble population, this final factor should also be considered. Birkin *et al.* [145] have suggested that the bubble population will have a significant influence on the pressure field developed within a reactor. Here the bubble population feeds back into the cell modes through changes in the speed of sound of the fluid. For example if a mode is weakly excited under bubble free conditions it may be strongly excited (and indeed 'locked into') when cavitation is induced in the fluid.

The results from experiments in which the hydrophone was varied axially (vertically in the z-direction) are shown in Figure 4.15. These were conducted with and without liquid flow. While no strong spatial variation was detected under these conditions, the data shows that the pressure developed on axis is independent of liquid flow. The reason for the absence of clear banding in the z direction (as expected and shown in the imaging experiments, see section 3.1) are unclear but could be as a result of the invasive nature of the hydrophone assembly employed or the exact mode symmetry that was generated under these conditions. Nevertheless the results suggest that the flow system did not affect the sound field generated under the conditions employed. This is significant as some of the

outgassing experiments (see section 4.2.2) rely on the generation of a sound field in the reactor under flowing conditions.

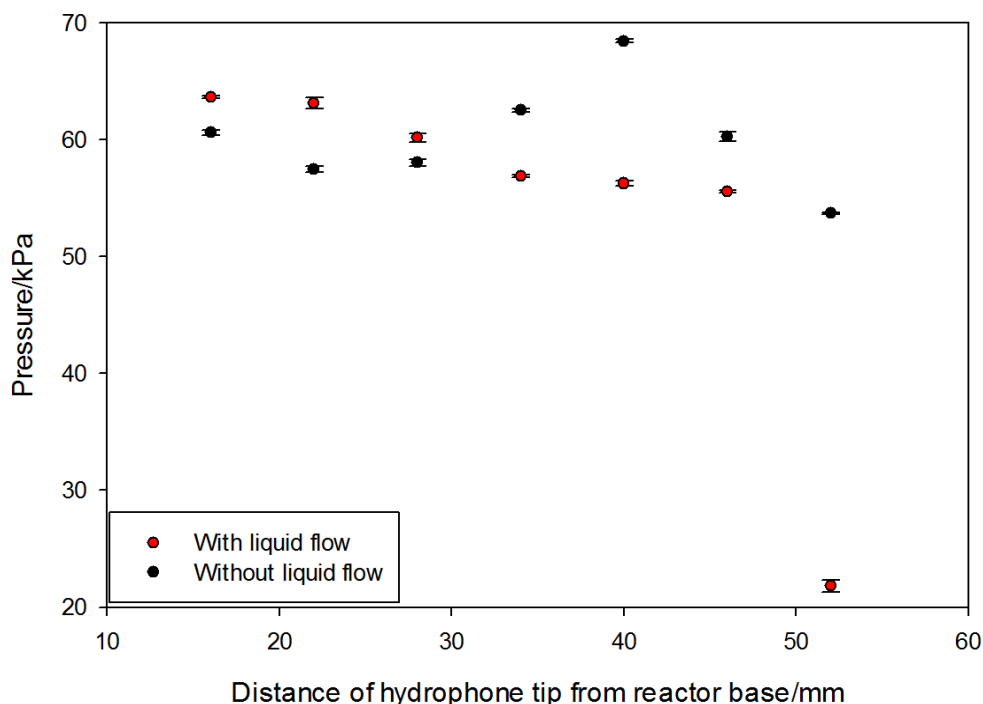


Figure 4.16 Graph showing the zero-to-peak pressure measured by a hydrophone (TC4013) with the tip position varied relative to the reactor base (16 to 52 mm, step 6mm, reactor 2). The reactor contained purified water (165 cm³ contained in Dreschel bottle). The experiments conducted with liquid flow had a rate of 0.910 dm³ min⁻¹. The transducer was driven at 27.9 kHz, 20 V_{pp}, 30 dB. The pressure recorded at 52 mm with the liquid flow was observed to exhibit considerable lateral movement, caused by the flow.

The recorded pressures without the liquid flow (black dots) appear to show a standing wave pattern. Here a mode of the system with axial symmetry is exhibited, shown by the sigmoidal variation in pressure as the axial position varies. The liquid flow (red dots) appears to partially dampen this effect, particularly at 52 mm above the base, where considerable lateral movement was observed resulting in a lower recorded pressure. However most of the recorded pressures were between 55 and 65 kPa, regardless of the flow conditions.

Clearly the pressures generated within the modified reservoir can be significant under the conditions employed. As a result this system and the effects of the acoustic field will be deployed to investigate the release of gas from solution.

Chapter 4: Ultrasound assisted gas release

4.2.2 Gas release

The experimental rig used for analysis of the electrolysis device (as shown in Figure 4.6) was employed to investigate the ultrasonic outgassing. The hydrogen sensor and the modular cell for R_u measurement at the reservoir outlet (see section 4.2.3) were also used to characterise the outgassing phenomenon. Reactor 2 was also used to excite the reservoir with ultrasound. The ultrasonic frequency was selected based on the resonant frequency of the transducer (confirmed by pressure measurements) and previous experimentation within the group, which has demonstrated successful coupling of similar sized reactors [92, 136, 177].

Figure 4.17 demonstrates a typical response from the hydrogen sensor (hydrogen level shown as a percentage of the airflow) upon irradiating the reservoir with ultrasound. The reservoir was pre-filled with a significant population of electrolytically produced gas bubbles, with the cell on for enough time so that the bubble population in the reservoir was constant (determined by a constant hydrogen gas production). Initiation of the ultrasonic field at 90 s coincided with rapid gas ejection from the liquid. Figure 4.18 shows images of the reservoir taken before and after ultrasonic irradiation (at points A and B on Figure 4.17). These demonstrate the complete clearing of observable bubbles from the reservoir.

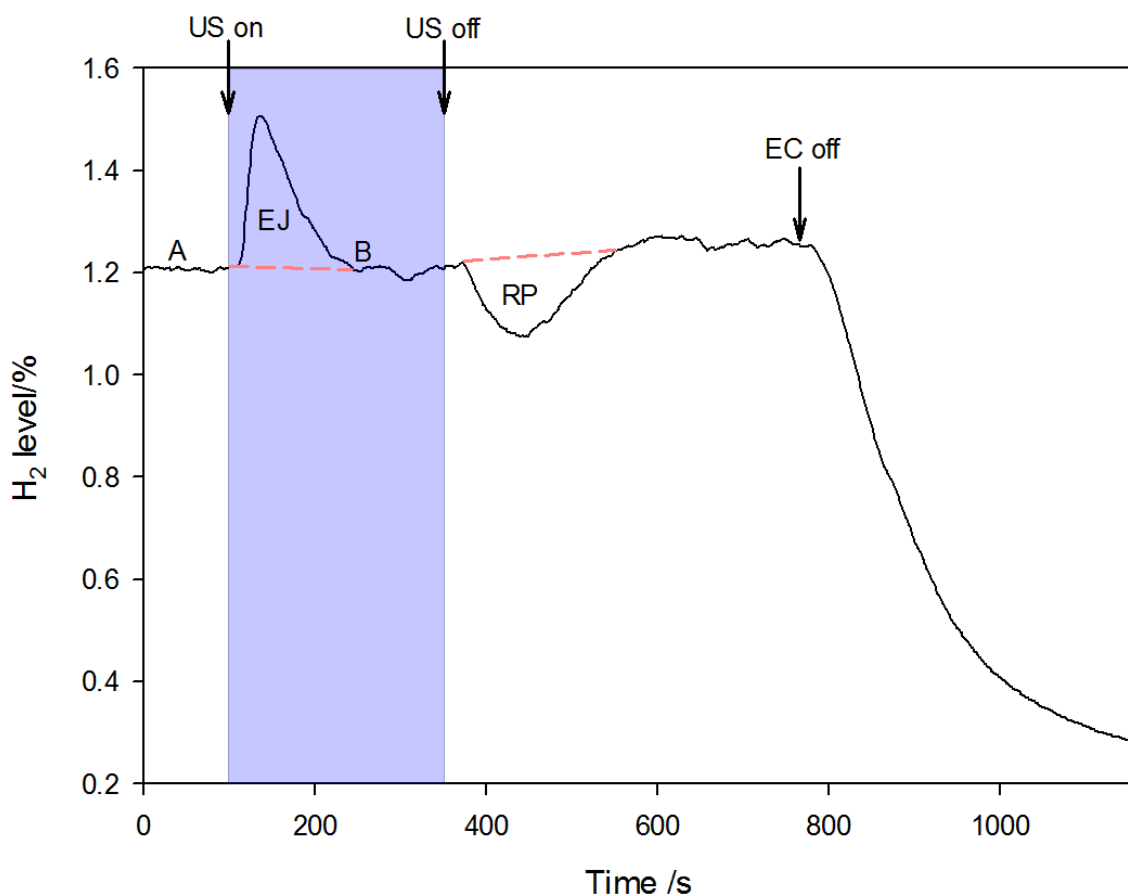


Figure 4.17 Plot showing the hydrogen level (as a percentage of the airflow) *vs.* time. The electrolysis cell was on from the start until 790 s at 150 mA. The ultrasonic irradiation was on from 90 to 350 s at 28.18 kHz, 20 Vpp, 30 dB, (~62 kPa). Airflow: 134 cm³ min⁻¹, liquid flow: 0.910 dm³ min⁻¹. The markers 'A' and 'B' correspond to the times at which the images shown in Figure 4.18 were taken. In highlighted peak and trough (— —) EJ = Ejection of bubbles through outgassing. RP = Re-population of reservoir.

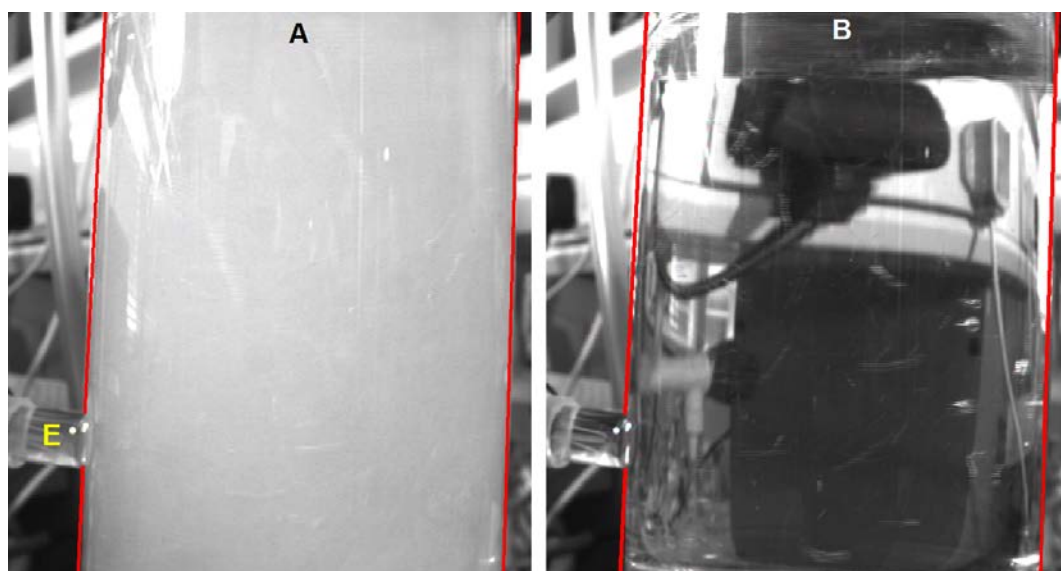


Figure 4.18 Photographs of the liquid reservoir taken before and after ultrasonic irradiation at points A and B as shown in Figure 4.17. The red lines highlight the edge of reactor and the letter E denotes the outlet.

Chapter 4: Ultrasound assisted gas release

The expelled hydrogen detected by the hydrogen sensor corresponds to a *ca.* 25% increase in the hydrogen content of the gas stream. Note the sensors temporal response is limiting under these conditions and the gas actually leaves in a much shorter time period. This is evident from the fast response observed by the modular resistance measurements and high-speed imaging experiments, which are subsequently discussed. Upon termination of ultrasonic irradiation of the reservoir a decrease in the hydrogen level was observed. This can be understood by considering the electrolyte as a reservoir for the gas bubbles. The reservoir of gas was depleted upon irradiation with ultrasound, after which point the equilibrium was re-established at $\sim 1.2\%$ (at *ca.* 250 s). This was confirmed visually by observation of the gas bubbles which flowed from the electrolysis device and into to the reservoir where they were forced out from the liquid. This outgassing mechanism ceased when the ultrasound was switched off, and the liquid reservoir begins to refill with gas bubbles being produced at a constant rate from the cell. During this period a decrease in the hydrogen level at the sensor was observed as would be expected. The difference between the gas release and repopulation continues until the liquid reservoir is fully populated with bubbles and the equilibrium is re-established. The steady-state response was then observed once again.

In order to further assess the rate of gas release, experiments using high-speed imaging and the modular resistance system were conducted simultaneously. Figure 4.19 shows four images of the reservoir taken immediately after ultrasonic irradiation was initiated. Frame (a) shows an image of the liquid reservoir pre-populated with gas bubbles taken at the moment when the function generator output was switched on. The clearing of the gas bubbles driven by the ultrasonic irradiation, can be seen over the subsequent frames (b)-(d). The images indicate that the bubble population was driven upwards out of the reservoir from the base. The outgassing of the entire reservoir occurs over a ~ 3 s period.

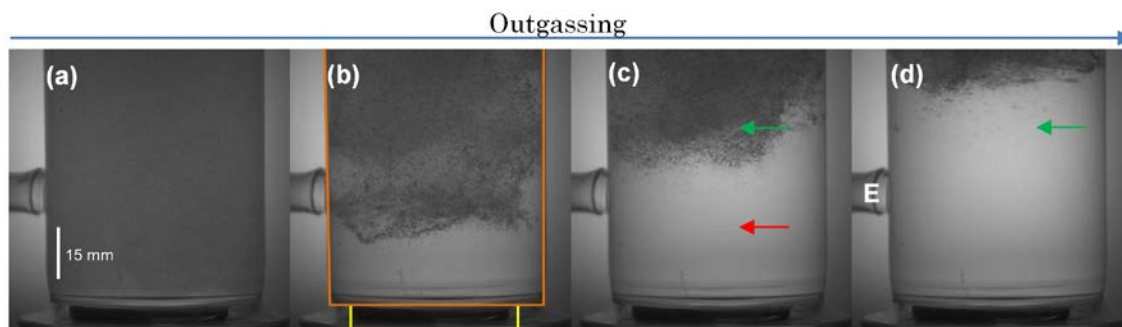


Figure 4.19 Sequence of images taken of the ultrasonic outgassing process in the Dreschel reservoir containing 0.1 M NaOH (165 cm³ in reactor) pre-populated with gas bubbles (steady-state). The liquid flow was switched off for the image capture. The images show the bottom half of the vessel and the liquid level is just above the shown image area. The sides of the vessel are highlighted with an orange line (—) and the transducer with a yellow line (—) in frame (b). Frame (a) shows the fluid populated with hydrogen and oxygen gas bubbles at the point where the ultrasonic irradiation (28.8 kHz, 20 V_{pp}, 35 dB, 62 kPa) was initiated. Frame (b)-(d) show the clearing of the liquid driven by the ultrasonic irradiation of the reservoir 0.609, 1.659, 2.584 s after the cell was excited respectively. The red arrow (—) highlights an area cleared of gas bubbles and the green arrows (—) highlight an area with bubbles that are subsequently cleared. ‘E’ denotes the liquid exit employed back to the electrolysis cell. The video from which these images were taken is presented on the accompanying DVD.

Figure 4.20 shows the results of an experiment in which the hydrogen level and resistance across the modular cell (as detailed in 4.1.3.3) were measured simultaneously with an outgassing event. Electrolysis was initiated at 50 s (325 mA) as highlighted by the dashed line. Here a faster airflow results in a lower concentration of hydrogen in the gas stream. Ultrasonic irradiation of the reservoir was initiated at 294 s for a duration of 200 s, highlighted by the shaded area.

Figure 4.20 shows that gas production through electrolysis increased the uncompensated resistance as expected. In addition the hydrogen concentration in the gas stream increases as the bubble population builds until a steady H₂ level was reached (at *ca.* 250 s). As well as an initial increase in R_u caused by bubble generation, Joule heating effects caused by bubble generation can be observed. This will be discussed further in section 4.4. Upon initiating the ultrasonic irradiation at 294 s, an increase of *ca.* 23 % in the hydrogen level was observed. This is very similar to the previously observed amount in Figure 4.17. The peak was followed by a plateau as the steady-state is re-established. A trough was then observed when ultrasonic irradiation was ceased, corresponding to the refilling of the reservoir with gas bubbles as previously discussed (see Figure 4.17).

Chapter 4: Ultrasound assisted gas release

The initiation of the ultrasonic excitation caused a rapid decrease in the uncompensated resistance (see black arrow at *ca.* 294 s). Figure 4.21 shows an expanded section of Figure 4.20 at the moment of ultrasound initiation.

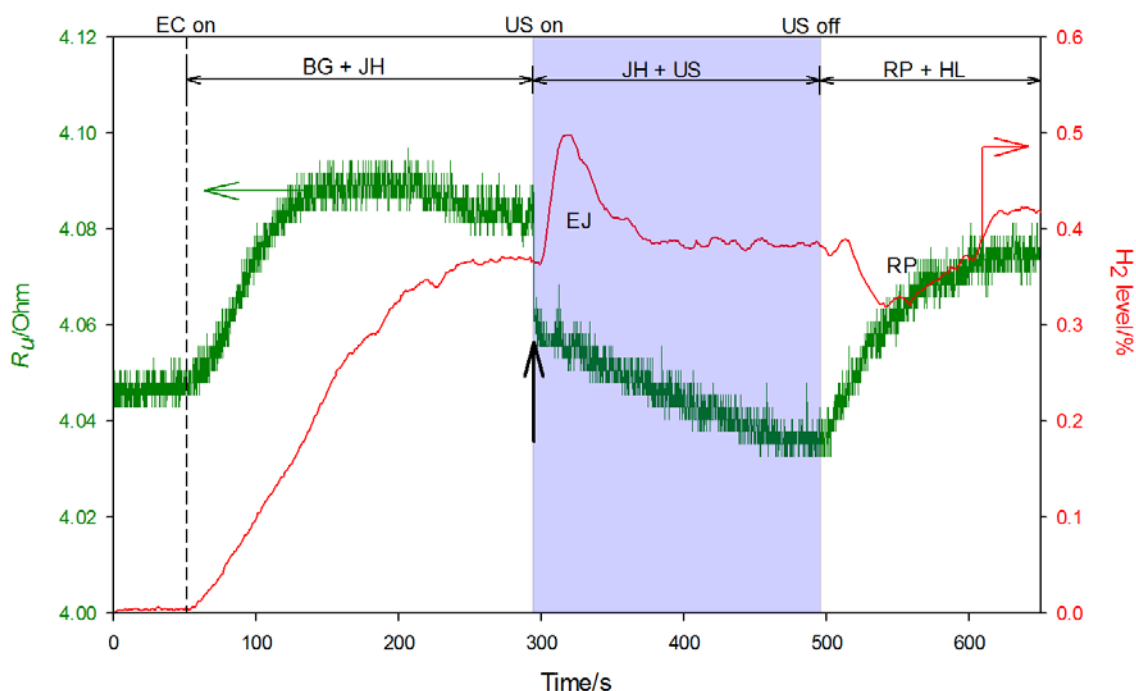


Figure 4.20 Plot showing the change in modular resistance (---) and hydrogen level (---) vs. time. The electrolysis cell was turned on at 50 s at 325 mA. The ultrasound was initiated from 294 s to 494 s highlighted by the blue shaded area (28.566 kHz, 20 Vpp, 35 dB, ~ 62 kPa). The electrolyte was 0.1 M NaOH (165 cm³ contained in reactor) and was flowed at 0.910 dm³ min⁻¹. The air flow rate was 630 cm³ min⁻¹. EJ = Ejection of bubbles through outgassing, RP = Re-population of reservoir, BG = Bubble generation, JH = Joule heating, EC = electrochemistry, US = Ultrasound, HL = Heat loss.

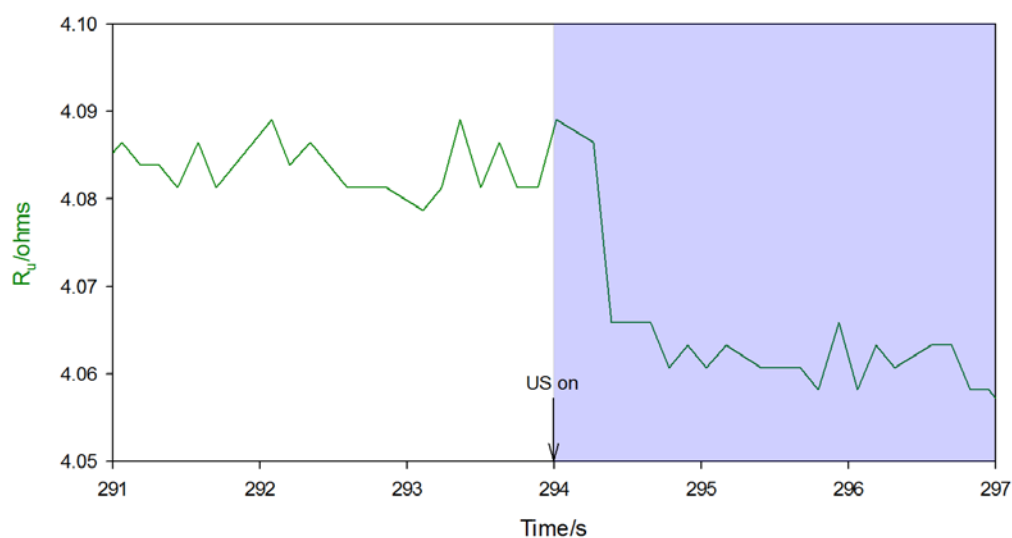


Figure 4.21 Plot showing the resistance change as a function of time from Figure 4.20, presented with a shorter time window.

Figure 4.21 shows that the uncompensated resistance decrease was caused by the ultrasonic field and occurs over < 1 s. The ultrasonic irradiation was switched on manually and so the time of initiation will have an error of $ca. \pm 0.5$ s. Nevertheless, the resistance change still occurs in $< ca. 1$ s indicating the rapid nature of this outgassing effect at the base of the reservoir. Figure 4.20 demonstrates that after this sharp drop the resistance then decreases more gradually. This decrease is a consequence of Joule heating from the electrolysis process and also calorific heating caused by the ultrasonic transducer. Hence this is the reason for the steeper gradient compared to that seen from $ca. 200$ to 294 s. These heating effects are examined further in section 4.4. Upon termination of ultrasound, the resistance increases and plateaus similarly to the initial filling of the reservoir with gas bubbles.

Further mechanistic detail regarding the outgassing effect can be gathered from high-speed imaging of the system. Figure 4.22 shows a series of images of the bubble population in the reservoir during the ultrasonic outgassing process. The images represent a region of the reactor approximately 150 mm vertically up from the base and backlit with an LED array. Due to the nature of the closed system, the calibration to produce a size reference scale was problematic as an object of known size (e.g. a $250\text{ }\mu\text{m}$ \varnothing wire) could not be placed in the same plane of focus as the object for investigation (the bubbles). Hence the size of the out-of-focus wire was estimated. Consequently the values for the bubble radii presented in the Figure 4.22 caption have a larger estimated error of $ca. 8\text{ }\mu\text{m}$, calculated according to the minimum and maximum potential sizes for the reference wire.

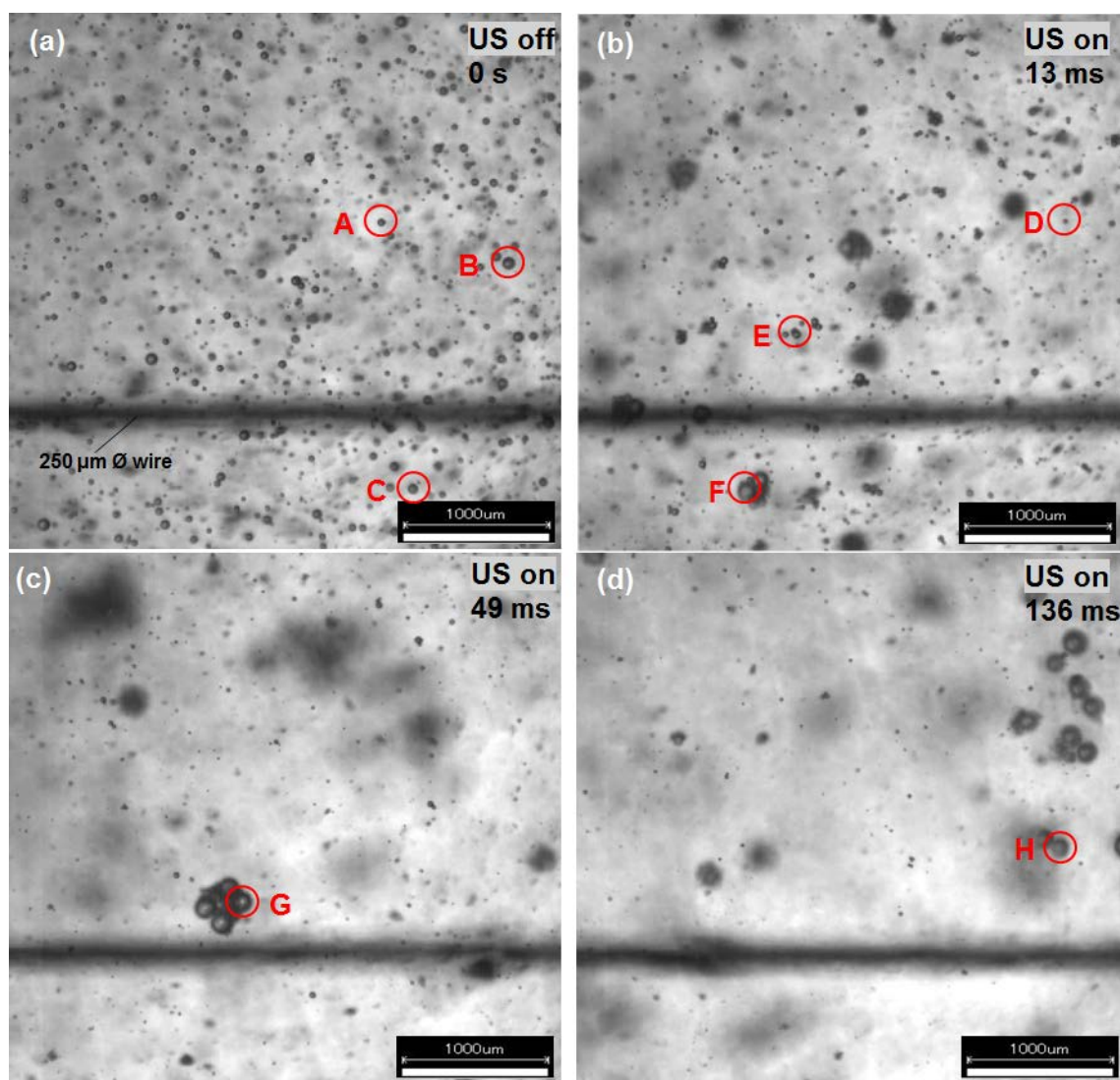


Figure 4.22 Images of the bubbles within the reservoir containing 0.1 M NaOH (165 cm^3) at the point of ultrasonic excitation (28.8 kHz, 20 Vpp, 35 dB, $\sim 62 \text{ kPa}$) of the system (frame (a), $t = 0 \text{ s}$) and 13, 49 and 136 ms after this point for frames (b)-(d) respectively. The 250 μm wire is out of focus in each picture due to the limited depth of field for these optics. Highlighted bubble radii ($\pm 8 \mu\text{m}$): A 40 μm , B 72 μm , C 53 μm , D 24 μm , E 45 μm , F 107 μm , G 104 μm , H 102 μm . The video from which these images were taken is presented on the accompanying DVD.

Figure 4.22, Frame (a) shows an image of the bubble population at the moment at which the ultrasonic irradiation was commenced. The initial population demonstrates a range of bubble radii from the optical limit of the images (*ca.* 10 μm) to a maximum of *ca.* 70 μm as highlighted by bubble ‘B’.

Figure 4.22, Frame (b) demonstrates the population 13 ms after ultrasonic excitation of the reservoir. Note some of the bubbles have now been drawn to one another and have formed clusters of bubbles or have coalesced to form bigger bubbles. The largest bubble (bubble ‘F’) was measured to be 107 μm in radius. This

bubble and several others that were grouped in clusters were observed to exhibit exaggerated oscillation and possible surface waves (Faraday waves).

Figure 4.22, Frame (c) demonstrates the bubble population 49 ms after ultrasonic excitation. Further coagulation and coalescence has occurred, with the population now mainly comprising only relatively large ‘rafts’ and small bubbles relative to frame (a). The cluster of bubbles with bubble ‘G’ was also oscillating with surface waves apparent (see Figure 4.22.avi on DVD). Lastly frame (d) demonstrates that the population of the smaller bubbles has decreased and the larger bubbles remain 136 ms after ultrasonic excitation of the vessel.

4.2.2.1 Outgassing mechanism

It is proposed that there are two effects that cause the observed outgassing of the reservoir. The first is caused by radiation pressure acting on the boundary between the ‘bubble free’ liquid and the ‘bubble cloud’. With any waveform, sound waves can be reflected at interfaces between two differing media. Hence the difference in acoustic impedance (proven by the difference in speed of sound of the two phases, see appendix 10) causes a net force upward on the bubble cloud. This is demonstrated in Figure 4.23.

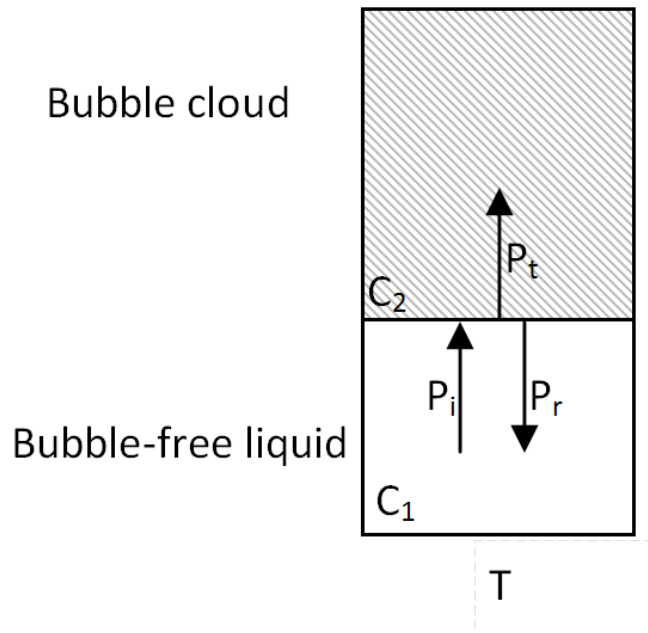


Figure 4.23 Diagram showing the normal forces acting on the boundary between the ‘bubble free’ liquid and the ‘bubble cloud’ which have associated measured speeds of sound: $C_1 = 1579 \text{ m s}^{-1}$ and $C_2 = 443 \text{ m s}^{-1}$ respectively (see appendix 10). P_i represents the incident pressure wave, P_r the reflected pressure wave and P_t the transmitted pressure wave. T denotes the transducer.

Chapter 4: Ultrasound assisted gas release

The ratio of the incident and reflected waves (and therefore the transmitted wave as $P_i + P_r = P_t$) is dictated by the bubble population which has direct influence on the effective speed of sound in the media. In order to investigate this notion further, resonant bubble sizes must be introduced. The resonant size, which is the natural frequency of a spherical gas bubble in a liquid undergoing low-amplitude simple harmonic motion [67], was first calculated by Minnaert in 1933 [198]. Leighton [67] discusses and defines the Minnaert resonance frequency and derives the following simplified (4-4).

$$\nu_o R_o = 3 \text{ m.s}^{-1} \quad (4-4)$$

Here, ν_o is the linear resonance frequency (s^{-1}) for bubble pulsations and R_o is the mean radius (m) of a bubble undergoing oscillation. At 28.8 kHz, a resonant radius of *ca.* 104 μm is relevant. According to the sample of bubbles in frame A, the vast majority of the gas bubbles in the population are smaller than this size prior to ultrasonic irradiation. Visual inspection of these bubbles confirms that there were no observed resonance effects occurring (see video on DVD, Figure 4.22.avi).

Therefore the initial driving force is caused by the forces acting on the boundary between the two media. Here C_2 is lower than C_1 causing the bubble cloud to be driven up as transmission is proportional to acoustic impedance, which is proportional to density and speed of sound. However in frames B, C and D, (Figure 4.22) several of the bubbles that were similar to the size that is resonant with the sound field were driven into oscillation and were observed to exhibit surface wave activity. This shows that $P_t \neq 0$ and that there are other forces acting within the bubble cloud.

To understand the implications of this, Bjerknes forces must be considered. When a gas bubble in liquid is subjected to an acoustic pressure field, it can undergo volume pulsations. If the acoustic pressure gradient is non-zero, then it can couple with the bubble oscillations to produce a translational force on the bubble. This is the primary Bjerknes force. Bubbles which are smaller than the size that is resonant with the sound field travel up a pressure gradient, and bubbles of a size larger than resonance travel down a pressure gradient. Therefore, in a planar standing-wave field, bubbles of smaller than resonance size collect at the pressure antinodes, whilst those larger than resonance aggregate at the pressure nodes [121, 199].

Hence there is a driving force for aggregation at the antinodes, where the bubbles cluster and coalesce. Larger bubbles are produced through coalescence including bubbles close to size that is resonant with the sound field (104 μm) as shown in figure 5.9 (b)-(d). As discussed, these bubbles are driven into more exaggerated oscillation and exhibit surface waves (Faraday waves). These bubbles initiate further coagulation through convection and secondary Bjerknes forces (time-averaged mutual interaction force of two gas bubbles). These effects of clustering and coalescence serve to enhance upward buoyancy forces.

In summary the two proposed mechanisms for the outgassing process are the radiation forces acting on the boundary between the phases, and the increased buoyancy forces associated with clustering and coalescence.

4.3 Gas void fraction calculation

De La Rue and Tobias [200] have conducted studies into models for the effective ionic conductance of a dispersion such as a gas bubble population in an electrolyte. This focussed on the effects of the volume fraction of the non-conducting phase. They conclude, from experimental evidence that for ionic conducting solutions containing random dispersions of spherical insulators with a large range of sphere radii (such as occurs in gas - electrolyte mixture produced by the electrolysis system) the Bruggemann equation [201] ((4-5) is best used to predict the effective conductivity.

$$K_e / K_c = (1 - f)^{3/2} \quad (4-5)$$

Here K_e (mS cm^{-1}) represents the electrolyte conductivity; K_c (mS cm^{-1}) represents the zero gas conductivity and f the gas void fraction (note $f = V_G / (V_G + V_L)$ in the presence of a gas bubble population, where V_G = gas volume and V_L = liquid volume).

Converting the uncompensated resistance values into conductivity values, the predicted volume of gas in the reservoir can be calculated. For the experiment shown in Figure 4.20, the resistance change equates to a gas void fraction change of 5.51×10^{-3} . The reservoir contains 165 cm^3 and the rest of the rig including tubing and electrolysis cell contains 125 cm^3 resulting in a calculated total gas volume of 1.60 cm^3 . Due to the nature of the electrolysis process, two thirds of this volume will be hydrogen, equating to 1.07 cm^3 of hydrogen released by the

Chapter 4: Ultrasound assisted gas release

outgassing process. This volume of hydrogen can be compared to the hydrogen detected by the sensor. In order to do this, the hydrogen percentage (see Figure 4.20) was converted into a rate in $\text{cm}^3 \text{min}^{-1}$ by multiplying by the air flow rate. Integration of the area under the peak yields the total volume of hydrogen detected by the sensor: 0.53 cm^3 . This value is *ca.* half of the predicted value from the resistance change (1.07 cm^3). Clearly this value is not in agreement; however by considering the method of hydrogen measurement by the sensor, this difference can be explained. The gas sensor is a three electrode amperometric electrochemical cell and in order for the gas to reach the sensor it must diffuse through a porous membrane. This diffusion barrier is in place to ensure that the process is diffusion limited and hence gives a linear response in proportion to the gas concentration. If we consider the case where the gas concentration outside of the barrier is constant (as in the sensor calibration experiments and at steady-state) then the concentration of gas flow past the sensor is constant and hence all of the gas diffuses in one direction, toward the sensor working electrode. However, in the case of a quick burst of hydrogen, as with the ultrasonic outgassing process, then the hydrogen was released as shown in Figure 4.24 a). At the the sensor this is seen as a short burst of hydrogen followed by a sharp drop as the air flow replenishes the environment. It is proposed that by the time the pocket of hydrogen has reached the diffusion barrier the environment in the tubing has been completely replenished by air. Hence the diffusion will occur both ways, with *ca.* 50% diffusing in each direction, as shown in figure 5.10 b).

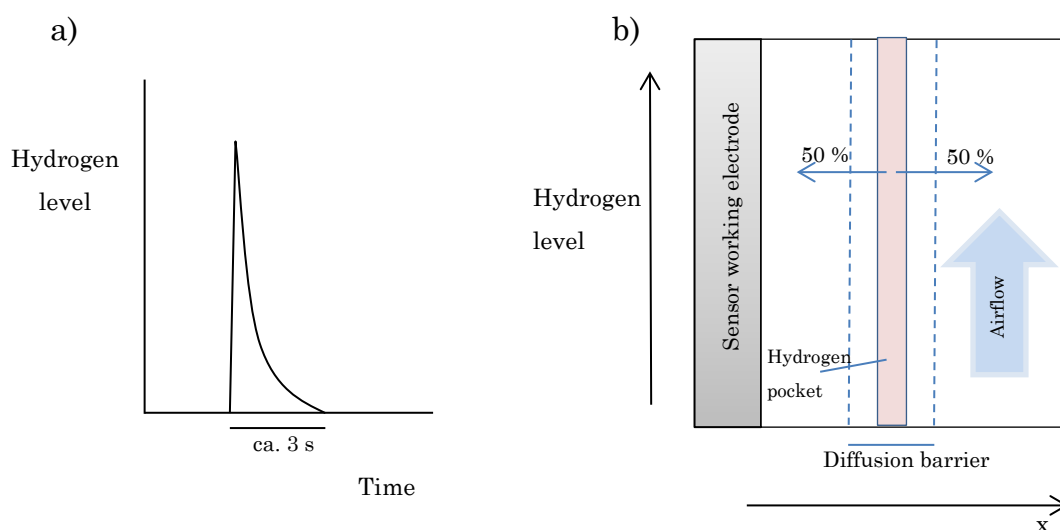


Figure 4.24 Hydrogen release from the liquid reservoir by ultrasonic outgassing. b) Diagram demonstrating diffusion of the hydrogen pocket to and away from the sensor electrode due to the rapid air replenishment.

This provides a possible explanation for the observed difference between the amount of hydrogen calculated from the response of the sensor and amount calculated from the change in resistance. It is apparent that the previous assessment of amount of hydrogen released by the ultrasonic outgassing process (*ca.* 25 %) is an underestimate by up to a factor of 2. In reality the peak amount of hydrogen released is an increase of *ca.* 50 % on the steady-state concentration.

The data from the applied AC-modulation technique for the determination of the uncompensated resistance can be used for the calculation of the gas void fraction in the liquid and therefore the amount of hydrogen gas contained in the liquid reservoir store. The resistance measurements are also useful in estimating heating effects, from Joule heating (electrochemical) and the outgassing system (ultrasonic). These two will now be discussed in more detail.

4.4 Heating effects

It is proposed that some of the measured uncompensated resistance changes are due to temperature variations of the electrolyte, caused by heating effects. This section aims to prove that the system used for measuring the uncompensated resistance responds as expected to electrolyte temperature changes. Furthermore it aims to quantify the temperature change associated with the phenomena.

McCleskey [202] reported a linear correlation between the specific conductivity of an electrolyte and the temperature (see appendix 5 for data and calculations relating to 0.1 M NaOH).

In order to exploit these phenomena, the temperature and uncompensated resistance were measured in the reservoir used for outgassing (reactor 2, modular cell for R_u) over a range of transducer drive amplitudes. In the experiment, the transducer was switched on (28.8 kHz, varying amplification, details in appendix 6) for 90 s bursts, with 60 s rests in between bursts. The temperature and resistance were measured simultaneously. Figure 4.25 demonstrates the changes in temperature (—) and uncompensated resistance across the module (—) as the transducer was switched on and off. The green shaded areas represent the times that the ultrasonic transducer was on.

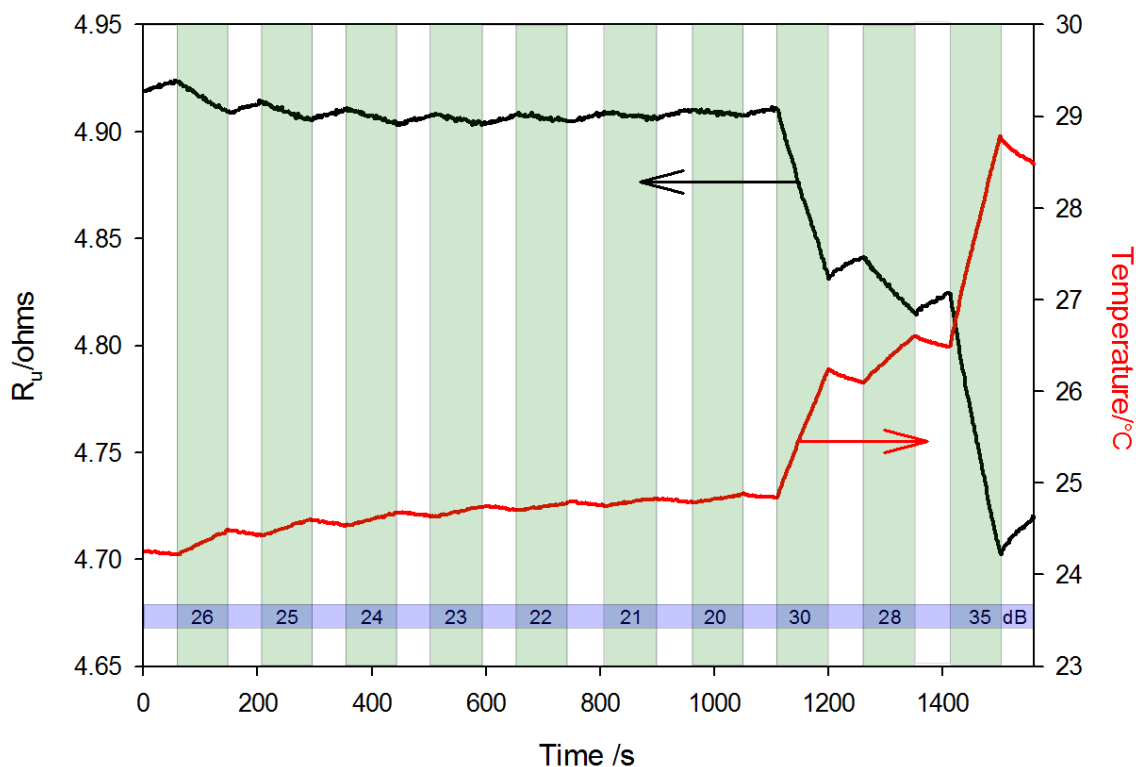


Figure 4.25 Plot showing the uncompensated resistance (black line)(across modular cell) and temperature (red line) as the ultrasonic transducer was turned off for 60 s then on for 90 s (28.8 kHz, varying amplification, details in appendix 5b). The green shaded areas represent the times at which the transducer was switched on. The amplification settings for each 'on' period are highlighted in the blue shaded area. The experiment was conducted in reactor 2 filled with 0.1 M NaOH (165 cm³ contained in reactor) flowing at 0.910 dm³ min⁻¹. The reactor was insulated with polystyrene.

Figure 4.25 shows that during each period in which the transducer is on, the thermocouple detects a temperature rise and the uncompensated resistance decreases. During the off periods there is a cooling effect and the resistance increases. Figure 4.25 shows that the higher amplification settings have a higher associated temperature and resistance change as expected. The gradients of each section (for example between 60 and 150 s for setting 26 dB) were calculated using linear regression to obtain a rate of resistance and temperature change for each amplification setting. Furthermore in an attempt to account for the heat loss from the system the gradients were adjusted. This was done by subtracting the gradient of the cooling period when the transducer was off. The average of the 'off' (cooling) gradients before and after each particular 'on' (heating) period was calculated and this was subtracted from the gradient in question. For example, for a gradient, m , observed during a particular section, n , then the new corrected gradient, M , is defined as,

$$M_n = m_n - [m_{n-1} + m_{n+1}] / 2 \quad (4-6)$$

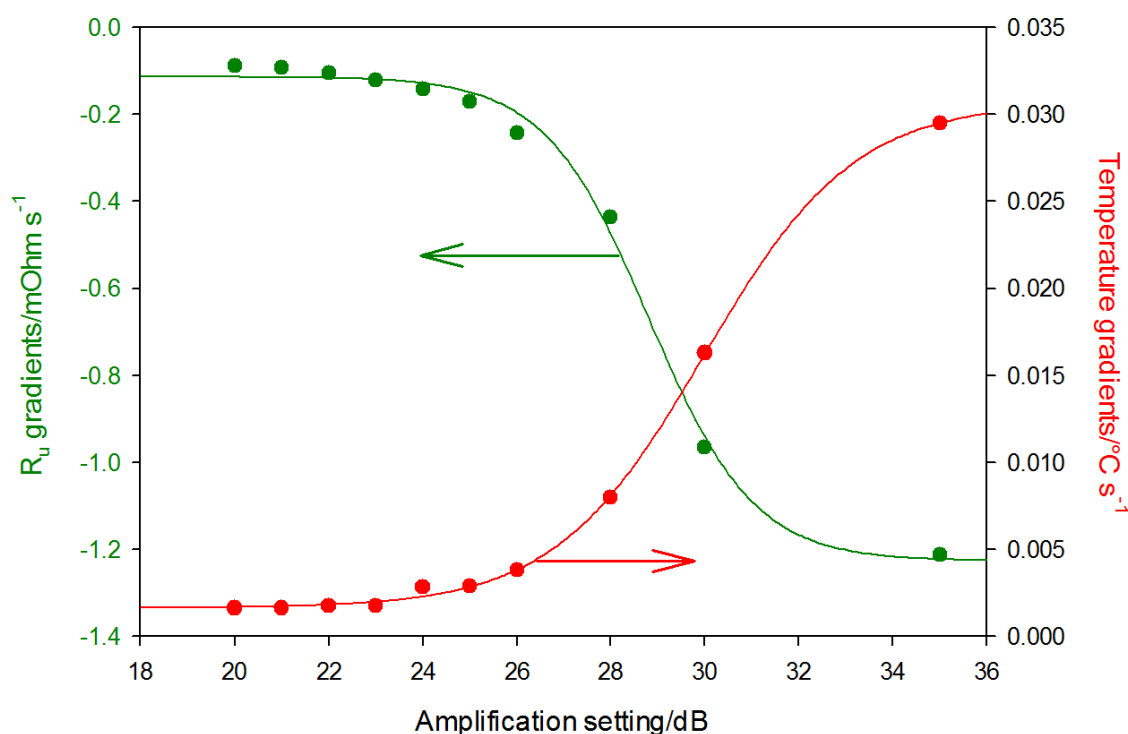


Figure 4.26 Graph showing the rates of change in uncompensated resistance (•) and temperature (•) with varying amplification setting at 28.8 kHz, 20 Vpp (corresponding pressure shown in Figure 4.27). Note the lines represent sigmoidal fits to the data.

Figure 4.26 demonstrates that the rates of change for the temperature and resistance both show a sigmoidal shape, which exhibits a sharp increase in the rate of change of the temperature and resistance upon increasing the amplification setting above a certain threshold (*ca.* 28 dB). Figure 4.27 demonstrates the pressure as a function of amplifier setting (same data as shown by coloured points Figure 4.15). As the amplification increases, a sharp increase in pressure is observed between 25 and 30 dB, due to resonance effects as previously discussed. Clearly the data suggest that higher pressure amplitudes are associated with higher heating rates as expected.

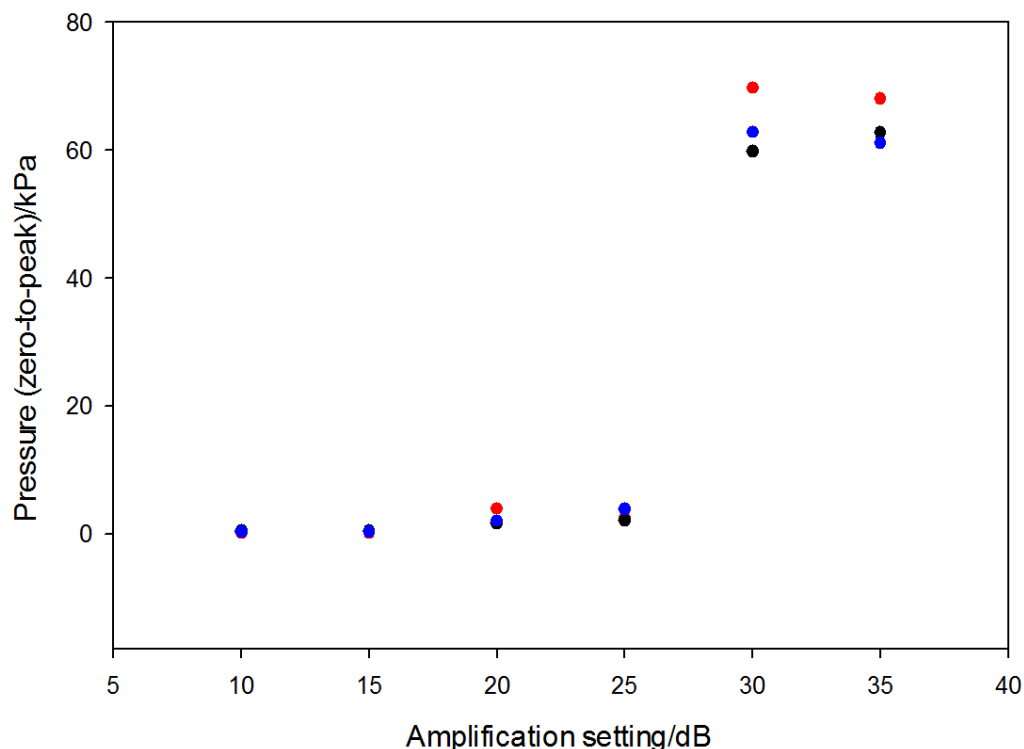


Figure 4.27 Pressure measurements taken with the hydrophone (TC4013) positioned 46 mm from the base of reactor 2 containing purified water (165 cm^3 in Dreschel bottle) flowing at $0.910 \text{ dm}^3 \text{ min}^{-1}$. The transducer was driven at three different frequencies (● 27.6 kHz, ● 28.4 kHz and ● 28.8 kHz (20 Vpp) at varying amplification 10 – 35 dB step 5 dB. This is the same data as shown by coloured points Figure 4.15.

The uncompensated resistance values can be converted into an effective solution temperature and in turn, heating rate. Figure 4.28 shows that the correlation between the predicted (from specific conductance) and actual (thermocouple) temperature values is very good, with gradient and r-squared values very close to 1. Hence it has been shown that the AC-modulation technique has high sensitivity to small temperature changes (ca. $\pm 0.1 \text{ }^\circ\text{C}$) and that the theory provides a well suited model for the calculation of the corresponding temperature change.

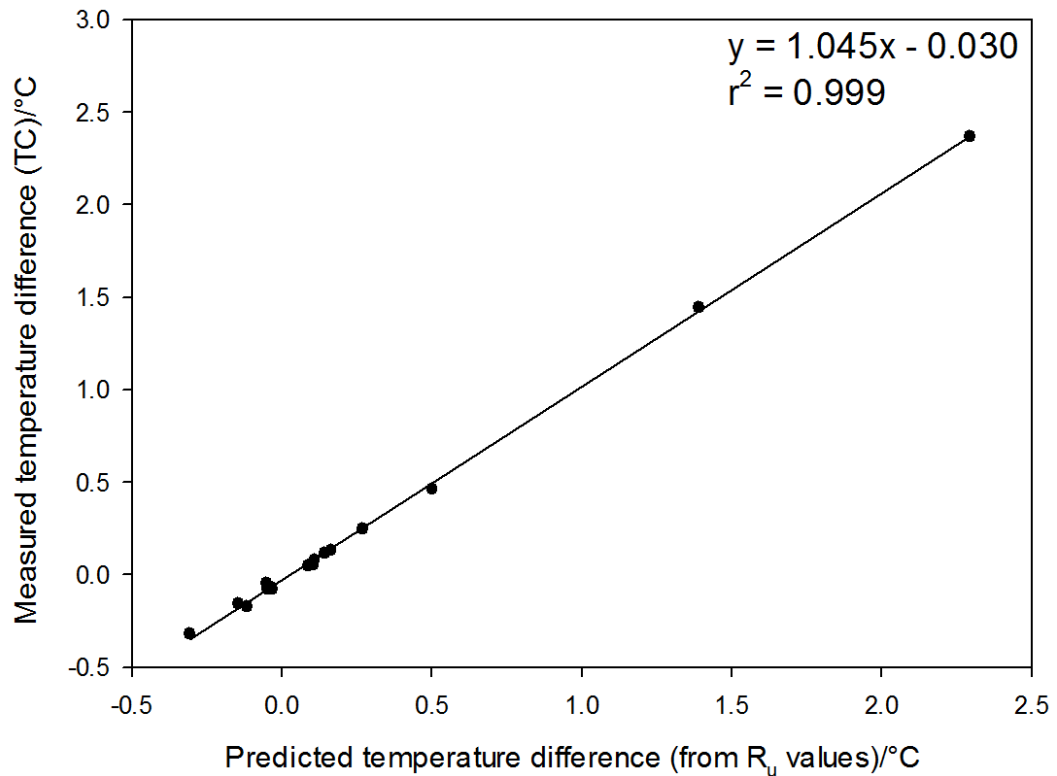


Figure 4.28 Graph demonstrating the relationship between the actual temperature difference (measured by the thermocouple, TC) and the predicted values calculated via the specific conductivity change (from R_u values across the module).

4.5 Conclusions

An experimental rig was designed and developed to provide effective analysis of the HTOGO electrolysis device under varying conditions. Examination of the performance of the electrolysis device in terms of current efficiency and response time was completed, by utilising the hydrogen flow rig and R_u measurements, across the device electrodes and in modular form. This resulted in the conveying of suggested improvements to HTOGO Ltd., the sponsors and manufacturers of the device. Specifically this included the introduction of forced electrolyte flow and the consideration of adapting a more advanced cell design, particularly with separated cells.

Furthermore the gas release for the investigated electrolysis system was shown to occur over a relatively long time period, with a time constant of the order of 100's of seconds. If the device (future generations) must meet the variable demands of an ICE then more rapid and controllable release of hydrogen is desirable. In efforts to

Chapter 4: Ultrasound assisted gas release

reduce the gas generation ‘inertia’ of these systems, an investigation of the integration of an ultrasonic outgassing system was conducted

Furthermore the resistance measurement technique was applied to estimate the gas void fraction of the bubbly liquid mixture. This highlighted some of the limitations of the sensor employed for the detection and quantification of short bursts of hydrogen gas. The high sensitivity of the technique has also been shown to lend itself to calculating small temperature changes within the liquid.

Chapter 5: Bubble populations

This chapter provides details of an investigation into the methods of characterising the bubble population produced by an electrolysis system. The aim of these experiments is to determine the sizes and numbers of bubbles, consequently providing beneficial information for a greater understanding and progression of the outgassing process discussed in chapter 4. Here, the Coulter principle is applied to estimate the bubble size distribution, which is further supported by estimation of the gas void fraction obtained by measurement of the resistance of the gas/liquid mixture between two steel plate electrodes. These well-established methods have been previously used for the sizing of bubbles via commercial systems [203-207], however the application for the estimation of the distribution of bubbles from an electrolysis system as employed here is novel. The chapter begins with an introduction to the Coulter method, followed by a description and analysis of the experimental work performed.

5.1 Coulter counter

The Coulter principle was discovered by Wallace H Coulter in the late 1940's. In 1953 he was granted a patent entitled "Means for counting particles suspended in a fluid" which refers to the use of an electric field for counting and sizing dilute suspensions of particles in conducting liquids. It is also commonly referred to as the 'electrozone sensing method'. Coulter originally applied the counting method to simplify and improve blood cell analysis so that large populations could be screened rapidly, as would be necessary in the event of nuclear war in Hiroshima and Nagasaki [208].

Since its inception, the method has been used for the characterization of a vast array of materials such as bacteria, platelets and particles [209-213]. In the research presented here, the Coulter principle is used to determine the bubble size distribution of a solution filled with electrolytically produced gas bubbles.

Chapter 5: Bubble populations

5.1.1 Theory

The Coulter principle states that the electrical resistance increase, which occurs upon an insulating particle passing through a pore initially filled with conducting solution over which a potential is applied, is directly proportional to the particle volume.

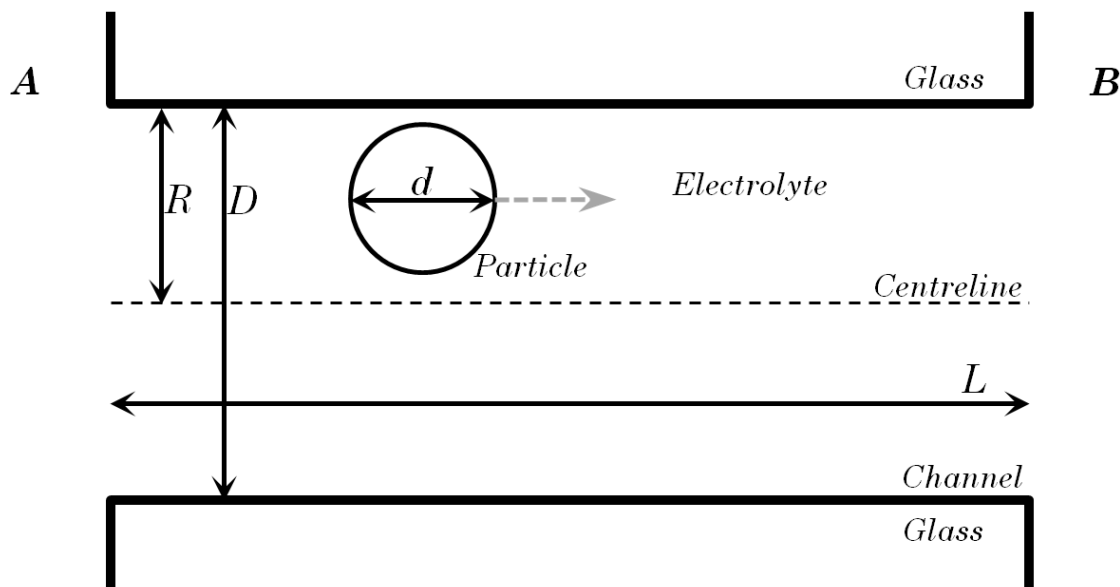


Figure 5.1 Diagram of an insulating spherical particle of diameter d , in a pore of diameter D , and length L , filled with electrolyte of resistivity ρ .

In reality the situation is more complex and the electrical response depends on the shape, size and position of the particle relative to the pore. This will be considered later in more detail with reference to Figure 5.1, which defines the discussed variables. Here the pore is a cylindrical channel of diameter, D , radius, R , and length, L , filled with conducting electrolyte through which an insulating particle of diameter, d , translocates (note this action of the particle to move from chamber A to chamber B for example).

The literature discusses the potential need to factor in other properties of the system, in particular the resistivity ratio of the particle and electrolyte [212, 213]. However, in practice it is found that the response is independent of the resistivity of the particle in many investigated systems [212-217]. Particle resistivity has been found to be many orders of magnitude greater than that of the electrolytes, with metal powders and other apparently good conductors behaving as insulators [217]. An explanation for this is given by Berg [217], who hypothesizes that this may be due to the formation of oxide surface films and the ionic inertia of the double layer

and associated solvent molecules at the surfaces of such particles. Regardless, here the technique is primarily applied for the sizing of bubbles, which conveniently provides a simpler circumstance, being volumes of insulating gas. However, this does bring about additional complications arising from the dynamic nature of bubble shapes; a problem encountered when measuring non-spherical particles [218, 219]. This will be subsequently discussed.

A solution to the problem of explaining the resistance change caused by the presence of insulating spheres in a conducting fluid was first proposed by James Clark Maxwell [220] and Lord Rayleigh [221] at the turn of the twentieth century. They considered the effective resistivity of an infinitely dilute solution of insulating spheres, ρ_{eff} , and conceived an expression in terms of the resistivity of the particle free solution, ρ , and the fractional volume of solution occupied by the sphere, f , (equation 5-1),

$$\rho_{eff} = \rho(1 + \frac{3f}{2}) \quad (5-1)$$

where f is defined as $V_P/(V_P+V_L)$. Here V_P is the volume occupied by the particles and V_L is the volume of liquid in the channel. This equation was derived by employing a solution to the Laplace equation for an insulating sphere in a uniform electric field. This can be applied to solve the problem of a single sphere in a pore in which the sphere is much smaller than the pore diameter ($d \ll D$). The resistance, R_P , of such a pore of diameter, D , and length, L , filled with a fluid of resistivity, ρ , can be approximated by equation (5-2).

$$R_P = \frac{4\rho L}{\pi D^2} \quad (5-2)$$

The volume fraction, f , of a single sphere in a pore is given by equation (5-3).

$$f = \frac{2d^3}{3D^2L} \quad (5-3)$$

Hence by substitution of equations (5-1), (5-2) and (5-3), an expression for the resistance, R , of a tube containing a small sphere, can be obtained.

$$R = \frac{4\rho_{eff}L}{\pi D^2} \quad (5-4)$$

Chapter 5: Bubble populations

$$= \left(\frac{4\rho L}{\pi D^2} \right) \left(1 + \frac{d^3}{D^2 L} \right) \quad (5-5)$$

Thus the resistance change, ΔR , is given by equation (5-6).

$$\Delta R = R - R_p = \frac{4\rho d^3}{\pi D^4} \quad (5-6)$$

Hence with knowledge of the tube diameter and solution resistivity, and by measuring the resistance change upon a particle translocation, the size of the insulating particle can be determined. However, this is only true within the limit that the diameter of the sphere is unaffected by the pore wall and is small compared to the diameter of the tube ($d \ll D$). The literature contains various methods to solve these problems to obtain a solution that is valid for more realistic conditions. Deblois and Bean [222] amongst others [212, 214, 223, 224] discuss how a correction function can be applied to overcome the size limit restrictions. This is usually expressed in terms of the sphere to pore diameter ratio (d/D) as demonstrated in equation (5-7). Deblois and Bean derived an approximation using only current streamlines which do not cross the sphere wall. They employed the solution to Laplace's equation for a sphere in an infinite medium [222]. The approximation to this solution is shown in equation (5-8) where F_1 is a numerically evaluated function.

$$\Delta R = \left(\frac{4\rho d^3}{\pi D^4} \right) \cdot F \left(\frac{d^3}{D^3} \right) \quad (5-7)$$

$$F_1 = 1 + 1.26 \left(\frac{d}{D} \right)^3 + 1.1 \left(\frac{d}{D} \right)^6 \quad (5-8)$$

Deblois and Bean also derived the following semi-empirical equation as a best fit to their experimental results.

$$F_2 = \left(1 + 0.73 \left(\frac{d}{D} \right)^3 \right) \quad (5-9)$$

Smythe [223, 225] also solved the problem employing a numerical approach using an integral formula relating spherical and cylindrical systems, satisfying simultaneously the insulating boundary conditions on the sphere and the pore wall, with a solution that is valid for diameter ratios (d/D) from 0.1 to 0.95. Smythe obtains the following solution and presents the vortex density coefficients, C_0 , which are reported in appendix 7.

$$F = \frac{2}{3} C_0 \left(\frac{d}{D} \right) \quad (5-10)$$

For ease of application, a sextic polynomial (equation 5-11, generated using regression analysis) was found to fit very well ($R^2=0.999$) to the Smythe data and was used to calculate the correction function (F_3) from the ratio of the diameters of the particle and pore.

$$F_3 = 372.01 \left(\frac{d}{D} \right)^6 - 1050.12 \left(\frac{d}{D} \right)^5 + 1162.93 \left(\frac{d}{D} \right)^4 - 634.31 \left(\frac{d}{D} \right)^3 + 177.14 \left(\frac{d}{D} \right)^2 - 23.29 \left(\frac{d}{D} \right) + 2.09 \quad (5-11)$$

Anderson and Quinn [225-227] present a summary of these correction functions and provide a comparison with respect to the ratio of d/D . A comparison of the correction factors (F_1 , F_2 and F_3) with varying sphere diameters (for a 40 μm diameter channel) is presented in Figure 5.2. This comparison enables the selection of the best suited function after calibration experiments with spheres of known size have been conducted.

For each correction function an explicit formula for the calculation of d in terms of ΔR is problematic to express, because both the Maxwellian formula (5-6) and the correction functions are expressed in terms of d^3 and higher powers. Solving the equations for d in these cases is not easily achievable. Hence to circumvent this problem an iterative process was employed; in this process, the ‘solver’ function in Microsoft Excel 2010 was used to iteratively calculate values for d across a range of ΔR values. Initially in each separate calculation, the constants were the resistance change, ΔR , the channel diameter, D , and the electrolyte resistivity, ρ_m (see footnote 2). In the computation, the solver calculates values for F (from eq. 5-7) and F_x (from eqs. 5-8, 5-9, 5-10) for varying d values. The solver continues until it finds a value where F and F_x are equal within a defined tolerance³ by changing the value of d . In mathematical form the process iteratively finds a value for which equation (5-12) is true, where F is expressed in equation (5-13), which is a rearranged form of (5-7) and F_x is either one of three correction functions expressed in equations (5-8, 5-9 and 5-10).

² For initial calculation the channel diameter was set to 40 μm , being that which was primarily used in experiments. The resistivity value at 25 °C was taken from the literature [202].

³ The tolerance value was set to 1×10^{-6} .

Chapter 5: Bubble populations

$$F - F_x = 0 \quad (5-12)$$

$$F = \left(\frac{\Delta R \pi D^4}{4 \rho d^3} \right) \quad (5-13)$$

This computation was performed across a range of ΔR values from 0 to 60000 ohms. In order to compute the iteration for a large amount of data the process was later adapted with the objective of making the sum of $F \cdot F_x$ values equal to zero across a range of resistance change values, with the constraint that each individual $F \cdot F_x$ value was a non-negative integer. This enabled the solver to automatically solve for a large range of values.

The results of these calculations are represented in Figure 5.2, which shows the theoretical relationship between the resistance change and calculated sphere diameter, with and without each correction method. These data were calculated using a channel diameter of 40 μm , as used in the calibration experiments. In every case, the overall trend is as expected for an inverse cubic relationship ($d \propto \Delta R^{1/3}$). Clearly there is variation in the predicted resistance change for a given sphere diameter. Furthermore, it is evident that the effect of the applied correction functions increases as d increases, shown by larger deviation from the uncorrected calculation. This demonstrates that the functions are tackling the widely accepted problem that as the d/D ratio increases, the resistance pulse generated is greater than predicted by assuming proportionality. The effect of the correction functions also becomes increasingly different with increasing resistance changes. This is shown by the D+B empirically based correction function ($F2$) approaching a d/D ratio limit of 1 ($d = 40 \mu\text{m}$) at *ca.* 25000 ohms, the D+B theoretically based correction function ($F1$) at *ca.* 47000 ohms and the Smythe's function ($F3$) not reaching the limit in this range.

The figure also highlights the size of the channel ($\emptyset = 40 \mu\text{m}$) and the size of the spheres used ($\emptyset = 25 \mu\text{m}$) in the calibration experiments with dashed lines. By finding the resistance change for a given sphere diameter, the best suited correction function can be selected as the method which calculates a sphere diameter closest to the real value. This will be discussed in section 5.1.3, after a description of the experimental setup and methods used to measure the resistance across a channel.

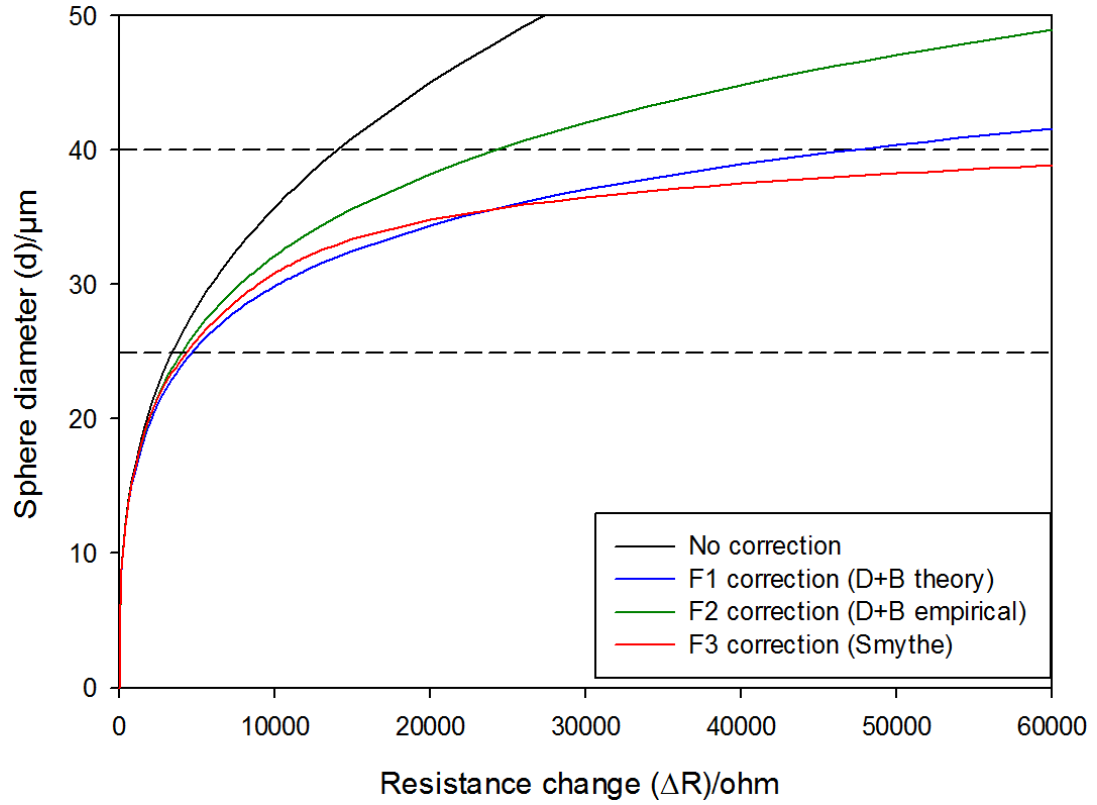


Figure 5.2 Plot demonstrating the relationship between the resistance change (ΔR) and the corresponding calculated insulating sphere diameter for a 40 μm diameter channel, with and without correction functions. The black line (—) shows the response without any correction function applied, the blue line (—) with the theoretically-based correction by Deblois and Bean [222]; the green line (—) with the empirically-based correction from the same source and the red line (—) from the correction published by Smythe [225]. The horizontal dashed lines (---) highlight the diameter of the channel ($d = 40 \mu\text{m}$) and the diameter of the polystyrene particles ($d = 24.9 \mu\text{m}$) used to calibrate the response.

5.1.2 Experimental details

This section contains general details of the fabrication and measurement methods used to quantify the ionic resistance across channels with diameters of the order of 10's of microns, filled with an electrolyte. Henceforth these are termed μ -channels. Exact details and conditions pertaining to individual experiments are given at the start of each relevant section and in the presentation of the results from each respective experiment.

5.1.2.1 μ -channel fabrication

Fabrication of the μ -channels was achieved by the electrochemical etching of copper wire, which had been sealed inside the end of a capillary tube.

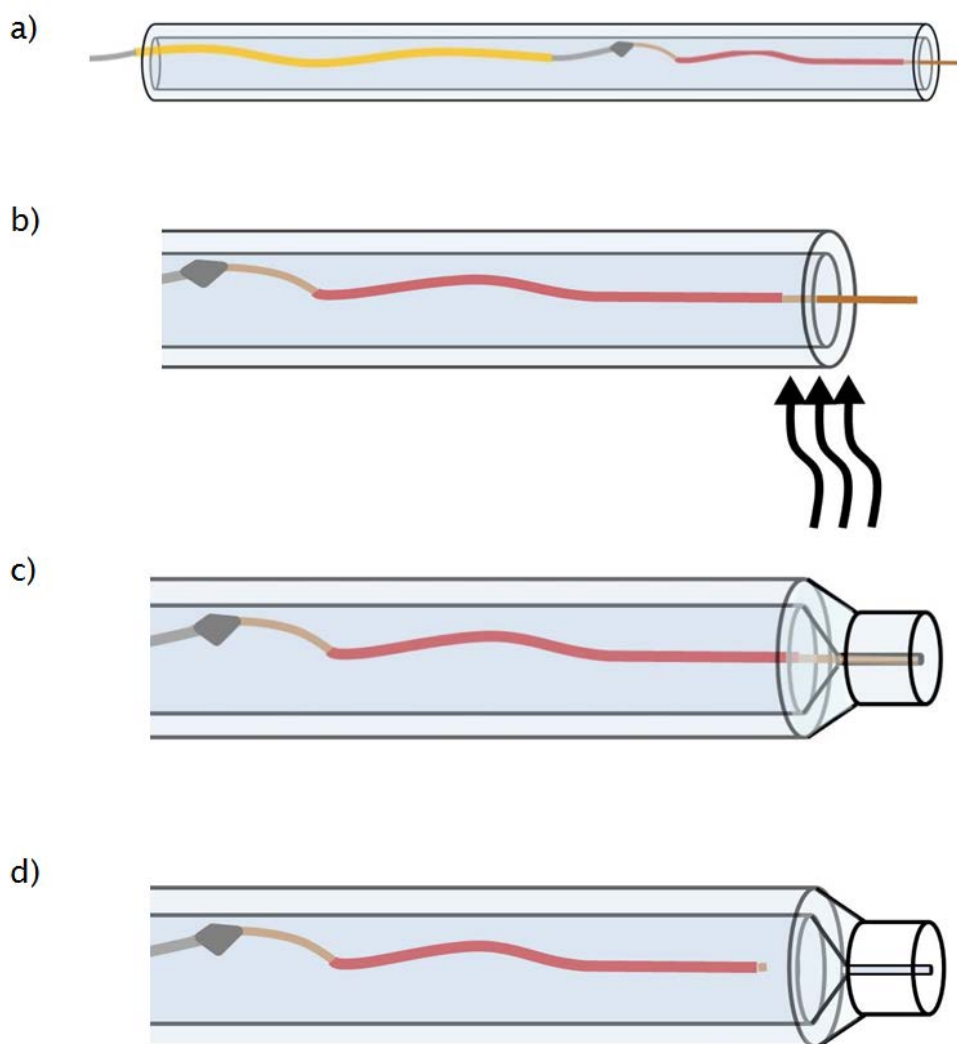


Figure 5.3 Drawings of the μ -channel etching process where a) shows the high-purity copper wire soldered to the connection wire placed inside the capillary tube, which is heated at the end (b) to seal the copper as shown in c). This is then electrochemically etched and the wire is removed and the tube cleaned to produce μ -channel at one end.

Figure 5.3 shows a schematic representation of the fabrication process. A short length (*ca.* 20 mm) of copper wire (Advent, $\varnothing = 100, 64, 50$ and $40\ \mu\text{m}$, 99.9 % purity) was solder joined to a longer length (*ca.* 100 mm) of copper wire (RS, $\varnothing = 0.25\ \text{mm}$, unknown purity) and placed in a soda-glass capillary tube (SAMCO, $\varnothing_{\text{outer}} = 2.0\ \text{mm}$, $\varnothing_{\text{inner}} = 1.68\ \text{mm}$), as shown in Figure 5.3(a). The micro-channel templating wire was sealed in one end of the capillary tube by heating with a flame generated from a butane/propane blowtorch (Bernzomatic TS1100) as depicted in Figure 5.3 (b) and (c). The sealed end of the tube was then polished with silicon carbide paper (Deer, P1200 grade) and alumina slurry ($1\ \mu\text{m}$ and $0.3\ \mu\text{m}$) on MicroCloth polishing pad (Buehler) until a smooth surface was evident upon inspection under a microscope (World Precision Instruments, model 500052). The copper was electrochemically etched using a standard three-electrode system. The copper wire was held a potential of 200 mV *vs.* a saturated mercurous sulphate reference electrode (SMSE, made in-house) with platinum gauze as the counter electrode in H_2SO_4 (0.1 M) electrolyte. The potentiostat (eDAQ, e-corder 401) applied the potential and measured and recorded the current *vs.* time with suitable sample rates and sensitivities.

Figure 5.4 shows a typical current *vs.* time trace for the etching process. This was monitored during the experiment to ensure that the etching was progressing and to provide indication of when the process was complete. Completion was exhibited by a large current increase as shown at around 16 hours in Figure 5.4, as the area of copper electrode available dramatically increases. The formation of the μ -channel was also confirmed by the observation of liquid being drawn up into the capillary tube. At this point of signal saturation the etching process was ceased and the connecting wire was removed from the capillary tube and any remaining copper was removed by soaking overnight in concentrated ferric chloride solution. The capillary was then rinsed with water, soaked in decon90 and rinsed again with water and the relevant experimental solution prior to use. Figure 5.5 shows images taken with a CCD camera (JAI CV-S3200) with macro-lens (Navitar 12x zoom) of a copper wire ($\varnothing = 50\ \mu\text{m}$) being etched as described above. The images show that the copper front progressively recedes. After the experiment, fragments of the copper remained, indicating the need for further treatment and cleansing prior to experimental application. Figure 5.6 shows images of a μ -channel before and after etching.

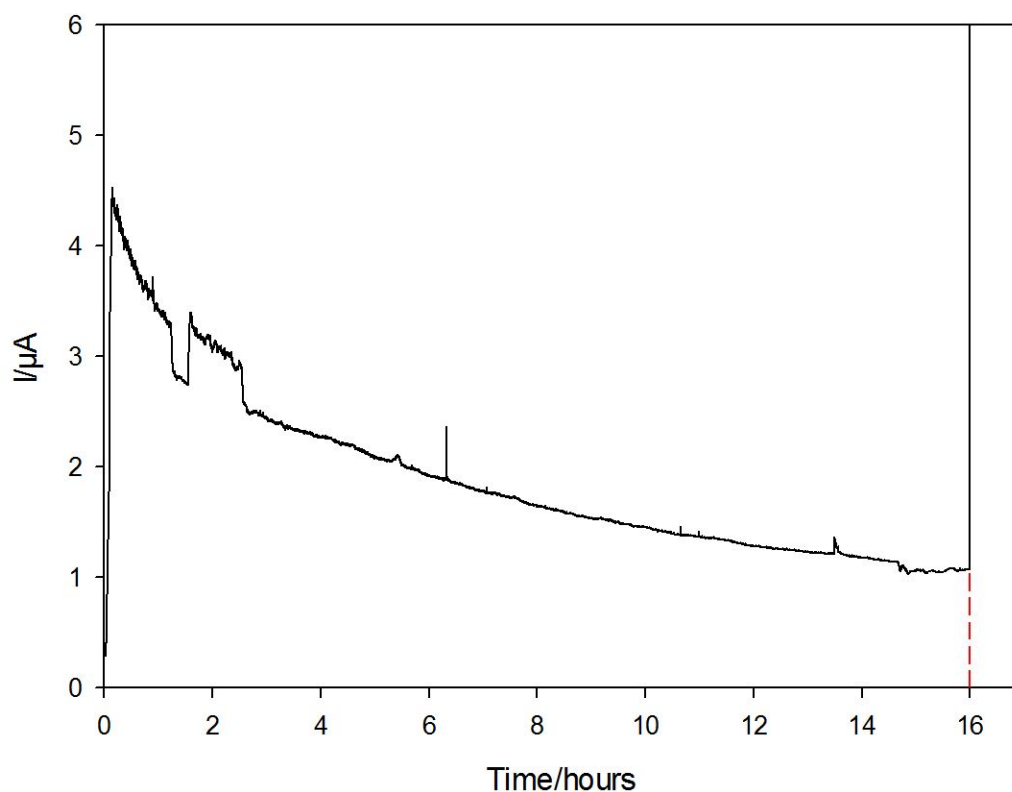


Figure 5.4 Plot of the current-time trace of a copper electrode ($\varnothing = 100 \mu\text{m}$) electrochemically etching in H_2SO_4 (0.1 M), held at a potential of 200 mV *vs.* SMSE. The counter electrode was Pt gauze. The dotted red line (---) highlights the moment that the channel was penetrated through to the other side.

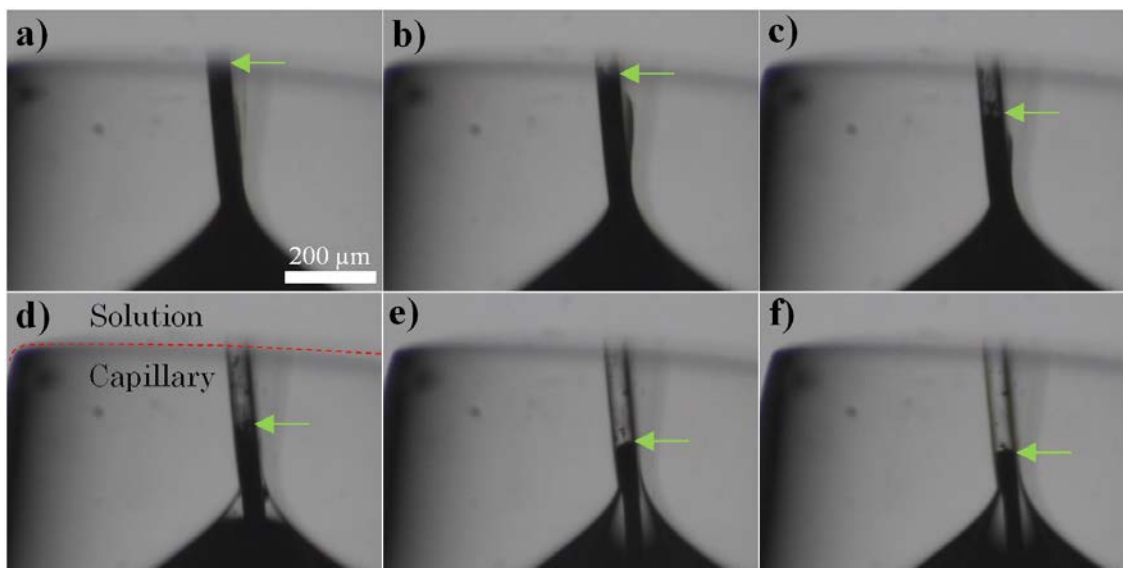


Figure 5.5 Sequential images of copper wire ($50 \mu\text{m}$) sealed in a glass capillary being electrochemically etched as described in section 5.1.2. The images were taken with a CCD camera (Jai CV-S3200) with macro-lens (Navitar 12x adjustable zoom) at a rate of 6 frames per minute. The images were taken at: a) 0 min, b) 33 min, c) 74 min, d) 116 min, e) 150 min, f) 204 min. The green (—) arrows highlight the copper front progressively being etched. The dashed red line (---) in image (d) illustrates the boundary between the capillary and solution.

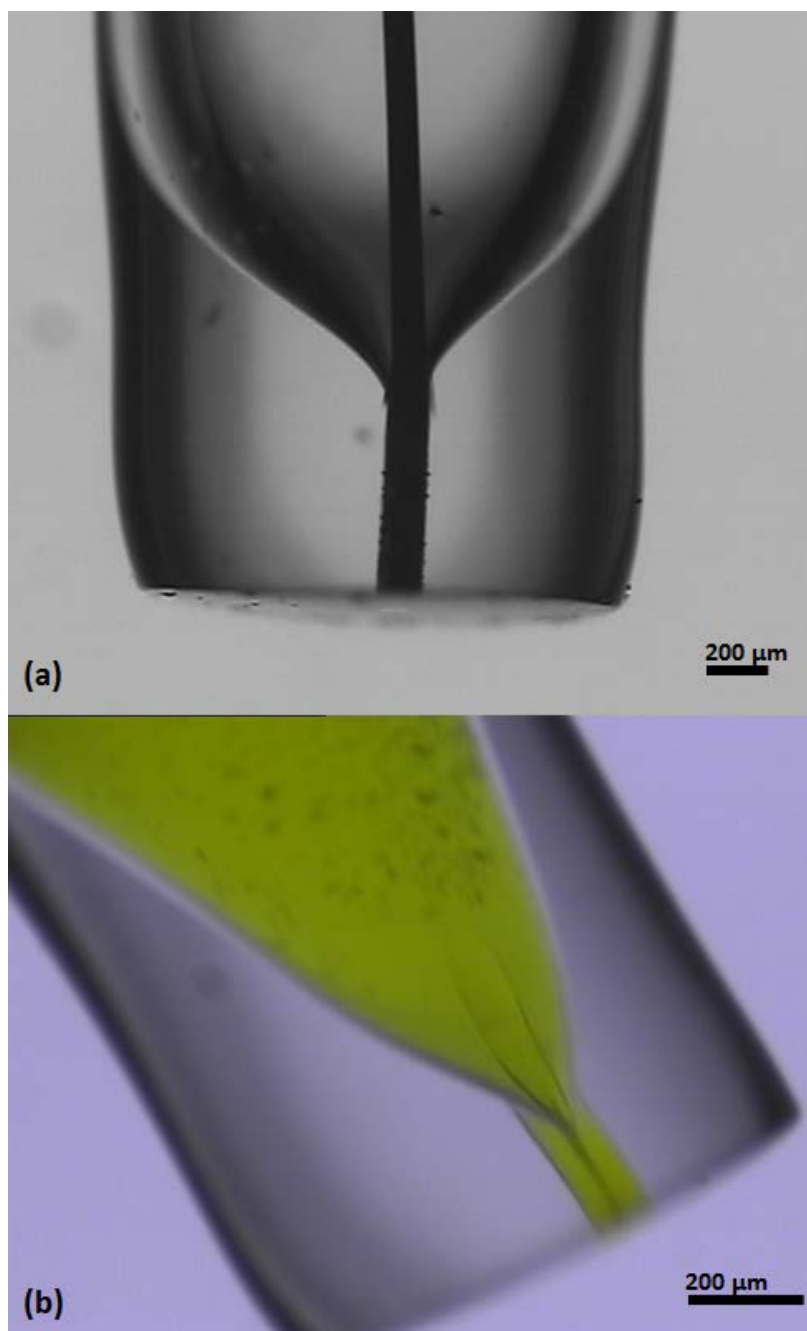


Figure 5.6 Images of (a) un-etched copper wire ($\varnothing = 100 \mu\text{m}$) sealed in a capillary tube and (b) an etched μ -channel ($\varnothing = 100 \mu\text{m}$) filled with ferric chloride solution.

5.1.2.2 Measuring the resistance across the channel

In order to measure the resistance, a potential difference (*ca.* 300 mV, stated precisely in each relevant legend) was applied between two Mercury-mercury oxide (MMO) electrodes, which were chosen due to their stability in alkaline hydroxide solutions. The electrodes were positioned either side of the μ -channel and the overall resistance was calculated from the measured current and known applied potential (*Ohm's law*). A schematic of the experimental setup is shown below in Figure 5.7.

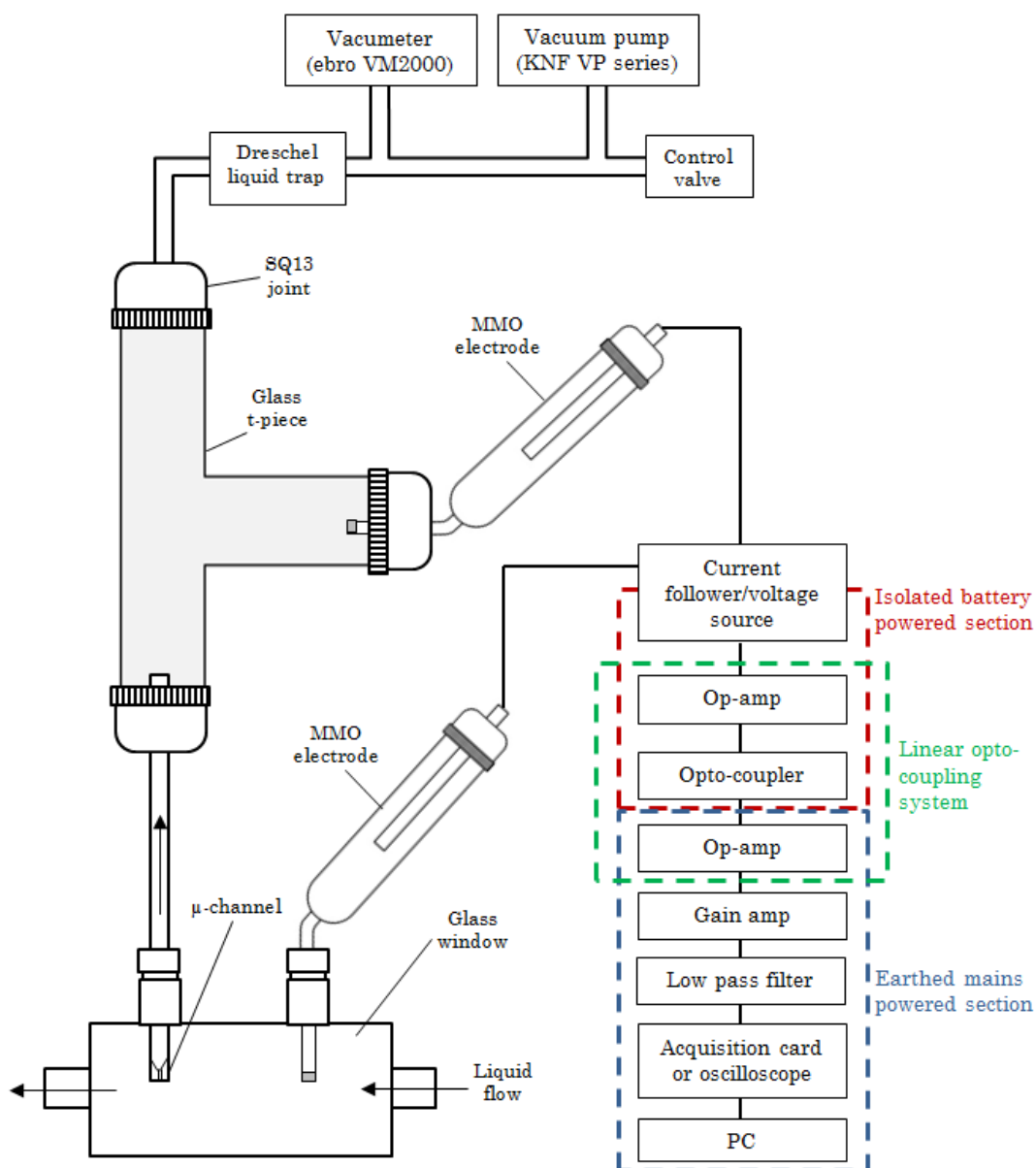


Figure 5.7 Schematic of the experimental system for measuring the electrical resistance across the μ -channel

Figure 5.7 shows a representation of the experimental arrangement used including a glass t-piece which holds the μ -channel and reference electrode in position within a flowing electrolyte. Liquid can be drawn up by a pressure drop created by a pump (KNF VP series), monitored by a pressure sensor (ebro VM2000) and controlled by a valve (Hoffman clip). A liquid trap was necessary to protect the vacuum equipment from the liquid electrolyte. In each experiment the glass t-piece was pre-filled with electrolyte (NaOH, 0.1 M) and the atmospheric and applied pressures were measured. The T-piece folding the μ -channel and reference electrode can be positioned for use in any relevant cell (containing the same electrolyte). During the investigation the channel was utilised in three different cells. Figure 5.7 shows a glass window flow cell. Alternatively a small quartz cuvette or a modified Dreschel flask (Figure 2.1 (c)) can be used. The flow cell also provided a flat transparent cell wall to enable the observation of bubbles translocating the channel without light refraction associated with a curved cell (section 5.1.3.3). The quartz cuvette was used as a vessel for the measurement of the polarisation curve (section 5.1.3.1) and the observation of polystyrene spheres (section 5.1.3.2). The Dreschel flask was used as a reservoir to sample directly from the bubbly liquid.

The current passing through the μ -channel was measured using an opto-isolator described below (section 5.1.2.3). This current was monitored using an oscilloscope (Owon SDS-7102V) after appropriate conversion accounting for the gain of the current follower, for the calibration experiments (section 5.1.3). However a USB data acquisition card (Cole Parmer 18200-20, 16 bit, sample rate = 50 kHz) was employed for the bubble population experiments (section 5.1.4). An in-house written VB program (appendix 11: Tcounter.vbp) was used to interface the acquisition card. The program contained a routine to find peaks below a threshold relative to the background current signal (between 99 and 99.6 % of the background level, stated with each relevant data analysis). In each case the threshold level was chosen as the maximum current level to detect peaks without identifying false positives associated with noise on the signal. The value of the peak for each event was then converted to a resistance change relative to the background level by Ohms law.

Chapter 5: Bubble populations

5.1.2.3 Opto-isolation

Initial versions of the experimental setup made used a potentiostat to control the electrochemistry. However, with this configuration, the signal-to-noise ratio was too low and did not provide a reliable measurement of the resistance changes. Note the electrolysis process necessitates for an electrochemical cell. Hence an opto-isolated system was utilised in order to reduce the noise level in the signal. This type of system has been previously employed in the Birkin research group, typically to avoid the associated noise interference of cavitation environments as demonstrated by Vian *et al.* [132]. The system employed here makes use of a linear optocoupler and current follower which are partly battery powered. In the optocoupler utilised here (IL300A), two photodiodes are coupled to the output of an LED which provides illumination dependent on the input signal. Hence the output from the optocoupler must be calibrated with a correction factor to give the correctly measured current. Further details are contained in appendix 8. This therefore provides a method for measuring the current in a manner completely isolated from mains-associated noise, which is then transferred to the mains powered section of the circuitry. Further measures taken to reduce the noise level of the signal included the use of a Faraday cage to shield the experiment from external electrical fields and the addition of a low pass filter (28 kHz) to remove high frequency noise.

5.1.3 Calibration and validation

A series of experiments were performed to validate and calibrate the response of the system to known particle and bubble sizes. These are discussed in the next three subsections.

Initial experiments tested different sizes of μ -channels with the conclusion that a channel diameter of 40 μm is the smallest possible to reliably achieve a flow of liquid by means of an applied pressure difference, to have the capability to draw particles through. More dilute solutions with lower viscosities did not have a significant effect. Hence this channel diameter was selected to measure the resistance change caused by the translocation of 10 μm and 25 μm polystyrene particles.

5.1.3.1 Polarisation curve

Prior to making any electrical measurements it is important to establish that the electrochemical response is linear with potential. This implies that the pore behaves as a resistor. Figure 5.8 shows the current response as a function of potential for a μ -channel. The electrodes were utilised as described in section 5.1.2.2. The graph shows a linear response ($R^2=1.000$) as expected for a μ -channel. Note the measured resistance is composed of several components; the channel, exterior electrolyte and the reference electrodes.

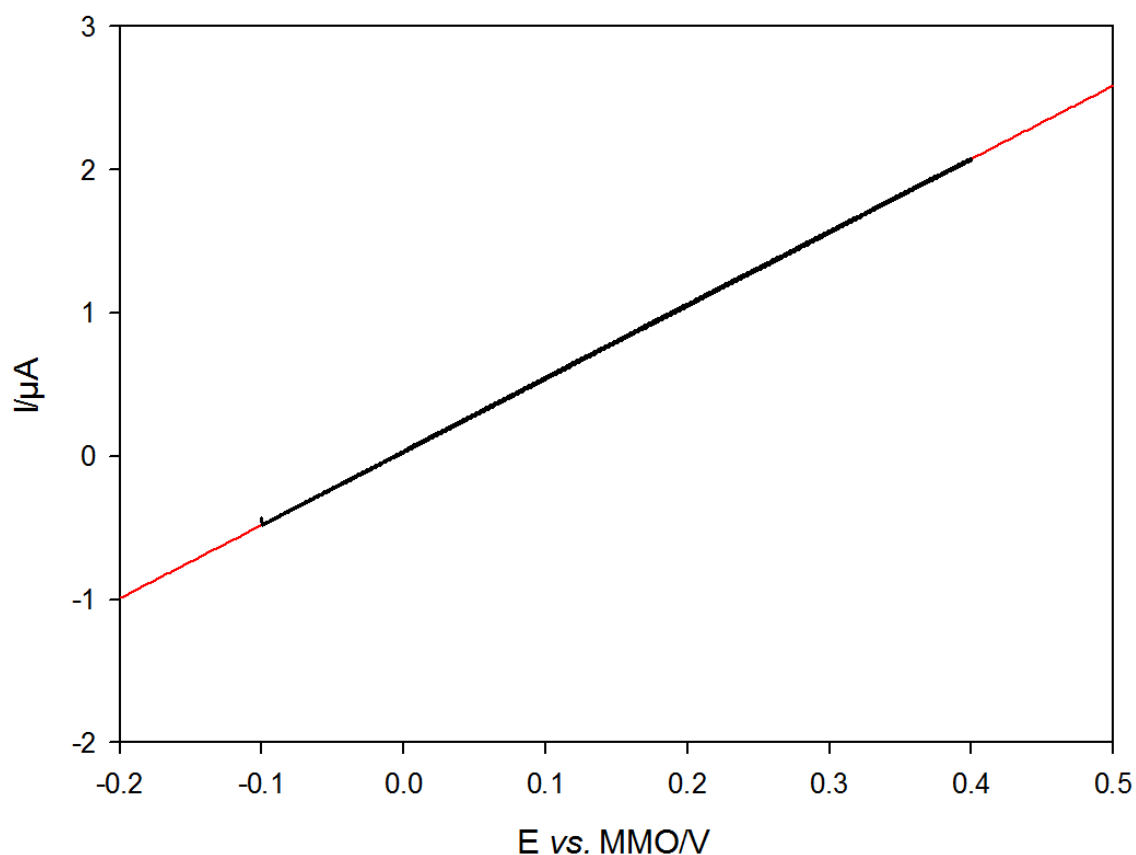


Figure 5.8 Polarisation curve (—) of an MMO electrode *vs.* MMO in 0.1 M NaOH through a μ -channel ($\varnothing = 50 \mu\text{m}$) with linear fit (—). The potential was swept from -0.1 to 0.4 V *vs.* MMO at 20 mV s^{-1} under aerobic conditions at 24.3°C . The linear fit ($R^2=1.000$) produced a slope of 0.0051 mA/V which equates to a resistance of 196 kOhms.

5.1.3.2 Particle calibration

Polystyrene spheres (Polysciences, $\varnothing = 10 \mu\text{m}$, $25 \mu\text{m}$) were drawn up through μ -channels ($\varnothing = 40 \mu\text{m}$, $50 \mu\text{m}$) as described in section 5.1.2.2. The μ -channel and MMO electrode were placed in a quartz cuvette ($10 \text{ mm} \times 10 \text{ mm} \times 45 \text{ mm}$) filled with 0.1 M NaOH (*ca.* 3 mL) and the liquid was drawn up by the vacuum pump at a variety of pressures. Two drops of the polystyrene sphere solution (1 drop = *ca.* 1

Chapter 5: Bubble populations

cm³/drop; for $\varnothing = 10\ \mu\text{m}$, conc. = 4.55×10^7 particles/cm³; for $\varnothing = 25\ \mu\text{m}$, conc. = 2.91×10^6 particles/cm³) were added to the cuvette for each experiment.

The current through the μ -channel was recorded simultaneously with images of the particles translocating through the channel using a high-speed camera (Photron APX-RS).

5.1.3.2.1 Particle translocation example

Figure 5.9 shows an example of the translocation of a polystyrene particle ($\varnothing = 25\ \mu\text{m}$) through a μ -channel ($\varnothing = 40\ \mu\text{m}$) Figure 5.10 shows the associated resistance change for this particular particle measured simultaneously.

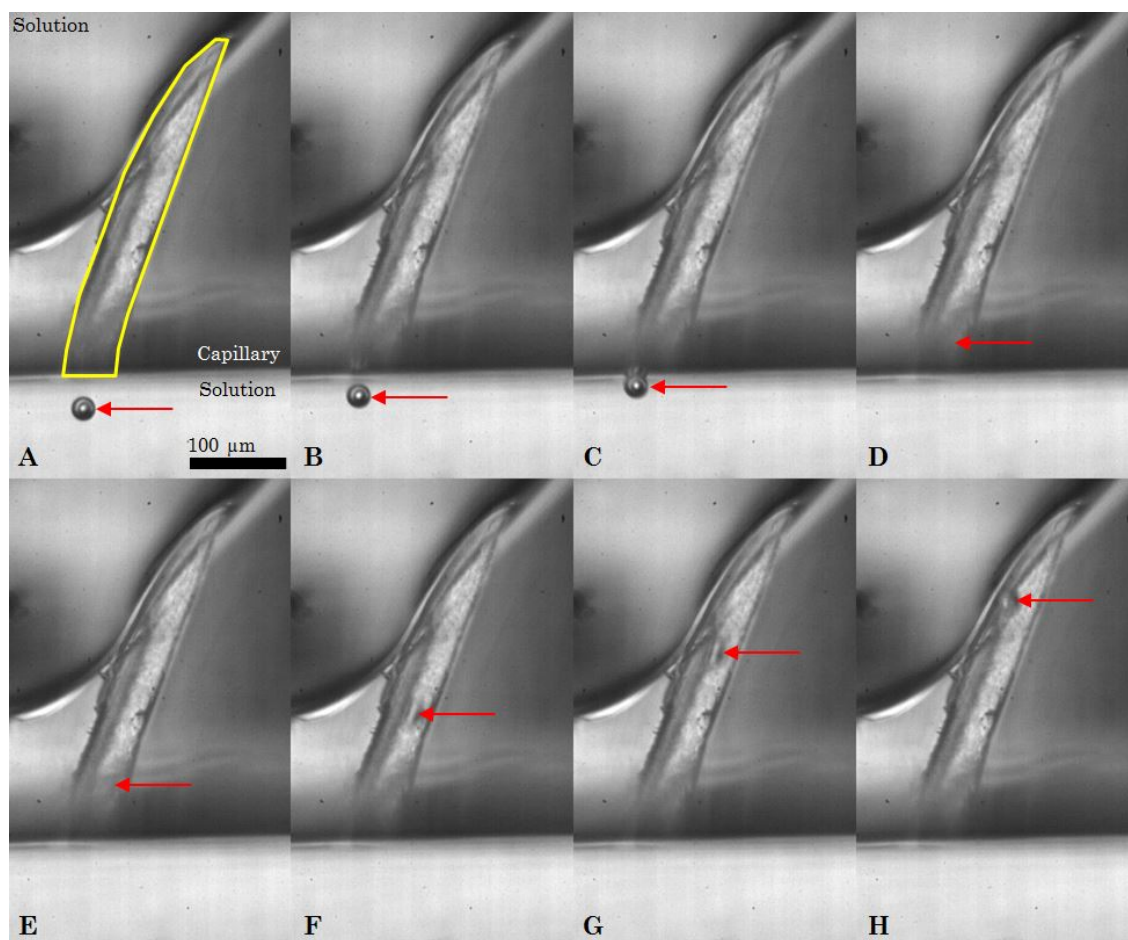




Figure 5.9 Sequential images of a polystyrene particle ($\varnothing=25\ \mu\text{m}$) translocating through a μ -channel ($\varnothing=40\ \mu\text{m}$). Image A highlights the μ -channel (yellow line, ) , the boundary between the capillary and solution and a scale bar which is valid for all images in the figure. The images were taken at A = 0 ms, B = 1 ms, C = 1.429 ms, D = 1.857 ms, E = 2.286 ms, F = 3 ms, G = 3.429 ms, H = 3.857 ms. The red arrows () highlight the position of the particle in each frame. The camera captured the images at a frame rate of 7000 fps and exposure time of 1/frame second (1/7000 s).

The amplitude of the resistance pulse is mainly determined by the particle size whilst the width of the pulse corresponds to the total time duration when the

particle is present in the channel. These results show that as the particle approaches the entrance to the channel (see images B to C), a resistance increase was observed. The increase in response between B and C shows that the sensing zone extends beyond the interior of the channel as the particle is outside of the channel at this time. The resistance continues to increase until image E, at which time the particle is completely inside the channel, producing the maximum signal response. The resistance plateaus at this maximum level as the sphere travels through the middle of the channel (E to F) and then begins to decrease as it nears the channel exit (F to G). Here the images appear to show that the particle is still completely inside the channel, however the resistance falls. This is because the channel is somewhat asymmetric and the particle is in fact closer to the exit on the opposite side. The resistance continues to decrease until the particle has completely exited the channel (shortly after H) at which point the resistance decreases to the background level again. This demonstrates a typical example of an individual particle translocation.

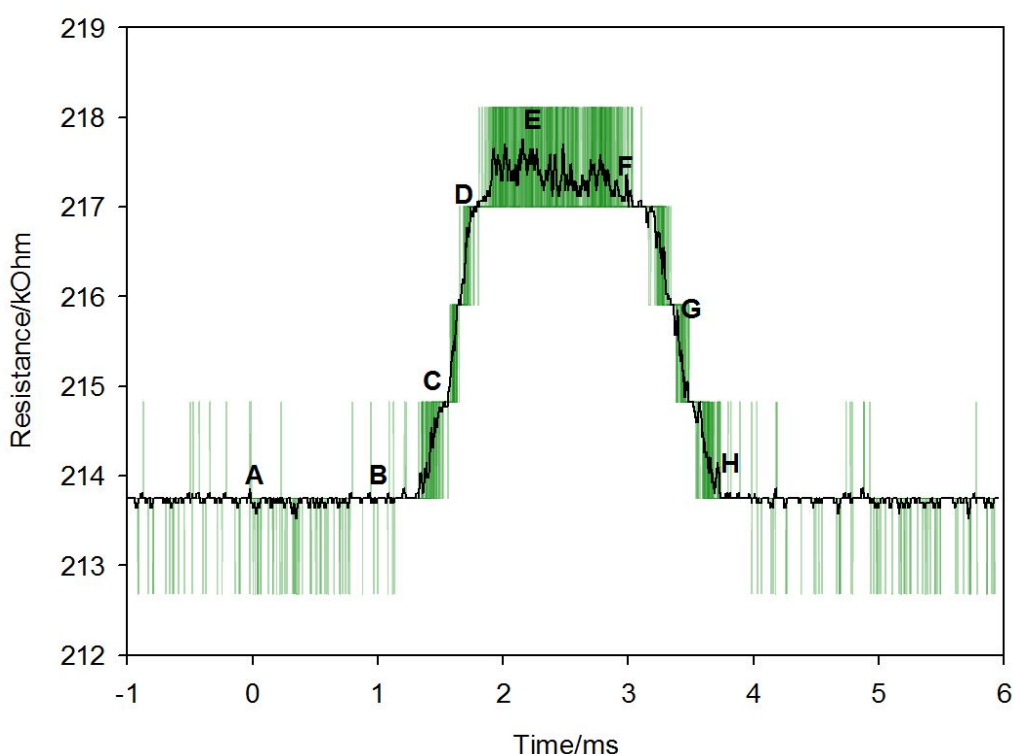


Figure 5.10 Plot showing the resistance change associated with the translocation of the polystyrene sphere through the channel, as shown in Figure 5.9 (particle $\varnothing = 25 \mu\text{m}$, channel $\varnothing = 40 \mu\text{m}$). The potential was held at 342 mV *vs.* MMO and the pressure measured by the vacuometer was 982 mbar. The signal was measured and recorded using an oscilloscope. The green line (—) represents the recorded data and the black line is a moving average (—). The temperature at the time of the experiment was recorded as 24.0 °C.

Chapter 5: Bubble populations

It should be noted that the data displayed in Figure 5.10 is limited by the acquisition resolution of the oscilloscope (8-bit) and as such, digital level limits are observed. In the further experiments in which many peaks are analysed for calibration data acquisition was achieved using a 16 bit data acquisition card, which offers a much greater vertical resolution. An example of a current/resistance change captured in this manner is displayed in Figure 5.11, which demonstrates a significantly improved signal-to-noise ratio compared to Figure 5.10. However, the same peak shape as reported in Figure 5.10 was observed for the data collected by this method.

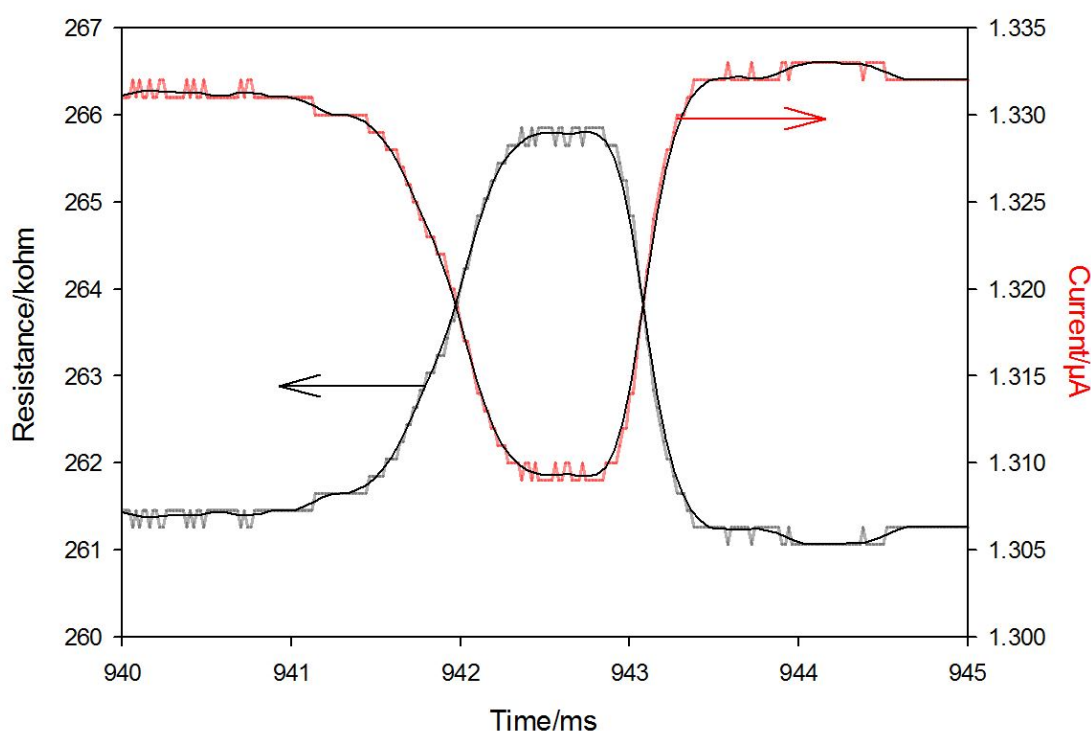


Figure 5.11 Plots showing the current (red line —, right axis) and resistance (black line —, left axis) change associated with the translocation of a polystyrene sphere ($\varnothing = 25 \mu\text{m}$) through a μ -channel ($\varnothing = 40 \mu\text{m}$) filled with 0.1 M NaOH. Moving averages of each plot are overlain with a black line (—). The potential was held at 348 mV *vs.* MMO and the pressure measured by the vacuumeter was 992 mbar. The signal was measured and recorded using a 16-bit USB data acquisition card at a rate of 50kS/s. The temperature was recorded as 25.6 °C.

5.1.3.2.2 Multiple particle translocations

The polystyrene sphere calibration experiments also captured the data using the opto-isolated system described in section 5.1.2.3. Tcounter.vbp (appendix 11) was used to interface the acquisition card (Cole Parmer 18200-20, 50 kHz) and to find and save peaks from the data. For each experiment, the program was set-up to

record data until 100 peaks had been counted. The threshold was set to 99 % of the background current signal which was measured at the start of the experiment before the spheres were added. The times and magnitudes of each of the 100 peaks were then saved. An example of the peak finding routine is shown for bubble translocations, in Figure 5.27. This was repeated at varied applied pressure differences across the μ -channel, ranging from 8 to 81 mbar. The temperature of the electrolyte was also measured using a temperature probe (CHY706 K-type thermocouple).

The sample size of 100 peaks for each experiment was chosen as the limit due to regular occurrence of μ -channel blocking, caused by a build-up of particles. This was observed to be caused by several particles becoming stuck in the middle of the channel whilst still allowing liquid flow around the stuck particles. A build-up of particles would then occur as shown in Figure 5.12. This would cause the resistance to dramatically increase and become unstable. This regular occurrence meant that the experiment could not be left to capture indefinitely (more than *ca.* 100 s). Any data from experiments affected by μ -channel blocking was disregarded.

As described in section 5.1.2.1 the μ -channels were soaked in Decon90 surfactant solution (*ca.* 3%) and rinsed with purified water after etching. Fresh washing of the μ -channels in this manner prior to experimentation helped to postpone such sphere build-up problems.

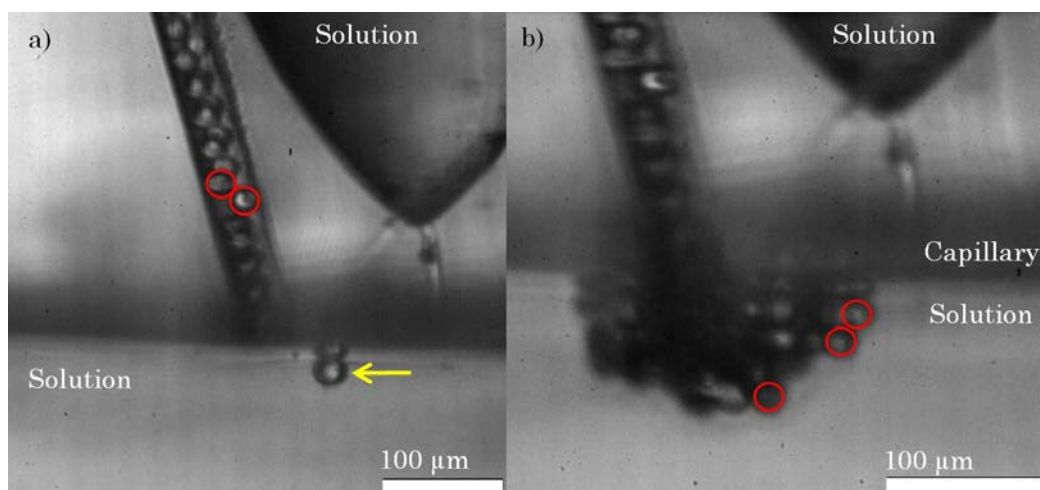


Figure 5.12 Images of a μ -channel ($\varnothing = 40 \mu\text{m}$) blocked with polystyrene spheres ($\varnothing = 25 \mu\text{m}$). The red circles highlight individual spheres. Image a) shows the moment at which the channel is blocked and the first sphere is built up outside of the channel (yellow arrow). Image b) demonstrates that liquid is still drawn up through the channel, causing a hemispherical build-up of many spheres around the orifice entrance.

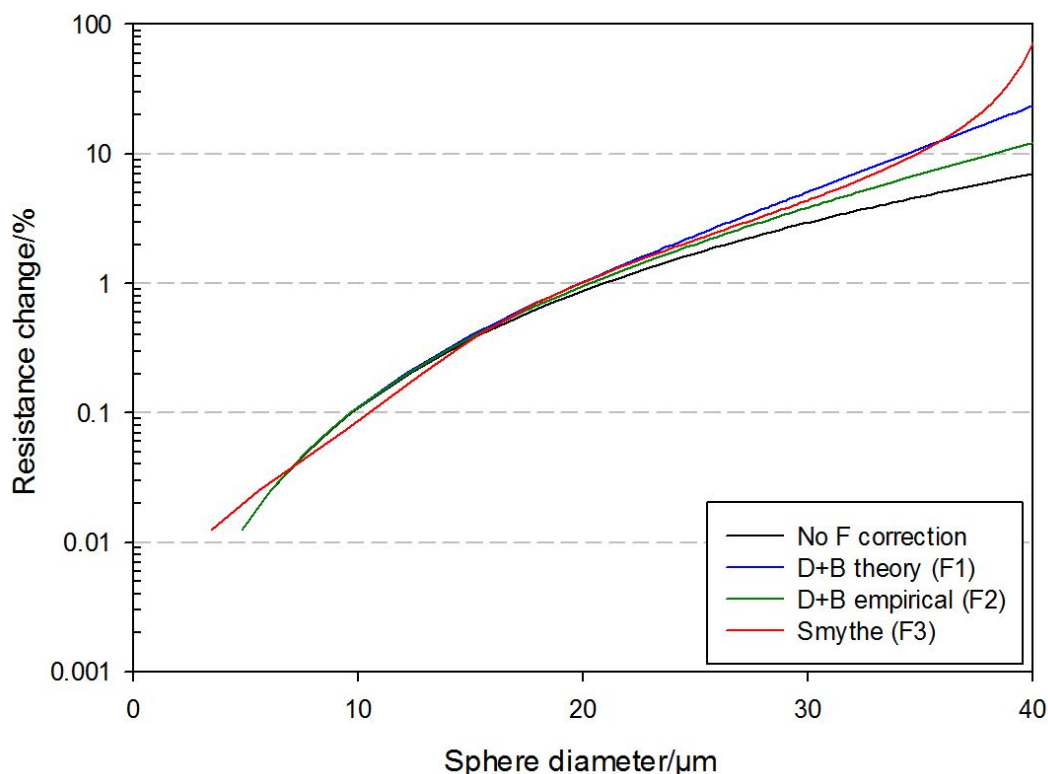


Figure 5.13 Plot showing the sensitivity of the resistance measurement compared to the background level (230 k Ω) with varied sphere diameter for a 40 μm diameter channel according to the different theoretical methods of calculation. The black line (—) represents the calculation without any F correction, the blue line (—) with the F1 correction, the green line (—) with the F2 correction and the red line (—) with the F3 correction. The relative resistance change is plotted on a logarithmic scale.

Note the detection of a resistance change from the translocation of 10 μm diameter polystyrene particles through a 40 μm diameter channel was not possible with the experimental setup employed. Figure 5.13 shows the theoretical sensitivity needed for the detection of different sized particles in a 40 μm diameter channel. According to the plots, a sensitivity of *ca.* 0.1 % is needed in order to detect particles of 10 μm diameter, regardless of the F correction method. Considerable measures were taken to reduce the noise level, resulting in a smallest noise level of *ca.* 0.3 %. However, this is still insufficient to be able to detect such particles and hence only the 25 μm diameter polystyrene spheres were used in the calibration experiments conducted with a 40 μm \varnothing channel. The same limitation was discovered for the use of 25 μm \varnothing particles (and obviously 10 μm \varnothing) with a 50 μm \varnothing channel.

Figure 5.14 displays a histogram of the resistance change values obtained from the translocation of 110 polystyrene spheres ($\varnothing = 25 \mu\text{m}$) drawn up through a μ -channel ($\varnothing = 40 \mu\text{m}$) at a pressure difference of 10 mbar. The threshold of 99 % (of the 229 k Ω background level) only identified resistance changes above 2291 Ω .

The histogram exhibits a Gaussian-type distribution, characterised by the bell-shaped curve centred at *ca.* 4200 ohms. The results demonstrate that even though the polystyrene particles are relatively mono-dispersed ($\varnothing = 24.9 \mu\text{m}$ with a standard deviation of $0.77 \mu\text{m}$), the range of resistance change values obtained is relatively large, ranging from *ca.* 3300 ohms to > 8000 ohms. A brief comparison of the resistance change values observed in Figure 5.14 to the equivalent particle diameters (theoretical) from Figure 5.2, demonstrates that this range of resistance values is larger than the range that would be expected from the range of diameters of the spheres. Some of the variation is due to the inherent distribution in particle size, but other phenomena may be the cause of the relatively broad range, in particular for the larger values observed outside of the bell curve (above $5.5 \text{ k}\Omega$). Possible causes of these measurements will now be given, followed by a further analysis of the polystyrene sphere calibration data.

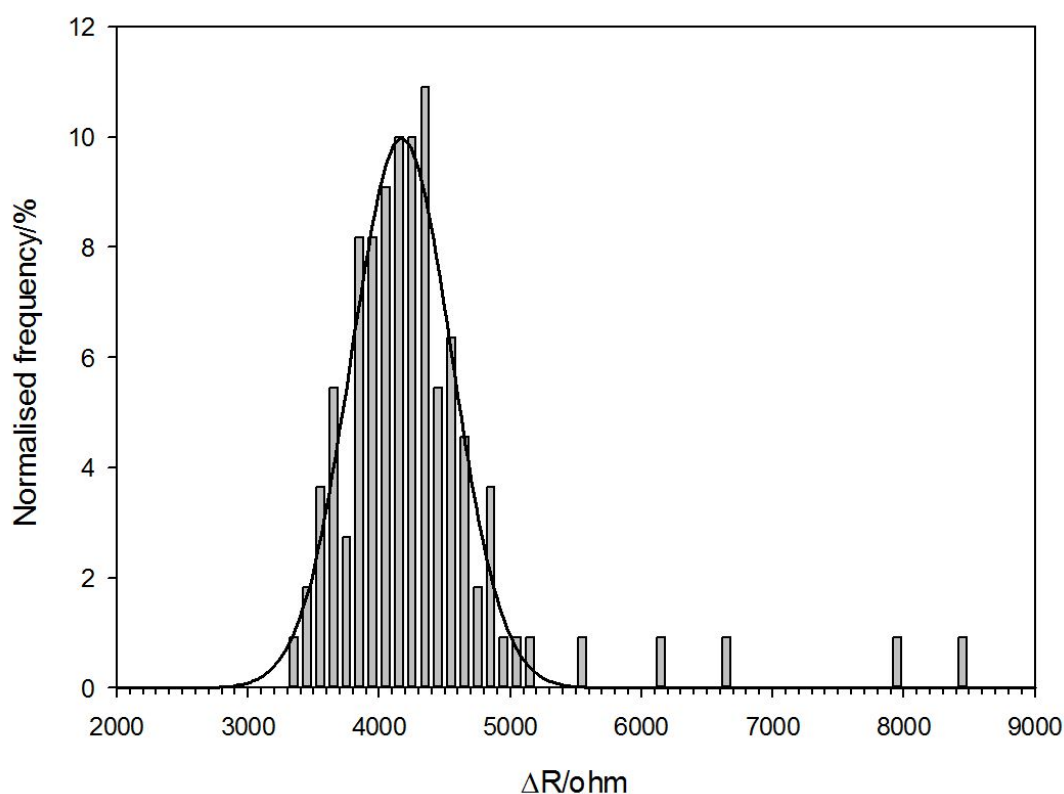


Figure 5.14 Plot showing a histogram of the resistance change values obtained from the translocation of 110 polystyrene spheres ($\varnothing = 25 \mu\text{m}$) through a μ -channel ($\varnothing = 40 \mu\text{m}$) filled with 0.1 M NaOH. The black line represents a Gaussian fit to the data. The bin widths were set to 100 ohms and the frequency is normalised to the total count. The potential was held at 348 mV *vs.* MMO and the pressure difference across the channel was 10 mbar. The average temperature was 25.3°C . A peak-finding routine was used to identify the pulses recorded via a data acquisition card which sampled at a sample rate of 50 kHz. The threshold for the peak finding was set to 99 % of the background level of 229 kOhms.

Chapter 5: Bubble populations

In ideal conditions, the concentration of particles would be at a low enough level to be able to assume that only one particle transverses the channel at a time.

However, if two particles are in the sensing zone at the same time, they may only be counted as one and, in addition, if they are very close together they may be sized as one particle of volume equal to their sum [212, 213].

Figure 5.13 demonstrates this ‘coincidence’ effect, showing that if particles are very close together, then they may be sized by one larger peak, the magnitude of which approaches the sum of their individual peaks as the distance between the particles decreases.

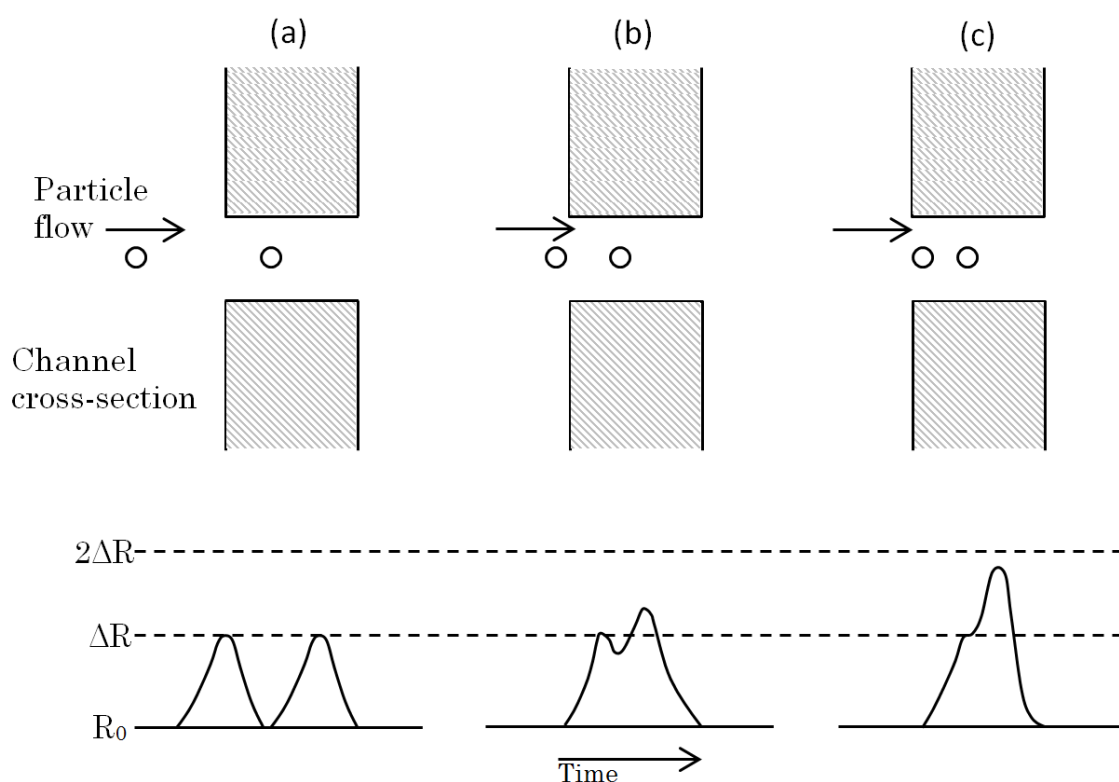


Figure 5.15 Diagram showing the effect of particle coincidence on the size of the resistance pulses produced as the particles translocate the centre of a channel. ‘ ΔR ’ represents the magnitude of the resistance pulse produced from the translocation of an individual particle through the channel. R_0 is the baseline resistance of the μ -channel. Diagram based on [213].

Further sizing errors may also be produced by particles that translocate the channel along differing paths [212, 213, 216]. Figure 5.16 demonstrates the expected resistance transients generated by different paths of the same particle through a channel. Hence particle oversizing may occur again, arising from a translocation of a particle in the vicinity of the channel walls. Theoretical and experimental studies conducted by Grover [215] demonstrated that the potential

field at the inlet and outlet edges is more dense, which gives a widely accepted explanation for the 'M'-shaped pulses generated by particles travelling near the walls that pass through two regions of high potential gradient.

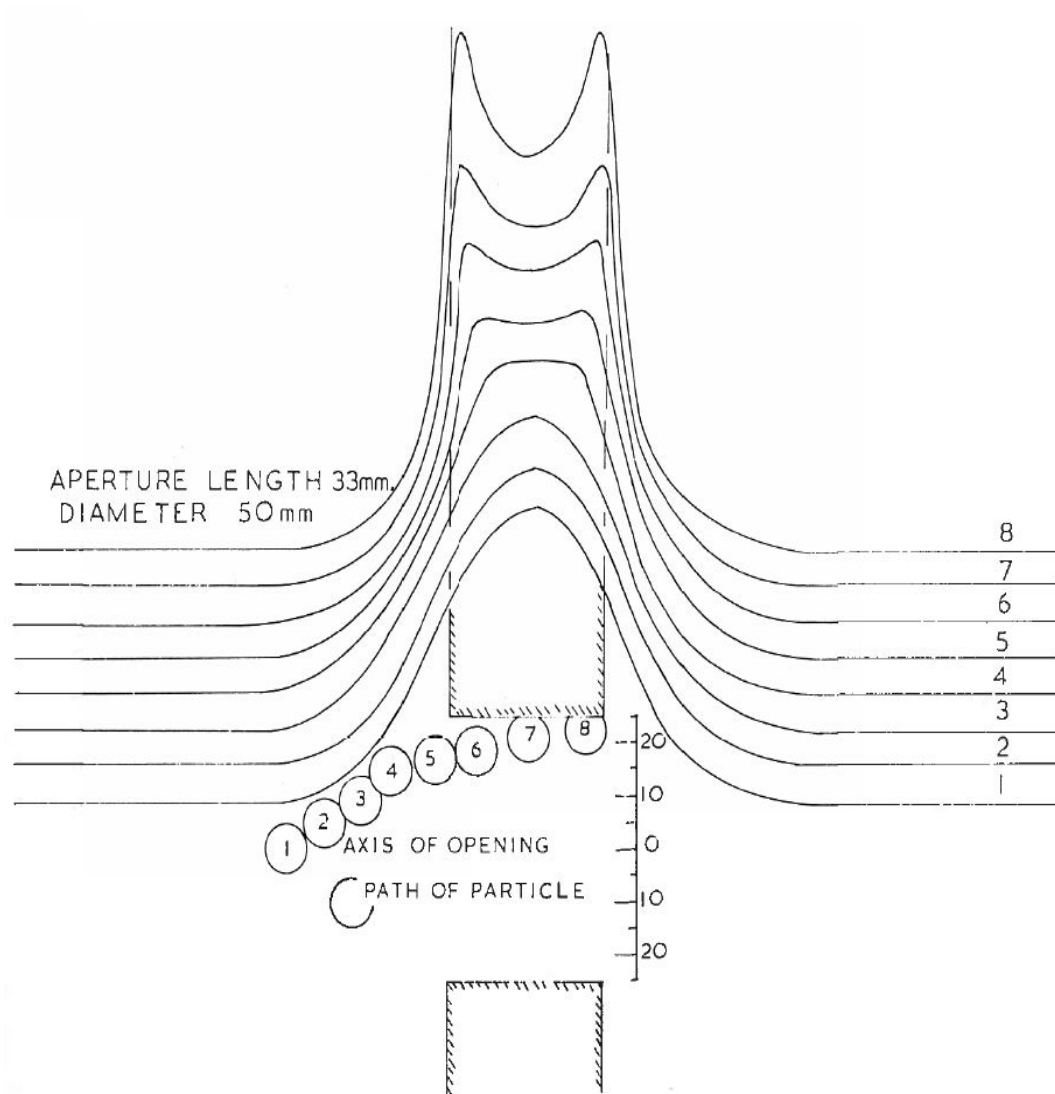


Figure 5.16 Diagram demonstrating the different shapes of resistance pulses generated by different paths of a particle through a channel. Taken from Allen [212], based upon results produced by Thom *et al.* [228].

In order to avoid the oversizing of particles in the calibration experimentation, it was assumed that any resistance change above a threshold of $5000\ \Omega$ (for $25\ \mu\text{m}$ \varnothing spheres through a $40\ \mu\text{m}$ \varnothing channel) was due the coincidence or particle position phenomena. The corrected data from the calibration experiments performed at a variety of pressure differentials will now be considered.

Chapter 5: Bubble populations

Figure 5.17 shows a contour plot representation of a collection of histograms (such as displayed in Figure 5.14) recorded at a variety of pressure differentials. In each individual experiment, a minimum of 100 resistance transients were collected, and the event frequency was normalised to the total number. A plot of the average of the resistance changes in each histogram set (at each pressure) is shown (●) with the errors bars indicating the standard deviation in this data set.

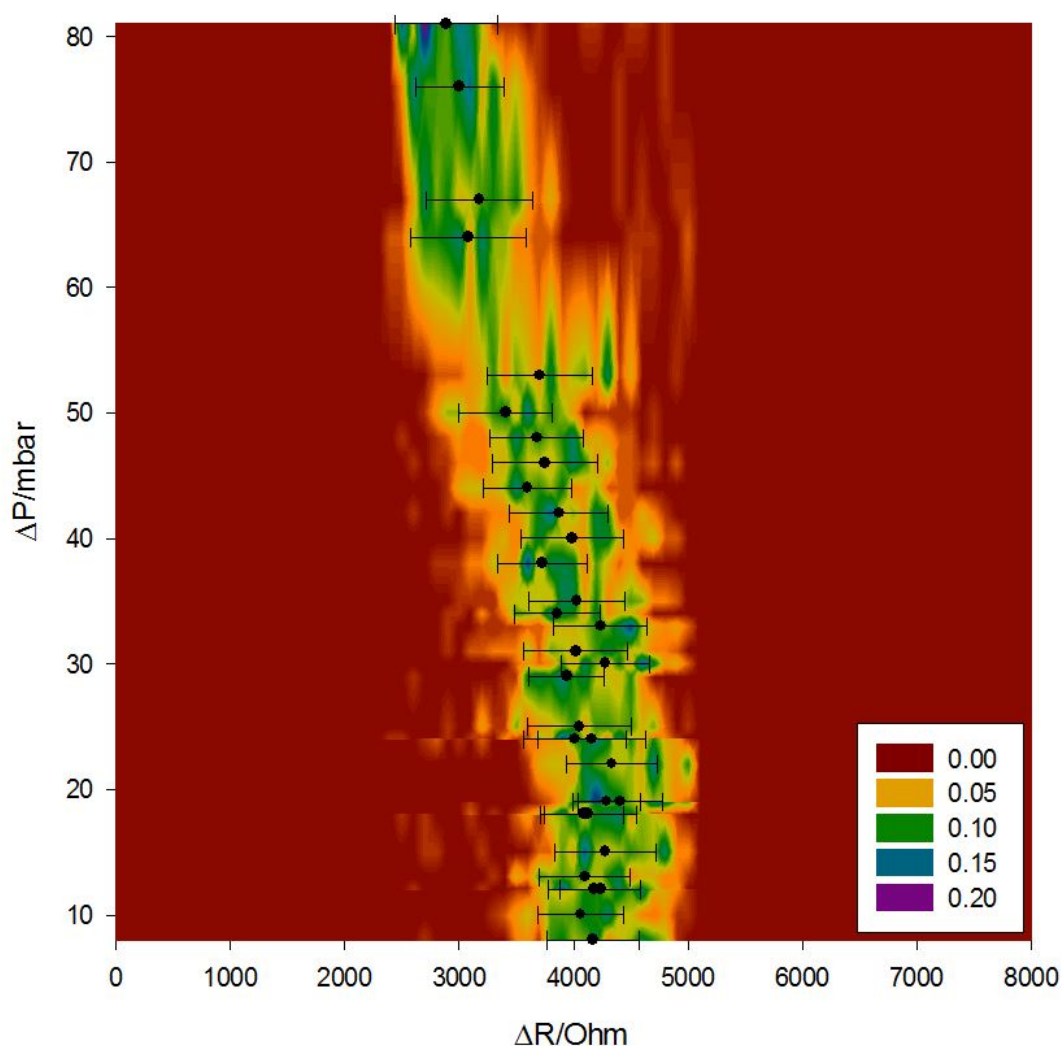


Figure 5.17 Contour plot (coloured) showing the normalised histogram distribution of resistance pulse magnitudes for 25 μm diameter polystyrene spheres translocating a 40 μm diameter channel filled with 0.1 M NaOH at varied pressure differences. The average temperature was 25.3 $^{\circ}\text{C}$. The coloured contour map represents the normalised frequency for each bin of width 100 Ω . A plot showing the average resistance pulse magnitude at each pressure is overlain. The error bars shown are the standard deviation for each data set. A peak-finding routine was used to identify the pulses recorded via a data acquisition card at a sample rate of 50 kHz at a 99 % threshold of *ca.* 260 kohms.

The contour plot demonstrates that the Gaussian-type distribution (normal) is evident at the majority of pressures measured. However the mode position of the distribution is only similar for pressure differentials from 8 mbar to *ca.* 30 mbar. At

larger pressure differentials, the distribution and average resistance change values shift to lower values. This is attributed to equipment limitations. Particles will travel through the channel more quickly at larger pressure drops as a result of increased fluid velocity [229]. This will place increasing strain on the measurement electronics as it must be able to respond to the resistance transients appropriately. Clearly at pressure differences above *ca.* 30 mbar this is limiting. Supporting data can be found by examination of the application note for the optocoupler, presented in Figure 5.18 [167], where the limiting nature of the electronic response can be inspected in more detail. The rectangular data points with the black line (left axis) in the figure demonstrate that the amplitude response of the optocoupler (IL300) decreases significantly with increasing frequency above *ca.* 10^4 Hz. A small decrease in the response is seen at frequencies lower than this, however this is insignificant compared to the ‘3 dB level’ which is the industry standard for quoting the non-limiting frequency bandwidth. The black irregular data points (black right axis) show that the phase response is also dependant on the signal frequency, above *ca.* 10^3 Hertz.

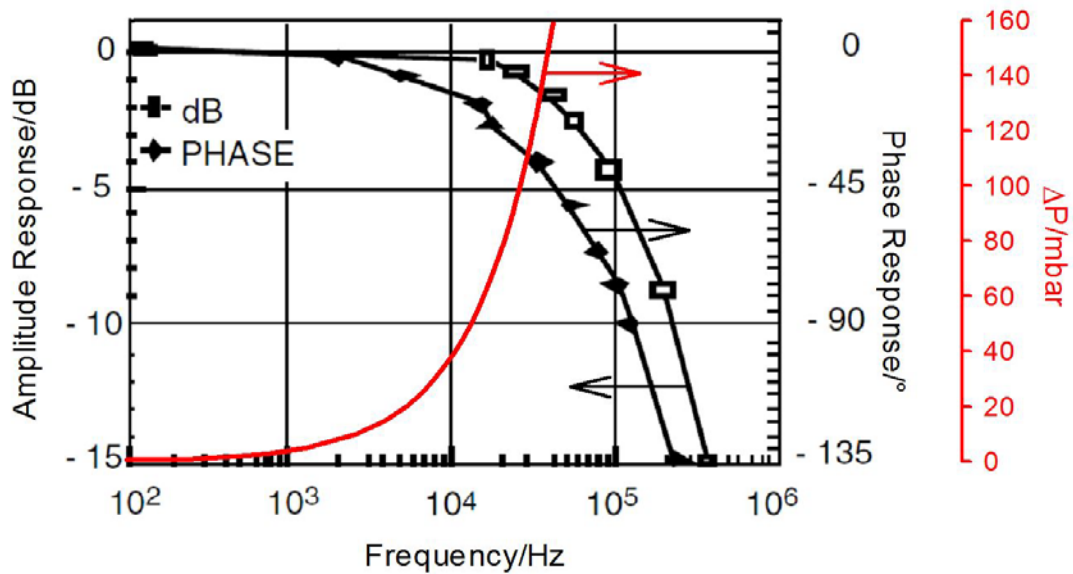


Figure 5.18 Plot of the amplitude response (rectangular points, black line —, left axis) and phase response (irregular points, black line —, black right axis) for varied frequencies, of the IL300 optocoupler used in the Coulter experimentation. The data was extracted from the application notes for the optocoupler [167]. The red line (—, red right axis) demonstrates the theoretical frequency response of particle translocation through a channel (same dimensions as in Figure 5.17 experimentation) produced from varied applied pressure differences. The frequency is plotted on a logarithmic scale.

The overlaid red line (—) shows an estimate of the effective frequency of a signal produced from a sphere passing through a channel at varying pressure differences. This was calculated using the Hagen-Poiseuille equation [229], which relates the

Chapter 5: Bubble populations

fluid flow rate to the pressure drop across the channel. This relationship is shown in eq. (5-13) where ΔP is the pressure difference across the channel (Pa), L is the channel length (m), r is the channel radius (m), Q is the volumetric flow rate ($\text{m}^3 \text{s}^{-1}$) and μ is the kinematic viscosity (Pa s).

$$\Delta P = \frac{8\mu L Q}{\pi r^4} \quad (5-14)$$

This formula (with estimates of L from imaging of the μ -channel) allows for Q and hence the translocation time of the particle to be obtained. The inverse of the translocation time is used to obtain the effective frequency (obtained assuming that the particle travels at the same rate as the liquid flow) for a particle resistance transient. The calculation was performed using the same channel dimensions as those used to conduct the experiments shown in Figure 5.17 (40 μm diameter, 150 μm length) and with a kinematic viscosity value of $1.027 \times 10^{-3} \text{ Pa.s}$, taken from the literature [230].

As discussed, the optocoupler is limiting at frequencies above 10's kHz. Figure 5.18 shows that in order to produce a flow rate fast enough to yield a signal frequency of this order, a pressure drop of *ca.* $> 35 \text{ mbar}$ is required. Consultation of the experimental results (Figure 5.17) shows that this is very similar to the pressure difference at which a decrease in the magnitude of the resistance pulses for the polystyrene particles was observed. It is therefore vital that the applied pressure difference stays within this boundary limit to ensure that the equipment response was not limiting.

The averaged results from the experiments in which the equipment was not limiting ($\Delta P < 30 \text{ mbar}$) are presented below in Figure 5.19 (grey bars). This histogram is a combination of the histograms presented in Figure 5.17 (before normalisation), from the experiments conducted with a pressure difference of less than 30 mbar. The combined histogram is normalised to the total number across the set. A Gaussian fit to the data yielded a peak of 4266.2 ohms with a standard deviation of 437.0 ohms, with a peak height of 8.76 %. This fit is not shown in the figure.

The lines on the plot show the predicted distribution of resistance change for each correction method, discussed in section 5.1.1. For each calculation, the distribution of particle diameters was obtained by utilising the 'NORM.DIST' function in

Microsoft Excel, which returns the normal distribution for a specified mean and standard deviation. These were obtained from the supplementary data included with the Polybead Microspheres, which gave a mean diameter of $24.9\ \mu\text{m}$ with a standard deviation of $0.77\ \mu\text{m}$. These values were then used to calculate the expected resistance change for the calibration experiment.

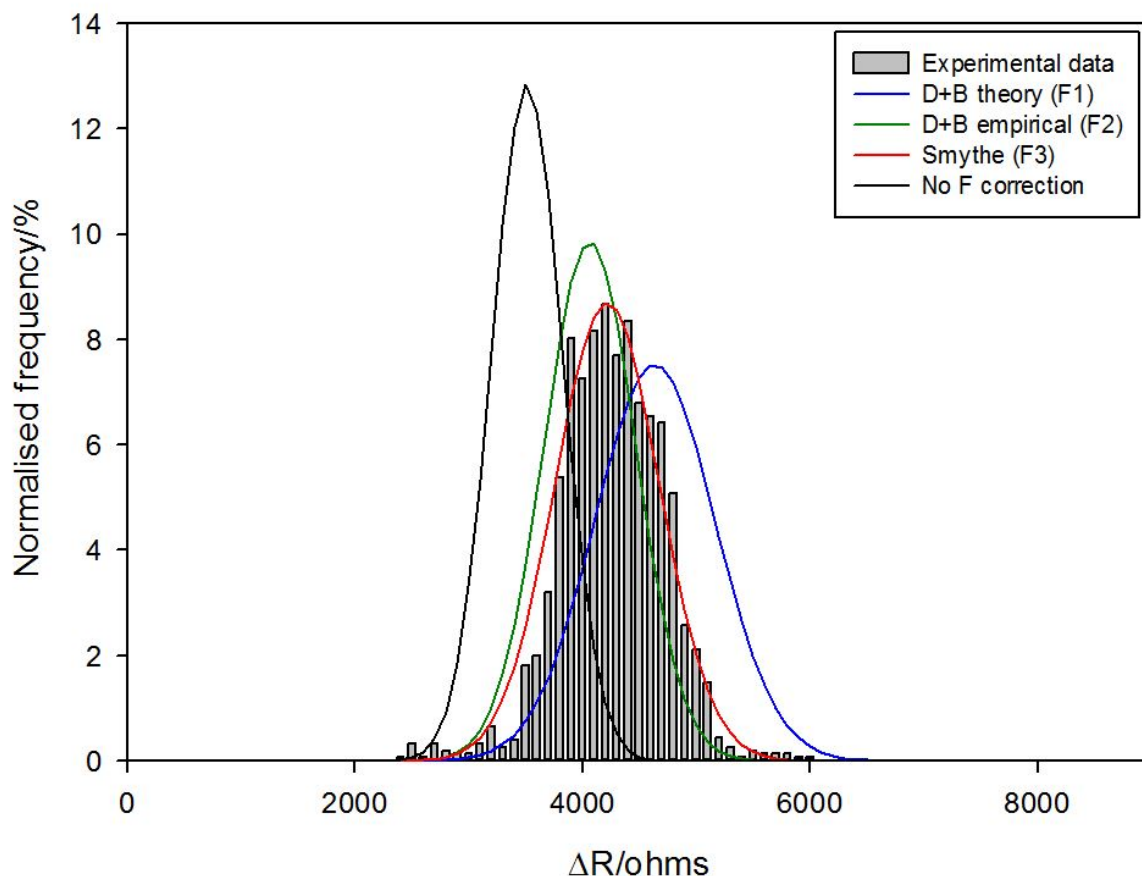


Figure 5.19 Histogram (grey bars, \equiv) showing the normalised distribution of measured resistance pulse magnitudes for $25\ \mu\text{m}$ diameter polystyrene spheres translocating a $40\ \mu\text{m}$ diameter channel filled with $0.1\ \text{M NaOH}$ at varied pressure differences below $30\ \text{mbar}$ (selected data from Figure 5.17). The temperature was $25.3\ ^\circ\text{C}$. The bin width was set at $100\ \text{ohm}$. A Gaussian fit (not shown) on the data yielded a peak of $4266.2\ \text{ohms}$ with a standard deviation of $437.0\ \text{ohms}$. The coloured lines show the predicted distribution of resistance pulse magnitudes expected from a normal distribution of particles with $\mu = 24.9$ and $\sigma = 0.77$, according to the different correction factor methods explained in 5.1.1., where the black line (—) is without any F correction, the blue line (—) with the F1 correction, the green line (—) with the F2 correction and the red line (—) with the F3 correction.

Clearly some of the calculated distributions are relatively varied, centred on peaks of 3512 , 4636 , 4065 and $4217\ \text{ohms}$ for the calculation with no F correction, and correction factors F1 to F3 respectively. There is also variation in the spread of each distribution, demonstrated by the difference in standard deviations. These are

Chapter 5: Bubble populations

311, 405, 530 and 459 Ohms for no F correction and F1 to F3 respectively. Clearly the F3 (Smythe) correction factor produces a distribution which is most similar to the distribution of resistance changes measured experimentally, in every way. The distribution centre, standard deviation and height of 4217 ohms, 459 ohms and 8.70 % are all very close to the experimentally measured resistance change values of 4266 ohms, 437 ohms and 8.76 %.

Further comparison of the correction functions can be made by converting the peak of the Gaussian fit of the experimental data (peak = 4266 ohms, not shown in Figure 5.19) to a calculated particle diameter using each method. This is presented in Figure 5.20, which is a rescaled version of the plot presented in Figure 5.2 on page 121. Again this shows that the Smythe correction function is best suited, being the only method to predict the 24.9 μm diameter from the resistance change, comfortably within the 95 % confidence limits. The other points show that without F correction then the resulting particle diameter is an overestimate; the D+B theoretical based method produces a diameter that is an underestimate and the D+B empirically-based function is an overestimate.

From the results presented thus far, clearly the F3 correction function derived by Smythe is best suited to calculate the diameters of 25 μm polystyrene particles using a 40 μm diameter channel. However, further calibration is needed to ensure that the function is valid for different sizes of spheres and channels. In addition further calibration is needed to confirm that the theory holds for bubbles as well as polystyrene particles. This will be discussed in the next section where the sizes of bubbles are ascertained via imaging and compared to the theoretical value calculated from the resistance change via the Smythe (F3) function.

It is important to note that in order to process the diameter calculations for large arrays of resistance changes, as acquired in the next section, a less computationally intensive method was needed. This was achieved using a polynomial fit of the theoretical relationship between the predicted diameter and resistance change. Figure 5.21 demonstrates the fits performed for the Smythe correction factor calculations for different channel sizes. This method does not introduce significant error as the regressions are very accurate fits to the data (all R^2 values > 0.999). Figure 5.22 shows the sensitivity required for each channel diameter for reference. In each case *ca.* 1 % change in the signal equates to a particle of *ca.* 50 % of the

channel diameter.

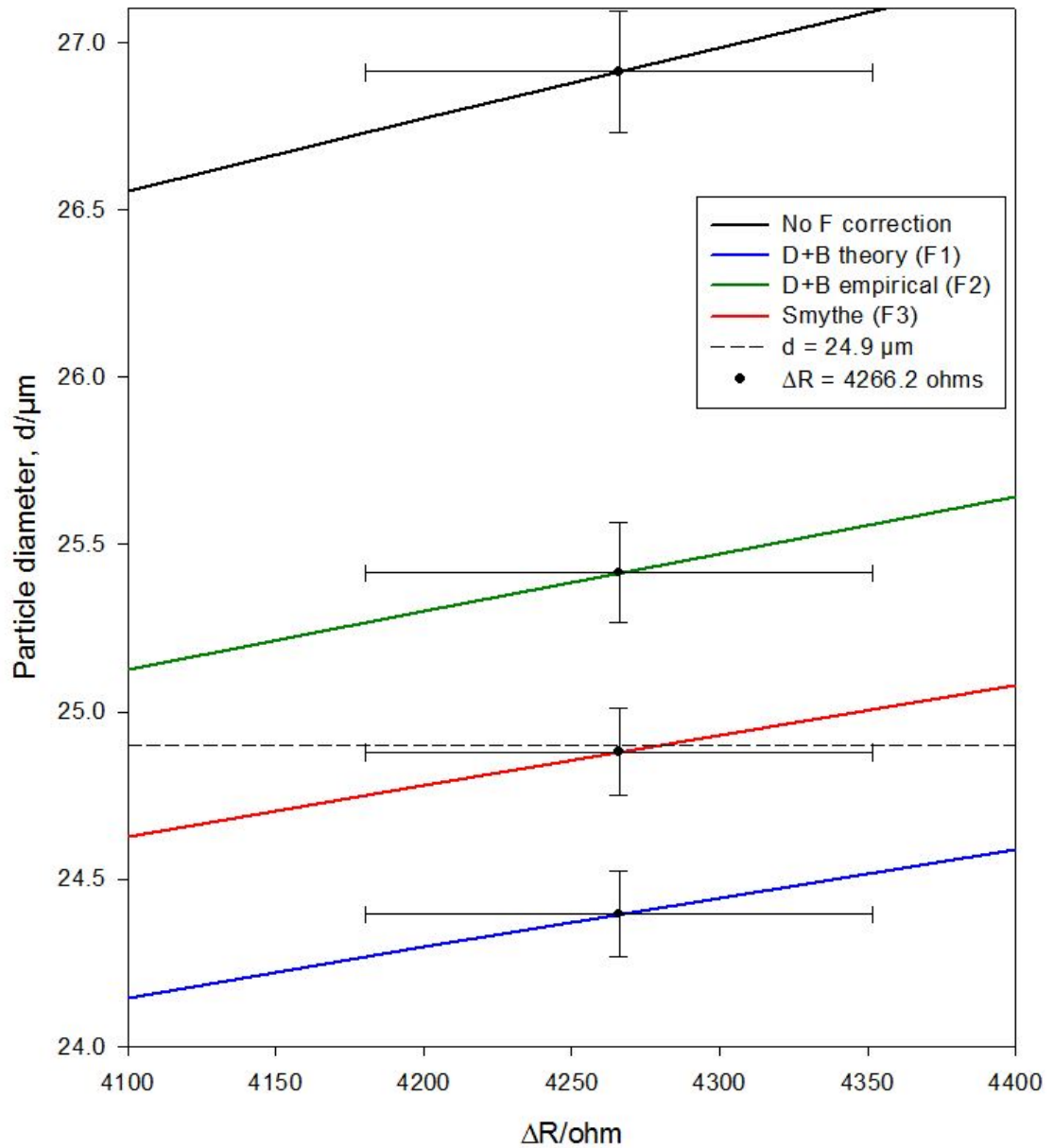


Figure 5.20 Plot demonstrating the relationship between the resistance change (ΔR) and the corresponding calculated particle diameter for a 40 μm diameter channel, with and without correction functions. This is a rescaled version of Figure 5.2 on page 121. The black line (—) shows the response without any correction function applied, the blue line (—) with the F1 correction, the green line (—) with the F2 correction and the red line (—) from the F3 correction. The horizontal dashed line highlights the diameter of the polystyrene particles ($d = 24.9 \mu\text{m}$). The black data points (•) are the corresponding calculated particle diameters at 4266 ohms for each correction factor. The horizontal error bars represent the 95 % confidence in the resistance values and the vertical error bars are the corresponding 95 % confidence in the diameter.

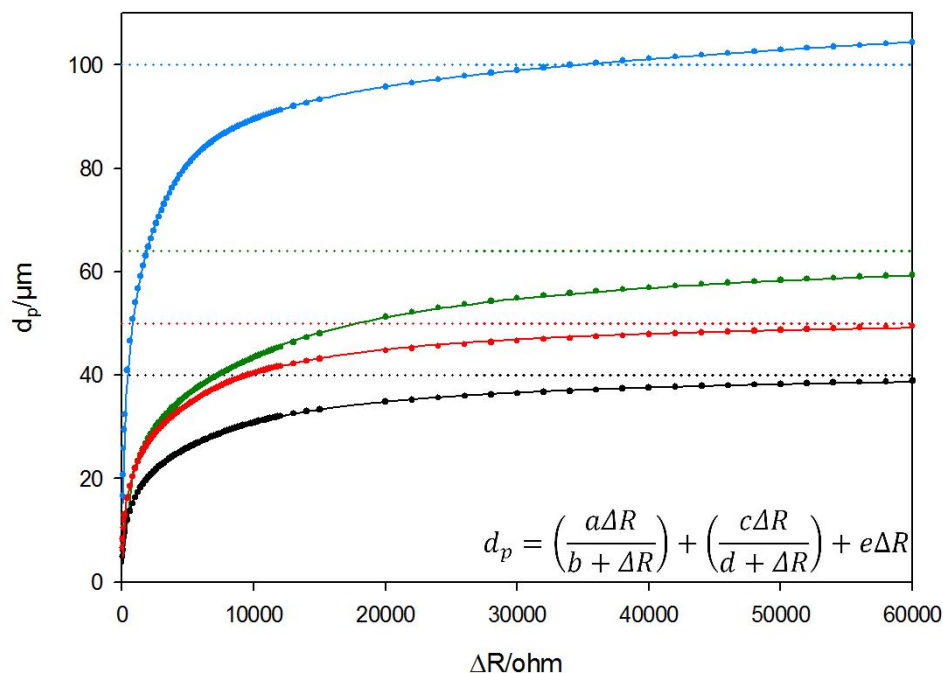


Figure 5.21 Plot showing the predicted particle diameters calculated from hypothetical resistance changes using the F3 Smythe correction function ([223, 225] equation 5-15) for channel diameters of 40 μm (●), 50 μm (●), 64 μm (●) and 100 μm (●). The solid lines are regressions based upon a hyperbolic functions (calculated by SigmaPlot 12.5), given in the form of the equation displayed on the plot, for the 40 μm (—), 50 μm (—), 64 μm (—) and 100 μm (—) diameter channels. The values of the coefficients are given in appendix 7 and the R^2 values are all > 0.999 . The dotted lines highlight the diameter of the channel in each case.

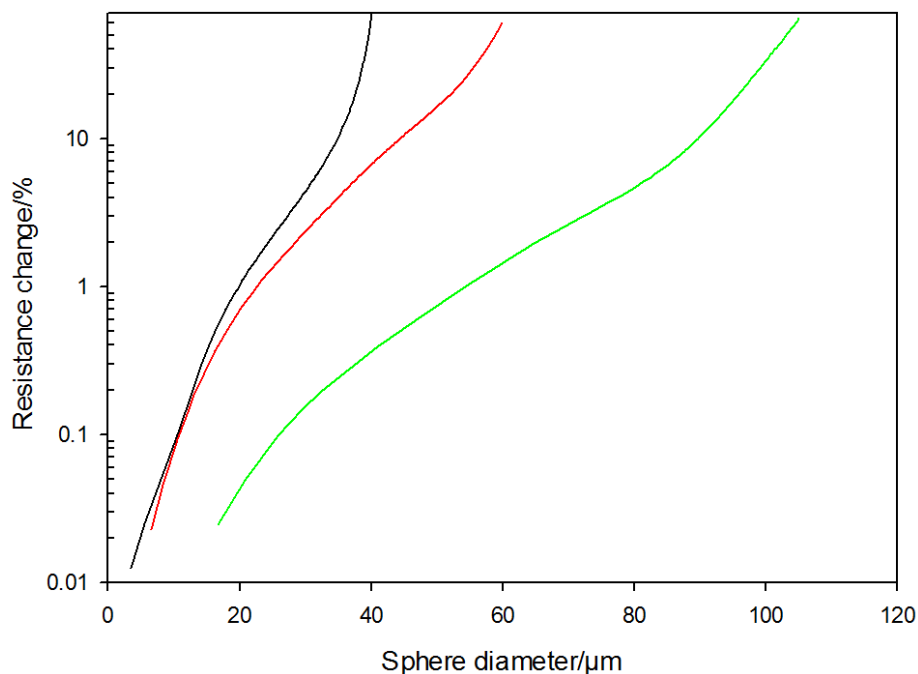


Figure 5.22 Plot showing the sensitivity of the resistance measurement compared to the background level (determined experimentally) with varied sphere diameter for a 40 μm (—), 64 μm (—) and 100 μm (—) diameter channel according to the Smythe correction method of calculation. The relative resistance change is plotted on a logarithmic scale.

5.1.3.3 Bubble calibration

In order to calibrate the response of the Coulter counter system for bubbles, it was necessary to determine the sizes of bubbles via another method. This was achieved via high-speed imaging through the flat window of the flow cell as briefly described in section 5.1.2.2.. Capturing images via this method avoided refraction problems associated with the curved surface of the main reservoir. The flow cell was positioned as shown in the dotted blue box (— —) in Figure 5.23 below, which shows a schematic of the experimental setup. The electrolysis cell described in section 2.1.2 was used to generate gas bubbles electrochemically in a looped flow system similar to that utilised in chapter 4.

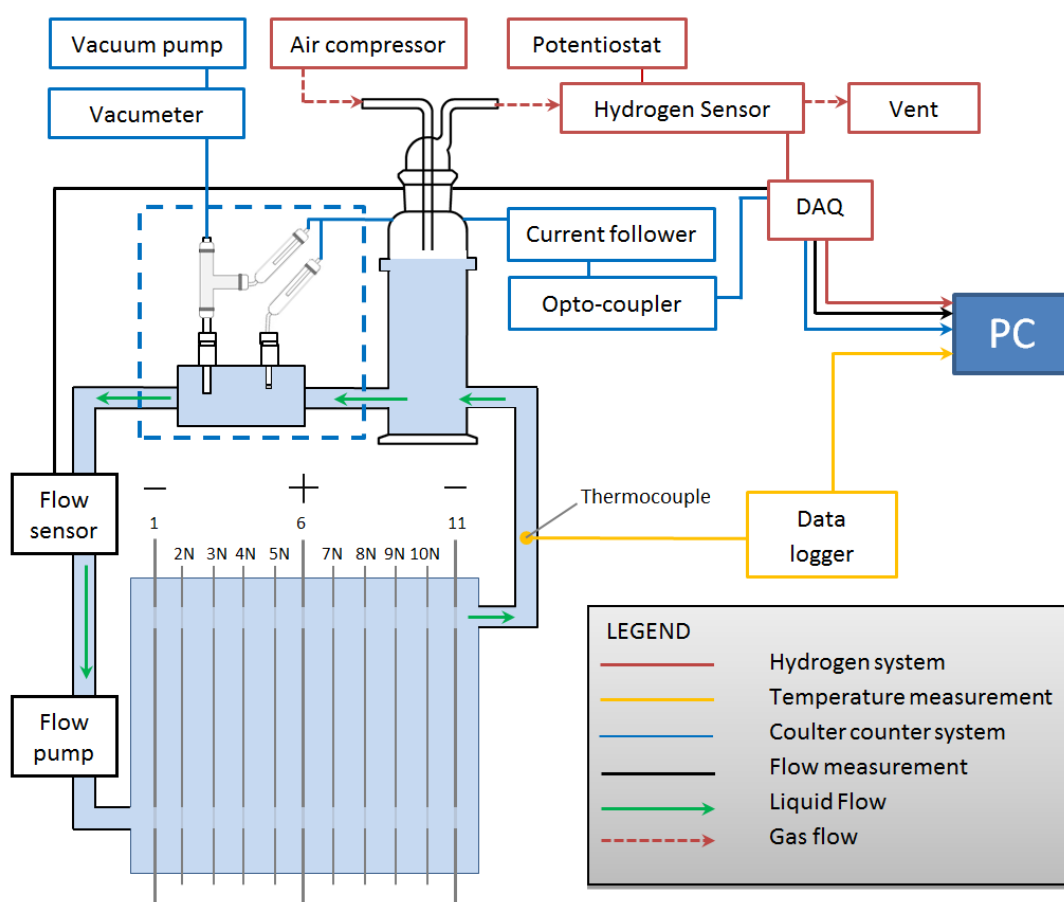


Figure 5.23 Schematic of experimental setup used in the Coulter counter experiments aimed at determining the sizes of bubbles generated by the electrolysis cell. The electrolyte was 0.1 M NaOH in all experiments.

The flow cell was constructed from two glass slides separated by double-sided foam tape, sealed with epoxy resin. The inlet and outlet were fashioned from 5 cm³ plastic pipette tips cut to size to fit the appropriate connecting tubes and sealed in place with more epoxy. Two glass tubes were also set into the top of the cell to

Chapter 5: Bubble populations

provide easy application of the μ -channel and MMO reference electrode, via suba-seals punched with appropriately sized holes.

For bubble generation in the calibration experiments, the electrolysis cell was operated at *ca.* 200 mA (ISO-TECH IPS-1820D power supply) for varying lengths of time (between 20 and 200 seconds) with the liquid (0.1 M NaOH) flowing at *ca.* 1 dm³ min⁻¹ (HAILEA HX8810 liquid pump) through the system. An air flow of *ca.* 400 cm³ min⁻¹ (Clarke Wiz air pump) was used to remove H₂/O₂ released from the main reservoir. However during experimentation the flow rate through the flow cell was too fast to enable bubbles to be drawn up by the liquid flow through the μ -channels. Hence the liquid flow was switched off *ca.* 1 second before acquisition of the data. As for the particle calibration experimentation, MMO electrodes were positioned either side of the μ -channel using the glass T-piece and a potential of *ca.* 340 mV was applied, measured with a voltmeter in each experiment. The current was measured using the previously described battery powered current follower/opto-isolated system and monitored using an oscilloscope (Owon SDS-7102V) at a sample rate of 1 M S/s for 1 second. Bubbles were drawn through the channel by the pressure difference applied across the channel, which was always < 30 mbar in order to avoid limitation by the optocoupler. The temperature was recorded using a K-type thermocouple and recorded using a datalogger (Pico TC-08). Three different sizes of μ -channel were employed (\varnothing = 40, 64, 100 μ m) for the measurement of the current change during the translocation of bubbles. The exact experimental conditions are specified in Table 5-1 and with each individual experiment discussion/results.

Channel \varnothing / μ m	Potential /mV	P _{atm} /mbar	P _{app} /mbar	Δ P /mbar	Temp. /°C	Camera frame rate /fps	Image calibration / μ m.pixel ⁻¹
40	349.3	999	971	28	25.19	37500	2.603
64	346.4	1002	980	22	20.80	37500	5.064
100	193.4	979	952	952	24.31	28000	5.071

Table 5-1 Experimental conditions of bubble calibration and imaging

Imaging of the bubble translocations was achieved using a high-speed camera (Photron APX-RS) recording at between 28000 to 37500 fps with an exposure time set as the reciprocal of the frame rate. A white LED array was used to backlight the cell in order to view the bubbles and channel at such short exposure times. A

trigger pulse was used to initiate the camera recording (centre triggered) whilst the second channel on the oscilloscope monitored the trigger signal to provide a reference time for the current data with respect to the imaging. After each experiment an image of a 100 μm wire placed in the cell without altering the optics was captured to provide a calibration value in microns/pixel which can be applied to calculate the size of the bubbles.

5.1.3.3.1 Bubble translocation example

Imaging and resistance transient examples of a bubble translocation through a μ -channel ($\varnothing = 64 \mu\text{m}$) are presented in Figure 5.24 and Figure 5.25 respectively.

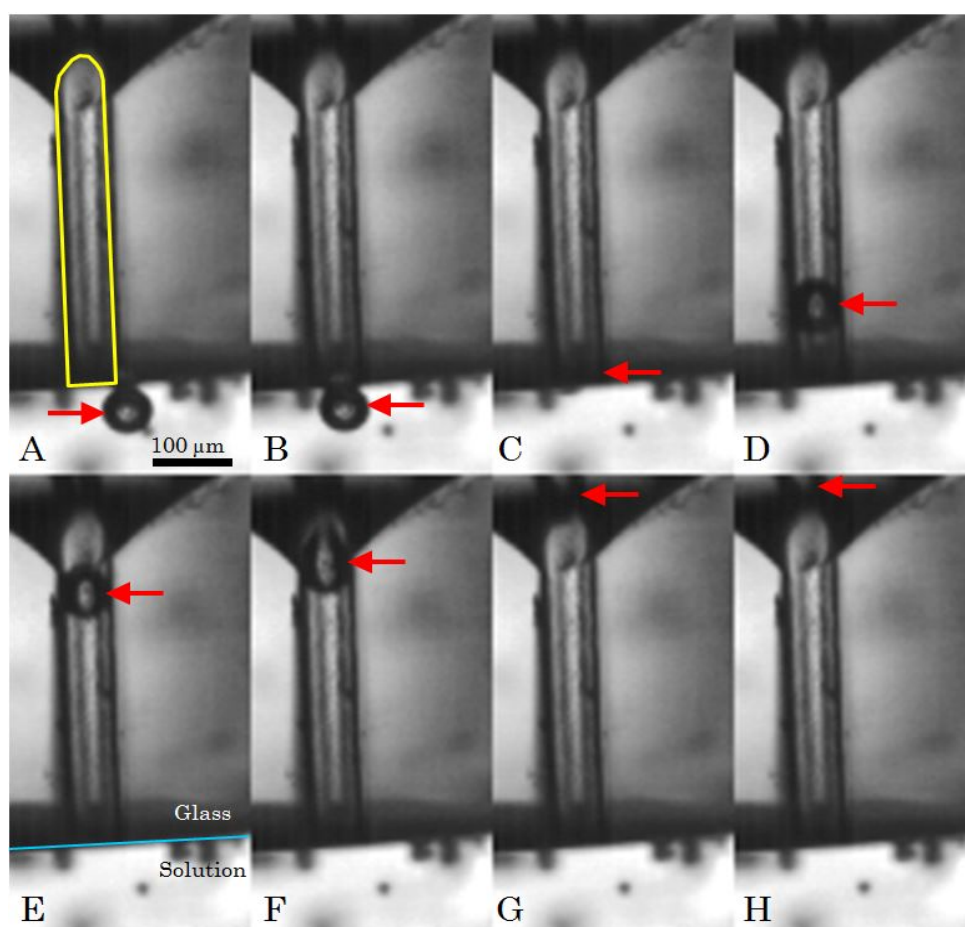
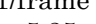
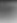



Figure 5.24 Sequential images (A to H) of the translocation of a bubble through a μ -channel ($\varnothing = 64 \mu\text{m}$). Image A highlights the μ -channel (yellow line, ) and a scale bar which is valid for all images in the figure. The boundary between the glass capillary and solution is highlighted by the blue line () in image E. The images were taken at A=684.1 ms, B=684.5 ms, C=684.7 ms, D=685.0 ms, E=685.7 ms, F=685.8 ms, G=686.1 ms and H=686.6 ms. The red arrows () highlight the position of the bubble in each frame. The images were captured at a frame rate of 37500 fps with an exposure time of 1/frame seconds (1/37500 s). The corresponding resistance trace is presented in Figure 5.25 with the image captures times highlighted with the same letters. The dark spots on the surface of the images are static bubbles outside of the focal plane. The pressure difference across the channel was 22 mbar.

Chapter 5: Bubble populations

The same trend seen in the particle calibration experiments was observed for this bubble translocation. Upon entering the sensing area at the mouth of the channel (see A, B) the bubble causes an increase in the resistance, which plateaus once the bubble was fully immersed in the channel. The resistance drops as the bubble exits the channel and returns back to the baseline resistance level as expected. The duration that the bubble is in the sensing area corresponds to the time length of the measured transient, which in this case was below the previously discussed optocoupler limit (10's kHz, see section Figure 5.18).

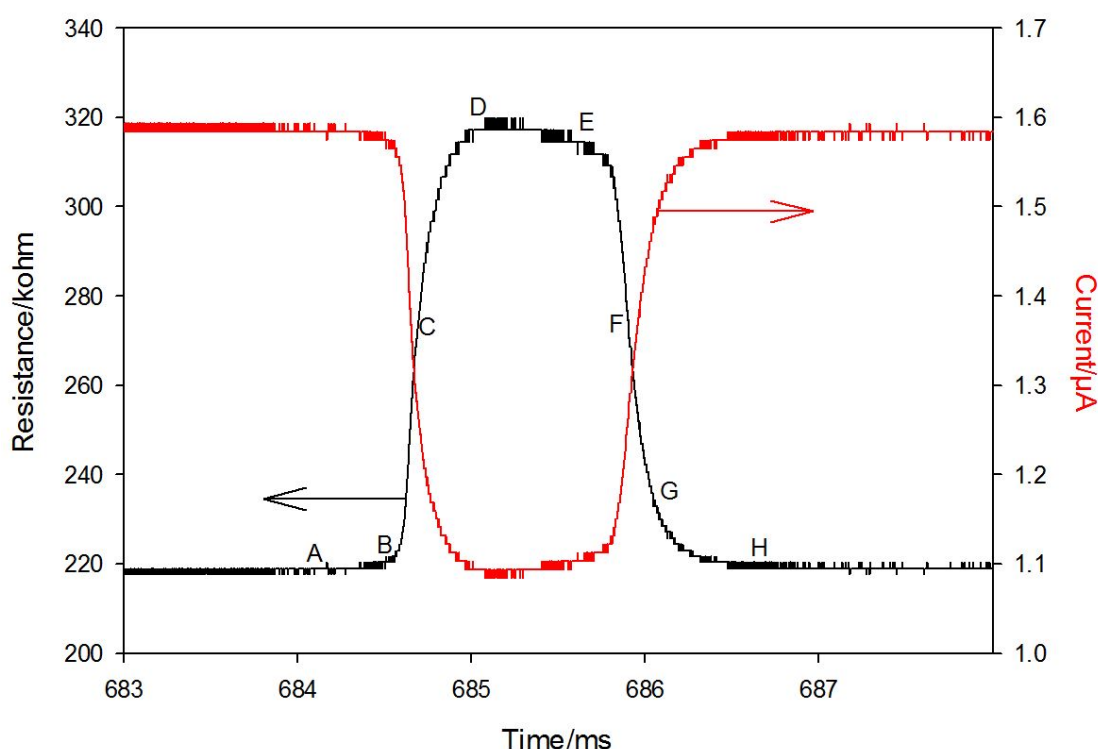


Figure 5.25 Plots of the current (red line, —, right axis) and corresponding resistance change (black line, —, left axis) for the translocation of a bubble through a 64 μm \varnothing channel. The letters A-H on the plot correspond to the times given in Figure 5.24. The applied potential was 346.8 mV and the pressure difference across the channel was 22 mbar. The current was recorded on an oscilloscope at a sample rate of 1 MS/s.

5.1.3.3.2 Multiple bubble translocations

The processes described above were repeated multiple times to obtain images and associated resistance changes for the translocation of many different bubble sizes through three channels of differing diameters. The images were processed using the pixel calibration data to obtain the known bubble sizes. In each case, three measurements of the diameter of the bubble were made using the FASTCAM viewer measurement tool, which measures the number of pixels between two

selected points. The 95 % error in the three measurements was calculated for all assessed bubbles.

The associated current-time traces were gain adjusted from the voltage/time recorded on the oscilloscope to determine the magnitude and time of each transient relative to the background level and trigger signal respectively. The Smythe F correction method approximation (Figure 5.21) was then applied to calculate the predicted bubble diameter for each channel diameter.

Figure 5.26 demonstrates the correlation between the predicted and measured bubble diameters for all three sizes of channels used. The plot shows that all of the bubbles measured using the 40 μm and 64 μm diameter channels that are smaller than the respective channels are accurately predicted within the 95 % confidence limits. This is highlighted by the dashed lines on the graph, where all of the red points below the red dashed line and all of the black points below the black dashed line are on the 1:1 perfect prediction line. The bubbles that were photographically measured to be greater than the size of the channel (all those with blue error bars) are not correctly predicted by the theory. This is as expected because the theory only takes into account bubbles which are smaller than the size of the channel and hence these can be disregarded. The observations suggest that any bubble larger than the channel will still produce a calculated diameter of *ca.* 40 μm , even if the bubble is 10 's of microns larger than this.

Unfortunately nearly all of the bubbles measured using the 100 μm diameter channel were larger than the size of the channel. Three of the four bubbles which were smaller than the channel (green data points below the green dashed line) show a successful prediction of the diameter from the resistance change, within the 95 % confidence. The fourth is not correctly predicted by the theory. Clearly a larger sample size is needed in order to draw more certain conclusions about the 100 μm diameter channel experiments.

In summary, the bubble calibration experiments have shown that the resistance changes produced from the translocation of bubbles through 40 μm and 64 μm diameter channels can be used to calculate the bubble diameters within 95 % confidence levels, according to the Smythe F3 correction method. Unfortunately, it was not possible to validate the results obtained for the 100 μm \emptyset channel. Clearly further experiments are needed with this particular system.

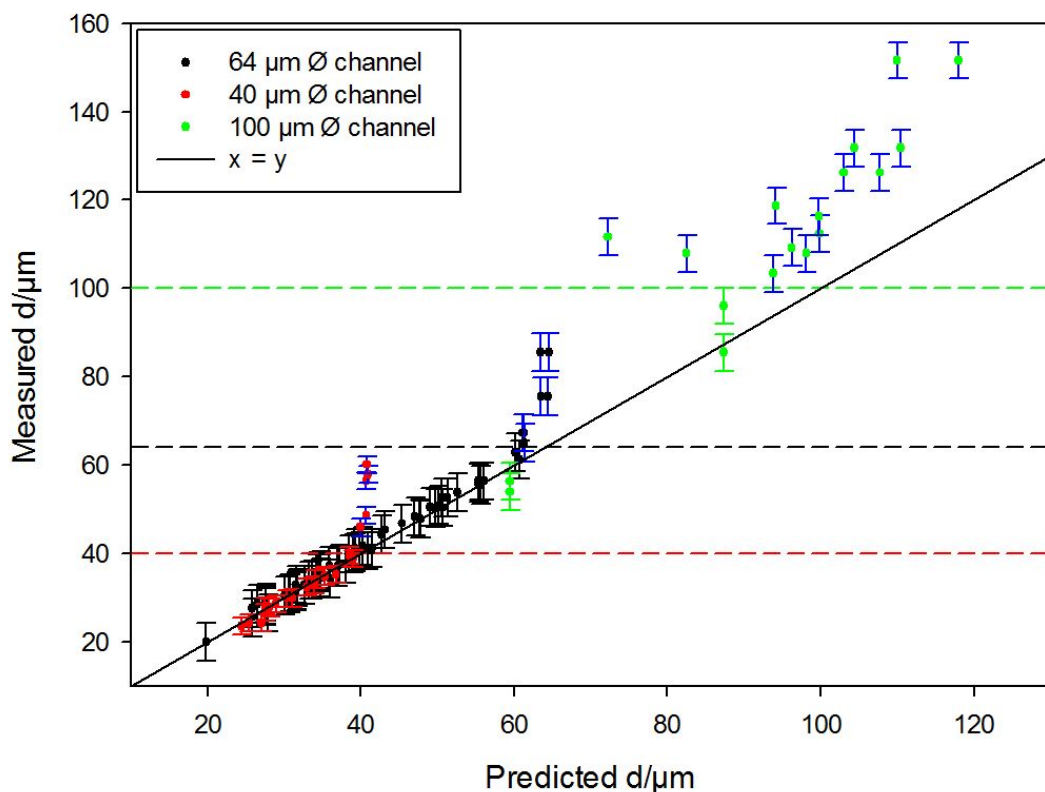


Figure 5.26 Plot showing the correlation between the bubble diameters calculated using the measured resistance change via the Smythe correction factor (predicted) and the bubble diameters measured via imaging techniques. The red data points (●) are the experiments conducted with a 40 μm diameter channel, the black (●) with a 64 μm diameter channel and the green (●) with a 100 μm diameter channel. The error bars are the maximum 95% confidence values in the measured sizes for each magnification. The error bar colours are the same as the data points for bubbles diameters measured to be smaller than the channel. Bubbles larger than the channel are highlighted with blue (—) error bars. The dashed lines highlight the size of the channel in each case following the same data point colour scheme. The solid black line (—) shows a 1:1 relationship between the predicted and measured diameters. The calibrations for the bubble sizing via imaging were 2.6028, 5.0642, and 5.0714 μm/pixel for the 40, 64 and 100 μm diameter channels respectively.

5.1.4 Measurement of the bubble size distribution

The same experimental system employed for the measurement of the resistance across the μ -channels in the calibration experiments was used for assessing the bubble population directly in the Dreschel reservoir. In the experiments discussed in this section, the μ -channels were positioned through an SQ-13 threaded port at the top of the vessel. The glass t-piece (holding one MMO electrode) connected the channel and vacuum pump. The other MMO electrode was secured through the second SQ-13 threaded port at the top of the reservoir.

The opto-isolated current follower system was employed, sampled with a USB DAQ (Cole Parmer 18200-20). In-house written software (appendix 11: Tcounter.vbp) was used to interface the acquisition card and find peaks below a pre-set threshold. This was set between 99 and 99.6 % of the background level, varying dependant on electrical noise limitations. The exact level is detailed in the appropriate figure legend. The current was sampled at 50 kHz for periods of 1 s in duration, with each period separated by *ca.* 0.75 s. This gap between sample periods allowed the program to run the peak finding routine, which provided the dynamic acquisition of a large number of peak magnitude values without the need to save and post-process large data files.

The electrolysis cell was operated set in constant current mode (*ca.* 200 mA) with forced liquid flow, positioned as shown in Figure 5.23. Air was pumped a compressor (Clarke Wiz Air) through the headspace of the reservoir to evacuate the released gases from the system. The atmospheric and applied pressure differentials were measured with the vacuometer while the liquid temperature measured using a thermocouple (K-type) and data logger (Pico TC-08).

At the start of each experiment a constant pressure differential across the μ -channel was applied and the liquid flow rate, air flow rate, temperature, background current level and potential difference across the MMO electrodes recorded. The data acquisition and electrolysis cell were initiated simultaneously. The current passing through the electrolysis cell was monitored using a DVM. Data sampling of the transients was looped (1 s duration) until between 500 and 2000 peaks had been counted in total. Three different sizes of μ -channel were employed ($\varnothing = 40, 64, 100\mu\text{m}$) in the experiments. The Smythe (F3) correction function was used in the calculation of the bubble diameters.

Chapter 5: Bubble populations

5.1.4.1 Results

Figure 5.27 shows a typical example of a 1 s window snapshot of the current-time history recorded as bubbles translocated a 40 μm diameter channel.

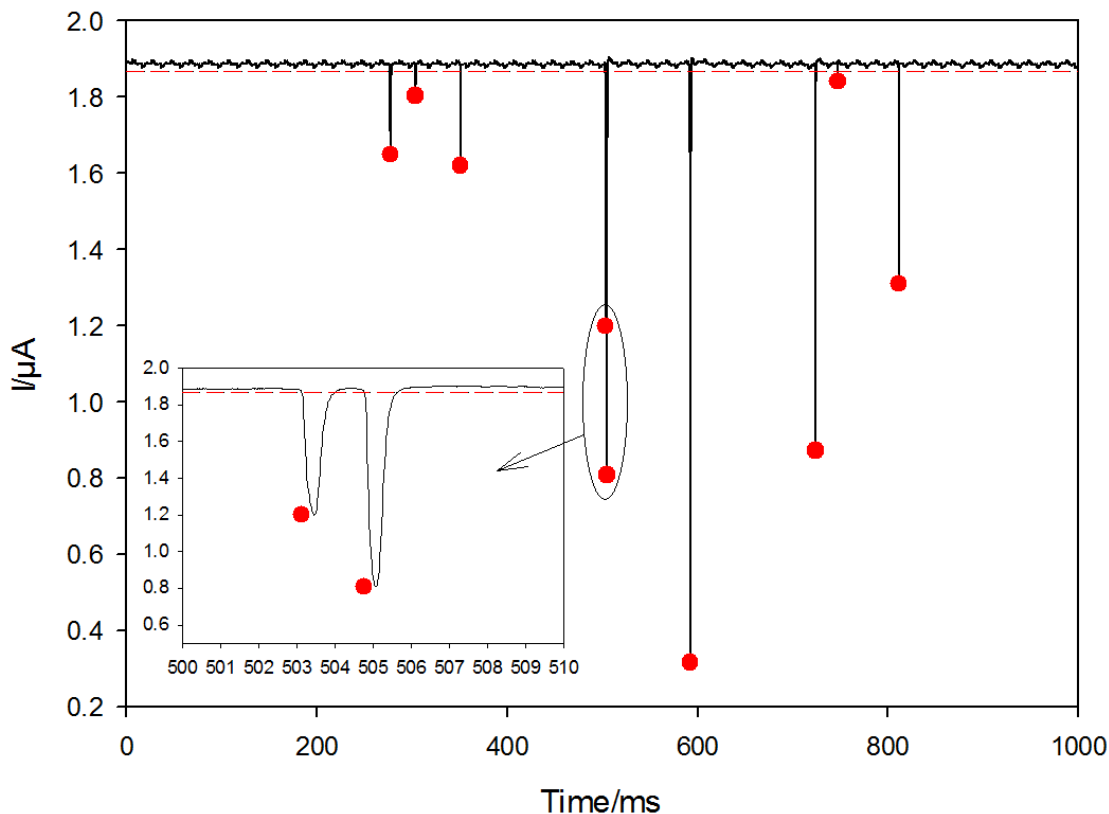


Figure 5.27 Plot showing a typical example of a 1 s window snapshot of the current-time (–) history measured as bubbles translocated a 40 μm diameter channel. The peaks found by the program algorithm (•) highlight the minimum current in each transient. The algorithm was written to consider events at a minimum time spacing of 1.5 ms. The pressure differential was 23 mbar. The potential difference across the channel was 338 mV *vs.* MMO. The temperature was 25.61 $^{\circ}\text{C}$. The threshold (– –) for the peak finding routine was set at 99 %.

The plot shows that the peak-finding algorithm correctly identifies the minimum current level in each transient. The peaks found in each 1 s window were saved and the current-time history disregarded. The data presented subsequently is the accumulation of these detected peak levels.

The bubble diameter distributions obtained using the three channels of different diameter are now presented in histogram form with associated discussion and analysis.

5.1.4.1.1 40 μm channel

The histogram presented in Figure 5.28 shows the distribution of bubble diameters calculated from the resistance changes generated by the translocation of bubbles through a 40 μm diameter channel. The bubble diameters measured to be below the size of the channel are represented by the grey bars, which show the normalised frequency on the left y-axis for each bin of 2 μm width. These sizes have been validated according to the previous section and hence correctly represent the sizes of less than 40 % of the 1505 bubbles sampled in the experiment, shown by the cumulative frequency in blue. The bubbles measured to be larger than the channel are represented by the red bar, which corresponds to the right y-axis, which is on a scale that is approximately ten times larger than the left y-axis. The calibration experiments showed that any bubbles that are much larger than the channel will still produce a calculated diameter that is only slightly above 40 μm . Hence bubble sizes represented by the red bar are certainly larger than 40 μm although their exact size cannot be determined with this diameter of μ -channel. The cumulative frequency count shows that the majority of the 1505 bubbles are bigger than the channel and so the distribution of the entire population cannot be determined from this data alone. Furthermore, Figure 5.13 demonstrates that a diameter of 20 μm is the lower limit of sensitivity for a 1 % threshold and bubbles are only detected above this limit. Hence bubbles smaller than this size cannot be measured using this method and would not appear on the distribution. In order to investigate below this range, a smaller channel would provide a greater sensitivity, however as discussed there are associated problems with achieving a liquid flow through such a small aperture.

The bubbles between the limits show a relatively even distribution across the whole of the detectable range. This indicates that *ca.* 40 % of the measured distribution is comprised of an assortment of differently sized bubbles between 20 and 40 μm in diameter with slightly less of the former and more of the latter according to the first and last bars in the middle range.

The other *ca.* 60 % of the sample set is comprised of bubbles with greater diameters which require a channel with a bigger aperture in order to reveal their size. Investigation was hence thereafter focussed on utilising the larger channels, with the aim of discovering the distribution of these\ larger bubbles as well as providing an indication of reproducibility of the distribution. Experiments conducted with a

Chapter 5: Bubble populations

larger channel, in attempts to extend the working range of the measurements, will now be presented.

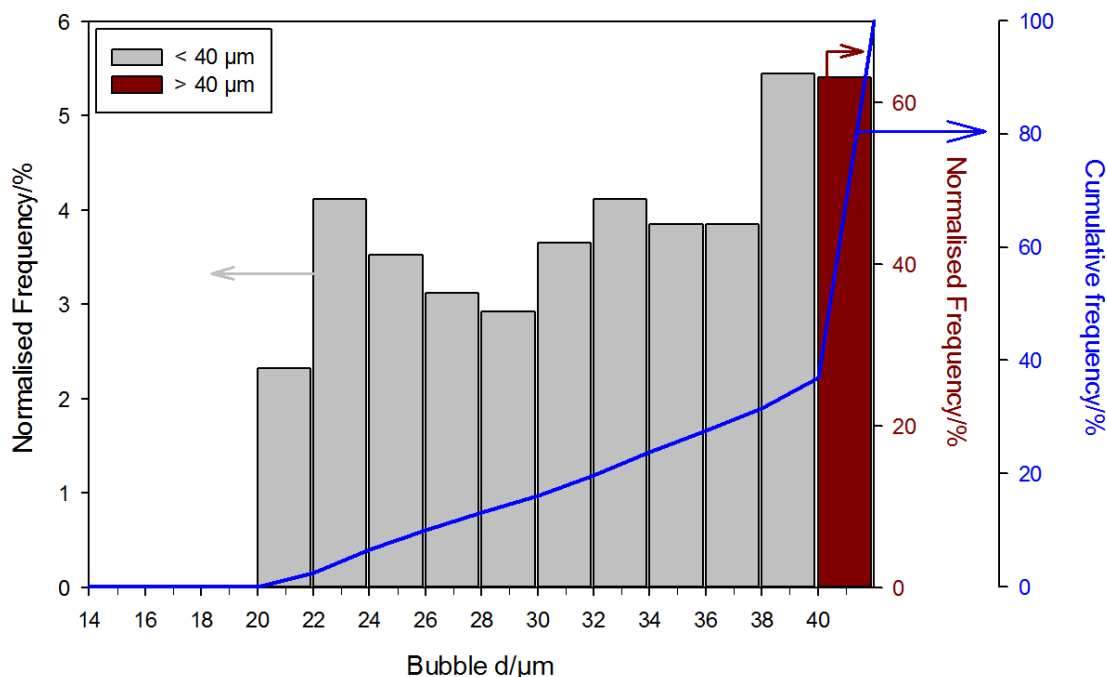


Figure 5.28 Histogram of bubbles diameters calculated from the resistance changes produced by the translocation of bubbles through a 40 μm diameter channel. The grey bars (\square) represent the bubble sizes below 40 μm in diameter and correspond to the left y-axis, and the red bar (\blacksquare) represents the bubbles calculated to be above 40 μm in diameter and corresponds to the right y-axis. The blue line (—) shows the cumulative normalised frequency. The Smythe F3 correction factor was applied in the calculation. The histogram is normalised to the total number of bubbles (1505) and has horizontal bin widths of 2 μm . The pressure difference across the channel was 23 mbar. The potential difference across the channel was 338 mV *vs.* MMO. The current through the electrolysis cell was 196 mA. The liquid flow rate was 1.002 $\text{dm}^3\text{min}^{-1}$ and the air was pumped through the headspace of the Dreschel bottle at 411 $\text{cm}^3\text{min}^{-1}$. The temperature was 25.61 $^\circ\text{C}$. The threshold for the peak finding routine was set at 99 %.

5.1.4.1.2 64 μm channel

Repeat experiments with a 64 μm \varnothing channel were performed. However, consecutive data sets (each with 2000 events) were acquired in order to assess the variation in the distributions as a function of time. Figure 5.29 and Figure 5.30 show the results from these experiments with each plot showing the distribution of 10000 bubbles. Figure 5.29 displays a mesh plot consisting of five consecutive histograms. The first histogram represents 2000 bubbles sampled between 0 and 143 s, highlighted by the horizontal dotted lines. The shaded areas demonstrate the times that were not sampled, whilst the data was being saved. It is important to note that the data shown in between $t = 0$ and 143 s is interpolated by the mesh plot

routine of the program (SigmaPlot 12.5). In the first case this is between a blank histogram plotted at $t = 0$ s and the histogram of the diameters of the first 2000 bubbles plotted at $t = 143$ s. Similarly the data in between each of the other horizontal dotted lines is interpolated, considering the time difference between them. This provides an estimate of the change in distribution between histograms.

A more detailed analysis (Figure 5.32 and Figure 5.33) is made subsequently which examines histograms of smaller sample populations to focus on the distribution progression. It is also important to note that the scale of the normalised frequency axis was chosen so that the distribution of bubbles with diameters below the size of the channel be can inspected in detail. Hence the frequency saturates at some of the points on the mesh above $64\text{ }\mu\text{m}$ and so rescaled versions of the plots are presented in Figure 5.31.

Figure 5.29 demonstrates that once a bubble population is established, there are two more populous regions in the distribution of bubble diameters, excluding those larger than the size of the channel. A consistent band in the 22 to $38\text{ }\mu\text{m}$ diameter region is present at a normalised frequency of between 5 and 8% for each $2\text{ }\mu\text{m}$ bin. This band corresponds to *ca.* 40% of the population, according to the cumulative frequency. This occurs in each of the histograms with an increase in the lower end of this range observed in the final histogram. A consistent band is also seen in the region of 57 to $64\text{ }\mu\text{m}$, at a frequency of 4 to 7% in each bin, and accounting for *ca.* 20% of the total population across the band. There are also some small regions of increased frequency observed at *ca.* 38 to $42\text{ }\mu\text{m}$, however these are not recurrent across the series. In between the two regions of greatest population density, bubbles of 38 to $57\text{ }\mu\text{m}$ in diameter are observed in lower numbers, at 2 to 3% in each bin. However, in total these bubbles account for a considerable amount, comprising *ca.* 30% of the population. The remaining 10% of the population is made up from bubbles larger in size than the channel, the exact size of which cannot be determined with the $64\text{ }\mu\text{m}$ channel.

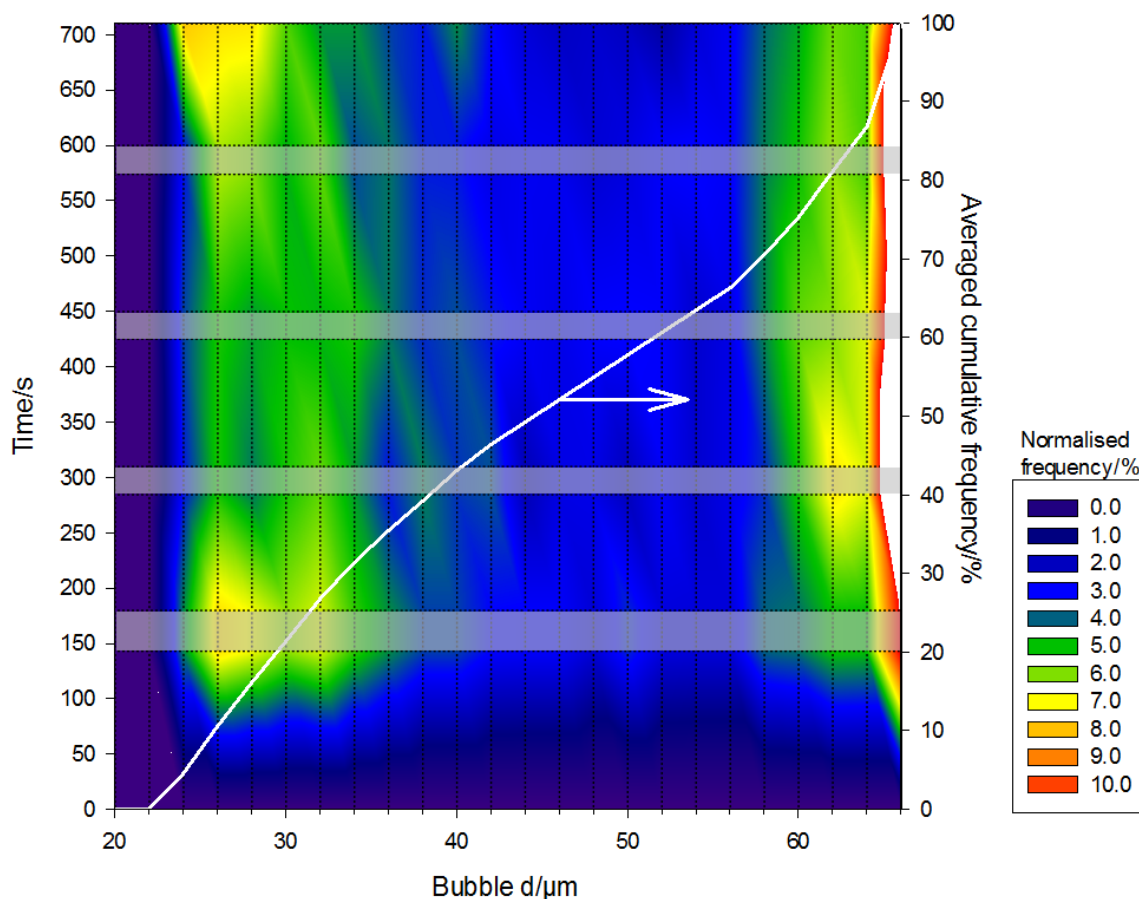


Figure 5.29 Mesh plot comprised of five consecutive normalised histograms, each one exhibiting the bubble diameter distribution of 2000 bubbles, acquired using a 64 μm diameter channel. The first histogram sampled bubbles from $t = 0$ and 143 s, the second from 180 to 285 s, the third from 310 to 425 s, the fourth from 450 to 574 s and the fifth from 600 to 710 s. The horizontal dotted lines demonstrate these time periods and the shaded areas in between show the times that were not sampled, whilst the data was saved. The electrolysis cell was switched on simultaneously with the start of the first acquisition at $t = 0$ s and was left on throughout. The current through the electrolysis cell was 210 mA. The normalised frequency colour scale is presented to the right of the plot. The bin width in each histogram is 2 μm . The white line corresponds to the right y-axis (shown by the arrow) and represents the normalised cumulative frequency, averaged from all five histograms. The pressure difference across the channel was 27 mbar. The potential difference across the μ -channel was 196.3 mV *vs.* MMO. The liquid flow rate was 1.071 $\text{dm}^3\text{min}^{-1}$ and the air was pumped through the headspace of the Dreschel bottle at 410 $\text{cm}^3\text{min}^{-1}$. The temperature was 25.61 $^{\circ}\text{C}$. The threshold for the peak finding routine was set at 99.4 %.

Similarly to Figure 5.29, Figure 5.30 displays a mesh plot of the progression of the distribution with five consecutive histograms of populations of 2000 bubbles per histogram, determined with the 64 μm diameter channel. The plot shows a very similar distribution to that presented in Figure 5.29 and demonstrates that the results are reproducible. The only evident differences between the plots are that there are slightly increased numbers of bubbles of 24 to 28 μm in diameter in the first histogram of Figure 5.30, and that the onset of bubbles with diameters larger than the channel occurs later in the second histogram in Figure 5.30 (286 s)

compared to the first histogram in Figure 5.29 (143 s). However greater time resolution is needed in order to fully examine these onset times and so histograms of smaller sample sizes are subsequently discussed. The rescaled plots shown Figure 5.31 demonstrate that the discussed features of Figure 5.29 and Figure 5.30 would not have been obvious with a scale that takes all of the data into account. They also show that the maximum frequency of bubbles larger than the channel is $< 16\%$. This is confirmed by the cumulative frequency of the plots.

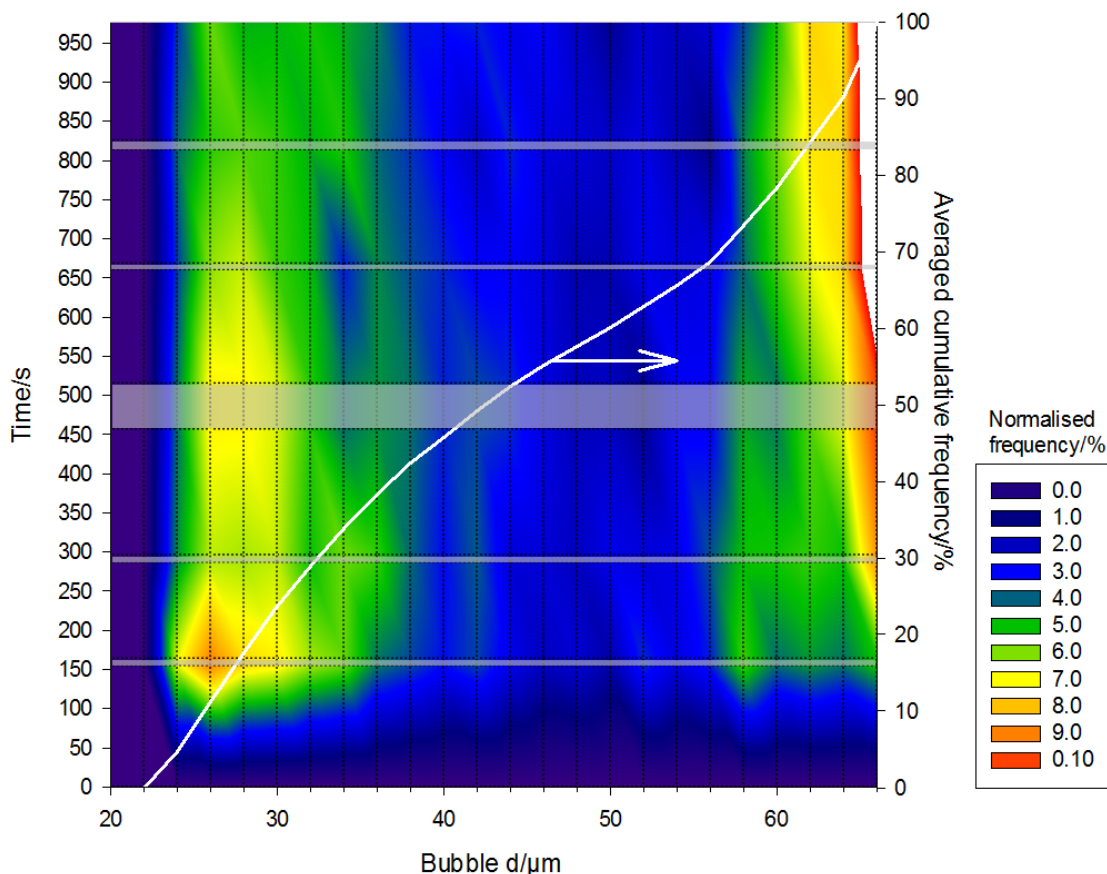


Figure 5.30 Mesh plot comprised of five consecutive normalised histograms, each one exhibiting the bubble diameter distribution of 2000 bubbles, acquired using a $64\ \mu\text{m}$ diameter channel. The first histogram sampled bubbles from $t = 0$ and $155\ \text{s}$, the second from 164 to $286\ \text{s}$, the third from 296 to $456\ \text{s}$, the fourth from 515 to $660\ \text{s}$, the fifth from 668 to $813\ \text{s}$ and the sixth from 825 to $976\ \text{s}$. The horizontal dotted lines demonstrate these time periods and the shaded areas in between show the times that were not sampled, whilst the data was saved. The electrolysis cell was switched on simultaneously with the start of the first acquisition at $t = 0\ \text{s}$. The normalised frequency colour scale is presented to the right of the plot. The bin width in each histogram is $2\ \mu\text{m}$. The white line corresponds to the right y-axis (shown by the arrow) and represents the normalised cumulative frequency, averaged from all six histograms. The applied pressure difference across the channel was $26\ \text{mbar}$. The potential difference across the channel was $193.7\ \text{mV vs. MMO}$. The current through the electrolysis cell was $210\ \text{mA}$. The liquid flow rate was $1.071\ \text{dm}^3\text{min}^{-1}$ and the air was pumped through the headspace of the Dreschel bottle at $410\ \text{cm}^3\text{min}^{-1}$. The temperature was $25.90\ ^\circ\text{C}$. The threshold for the peak finding routine was set at $99.4\ \%$.

Chapter 5: Bubble populations

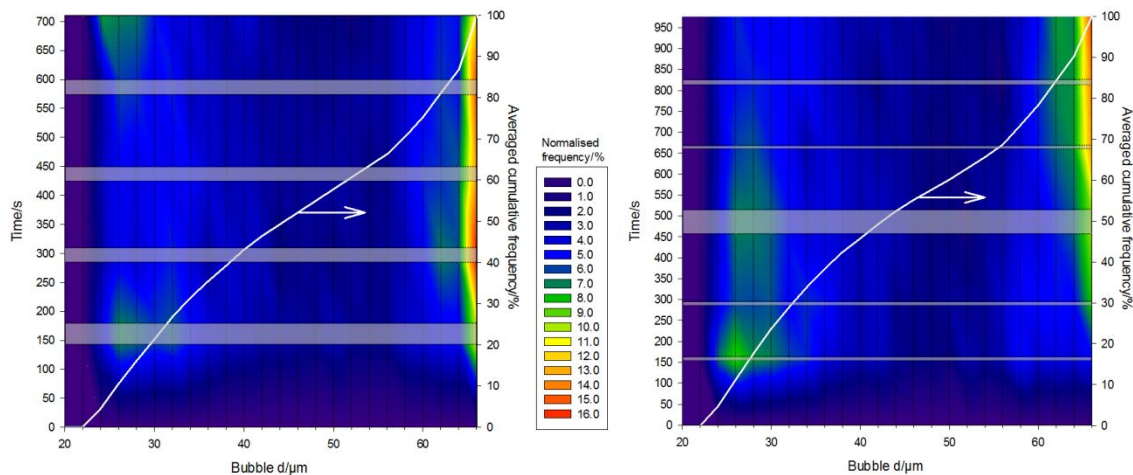


Figure 5.31 Mesh plots as presented in Figure 5.29 (left) and Figure 5.30 (left), with rescaled frequency axes, which applies to both graphs. The experimental conditions are given with the associated plots.

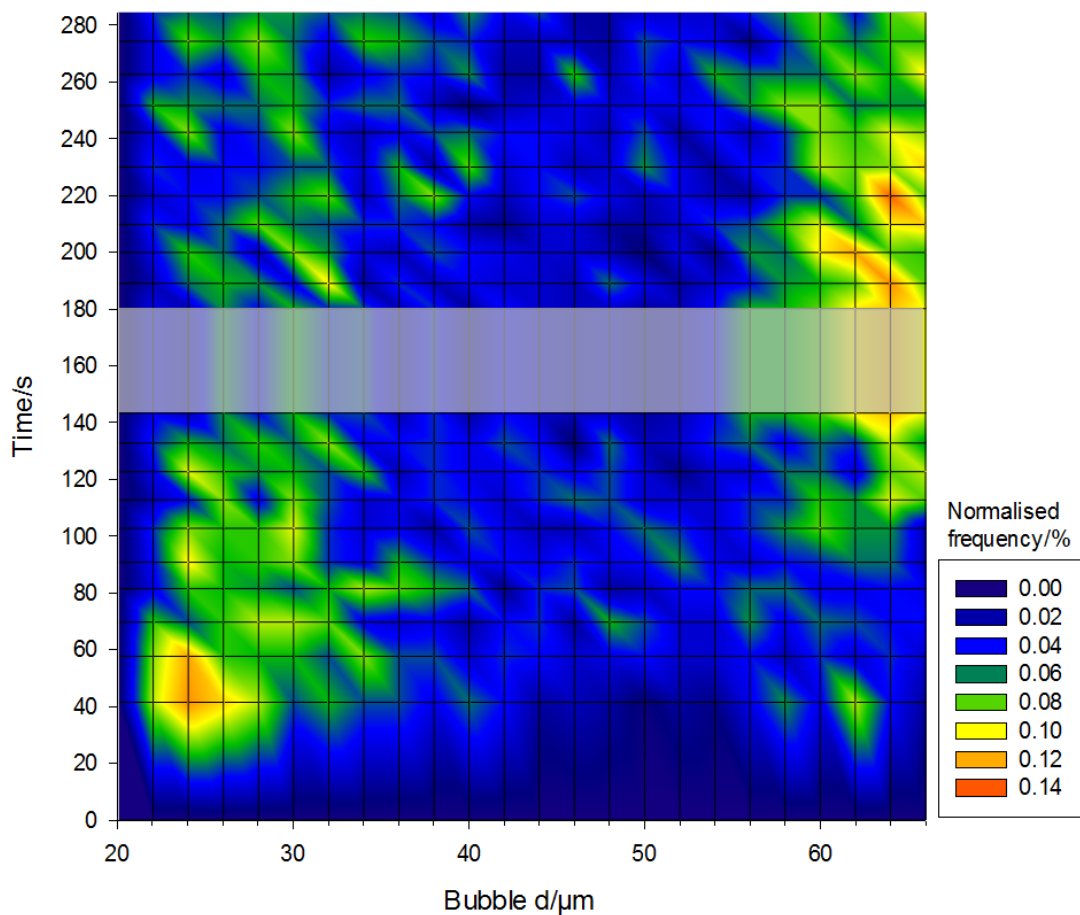


Figure 5.32 Mesh plot comprised of 20 consecutive histograms, each one exhibiting the bubble diameter distribution of 200 bubbles. The horizontal black lines show the times for each histogram, in between which, interpolation is used to produce the plot. These 4000 bubble diameters are the same as those used to produce the histogram in Figure 5.29 and as such the experimental conditions are given with the associated caption. The shaded area shows the time that the bubbles were not sampled whilst the data was being saved.

By considering histograms of smaller samples, the difference in the sizes of bubbles between the figures during the onset of the population can be investigated in greater detail. Figure 5.32 and Figure 5.33 were produced from the same data as for the first two histograms of Figure 5.29 and Figure 5.30 respectively, however with smaller samples of 200 bubble translocations for each histogram.

In both plots the time taken to detect the translocation of the first 200 bubbles is the longest (41 and 45 s resp.) compared to the rest of the histograms (*ca.* 10 s). This is demonstrated by the largest distance between the first two horizontal lines. This is as expected as there are no bubbles in the liquid at $t = 0$ s and the population builds up as electrolysis occurs and the liquid reservoir fills up. The translocation of the following 200 bubbles is shorter (16 and 17 s resp.) and a steady rate of translocation is then achieved with an average of 12.5 s per 200 bubbles (95 % conf. = 1.3 s) for Figure 5.32 and 14.5 s per 200 bubbles (95 % conf. = 1.7 s) for Figure 5.33. During this steady state the amount of gas leaving the system will be equal to the amount being produced by electrolysis.

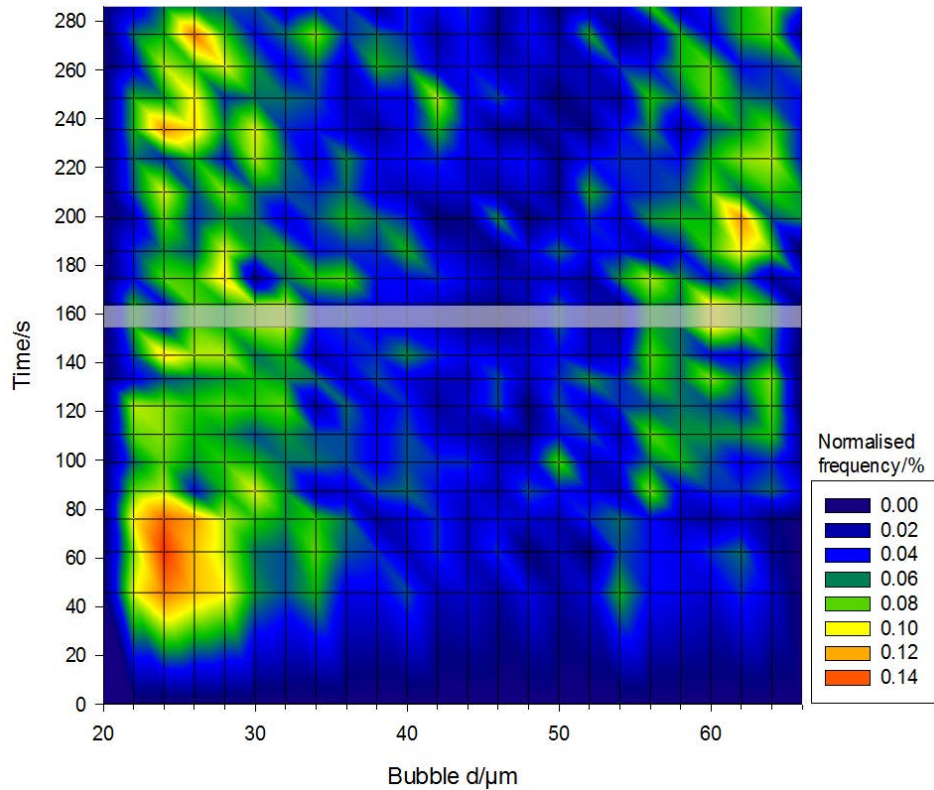


Figure 5.33 Mesh plot comprised of 20 consecutive histograms, each one exhibiting the bubble diameter distribution of 200 bubbles. The horizontal black lines show the times for each histogram, in between which, interpolation is used to produce the plot. The 4000 bubble diameters used here are the same as those used to produce the histogram in Figure 5.30 and as such the experimental conditions are given with the associated caption. The shaded area shows the time that the bubbles were not sampled whilst the data was being saved.

Chapter 5: Bubble populations

In both cases the diameters of the majority of the first 1000 bubbles (initial 90 to 100 s) are between 22 and 30 μm , with very few bubbles outside of the 22 to 38 μm range discussed in the previous plots with histograms of 2000 bubbles. After the influx of these smaller bubbles the relative frequency in this range decreases and an increase in the frequency of larger bubbles between 56 and 64 μm is observed in both plots at *ca.* $t = 90$ s. Figure 5.32 also demonstrates an increase in the number of bubbles above 64 μm , compared to a very small increase in this range observed in Figure 5.33.

Considering all of the histograms generated using the 64 μm channel, a well-defined bubble diameter distribution and progression is evident as discussed. The vast majority of bubbles are sized within the calibrated range. The difference in the onset distribution of bubble diameters observed in the histograms of larger sample sizes is shown to be misleading, by examination of the distribution with histograms of smaller samples.

It is apparent that there are still a small number of bubbles outside of the detection range of the channel and hence a 100 μm diameter channel was utilised in a similar fashion. Succeeding discussion of these experiments, a comparison between the distributions detected with the different channel sizes will be made.

5.1.4.1.3 100 μm channel

Although the calibration for the 100 μm channel was incomplete, the data is analysed similarly to the manner in which the results from the smaller channels were. This is because potential validation may arise from comparison of the produced distribution to the distribution from other channels. Hence the validity of these results will be discussed after the comparison is made, succeeding the presentation of the results.

Experimentation with the 100 μm channel was conducted in a similar manner as the 64 μm diameter channel experiments. Consecutive data sets were acquired in order to obtain further sets of peaks shortly after the initial set with a short delay in between each histogram to save the data. The plots shown in Figure 5.34 and Figure 5.35 are the results from these experiments. The only significant difference in the experimental conditions between the two plots is that the Figure 5.34 experiments used a pressure difference of 11 mbar across the channel, whilst Figure 5.35 was produced using a pressure difference of 26 mbar to draw the liquid

through. Also the total number of bubbles sampled in Figure 5.34 experiment was 6000 with 1000 in each histogram, which is less compared with the experiment that produced Figure 5.35 which sampled a total of 10000 bubbles with 2000 for each histogram.

The scale of the normalised frequency axis on the plots was again chosen with the focus on the bubbles with diameters below the size of the channel. Hence the frequency saturates at some of the points on the mesh above 100 μm , however the cumulative plot provides information on the frequency in this range. The lower sensitivity of the measurement for these conditions (99.6 % threshold) is *ca.* 42 μm , hence bubbles smaller than this are not detected.

Figure 5.34 shows that *ca.* 60 % of the 6000 bubbles are have diameters smaller than the 100 μm diameter of the channel. Bubbles with diameters from 40 to 70 μm account for *ca.* 12 % of the population, spread relatively evenly across this range. Bubbles with diameters from 70 to 90 μm account for *ca.* 23 % with slightly more of the higher end of this range. A further 25 % of the population is comprised of bubbles between 90 and 100 μm , shown by the strongest band on the plot, below the size of the channel. The bubbles with diameters larger than the channel cannot be determined. The progression of the distribution with time is even across the whole range in both 100 μm channel plots; except for a small influx in the number of bubbles with diameters at *ca.* 98 μm , observed in the second histogram.

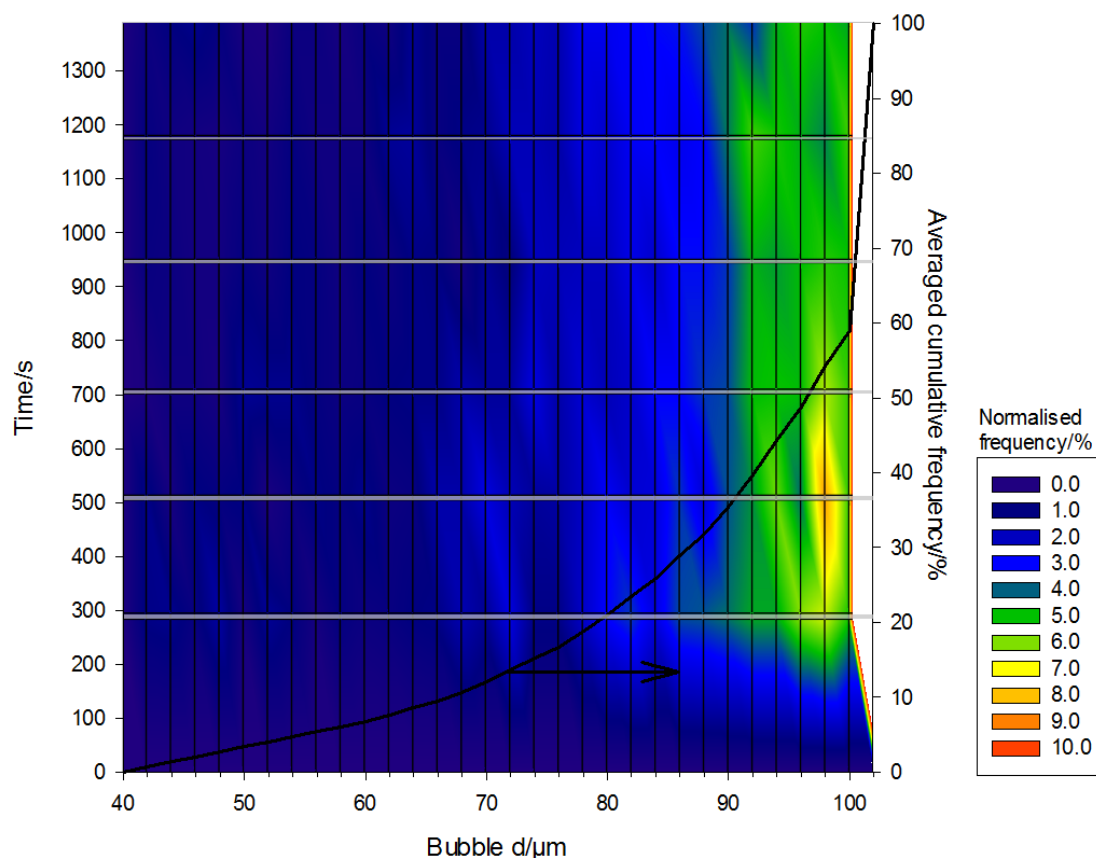


Figure 5.34 Mesh plot comprised of six consecutive normalised histograms, each one exhibiting the bubble diameter distribution of 1000 bubbles, acquired using a 100 μm diameter channel. The horizontal black lines show the times for each histogram, in between which, interpolation is used to produce the plot. The shaded areas show the times that were not sampled, whilst the data was saved. The electrolysis cell was switched on simultaneously with the start of the first acquisition at $t = 0$ s. The normalised frequency colour scale is presented to the right of the plot. The bin width in each histogram is 2 μm . The black line corresponds to the right y-axis (shown by the arrow) and represents the normalised cumulative frequency, averaged from all six histograms. The applied pressure difference across the channel was 11 mbar. The potential difference across the channel was 191.3 mV *vs.* MMO. The current through the electrolysis cell was 211 mA. The liquid flow rate was 0.982 $\text{dm}^3\text{min}^{-1}$ and the air was pumped through the headspace of the Dreschel bottle at 410 $\text{cm}^3\text{min}^{-1}$. The temperature was 23.9 $^{\circ}\text{C}$. The threshold for the peak finding routine was set at 99.6 %.

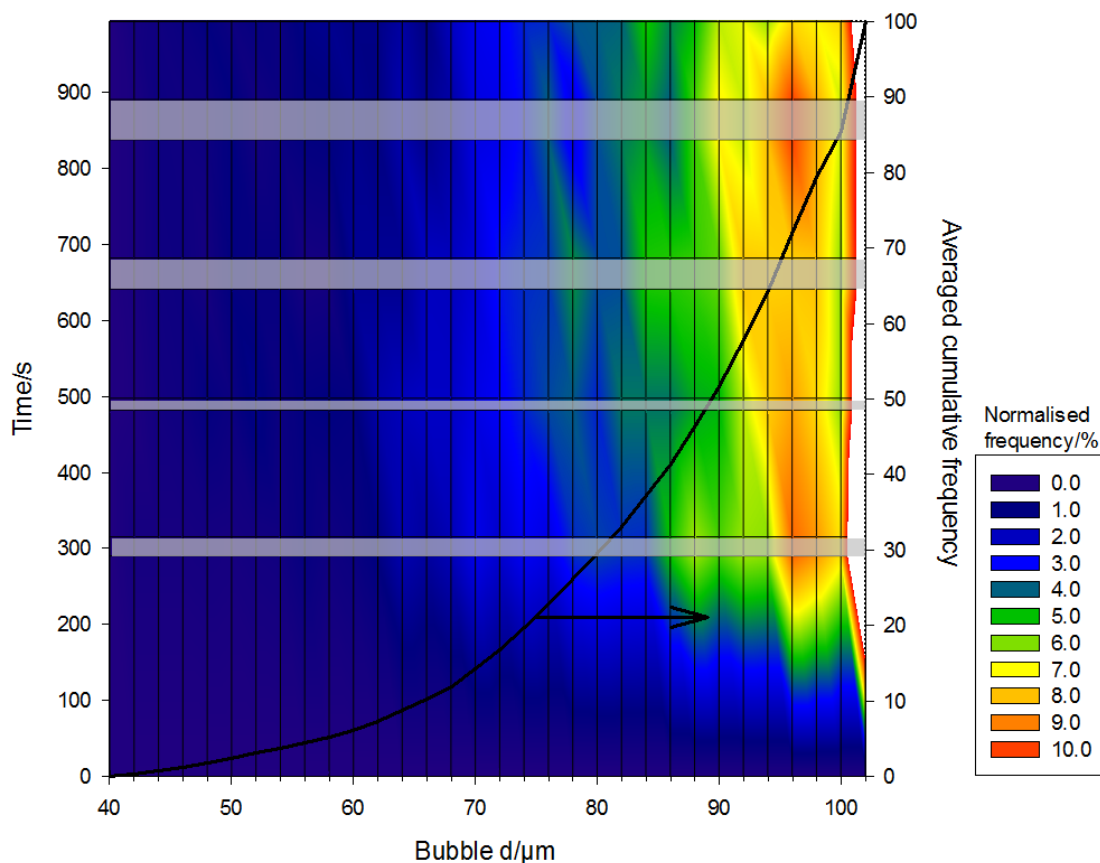


Figure 5.35 Mesh plot comprised of five consecutive normalised histograms, each one exhibiting the bubble diameter distribution of 2000 bubbles (except last histogram of 1420 bubbles), acquired using a 100 μm diameter channel. The horizontal black lines show the times for each histogram, in between which, interpolation is used to produce the plot. The shaded areas show the times that were not sampled, whilst the data was saved. The electrolysis cell was switched on simultaneously with the start of the first acquisition at $t = 0$ s. The normalised frequency colour scale is presented to the right of the plot. The bin width in each histogram is 2 μm . The black line corresponds to the right y-axis (shown by the arrow) and represents the normalised cumulative frequency, averaged from all six histograms. The applied pressure difference across the channel was 26 mbar. The potential difference across the channel was 199.9 mV *vs.* MMO. The current through the electrolysis cell was 209 mA. The liquid flow rate was 0.989 $\text{dm}^3\text{min}^{-1}$ and the air was pumped through the headspace of the Dreschel bottle at 411 $\text{cm}^3\text{min}^{-1}$. The temperature was 23.6 $^{\circ}\text{C}$. The threshold for the peak finding routine was set at 99.6 %.

Considerably more (*ca.* 85 %) of the detected population of bubbles have smaller diameters than the channel for the experiments presented in Figure 5.35 compared to Figure 5.34. Figure 5.35 demonstrates that bubbles with diameters from 40 to 70 μm comprise *ca.* 15 % of the population, with more bubbles comprising the end of this range. Bubbles with diameters from 70 to 90 μm make up 38 % of the population, again with an increase at the end of this range. The most densely populated area on the plot is the same as for Figure 5.34, with bubbles between 90 and 100 μm in diameter, which accounts for 32 % of the population.

Chapter 5: Bubble populations

The only significant difference between the two conducted experiments with the 100 μm channel was the pressure difference across the channel. This accounts for the difference in the bubble sample rate between the two experiments. The experiments with the lower pressure difference of 11 mbar and hence a slower flow had a bubble sample rate of 4.7 bubbles per second. Contrariwise the experiments conducted with the higher pressure difference of 26 mbar and hence a faster flow had a bubble sample rate of 12.9 bubbles per second, as expected. These values were both calculated excluding the first histogram in each respective case to ensure that a steady state was reached. However the distribution of bubble diameters measured with the lower pressure shows a relatively larger number of bigger bubbles compared to the higher pressure results. This is unexpected when considering that a faster flow rate has a larger area of effect and a greater influence to overcome the larger buoyancy forces associated with bigger bubbles. Hence this difference is unexplained and attributed to either, the experimental variation in population itself, the sampling method or the un-calibrated conversion to the diameter values from the magnitudes of the pulses. Further investigation is needed in order to discover which.

5.1.4.2 Comparison of distributions

In summary, the 40 μm diameter channel experiments demonstrated that most of the bubbles detected were larger than the channel. However 40% of the bubbles detected were in the calibrated region and showed a relatively even distribution in the 20 to 40 μm diameter range. This is in very good agreement with the 64 μm channel experimental results, which also showed that *ca.* 40 % of the detected sample had diameters in the 20 to 40 μm range. The remaining 60 % consisted of two quantifiable regions; the first in which the diameter distribution was even from *ca.* 40 to 58 μm comprising just under 30 % of the total population and the second in which a more densely populated region of 58 to 64 μm was observed comprising *ca.* 20 % of the population. The remaining 10 % of the population was comprised of bubbles larger than 64 μm in diameter. This was reproducibly observed in both experiments with the 64 μm channel.

The results from the 100 μm diameter channel do not agree with the results obtained using the other channels diameters. As expected the increased population density below 40 μm observed with the other channels is not exhibited, as this is below the lower sensitivity threshold. However the results are also void of an influx

of bubbles with a diameter of *ca.* 60 μm , observed with the other channels. Instead only 30 % of the population is less than 80 μm with the most of these apparent in the 70 to 80 μm range. The vast majority of the measured population is in the 85 μm to 100 μm range, again in disagreement with the results from the other channels.

Supplementary results are provided by the distribution of bubbles measured during the calibration experiments, shown in Figure 5.36. Here the distribution of bubble diameters measured visually compared to a reference size. These are the combined results from the calibration experiments for each channel (presented in Figure 5.26) where a known size was used as a reference to measure the bubble size, which was used to calibrate the respective transient magnitude response. The plot shows that the most densely populated region of the bubbles detected is between 20 and 60 μm , in good agreement with the 40 and 64 μm diameter channels. There are very few larger bubbles detected with only *ca.* 10 % of the population with diameters larger than 80 μm . Again these do not coincide with the distribution produced by the 100 μm channel.

Hence considering that the calibration experiments conducted with the 100 μm channel were inconclusive and that there is no validation through coincidence with other results; the results generated with the 100 μm channel are to be disregarded.

There is a variety of conceivable reasons for these irregular results. The first possibility is that the distribution of bubbles is real and that the calculated bubbles sizes obtained with the 100 μm are correct. However this is not likely considering Figure 5.36 and until successful calibration experiments are performed with the channel then this cannot be assumed. Furthermore the experimental conditions set for the generation of bubbles was maintained and the measured current density, flow rates and temperatures were consistent through all experiments and hence there is no reason to suggest an inconsistent distribution of bubbles between experiments.

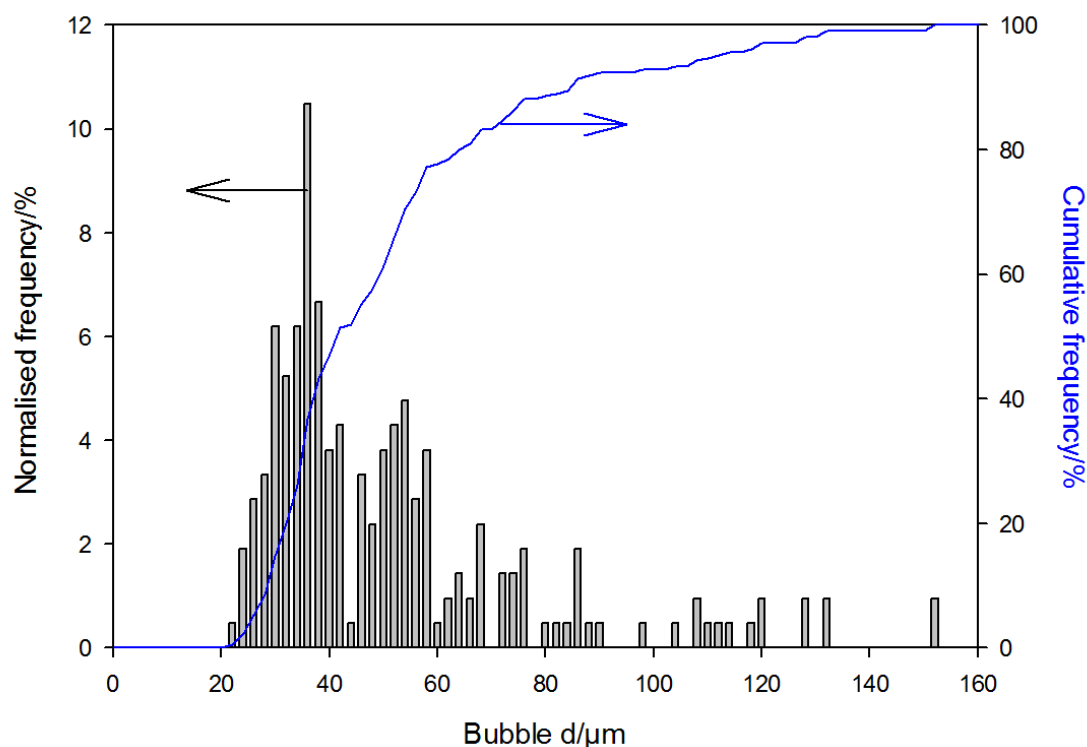


Figure 5.36 Histogram showing the distribution of bubble diameters detected in the calibration experiments (Figure 5.26) measured visually versus a known reference size. The grey bars (▒) show the frequency of occurrence for each bin width of 2 μm which is normalised to the total number of bubbles (1505). The blue line (—) shows the cumulative normalised frequency.

Another possibility is that the distribution of the sampled population depends upon the size of channel used. This is likely as the calibration plot (Figure 5.26) also shows this dependency. By considering the previously utilised Hagen Poiseuille calculations (Figure 5.18) it can be determined that the flow through the channel is faster for larger channel diameters, provided that the channel length remains proportional to the diameter. Indeed analysis of the flow rate of the 100 μm diameter channel using the Hagen Poiseuille equation (see Figure 5.18 for 40 μm example) demonstrates that a pressure differential of *ca.* 10 to 15 mbar produces bubble translocation times that are very close to the limiting frequency for the optocoupler (*ca.* 10's of kHz). Hence it is likely that this is the cause of the discrepancy between the measured sizes of bubble with the 100 μm diameter channel compared to the smaller sized channels. Experiments with a faster optocoupler or slower flow (lower pressure differential) would provide evidence for this theory.

As formerly discussed in the chapter, the translocation of multiple particles can cause oversizing and a faster flow rate will cause increase the incidence of this

effect. Additionally localisation of more bubbles generated by the faster flow may cause an increase in bubble coalescence where smaller bubbles join to form bigger bubbles which are then detected with the 100 μm channel. However more supporting evidence for this theory is needed to warrant serious consideration.

A final possible reason for the discrepancy was also suggested as the cause of the inconsistency between the two distributions produced with the 100 μm diameter channel. It may be that the sampling method or the un-calibrated conversion of the pulse magnitudes to the diameter values is flawed; if the channel was not correctly etched then the interpretation of the pulse in the calculation would be incorrect. This could conceivably cause a shift in the overall distribution. Again further investigation with another channel is needed in order to reveal more details.

5.2 Conclusions and discussion

A novel application of the Coulter principle has been employed for the *in-situ* determination of the size distribution of bubbles in a bubbly liquid generated by a commercial electrolysis cell. A study of the theory underpinning the principle was completed, resulting in the determination of the best suited calculation method required for successful calibration and accurate measurement of bubble sizes.

The experimental results demonstrate that the distribution of measureable bubbles is comprised mainly of bubbles between 20 and 80 μm in diameter with two more populous regions at either extreme of this range. A small number of larger bubbles were also detected but were not accurately measured. Furthermore there are presumably bubbles smaller than this size, which cannot be detected due to the flow limitation of smaller μ -channel diameters.

Possible reasoning for the two regions of increased population density at different diameters can be made by considering the facets of electrolysis cell design. The liquid path through the device travels across the plane faces of the plates and through the holes in the plates. The rate of flow across the planes will be slower than through the small holes and hence the bubbles produced at the planes may detach comparatively later. In this case there would be larger bubbles produced at the planes compared to the edges of the holes. This could be proven by visually observing the bubbles produced at a plane and edge, however the inward-facing planes cannot be observed from outside of the device.

Chapter 5: Bubble populations

Another conceivable cause for the different bubble sizes may again originate from the cell design. As discussed in the previous chapter, the gaps and headspaces in the device promote bubble localisation and coalescence to form bigger bubbles. This would therefore affect the distribution of bubble sizes.

Finally the inherent nature of the electrolysis process may produce a population distribution as observed; the volumetric rate of hydrogen gas production is twice that of oxygen. Hence interaction between the flowing solution and the different rates of bubble growth on the electrode surfaces may produce such variation in the distribution. Analysis of the gas bubbles produced from an electrolysis device with a separated cell design would confirm this theory.

Chapter 6: Conclusions and further work

This thesis presented a study of acoustic cavitation and hydrogen production employing established and novel techniques. The research spanned a broad range of experimental areas, linked by the focus of the manipulation of gas bubbles in liquids using ultrasound, for the benefit of the scientific research community and the sponsoring company.

Enhanced stabilisation of cavitation clusters in cylindrical ultrasonic reactors has been demonstrated, induced by the precise positioning of a hard rod surface upon which the cluster formed. This has been termed ‘reactor induced cavitation cluster stabilisation’ (RICCS). The application of rheoscopic particles within such reactors has revealed a novel and useful method for the characterisation of standing wave fields within reactors of this type. The mechanism of interaction between the particles and sound field is unclear and requires further investigation.

The erosion/corrosion of an aluminium electrode resulting from the collapse of bubble clusters formed in RICCS has been demonstrated. These studies have shown that the collapse of the hemispherical cluster can occur with varied periodicity. Furthermore, studies of the cluster on long timescales (100’s of s) have shown that the stability and erosive properties of the cluster are dependent on state (roughness) of the aluminium surface and the support. Further work with enhanced control of the initial condition of the electrode surface would be beneficial for the conformation of the proposed theories.

Imaging of the cluster (RICCS) has demonstrated the occurrence of sonochemiluminescence. This indicates a highly local sonochemical ‘hotspot’, the spatial extent of which was correlated with the drive pressure amplitude of the sound field. A ‘shimmer’ effect emanating from these clusters (RICCS) has been reported for the first time. This shimmer is attributed to a heat induced refractive index change, the imaging of which was enhanced through the use of a Schlieren technique. Further work with both SCL and Schlieren imaging should focus on monitoring the effects of cavitation clusters formed on surfaces of varied roughness (as performed for the erosion/corrosion experiments). This would divulge additional

Conclusions and further work

information on the clusters stability and its influence on sonochemical yield and 'shimmer' generation.

An initial aim of the research has not been achieved; sonochemically accelerated molecular hydrogen generation from aluminium corrosion in alkaline conditions has shown little or no enhancement. A small observed increase in the rate of gas evolution upon subjecting the reactor to ultrasound was most likely caused by the rise in temperature associated with bulk heating of the fluid as a result of the sound field employed.

Analysis of a prototype electrolysis cell was performed under varying conditions. Assessment of current efficiency and response time of the system was made via measurement of the produced hydrogen and uncompensated resistance, across the device. This resulted in the conveying of suggested improvements to the sponsors and manufacturers of the device. Furthermore this provided inspiration for investigation into the enhancement of gas release from the system, which was shown to occur over an undesirably long time period. An innovative method to control the release of gas using ultrasonic outgassing of a liquid reservoir containing hydrogen and oxygen gas bubbles has been demonstrated. The technique has been shown to rapidly accelerate the response time of an electrolysis cell, characterised via high-speed imaging, hydrogen sensing and the novel application of the uncompensated resistance measurements of the electrolyte leaving the reservoir. Furthermore the resistance measurement technique was applied to estimate the gas void fraction of the bubbly liquid mixture. This highlighted some of the limitations of the sensor employed for the detection and quantification of short bursts of hydrogen gas.

Finally, the thesis presented work using a novel application of the Coulter principle for the *in-situ* determination of the size distribution of bubbles in a bubbly liquid generated by the electrolysis device. An assessment of the theory underpinning the principle was completed, resulting in the determination of the best suited calculation method required for successful and accurate measurement of bubble sizes within the systems deployed. The results showed that the distribution of measureable bubbles generated by the system is comprised mainly of diameters between 20 and 80 μm . A small number of larger bubbles were also detected but were not accurately measured. Further work should aim to investigate the larger bubbles and examine the proposed reasoning for the measured

distribution and anomalous results obtained with the larger 100 μm diameter channel. Investigation of the bubble sizes produced by an alternate electrolysis cell would also be beneficial particularly if the bubble size distribution could be controlled in order to enable the Coulter counter method to be systematically assessed.

Appendices

<i>Appendix</i>	<i>Page number</i>
1: Grade 316L steel composition	175
2: CO sensor aluminium casing	176
3: CO sensor calibration	177
4: SEM images of rheoscopic particles	178
5: Conductivity data for 0.1 M NaOH	179
6: Experimental details for Figure 4.25	182
7: Vortex density coefficients	183
8: Optocoupler calibration details	184
9: Smythe model coefficients	185
10: Speed of sound measurements	186
11: Visual Basic programs	187

Appendix 1. 316L grade steel composition

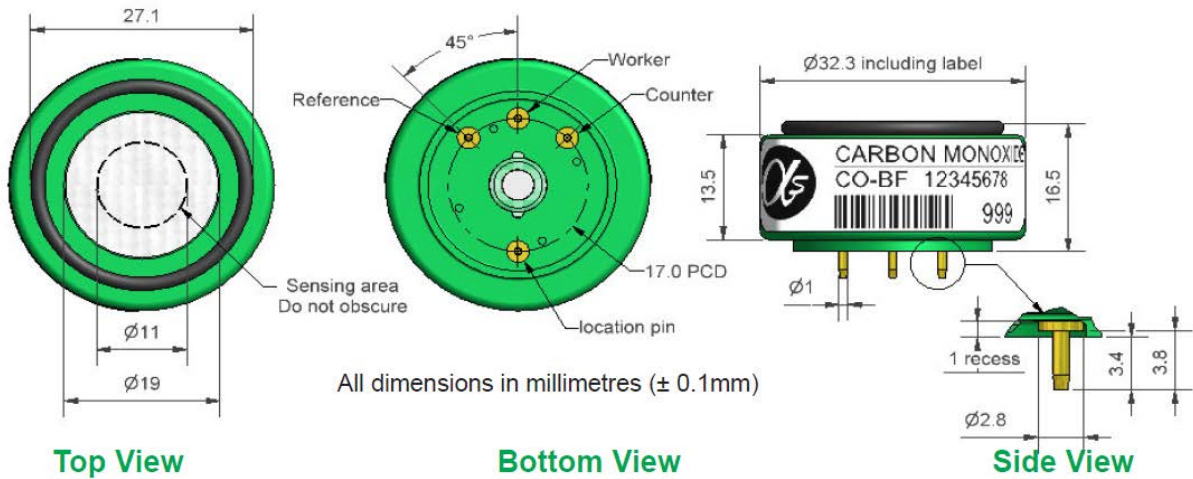
<i>Element</i>	<i>Composition Percentage / %</i>	
	Minimum	Maximum
Carbon (C)	0	0.03
Chromium (Cr)	16.50	18.50
Molybdenum (Mo)	2.00	2.50
Silicon (Si)	0	1.00
Phosphorous (P)	0	0.05
Sulphur (S)	0	0.01
Nickel (Ni)	10.00	13.00
Manganese (Mn)	0.0	2.00
Iron (Fe)	Balance	

Appendix 1. Elemental composition details for 316L grade stainless steel

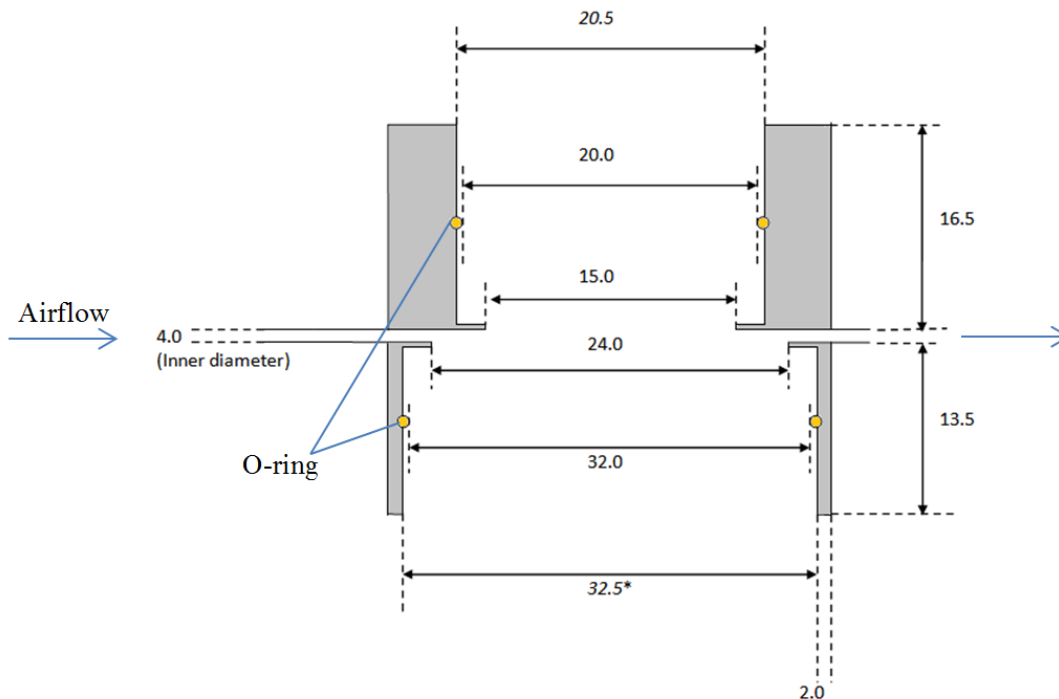
Appendix 2

Appendix 2. CO sensor and aluminium casing

Schematic of the aluminium CO sensor holder. The sensor sits in the bottom section (the top part was used for another sensor which is now redundant).



Appendix 2a. Carbon monoxide (CO-BF) sensor made by Alphasense

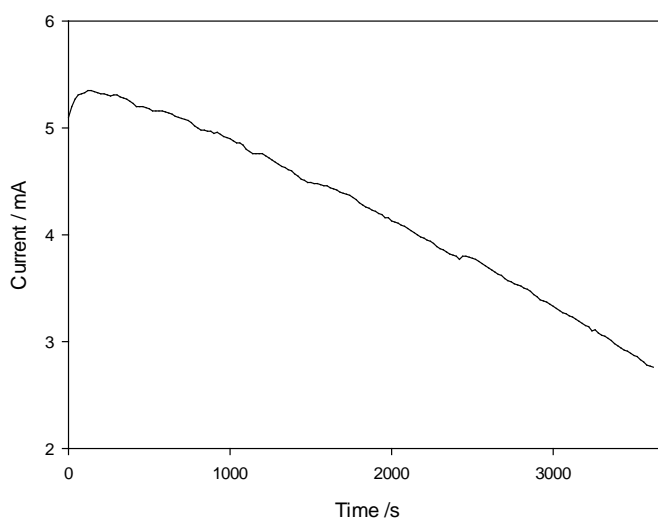


Appendix 2b. Schematic of aluminium holder for CO sensor made in-house

Appendix 3. CO sensor calibration to hydrogen

<i>Airflow</i> <i>/cm³ min⁻¹</i>	<i>I_{electrolysis}</i> <i>(Pt cell)</i> <i>/A</i>	<i>Theoretical</i> <i>H₂ rate</i> <i>/cm³ min⁻¹</i>	<i>Theoretical H₂</i> <i>rate</i> <i>/%</i>	<i>CO sensor</i> <i>response</i> <i>/μA</i>
630.3058	0.0151	0.1154	0.0183	0.2757
768.1436	0.0151	0.1154	0.0150	0.3189
399.1435	0.0151	0.1154	0.0289	0.3261
151.6219	0.0151	0.1154	0.0761	0.3228
151.5360	0.0151	0.1154	0.0761	0.3594
308.0748	0.0151	0.1154	0.0374	0.2966
308.5416	0.0151	0.1154	0.0374	0.3102
308.7160	9.0900e-3	0.0693	0.0225	0.3253
158.8903	9.0900e-3	0.0693	0.0436	0.3991
500.1877	9.0900e-3	0.0693	0.0139	0.3740
124.1585	9.0900e-3	0.0693	0.0558	0.4068
743.2489	9.0900e-3	0.0693	9.3273e-3	0.3026
327.8623	9.0900e-3	0.0693	0.0211	0.3330
487.7383	9.0900e-3	0.0693	0.0142	0.3386

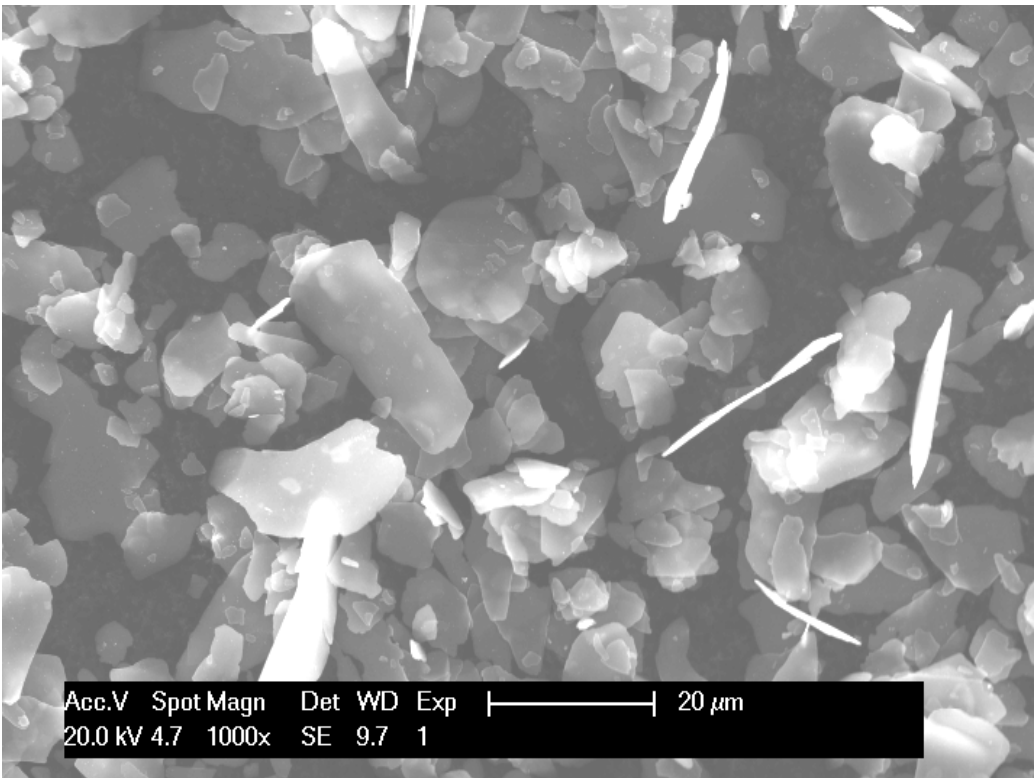
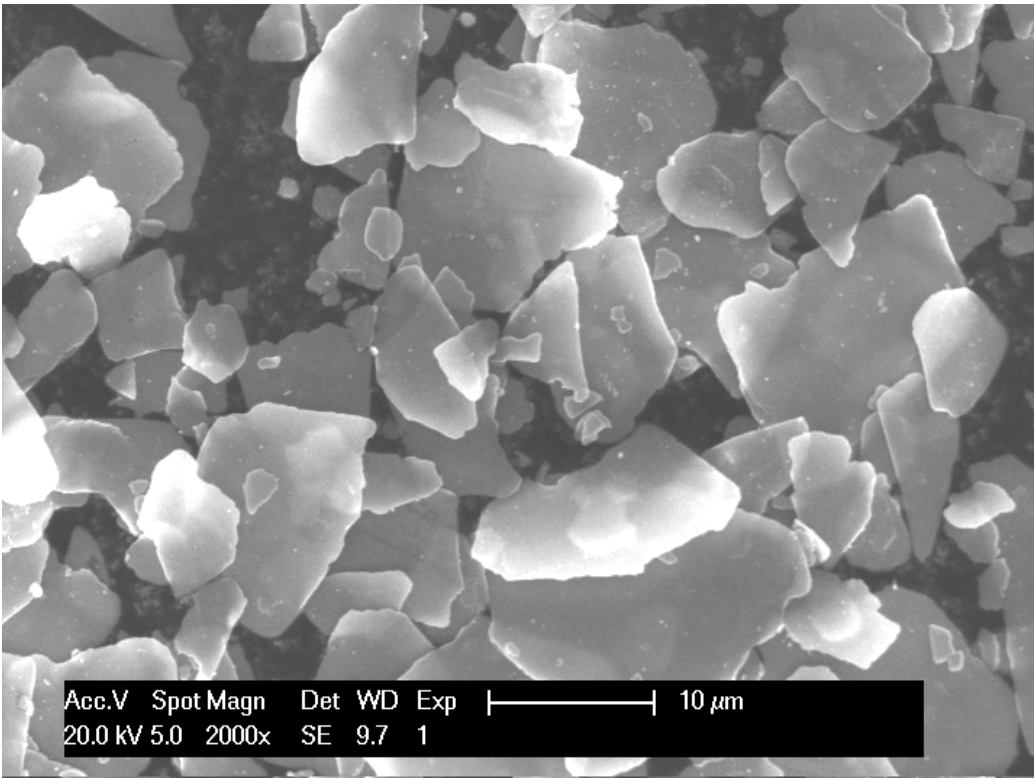
Appendix 3a. Experimental conditions for CO sensor calibration.



<i>Time / s</i>	<i>Cumulative</i> <i>volume / cm³</i>
1520	1
1960	1.3
2180	1.4
2420	1.5
2860	1.7
3240	1.9
3600	2

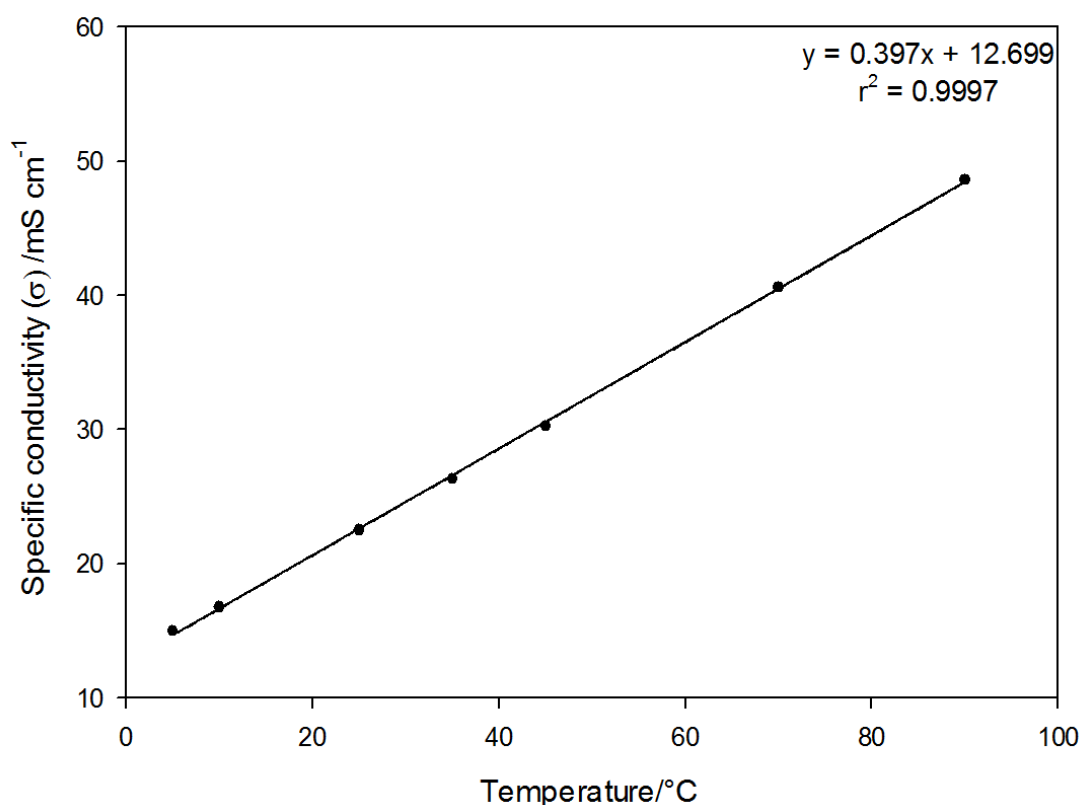
Appendix 3b. Current vs. time for platinum cell volume calibration. The total charge passed was 15.31 C, equating to 1.95 cm³ of hydrogen. The table shows the cumulative volume of hydrogen collected in the gas syringe.

Appendix 4. SEM images of rheoscopic particles



Appendix 4. Scanning electron microscope (SEM) images of rheoscopic particles (PM-01 tracers, Kalliroscope)

Appendix 5a. Conductivity data for 0.1 M NaOH



Graph of the specific conductivity *vs.* temperature for 0.1 M NaOH. The data was extracted from McCleskey [202]. The linear regression shows a very good fit to the data ($r^2=0.9997$).

Here the relationship is approximated for 0.1 M NaOH using data from the literature which correlates the two variables. A linear regression was performed on the data and is shown to be an extremely good fit ($r^2 = 0.9997$).

Hence by converting the uncompensated resistance to specific conductivity, the temperature can be predicted according to this relationship.

The specific conductivity is calculated using the relationship shown in eq. 6-1.

$$R = L / \sigma A \quad (6-1)$$

Where,

R = Resistance (Ω)

L = Distance between electrodes (cm)

A = Electrode area (cm²)

σ = Specific conductivity (S cm⁻¹)

Appendix 5

Note the plate dimensions presented in Figure 4.11 are 52 mm x 11 mm, however the capillary tubes separating the plates block a portion of the plate and hence decrease the exposed area. The exposed width of each plate is 8 mm.

Therefore for the resistance module, $L = 3 \text{ mm}$ and $A = 4.16 \text{ cm}^2$

Care must be taken in the manipulation of the uncompensated resistance, as the value corresponds to the resistance of the electrodes as well as the electrolyte.

Therefore it is not possible to obtain the specific conductivity of the electrolyte from a singular resistance value. In order to account for the uncompensated resistance of the electrode, the resistance change (ΔR) is instead used. This assumes that the change in the resistance of the electrode during the electrolyte temperature change is negligible and cancels out in the subtraction.

Hence by equating for two conductivities, σ_1 and σ_2 , an expression for one in terms of the other can be derived (6-3).

$$\Delta R.(A/L) = (1/\sigma_1) - (1/\sigma_2) \quad (6-2)$$

$$\sigma_2 = 1 / [(1/\sigma_1) - \Delta R.(A/L)] \quad (6-3)$$

By measuring the temperature at the start of an experiment, the baseline specific conductivity can be obtained via the relationship derived from McCleskey [202]. Plugging this σ_1 value into eq. (6-3), with the measured resistance change, ΔR , and the cell dimensions, A and L , generates the specific conductivity, σ_2 , after heating effects. The predicted temperature change can then be obtained by calculating the difference between specific conductivity values ($\sigma_2 - \sigma_1$) and the linear correlation.

Appendix 5b. Experimental variables for Figure 4.25

Time /s	Amp /dB	I/O	Temp. min /°C	Temp. max /°C	Temp. diff /°C	Ru _{max} /ohm	Ru _{min} /ohm	ΔRu /ohm	ΔRu*(A/L) /ohm cm	σ1 /mSc m ⁻¹	σ2 /mS cm ⁻¹	Temp. predicted /°C	ΔTemp /°C
0-60		Off	24.265	24.221	-0.044	4.9191	4.923	-0.0039	-0.05408	22.3362	22.3093	24.19715	-0.06785
60-150	26	On	24.222	24.49	0.268	4.9237	4.9095	0.0142	0.196906667	22.3191	22.4176	24.47006	0.248055
150-210		Off	24.479	24.432	-0.047	4.9088	4.9127	-0.0039	-0.05408	22.4212	22.3940	24.41063	-0.06837
210-300	25	On	24.436	24.599	0.163	4.9134	4.9058	0.0076	0.105386667	22.4041	22.4571	24.5695	0.133502
300-360		Off	24.593	24.543	-0.05	4.9061	4.9104	-0.0043	-0.059626667	22.4665	22.4364	24.51733	-0.07567
360-450	24	On	24.537	24.678	0.141	4.9111	4.9044	0.0067	0.092906667	22.4442	22.4911	24.65508	0.118082
450-510		Off	24.682	24.643	-0.039	4.9037	4.908	-0.0043	-0.059626667	22.5018	22.4717	24.60609	-0.07591
510-600	23	On	24.64	24.748	0.108	4.9088	4.9044	0.0044	0.061013333	22.4851	22.5160	24.71777	0.077774
600-660		Off	24.748	24.716	-0.032	4.904	4.9083	-0.0043	-0.059626667	22.5280	22.4978	24.67191	-0.07609
660-750	22	On	24.702	24.807	0.105	4.908	4.9049	0.0031	0.042986667	22.5098	22.5316	24.75689	0.054893
750-810		Off	24.796	24.758	-0.038	4.9048	4.9085	-0.0037	-0.051306667	22.5471	22.5211	24.7304	-0.0656
810-900	21	On	24.747	24.833	0.086	4.9083	4.9056	0.0027	0.03744	22.5276	22.5467	24.79488	0.04788
900-960		Off	24.83	24.792	-0.038	4.906	4.9102	-0.0042	-0.05824	22.5606	22.5310	24.75546	-0.07454
960-1050	20	On	24.789	24.886	0.097	4.9106	4.9077	0.0029	0.040213333	22.5443	22.5648	24.84051	0.051506
1050-1110		Off	24.89	24.837	-0.053	4.9081	4.9108	-0.0027	-0.03744	22.5844	22.5654	24.84196	-0.04804
1110-1200	30	On	24.863	26.252	1.389	4.9103	4.8312	0.0791	1.096853333	22.5737	23.1468	26.30599	1.442993
1200-1260		Off	26.238	26.093	-0.145	4.833	4.8415	-0.0085	-0.117866667	23.1198	23.0570	26.0798	-0.1582
1260-1350	28	On	26.108	26.608	0.5	4.8406	4.8158	0.0248	0.343893333	23.0682	23.2527	26.57244	0.464441
1350-1410		Off	26.608	26.49	-0.118	4.8158	4.8249	-0.0091	-0.126186667	23.2668	23.1987	26.43651	-0.17149
1410-1500	35	On	26.494	28.788	2.294	4.8242	4.7032	0.121	1.677866667	23.2215	24.1630	28.86438	2.370384
1500-1560		Off	28.788	28.481	-0.307	4.7032	4.719	-0.0158	-0.219093333	24.1326	24.0057	28.46843	-0.31957

Appendix 6. Coulter counter theoretical function comparison

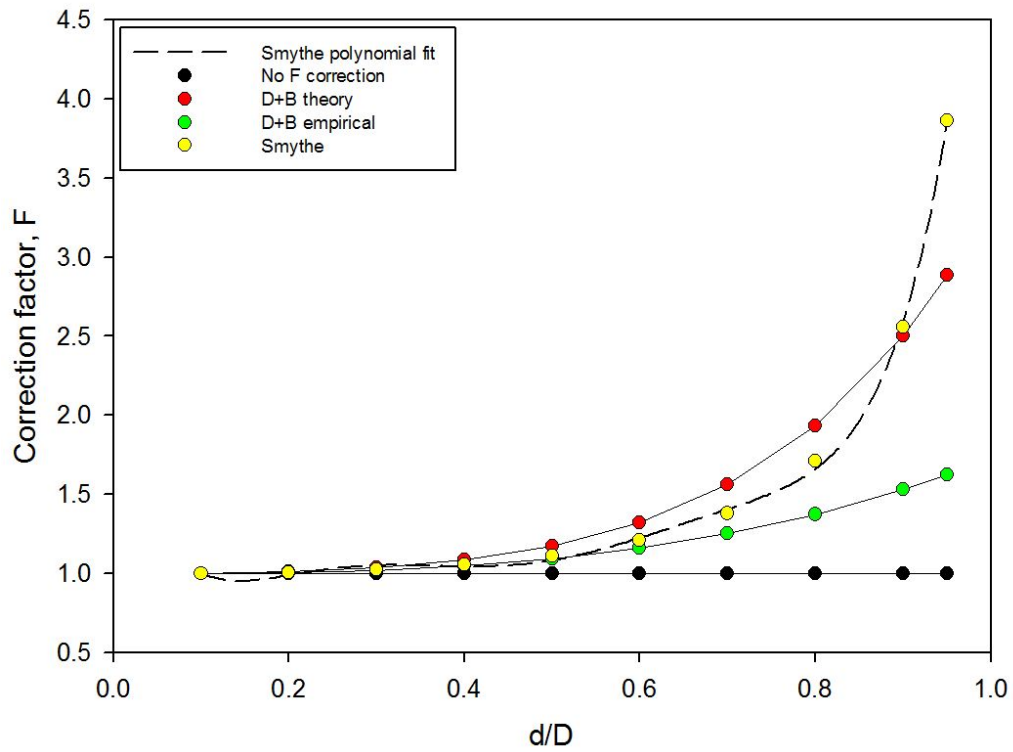


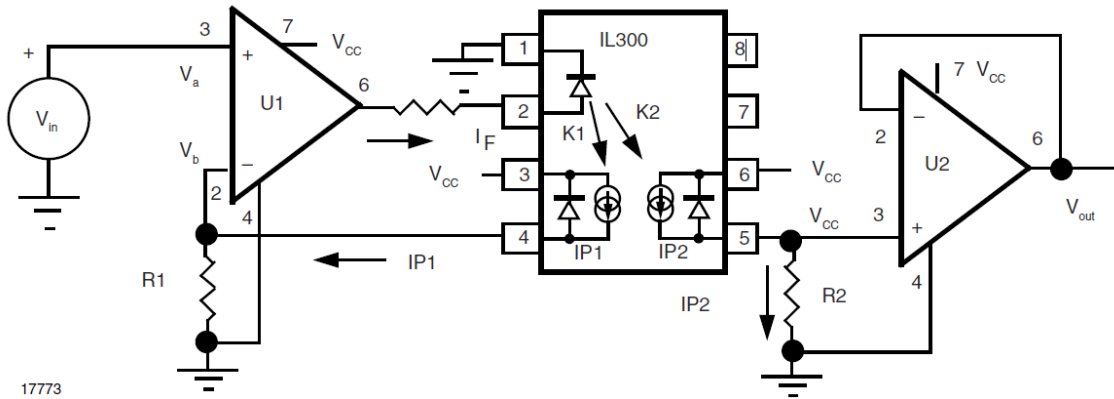
Figure 6.1 Graphical comparison of the correction functions with varied bubble to channel diameter ratios (d/D) employed in the calculation of insulating sphere diameters, as given in equation (5–7). The polynomial fit to the Smythe function is also shown.

Appendix 7. Vortex density coefficients

d/D	$F1$	$F2$	$C_0(F3)$	$F3$
0.1	1.001261	1.00073	1.5011956	1.0007975
0.2	1.01015	1.00584	1.5096182	1.0064155
0.3	1.034822	1.01971	1.5329642	1.0219876
0.4	1.085146	1.04672	1.5805729	1.0537441
0.5	1.174688	1.09125	1.6659472	1.110694
0.6	1.323482	1.15768	1.8124644	1.208438
0.7	1.561594	1.25039	2.0688531	1.379503
0.8	1.933478	1.37376	2.5643499	1.71086
0.9	2.503125	1.53217	3.8319456	2.556723
0.95	2.888894	1.625884	5.7826704	3.861028

Appendix 7. Numerical comparison of the correction functions employed in the calculation of insulating sphere diameters, as given in equation (5–10).

Appendix 8. Optocoupler calibration details



Appendix 8.Unipolar Photoconductive Isolation Amplifier circuit schematic [167].

From the application note: $R_1 = V_{in\ max}/(K_1 \cdot I_{o\ max})$

Here $I_{o\ max} = I_f$, which is the max current through the LED which is set at 20 mA (5V max from op amp through 250 Ohm resistor).

Hence for an estimated 4 V range,

$R_1 = 28.6\ k\Omega$ s (as $K_1 = 0.007$ from data sheet for our IL300 isolator).

From the application note: $R_2 = (R_1 \cdot G)/K_3$ where $G = \text{gain (ideally 1)}$

Therefore $R_2 = 48.4\ k\Omega$ s.

Attempt to set R_1 and R_2 resistor values close to calculated values as possible resistors:

Real values employed in circuit: $R_1 = 32\ k\Omega$ s, $R_2 = 47\ k\Omega$ s.

Therefore in employed circuit: $G = 0.866$ (as $K_3 = 0.59$ for the IL300).

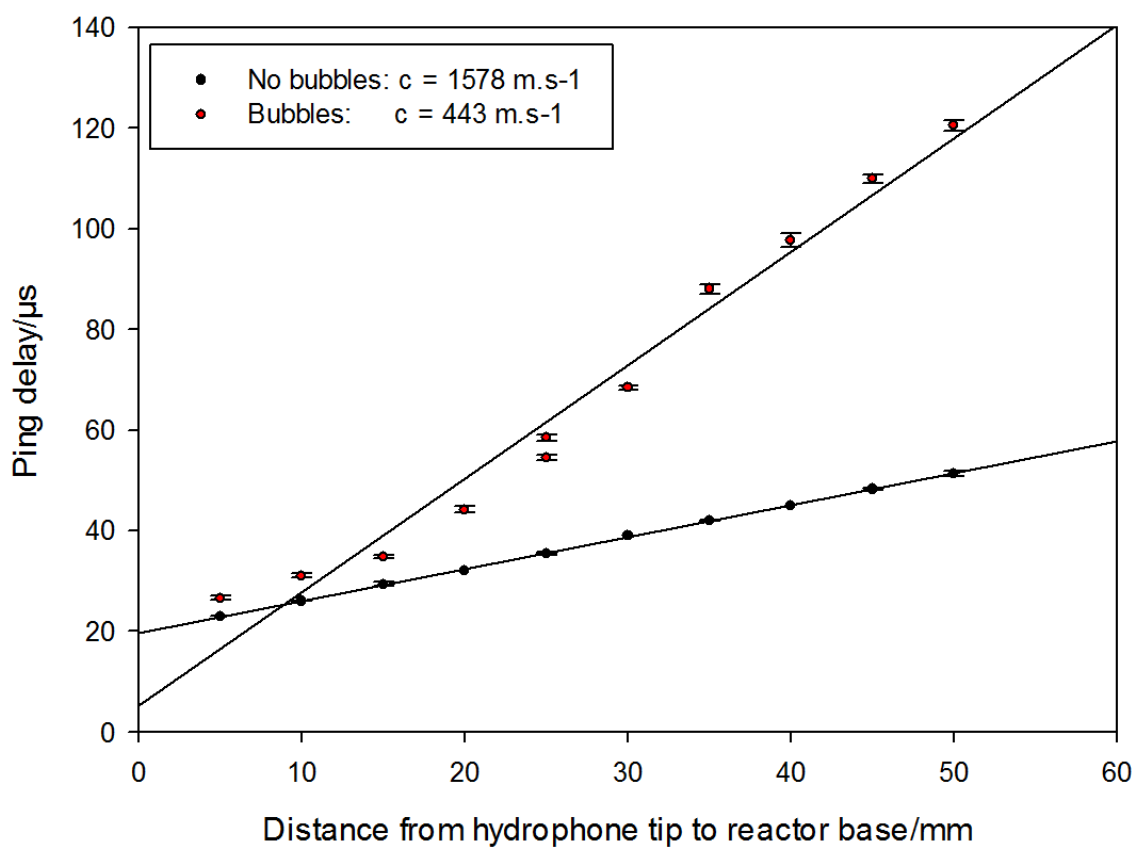
Thus to get the real current in pore $I = (V_{out}/0.866) \cdot 10^6\ V\ A^{-1}$.

Appendix 9. Smythe model coefficients

$d/\mu m$ Coeff.	40	50	64	100
a	12.894	16.409	19.773	30.286
b	71.181	61.719	99.938	27.982
c	28.180	35.238	45.217	69.416
d	5607.101	4648.078	8699.690	1949.962
e	0	0	0	1.14E-04
R ²	0.9988	0.9989	0.9985	0.9996

Appendix 9. Coefficients for the hyperbolic fits shown in Figure 5.21

Appendix 10: Speed of sound measurements



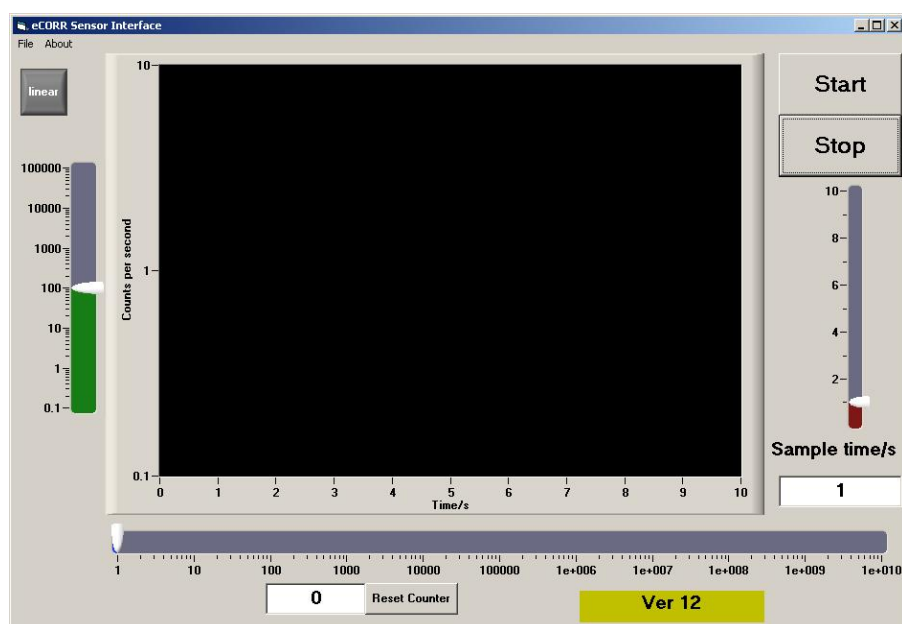
Appendix 10. Speed of sound measurements made in 'bubble free' (●) and bubble saturated (●) NaOH (0.1 M). The measurements were made by sending an acoustic 'ping' signal from the transducer to the hydrophone, which was positioned at varied axial distances. AXIS CAPTION

Appendix 11: Visual Basic Programs

<i>Program Number</i>	<i>Program</i>	<i>Page</i>
1.	Cavitation sensor interface	189
2.	Oscilloscope interface	192
3.	Hydrogen/air flow/liquid flow/temperature sensor interface with R_u calcs.	195
4.	Interface for coulter counter system with peak finding and processing routines	203

1. Cavitation Sensor (Cavitation sensor.vbp)

Reads erosion count data from acquisition card and plots and saves in csv format.



```

Const BoardNum = 1
Dim timesample As Double
Dim StartTime As Double
Dim t(10000)
Dim wey
Dim x
Dim ctot
Dim ti$
Dim coi$
Dim co(10000)
Const CounterNum% = 1      ' number of counter used
Const RegName% = LOADREG1  ' register name of counter 1

```

Appendix 11

```
Private Sub bli_Click()
frmCountTest.Visible = True
End Sub

Private Sub cmdStopRead_Click()
wey = 0
End Sub

Private Sub Command1_Click()
wey = 1
x = 0
CWGraph1.ClearData
CWGraph1.ChartLength = 100000
startit = Timer

Do
LoadValue% = 0          'event counters can only be reset to 0
ULStat% = cbCLoad(BoardNum, RegName%, LoadValue%)
If ULStat% <> 0 Then Stop

StartTime = Timer
Do
Loop Until Timer - StartTime > CWSlide2.Value
t(x) = Timer - startit

ULStat% = cbCIn32(BoardNum, CounterNum%, CBCCount&)
If ULStat% <> 0 Then Stop

CWGraph1.ChartXvsY t(x), (CBCCount& / CWSlide2.Value)
co(x) = (CBCCount& / CWSlide2.Value)
ctot = ctot + CBCCount&
Text2 = ctot
CWSlide1.Pointers.Item(1) = ctot

DoEvents
x = x + 1
Loop Until wey = 0
End Sub

Private Sub Command2_Click()
ctot = 0
End Sub

Private Sub CWKnob1_PointerValueChanged(ByVal Pointer As Long, Value As Variant)
Text1 = CWKnob1.Value
End Sub

Private Sub CWButton1_ValueChanged(ByVal Value As Boolean)
If CWButton1.Value = True Then
CWGraph1.Axes.Item(2).Log = False
Else
CWGraph1.Axes.Item(2).Log = True
End If
End Sub

Private Sub CWSlide2_PointerValueChanged(ByVal Pointer As Long, Value As Variant)
Text1 = Format(CWSlide2.Value, "0.00")
End Sub

Private Sub CWSlide3_PointerValueChanged(ByVal Pointer As Long, Value As Variant)
CWGraph1.Axes(2).Maximum = CWSlide3.Pointers.Item(1).Value
End Sub
```

```

Private Sub Ele_Click()

End Sub

Private Sub Form_Load()

    ULStat% = cbErrHandling(PRINTALL, DONTSTOP)
    If ULStat% <> 0 Then Stop

    LoadValue% = 0          'event counters can only be reset to 0

    ULStat% = cbCLoad(BoardNum, RegName%, LoadValue%)
    'If ULStat% <> 0 Then Stop

End Sub

Private Sub Open_Click()
frmCountTest.CommonDialog1.CancelError = True
    On Error GoTo ErrHandle
    frmCountTest.CommonDialog1.Flags = &H2&
    frmCountTest.CommonDialog1.Filename = "*.*)"
    frmCountTest.CommonDialog1.InitDir = "C:\Tom\"
    frmCountTest.CommonDialog1.Action = 1
    frmCountTest.Caption = frmCountTest.CommonDialog1.Filename
    Open frmCountTest.CommonDialog1.Filename For Input As #2
    CWGraph1.ClearData
    CWGraph1.ChartLength = 100000

    Input #2, ti$ ' removes header
    Input #2, ti$ ' removes header

    Do
    Input #2, ti$
    Input #2, coi$
    CWGraph1.ChartXvsY Val(ti$), Val(coi$) 'plots the sample i
    Loop Until EOF(2)

    Close #2

ErrHandle:  Exit Sub
End Sub

Private Sub Save_Click()
    frmCountTest.CommonDialog1.CancelError = True
    On Error GoTo ErrHandle
    frmCountTest.CommonDialog1.Flags = &H2&
    frmCountTest.CommonDialog1.Filename = "*.dat"
    frmCountTest.CommonDialog1.InitDir = "C:\Tom\"
    frmCountTest.CommonDialog1.Action = 2
    frmCountTest.Caption = frmCountTest.CommonDialog1.Filename
    Open frmCountTest.CommonDialog1.Filename For Output As #2

    Print #2, "Time/s, Count/Hz"
    ns = 0
    Do
        ns = ns + 1
        Print #2, Format(t(ns), "0.00"); ", "; Format(co(ns), "0")
    Loop Until ns = x - 1

    Close #2

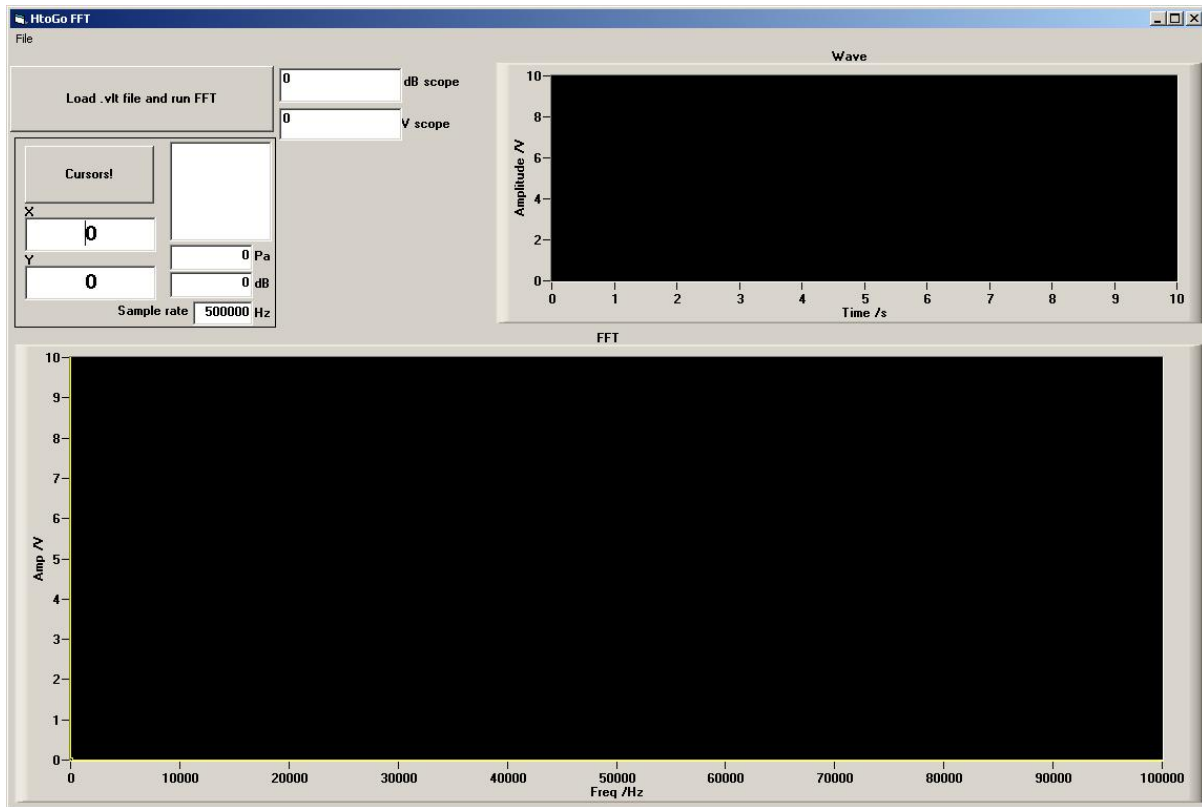
ErrHandle:  Exit Sub
End Sub

```

Appendix 11

2. Oscilloscope interfacing (FFT Oscilloscope.vbp):

Reads data from oscilloscope (Owon SDS-7102V or Gould DSO 465) and performs FFT. Calculates pressure in Pa from hydrophone sensitivity calibration data.



```
Dim timest(50000)
Dim pwrspc outa As Variant
Dim Famp(500) ' As Variant
Dim info(500)
Dim adb(500)
Dim aconv(500)
Dim apressure(500)

Private Sub Command1_Click()
    Dim a As String
    CWGraph1.ClearData
    CWGraph2.ClearData
    form1.filebox.CancelError = True
    On Error GoTo errhandle
    form1.filebox.Flags = &H2&
    form1.filebox.FileName = "*.vlt"
    form1.filebox.InitDir = "C:\Tom\Electrolysis cell\"
    form1.filebox.Action = 1
    form1.Caption = form1.filebox.FileName
    Open form1.filebox.FileName For Input As #2
    n = 0

    For nn = 0 To 6
        Input #2, a$
        Next nn
    Do
```

```

Input #2, a$
Famp(n) = Val(-a$)
CWGraph1.ChartLength = 501
List1.AddItem Str(Famp(n))
CWGraph1.ChartY Famp(n), 0.000002, bplotperrow = True 'xinc=timebase/num points
n = n + 1
Loop Until EOF(2)
Close #2

dttime = 1 / Sample.Text
CWDSP1.AutoPowerSpectrum Famp, dttime, pwrspecouta, df
rm = (Sqr(2))
pwrspecouta(0) = (Sqr(pwrspecouta(0)))
  For se = 1 To 249
    pwrspecouta(se) = rm * (Sqr(pwrspecouta(se)))
  Next se
CWGraph2.PlotY pwrspecouta, 0, df
errhandle:  Exit Sub
End Sub

Private Sub CWGraph2_Click()
text3x.Text = Format(CWGraph2.Cursors.Item(1).XPosition, "0.0000")
text3y.Text = Format(CWGraph2.Cursors.Item(1).YPosition, "0.0000")

xf = text3x.Text ' frequency value
'now the db scale
'ydb = ((-1.238984E-18) * (xf ^ 5)) + ((1.569604E-13) * (xf ^ 4)) - ((0.0000000007899374) * (xf ^ 3)) +
((0.0001973692) * (xf ^ 2)) - (2.4478 * xf) + 11842
ydb = -212.5
conv = (10 ^ (ydb / 20)) * 1000000 'gives V per pascal
dbtext.Text = Format(ydb, "0.00")
pressure.Text = Format((text3y / conv), "0.00") ' pascals at frequency f

scopev.Text = 10 ^ (scopedb.Text / 20)
'pressure.Text = Format((scopev / conv), "0.00") ' pascals at frequency f
End Sub

Private Sub Exit_Click()
End
End Sub

Private Sub load_Click()
Dim a As String
CWGraph1.ClearData
CWGraph2.ClearData

form1.filebox.CancelError = True
On Error GoTo errhandle
form1.filebox.Flags = &H2&
form1.filebox.FileName = "*.dat"
form1.filebox.InitDir = "C:\\"
form1.filebox.Action = 1
form1.Caption = form1.filebox.FileName
Open form1.filebox.FileName For Input As #2
Erase Famp

For nn = 0 To 6
Input #2, a$
Next nn
Do
  Input #2, a$
  Famp(n) = Val(a$)

  CWGraph1.ChartLength = 501

```

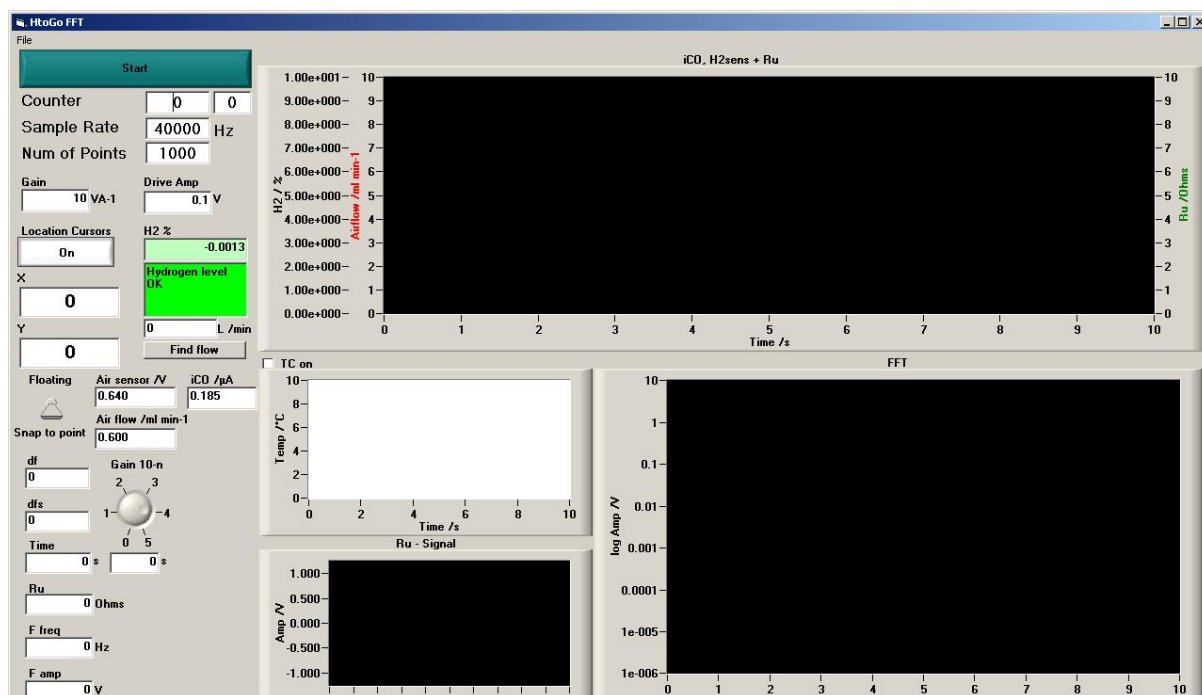
Appendix 11

```
List1.AddItem Str(Famp(n))
CWGraph1.ChartY Famp(n), 0.0000002, bplotperrow = True 'xinc=timebase/num points
Loop Until EOF(2)
Close #2
dttime = 0.000001
CWDSP1.AutoPowerSpectrum Famp, dttime, pwrspecouta, df
rm = (Sqr(2))
pwrspecouta(0) = (Sqr(pwrspecouta(0)))
For se = 1 To 249
    pwrspecouta(se) = rm * (Sqr(pwrspecouta(se)))
Next se
CWGraph2.PlotY pwrspecouta, 0, df
errhandle: Exit Sub
End Sub
Private Sub save_Click()
Dim ns
    form1.filebox.CancelError = True
    On Error GoTo errhandle
    form1.filebox.Flags = &H2&
    form1.filebox.FileName = "*.dat"
    form1.filebox.InitDir = "C:\Tom\htogo resistance tests\"
    form1.filebox.Action = 2
    form1.Caption = form1.filebox.FileName
    Open form1.filebox.FileName For Output As #2

    ns = 0
    Print #2, "Samplerate="; Samplerate.Text; "Hz"; ","; "Drive Amp="; Drive.Text; "V"; ","; "Gain=";
GainBoard.Text; "VA-1"
    Print #2, "Time/s,F amp/V, Ru /Ohms, F Freq/Hz"
    Do
        ns = ns + 1
        Print #2, Format(timest(ns), "0.0000"); ","; Format(Famp(ns), "0.00000"); ",";
Format(ru(ns), "0.00000"); ","; Format(Ffreq(ns), "0.0000")
        Loop Until ns = lloop - 1
    Close #2
errhandle: Exit Sub
End Sub
```

3. Electrolysis cell program (HTOGO FFT.vbp)

Takes inputs from CO sensor, thermocouple, airflow sensor, liquid flow sensor and resistance module. Calculates hydrogen percentage from calibration and airflow. Performs FFT on resistance data. Plots and saves all in csv format.



```

Const NumPoints& = 999      ' Number of data points to collect
Const FirstPoint& = 0      ' set first element in buffer to transfer to array
Dim ADData%(NumPoints&)    ' dimension an array to hold the input values
Dim MemHandle&             ' define a variable to contain the handle for
Dim idata(999)
Dim datagraph1(3)
Dim datagraph2(1)
Dim wey
Dim lloop As Integer
Dim timest(50000)
Dim temp(50000)
Dim ach2(10000)
Dim HighChan%
Dim EngUnits(NumPoints&)
Dim pwrspecouta As Variant
Dim pwrspecoutav(500) ' As Variant
Dim ru(50000)
Dim Famp(50000)
Dim Ffreq(50000)
Dim tc08_handle As Integer
Dim in_timer As Integer
Dim temp_buffer(9) As Single
Dim ipt(50000)
'Dim h2sens(50000)
Dim airflow(50000)
Dim airflowcal(50000)
Dim timestb(50000)
Dim startt
Dim timesample As Double
Dim StartTime As Double

```


Appendix 11

```
Dim t(10000)
Dim weyl
Dim x
Dim ctot
Dim ti$
Dim coi$
Dim co(10000)
Const CounterNum% = 1      ' number of counter used
Const RegName% = LOADREG1  ' register name of counter 1

Private Sub Command1_Click()
BoardNum% = 1

    LoadValue% = 0          'event counters can only be reset to 0
    ULStat% = cbCLoad(BoardNum%, RegName%, LoadValue%)
    If ULStat% <> 0 Then Stop

    StartTime = Timer
    Do
    Loop Until Timer - StartTime > 5

    ULStat% = cbCIn32(BoardNum%, CounterNum%, CBCount&)
    If ULStat% <> 0 Then Stop

    Flowtext.Text = Format((CBCount& / 752) * 12, "0.000")

    DoEvents
End Sub

Private Sub Timer1_Timer()
Dim flag As Integer
If TCswitch.Value = 1 Then
If CWButton1.Value = True Then

    If (tc08_handle > 0) Then
        If (Not in_timer) Then
            in_timer = True

            ok = usb_tc08_get_single(tc08_handle, temp_buffer(0), overflow_flag, 0)

            If (ok) Then
                'loop = 0

                'txtCJC.Text = temp_buffer(0)
                ' txtChannel1.Text = temp_buffer(1)
                'txtChannel2.Text = Format(temp_buffer(2), "0.00")
                temp(loop) = temp_buffer(2)
                datagraph2(0) = timest(loop)
                datagraph2(1) = temp(loop)
                'loop = loop + 1
                CWGraph4.ChartXY datagraph2, bchartperrow = True

            End If
            in_timer = False
        End If
    End If
End If

    LowChan% = 0          ' first channel to acquire
    HighChan% = 2
```

```

CBCCount& = 999 'CWSlide1.Value) * 2      ' total number of data points to collect
CBRate& = 5000 ' sampling rate (samples per second) per channel
Gain = BIP5VOLTS      ' set the gain
Options% = CONVERTDATA 'Or EXTTRIGGER ' return data as 12-bit values

ULStat% = cbAInScan(0, LowChan%, HighChan%, CBCCount&, CBRate&, Gain, MemHandle&,
Options%)

' Transfer the data from the memory buffer set up by Windows to an array for use by Visual Basic

ULStat% = cbWinBufToArray(MemHandle&, ADDData%(0), FirstPoint&, CBCCount&)

For x = 0 To 998
ULStat% = cbToEngUnits(BoardNum%, Gain, ADDData%(x), EngUnits(x))
Next x

'CWGraph1.ChartLength = 999
ipot = 0
air = 0
'h2sensor = 0
'pell = 0
n = 0
'gainpel = 10 ^ (CWKnob1.Value)

For x = 0 To 998 Step 3 'CWSlide1.Value * 2) - 1 Step 2 ' channel 0 data
ipot = ipot + EngUnits(x)
'h2sensor = h2sensor + EngUnits(x + 1)
air = air + EngUnits(x + 2)

    n = n + 1
Next x

    ipt(loop) = (ipot / 333) / (10 ^ CWKnob1.Value)
'h2sens(loop) = h2sensor / 333
airflow(loop) = air / 333

'airflowcal(loop) = 6.562 * airflow(loop) ^ 6 - 101.84 * airflow(loop) ^ 5 + 608.31 * airflow(loop) ^ 4 -
1722.1 * airflow(loop) ^ 3 + 2285.1 * airflow(loop) ^ 2 - 1076.2 * airflow(loop)
'airflowcal(loop) = 0.03 * airflow(loop) ^ 6 - 0.5743 * airflow(loop) ^ 5 + 4.3916 * airflow(loop) ^ 4 -
16.863 * airflow(loop) ^ 3 + 32.963 * airflow(loop) ^ 2 - 27.176 * airflow(loop) + 7.2286
airflowcal(loop) = 0.9 * (Exp(0.0300330895 * airflow(loop) ^ 6 - 0.5742951525 * airflow(loop) ^ 5 +
4.3915924818 * airflow(loop) ^ 4 - 16.8631186484 * airflow(loop) ^ 3 + 32.9634552283 * airflow(loop)
^ 2 - 27.1762451665 * airflow(loop) + 7.2285843553))

Hper.Text = Format(((ipt(loop) - 0.0000005502) / 0.0002831377), "0.0000")

datagraph1(2) = airflowcal(loop)

airtext.Text = Format(airflow(loop), "0.000")
aircext.Text = Format(airflowcal(loop), "0.000")

Text5.Text = Format(ipt(loop) * 10 ^ 6, "0.000")

If CWButton1.Value = True Then
timestb(loop) = Timer - startt
Timeboxb = Format(timestb(loop), "0.000")
Text4b = loop
End If

datagraph1(3) = ((ipt(loop) - 0.0000005502) / 0.0002831377)

If ((ipt(loop) - 0.0000005502) / 0.0002831377) > 14 Then
Hok.Visible = False

```

Appendix 11

```
warning.Visible = True
Else
Hok.Visible = True
warning.Visible = False
End If
End Sub

Private Sub CWButton1_ValueChanged(ByVal Value As Boolean)

Dim ok As Integer
'Dim usbt08Info As String * 80

'Click.pelcocav.CWButton1
'Call pelcocav.CWButton1_ClickEvent
'pelcocav.CWButton1 = True

If CWButton1.Value = True Then
Erase timestb
'Erase h2sens
Erase ipt
Erase airflow
Erase temp
End If

' timestb(ns2), "0.0000"); ","; Format(h2sens(ns2), "0.0000000000"); ","; Format(ipt(ns2),
"0.0000000000")
If (tc08_handle < 1) Then
'txtComments.Text = "Opening TC-08"
'txtComments.Refresh
tc08_handle = usb_tc08_open_unit()
If (tc08_handle > 0) Then

    ok = usb_tc08_get_unit_info2(tc08_handle, usbt08Info, 80, 4)
    ' txtComments.Text = "USBTC-08 Opened  " + "Serial: " + usbt08Info

    Call usb_tc08_set_mains(tc08_handle, True)
    ok = usb_tc08_set_channel(tc08_handle, 0, Asc("K"))
    ok = usb_tc08_set_channel(tc08_handle, 1, Asc("K"))
    ok = usb_tc08_set_channel(tc08_handle, 2, Asc("K"))
Else
' If (tc08_handle = 0) Then
' txtComments.Text = "Unable to open TC-08"
' Else
' txtComments.Text = "Error Code: " & usb_tc08_get_last_error(0)
' End If
End If
End If

CWGraph1.ChartLength = 999
BoardNum% = 1      ' Board number
wey = 0

If CWButton1.Value = True Then
CWGraph1.ClearData
CWGraph3.ClearData
CWGraph3.ChartLength = 50000
CWGraph4.ClearData

Else
End If

startt = Timer

If CWButton1.Value = True Then
```

```

lloop = 0

Do
Erase ADDData, EngUnits
    LowChan% = 2          ' first channel to acquire
    HighChan% = 2

    CBCCount& = numofpoints.Text ' total number of data points to collect
    CBRate& = Samplerate.Text    ' sampling rate (samples per second) per channel
    Gain = BIP1p25VOLTS         ' set the gain
    Options% = CONVERTDATA 'Or EXTTRIGGER ' return data as 12-bit values

    Erase pwrspecoutav

    For av = 1 To 10

        ULStat% = cbAInScan(BoardNum%, LowChan%, HighChan%, CBCCount&, CBRate&, Gain,
MemHandle&, Options%)
        ' Transfer the data from the memory buffer set up by Windows to an array for use by Visual
Basic

        ULStat% = cbWinBufToArray(MemHandle&, ADDData%(0), FirstPoint&, CBCCount&)

Erase idata

    For x = 0 To 999
        ULStat% = cbToEngUnits(BoardNum%, Gain, ADDData%(x), EngUnits(x))
    Next x
    For x = 0 To 999
        idata(x) = EngUnits(x)

    Next x
    timest(lloop) = Timer - startt
    datagraph1(0) = timest(lloop)
    Timebox = Format(Timer - startt, "0.000")
    Text4 = lloop

    CWGraph1.PlotY idata, 0, 1, bchartperrow = False

    dttime = 1 / CBRate&

    dfs = 1 / (100 * dttime) ' this represents the frequency step

    CWDSP1.AutoPowerSpectrum idata, dttime, pwrspecouta, df
    rm = (Sqr(2))

    pwrspecouta(0) = (Sqr(pwrspecouta(0)))

    For se = 1 To 499
        pwrspecouta(se) = (rm * (Sqr(pwrspecouta(se))))
    Next se

    For se = 1 To 499
        pwrspecoutav(se) = pwrspecoutav(se) + pwrspecouta(se)
    Next se

    Text1 = df
    Text2 = dfs

    Next av

    For se = 1 To 499
        pwrspecoutav(se) = pwrspecoutav(se) / 10
    Next se

```

Appendix 11

```
CWGraph2.PlotY pwrspecoutav, 0, df
If CWButton3 = True Then
CWGraph2.Cursors.Item(1).Visible = True
If CWButton4.Value = False Then
CWGraph2.Cursors.Item(1).SnapMode = cwCSnapPointsOnPlot
End If

If CWButton4.Value = True Then
CWGraph2.Cursors.Item(1).SnapMode = cwCSnapFloating
End If

Else: CWGraph2.Cursors.Item(1).Visible = False
text3x = 0
text3y = 0
End If

text3x = Format(CWGraph2.Cursors.Item(1).XPosition, "0.0000")
text3y = Format(CWGraph2.Cursors.Item(1).YPosition, "0.0000000")

Famp(loop) = Format(CWGraph2.Cursors.Item(1).YPosition, "0.0000") 'to get F amp from cursor
ru(loop) = Drive / ((text3y.Text + 0.000000000000001) / GainBoard.Text) 'to get resistance value from
cursor
datagraph1(1) = ru(loop)
Ffreq(loop) = CWGraph2.Cursors.Item(1).XPosition

Res.Text = Format(ru(loop), "0.000")
FampV.Text = Format(Famp(loop), "0.00000")
FfreqH.Text = Format(Ffreq(loop), "0.00")

CWGraph3.ChartXY datagraph1, bchartperrow = True

Erase pwrspecoutav

DoEvents
lloop = lloop + 1
DoEvents

Loop Until CWButton1.Value = False
Else
End If

End Sub

Private Sub Exit_Click()
End
End Sub

Private Sub Form_Load()
form1.Width = Screen.Width
form1.Height = Screen.Height
form1.Top = 0
form1.Left = 0

' declare revision level of Universal Library

ULStat% = cbDeclareRevision(CURRENTREVNUM)

' Initiate error handling
' activating error handling will trap errors like
' bad channel numbers and non-configured conditions.
```

```

' Parameters:
' PRINTALL :all warnings and errors encountered will be printed
' DONTSTOP :if an error is encountered, the program will not stop,
'           errors must be handled locally

ULStat% = cbErrHandling(PRINTALL, DONTSTOP)
If ULStat% <> 0 Then Stop

' If cbErrHandling% is set for STOPALL or STOPFATAL during the program
' design stage, Visual Basic will be unloaded when an error is encountered.
' We suggest trapping errors locally until the program is ready for compiling
' to avoid losing unsaved data during program design. This can be done by
' setting cbErrHandling options as above and checking the value of ULStat%
' after a call to the library. If it is not equal to 0, an error has occurred.

MemHandle& = cbWinBufAlloc(100000) ' set aside memory to hold data
If MemHandle& = 0 Then Stop

End Sub

Private Sub load_Click()
Dim temp_found As Boolean
temp_found = False

Dim a As String
CWGraph1.ClearData
CWGraph2.ClearData
CWGraph3.ClearData
CWGraph3.ChartLength = 50000

form1.filebox.CancelError = True
On Error GoTo ErrHandle
form1.filebox.Flags = &H2&
form1.filebox.Filename = "*.dat"
form1.filebox.InitDir = "C:\\"
form1.filebox.Action = 1
form1.Caption = form1.filebox.Filename
Open form1.filebox.Filename For Input As #2
n = 0

For nn = 0 To 7 'skip top two lines
Input #2, a$
Next nn

Do
Input #2, a$
timest(n) = Val(a$)
datagraph1(0) = timest(n)

Input #2, a$
Famp(n) = Val(a$)
Input #2, a$
ru(n) = Val(a$)
datagraph1(1) = ru(n)
Input #2, a$
Ffreq(n) = Val(a$)
Input #2, a$
temp(n) = Val(a$)

If temp_found = False Then
' If temp(n) > 0 Then
' temp_found = True
' For k = 0 To (n - 1)

```

Appendix 11

```
' temp(k) = temp(n)
' Next k
' End If
' Else
' If temp(n) = 0 Then
'temp(n) = temp(n - 1)
'End If
'End If

' datagraph1(2) = temp(n)

CWGraph3.ChartXY datagraph1, bPlotPerRow = True
n = n + 1
Loop Until EOF(2)
Close #2
ErrHandle: Exit Sub

End Sub

Private Sub Save_Click()
Dim ns
Dim ns2
Dim filenames As String
Dim firstbit As String
Close #2
Close #3

form1.filebox.CancelError = True
On Error GoTo ErrHandle
form1.filebox.Flags = &H2&
form1.filebox.Filename = "*.dat"
form1.filebox.InitDir = "C:\Tom\Resistance measurements\120912\"
form1.filebox.Action = 2
form1.Caption = form1.filebox.Filename
Open form1.filebox.Filename For Output As #2
filenames = form1.filebox.Filename
firstbit = Mid(filenames, 1, InStr(1, filenames, ".dat") - 1)

Open firstbit + "(H2+iCO).dat" For Output As #3

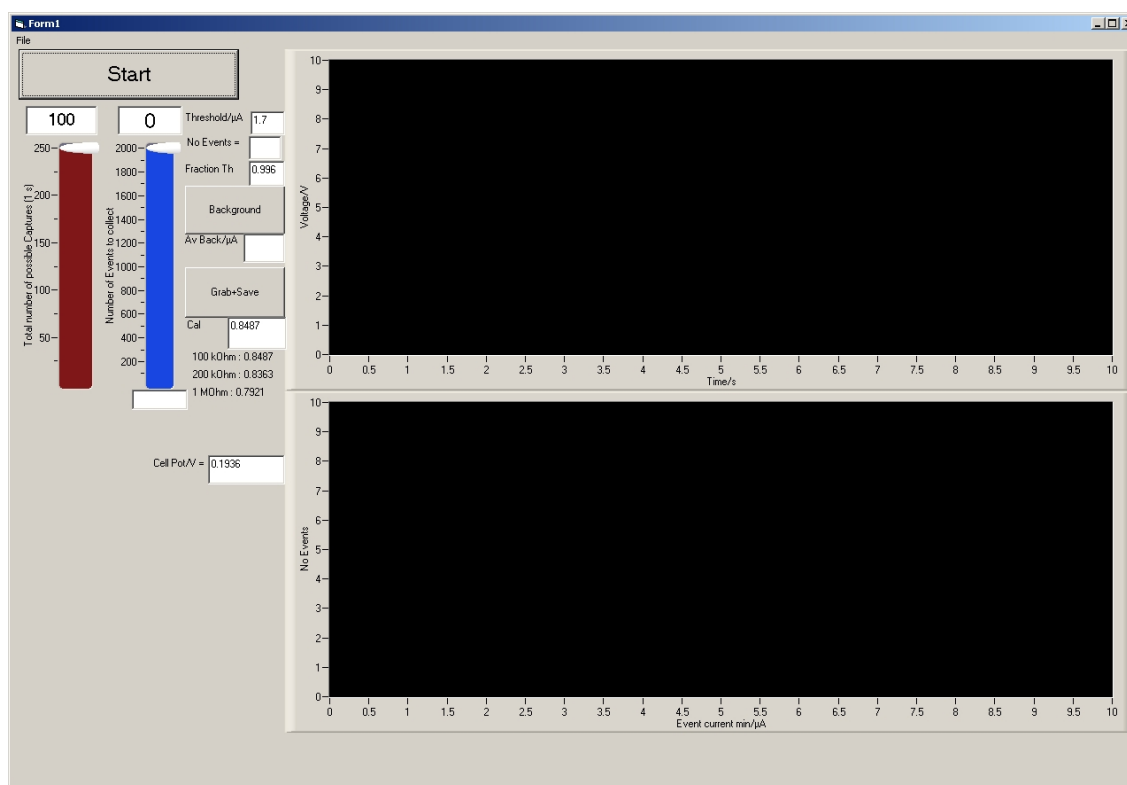
ns = 0
Print #2, "Samplerate="; Samplerate.Text; "Hz"; ";"; "Drive Amp="; Drive.Text; "V"; ";"; "Gain=";
GainBoard.Text; "VA-1"; ";"; "Liquid Flow="; Flowtext.Text; "L min-1"
Print #2, "Time/s,F amp/V, Ru/Ohms, F Freq/Hz, Temp/°C"
Do
    ns = ns + 1
    Print #2, Format(timest(ns), "0.0000"); ";"; Format(Famp(ns), "0.00000"); ";"; Format(ru(ns),
"0.00000"); ";"; Format(Ffreq(ns), "0.0000"); ";"; Format(temp(ns), "0.000")

    Loop Until ns = lloop - 1
    Close #2

ns2 = 0
Print #3, "Time/s, Airflow/ml min-1, iCO/A, H2/%"
Do
ns2 = ns2 + 1
If airflow(ns2) > 0 Then
Print #3, Format(timestb(ns2), "0.0000"); ";"; Format(airflowcal(ns2), "0.0000"); ";"; Format(ipt(ns2),
"0.0000000000"); ";"; Format(((ipt(ns2) - 0.0000005502) / 0.0002831377), "0.0000")
End If
Loop Until ns2 = lloop - 1
Close #3
ErrHandle: Exit Sub
End Sub
```

4. Coulter counter program (Tcounter.vbp)

Program used to interface data acquisition card and measure and save the current data for Coulter counter experimentation. The program also provides a peak finding routine. The background level is obtained and peaks found according to a variable threshold level. The program can be set to obtain a set number of peaks or a total number of captures of 1 second duration.



```
'ULAI02.VBP=====
=====
' File:                ULAI02.VBP
' Library Call Demonstrated:  cbAInScan(), FOREGROUND mode
' Purpose:              Scans a range of A/D Input Channels and stores the sample
                        data in an array.
' Demonstration:         Displays the analog input on up to eight channels.
' Other Library Calls:    cbErrHandling()
' Special Requirements:   Board 0 must have an A/D converter.
'                        Analog signals on eight input channels.
'=====
```

Option Explicit

Const BoardNum As Long = 1 ' Board number

Dim CBRange As Long

Dim ADResolution As Long, NumAIChans As Long

Dim HighChan As Long, LowChan As Long, MaxChan As Long

Dim photocal

Const NumPoints As Long = 50000 ' Number of data points to collect for 1 s

Const FirstPoint As Long = 0 ' set first element in buffer to transfer to array

Appendix 11

```
Dim EngUnits(NumPoints - 1)
Dim ADDData(NumPoints - 1) As Integer ' dimension an array to hold the input
values
```

```
Dim MemHandle As Long ' define a variable to contain the handle for
' memory allocated by Windows through cbWinBufAlloc()
```

```
Dim ULStat As Long
Dim timevent(10000)
Dim min(10000)
Dim engunits2(49999)
Dim x
Dim p
Dim zs
Dim z
Dim c
Dim bp
Dim sumbac
Dim threshold
Dim n
Dim w
Dim bin
Dim pbin(100)
Dim peakt(10000)
Dim deltaR(10000)
Dim pbac(10000)
Dim reltime(10000)
Dim peak(10000)
Dim dttime
Dim sumt(200)
Dim minp
```

```
Private Sub Command1_Click()
```

```
Dim CBCount As Long
```

```
CWGraph1.ClearData
```

```
Dim CBRate As Long
```

```
Dim Options As Long
```

```
Dim i As Long, j As Long
```

```
Dim Gain
```

```
Dim TrigType
```

```
Dim DataValue
```

```
Dim threshold
```

```
photocal = Text7
```

```
Dim tstart
```

```
dttime = 1 / 50000
```

```
' Collect the values with cbAInScan()
```

```
' Parameters:
```

```
' BoardNum :the number used by CB.CFG to describe this board
```

```
' LowChan :the first channel of the scan
```

```
' HighChan :the last channel of the scan
```

```
' CBCount :the total number of A/D samples to collect
```

```
' CBRate :sample rate
```

```
' CBRange :the gain for the board
```

```

' ADDData :the array for the collected data values
' Options :data collection options
LowChan = 0
HighChan = 0 ' last channel to acquire
CBCount = NumPoints ' total number of data points to collect
Gain = BIP5VOLTS ' set the gain
' per channel sampling rate ((samples per second) per channel)
CBRate = 50000
Options = CONVERTDATA ' return data as 12-bit values
tstart = Timer
z = -1
zs = 0
Erase pbin, peak, peakt
CWGraph2.ClearData
For p = 0 To CWSlide1.Value
    Erase ADDData, engunits2
    timeevent(p) = Timer - tstart
    ULStat = cbAInScan(BoardNum, 0, 0, CBCount, CBRate, Gain, MemHandle,
Options)
    If ULStat <> 0 And ULStat <> 91 Then Stop
' Transfer the data from the memory buffer set up by
' Windows to an array for use by this program
    ULStat = cbWinBufToArray(MemHandle, ADDData(0), FirstPoint, CBCount)
    If ULStat <> 0 Then Stop

    For x = 0 To 49999
        ULStat = cbToEngUnits(BoardNum, Gain, ADDData(x), engunits2(x))
        engunits2(x) = engunits2(x) / photocal ' convert for opto coupler
    Next x
    engunits2(0) = Text5
    CWGraph1.PlotY engunits2, 0, 0.00002
'now sort it
'chn1s is the current
sumt(p) = 0
For x = 0 To 49999
    sumt(p) = sumt(p) + engunits2(x)
Next x
Text3 = Text6 * (sumt(p) / 50000)
x = 0
'peak finding
Do
If engunits2(x) > engunits2(x + 1) And engunits2(x + 1) < Val(Text3) Then
z = z + 1
peakt(z) = (dtttime * (x))
reltime(z) = peakt(z) + timeevent(p)
minp = 10
n = x
w = 0
Do
If engunits2(n + w) < minp Then minp = engunits2(n + w)
w = w + 1
peak(z) = minp

```

Appendix 11

```
deltaR(z) = Abs((Text9 / ((sumt(p) / 50000) / 1000000#)) - (Text9 / (peak(z) /
1000000#)))
pbac(z) = (sumt(p) / 50000)
x = x + 1
Loop Until w = 75 ' 1.5 ms event window
Else
End If
x = x + 1
Loop Until x > 49925
CWGraph1.Plots.Item(2).PlotXvsY peakt, peak
Text4 = z
DoEvents
bin = (Val(Text3)) / 99 ' this is the divisions needed
For c = zs To z
bp = 0
Do

If (bp * bin) > peak(c) Then
pbin(bp) = pbin(bp) + 1
Else
End If

bp = bp + 1
Loop Until ((bp - 1) * bin) > peak(z)
Next c
CWGraph2.PlotY pbin, 0, bin
zs = z + 1
Text2 = p + 1
DoEvents
If z > CWSlide2.Value Then GoTo break
Next p
break:
End Sub

Private Sub Command2_Click()
Dim CBCount As Long
CWGraph1.ClearData
Dim CBRate As Long
Dim Options As Long
Dim i As Long, j As Long
Dim Gain
Dim TrigType
Dim DataValue
Dim tstart
dttime = 1 / 50000
photocal = Text7

' Collect the values with cbAInScan()
' Parameters:
' BoardNum :the number used by CB.CFG to describe this board
' LowChan :the first channel of the scan
' HighChan :the last channel of the scan
```

```

' CBCCount :the total number of A/D samples to collect
' CBRate :sample rate
' CBRange :the gain for the board
' ADDData :the array for the collected data values
' Options :data collection options
LowChan = 0
HighChan = 0 ' last channel to acquire

CBCCount = NumPoints ' total number of data points to collect
Gain = BIP5VOLTS ' set the gain
' per channel sampling rate ((samples per second) per channel)
CBRate = 50000
Options = CONVERTDATA ' return data as 12-bit values
tstart = Timer
CWGraph2.ClearData

ULStat = cbAInScan(BoardNum, 0, 0, CBCCount, CBRate, Gain, MemHandle,
Options)
If ULStat <> 0 And ULStat <> 91 Then Stop
timeevent(p) = Timer - tstart
' Transfer the data from the memory buffer set up by
' Windows to an array for use by this program

ULStat = cbWinBufToArray(MemHandle, ADDData(0), FirstPoint, CBCCount)
If ULStat <> 0 Then Stop

For x = 0 To 49999
ULStat = cbToEngUnits(BoardNum, Gain, ADDData(x), engunits2(x))
engunits2(x) = engunits2(x) / photocal ' convert for opto coupler
Next x
sumbac = 0
CWGraph1.PlotY engunits2, 0, 0.00002

For x = 0 To 49999
sumbac = sumbac + engunits2(x)
Next x
sumbac = sumbac / 50000
Text3 = Format(Text6 * sumbac, "0.0000") ' set threshold
Text5 = Format(sumbac, "0.0000")
End Sub

Private Sub Command3_Click()
Dim CBCCount As Long
CWGraph1.ClearData
Dim CBRate As Long
Dim Options As Long
Dim i As Long, j As Long
Dim Gain
Dim TrigType
Dim DataValue
Dim threshold

```

Appendix 11

```
Dim tstart

dttime = 1 / 50000

LowChan = 0
HighChan = 0 ' last channel to acquire
photocal = Text7

CBCount = NumPoints      ' total number of data points to collect
Gain = BIP5VOLTS         ' set the gain
' per channel sampling rate ((samples per second) per channel)
CBRate = 50000
Options = CONVERTDATA    ' return data as 12-bit values

tstart = Timer

CWGraph2.ClearData

ULStat = cbAInScan(BoardNum, 0, 0, CBCount, CBRate, Gain, MemHandle,
Options)
If ULStat <> 0 And ULStat <> 91 Then Stop
timeevent(p) = Timer - tstart

' Transfer the data from the memory buffer set up by
' Windows to an array for use by this program

ULStat = cbWinBufToArray(MemHandle, ADDData(0), FirstPoint, CBCount)
If ULStat <> 0 Then Stop

For x = 0 To 49999
ULStat = cbToEngUnits(BoardNum, Gain, ADDData(x), engunits2(x))
engunits2(x) = engunits2(x) / photocal ' convert for opto coupler
Next x

CWGraph1.PlotY engunits2, 0, 0.00002

CommonDialog1.Flags = &H2&
CommonDialog1.Filename = "*.dat"
CommonDialog1.InitDir = "C:\Tom\Microchannel 50um\050913\"
CommonDialog1.Action = 2

Caption = CommonDialog1.Filename
Open CommonDialog1.Filename For Output As #2
Print #2, "Photocalibration = "; photocal
Print #2, "time/s, i/μA"

For x = 0 To 49999
Print #2, x * (1 / 50000); ","; Format(engunits2(x), "0.000")
Next x
Close #2
End Sub
```

```
Private Sub CWSlide1_PointerValueChanged(ByVal Pointer As Long, Value As Variant)
Text1 = Format(CWSlide1.Value, "0.000")
DoEvents
```

```
End Sub
```

```
Private Sub CWSlide2_PointerValueChanged(ByVal Pointer As Long, Value As Variant)
Text8 = CWSlide2.Value
```

```
End Sub
```

```
Private Sub Form_Load()
```

```
    ' declare revision level of Universal Library
```

```
    ULStat = cbDeclareRevision(CURRENTREVNUM)
```

```
    ' Initiate error handling
```

```
    ' activating error handling will trap errors like
```

```
    ' bad channel numbers and non-configured conditions.
```

```
    ' Parameters:
```

```
    ' PRINTALL :all warnings and errors encountered will be printed
```

```
    ' DONTSTOP :if an error is encountered, the program will not stop,
```

```
    ' errors must be handled locally
```

```
    ULStat = cbErrHandling(PRINTALL, DONTSTOP)
```

```
    If ULStat <> 0 Then Stop
```

```
    ' If cbErrHandling% is set for STOPALL or STOPFATAL during the program
```

```
    ' design stage, Visual Basic will be unloaded when an error is encountered.
```

```
    ' We suggest trapping errors locally until the program is ready for compiling
```

```
    ' to avoid losing unsaved data during program design. This can be done by
```

```
    ' setting cbErrHandling options as above and checking the value of ULStat%
```

```
    ' after a call to the library. If it is not equal to 0, an error has occurred.
```

```
    MemHandle& = cbWinBufAlloc(NumPoints) ' set aside memory to hold data
```

```
    If MemHandle& = 0 Then Stop
```

```
    ULStat = cbWinBufFree(MemHandle) ' Free up memory for use by other
programs
```

```
    If ULStat <> 0 Then Stop
```

```
    End
```

```
End Sub
```

```
Private Sub saveb_Click()
```

```
CommonDialog1.Flags = &H2&
```

```
CommonDialog1.FileName = "*.dat"
```

```
CommonDialog1.InitDir = "C:\Tom\Microchannel 50um\210114\"
```

```
CommonDialog1.Action = 2
```

```
    Caption = CommonDialog1.FileName
```

Appendix 11

```
Open CommonDialog1.FileName For Output As #2
Print #2, "Photocalibration = "; photocal
Print #2, "Bin Value/ $\mu$ A, No of Events"
n = 0
Do
Print #2, bin * n; ","; pbin(n)
n = n + 1
Loop Until n = 99
Close #2
ErrHandle:      Exit Sub
End Sub

Private Sub savef_Click()
CommonDialog1.Flags = &H2&
CommonDialog1.FileName = "*.dat"
CommonDialog1.InitDir = "C:\Tom\Microchannel 50um\210114\"
CommonDialog1.Action = 2

Caption = CommonDialog1.FileName
Open CommonDialog1.FileName For Output As #2
Print #2, "Photocalibration = "; photocal
Print #2, "Av. background (start)= "; Format(sumbac, "0.0000000")
Print #2, "time/s, imin/ $\mu$ A, deltaR/Ohms, backgroundi/ $\mu$ A, time/s"
n = 1
Do
Print #2, peakt(n); ","; peak(n); ","; deltaR(n); ","; pbac(n); ","; reltime(n)
n = n + 1
Loop Until n = Val(Text4)
Close #2
ErrHandle:      Exit Sub
End Sub
```

List of References

1. Cassidy, J., *Emissions and Total Energy Consumption of a Multicylinder Piston Engine Running on Gasoline and a Hydrogen-Gasoline Mixture*. NASA Technical Note, 1977. NASA Tn D-8487.
2. Dulger, Z. and K.R. Ozcelik, *Fuel Economy Improvement by on Board Electrolytic Hydrogen Production*. International Journal of Hydrogen Energy, 2000. 25(9): p. 895-897.
3. Sfinteanu, D. and N. Apostolescu, *Efficiency, Pollution-Control and Performances of Hydrogen-Fueled Passenger Cars*. International Journal of Hydrogen Energy, 1992. 17(7): p. 539-542.
4. Verhelst, S. and T. Wallner, *Hydrogen-Fueled Internal Combustion Engines*. Progress in Energy and Combustion Science, 2009. 35(6): p. 490-527.
5. Verhelst, S., et al., *Efficiency Comparison between Hydrogen and Gasoline, on a Bi-Fuel Hydrogen/Gasoline Engine*. International Journal of Hydrogen Energy, 2009. 34(5): p. 2504-2510.
6. Bortnikov, L.N., *Combustion of a Gasoline-Hydrogen-Air Mixture in a Reciprocating Internal Combustion Engine Cylinder and Determining the Optimum Gasoline-Hydrogen Ratio*. Combustion Explosion and Shock Waves, 2007. 43(4): p. 378-383.
7. Birkin, P.R., et al., *Electrochemical Measurement of Erosion from Individual Cavitation Events Generated from Continuous Ultrasound*. Journal of the Chemical Society-Faraday Transactions, 1998. 94(22): p. 3365-3371.
8. Birkin, P.R., C.J.B. Vian, and T.G. Leighton, *Opto-Isolation of Electrochemical Systems in Cavitation Environments*. Anal Chem, 2009. 81(12): p. 5064-5069.
9. Great Britain. Dept. of Trade and Industry., *Meeting the Energy Challenge : A White Paper on Energy*. 2007, London: Stationery Office. 342 p.
10. Dunn, S., *Hydrogen Futures: Toward a Sustainable Energy System*. International Journal of Hydrogen Energy, 2002. 27(3): p. 235-264.
11. Midilli, A. and I. Dincer, *Key Strategies of Hydrogen Energy Systems for Sustainability*. International Journal of Hydrogen Energy, 2007. 32(5): p. 511-524.
12. Johnston, B., M.C. Mayo, and A. Khare, *Hydrogen: The Energy Source for the 21st Century*. Technovation, 2005. 25(6): p. 569-585.
13. Jain, I.P., C. Lal, and A. Jain, *Hydrogen Storage in Mg: A Most Promising Material*. International Journal of Hydrogen Energy, 2010. 35(10): p. 5133-5144.
14. Hamelinck, C.N. and A.P.C. Faaij, *Future Prospects for Production of Methanol and Hydrogen from Biomass*. Journal of Power Sources, 2002. 111(1): p. 1-22.
15. Veziroglu, T.N. and F. Barbir, *Hydrogen - the Wonder Fuel*. International Journal of Hydrogen Energy, 1992. 17(6): p. 391-404.
16. Choudhary, T.V., C. Sivadinarayana, and D.W. Goodman, *Catalytic Ammonia Decomposition: Cox-Free Hydrogen Production for Fuel Cell Applications*. Catalysis Letters, 2001. 72(3-4): p. 197-201.
17. Brown, L.F., *A Comparative Study of Fuels for on-Board Hydrogen Production for Fuel-Cell-Powered Automobiles*. International Journal of Hydrogen Energy, 2001. 26(4): p. 381-397.

Bibliography

18. Soler, L., et al. *Hydrogen Generation from Aluminum in a Non-Consumable Potassium Hydroxide Solution*. in *Proceedings International Hydrogen Energy Congress and Exhibition IHEC 2005*. **2005**. Istanbul, Turkey,.
19. Belitskus, D., *Reaction of Aluminum with Sodium Hydroxide Solution as a Source of Hydrogen*. *Journal of the Electrochemical Society*, **1970**. 117(8): p. 1097-&.
20. Bartels, J.R., M.B. Pate, and N.K. Olson, *An Economic Survey of Hydrogen Production from Conventional and Alternative Energy Sources*. *International Journal of Hydrogen Energy*, **2010**. 35(16): p. 8371-8384.
21. Hefner, R.A., *The Age of Energy Gases*. *International Journal of Hydrogen Energy*, **2002**. 27(1): p. 1-9.
22. Forsberg, C., *Futures for Hydrogen Produced Using Nuclear Energy*. *Progress in Nuclear Energy*, **2005**. 47(1-4): p. 484-495.
23. Wang, H.Z., et al., *A Review on Hydrogen Production Using Aluminum and Aluminum Alloys*. *Renewable & Sustainable Energy Reviews*, **2009**. 13(4): p. 845-853.
24. Heinzl, A., B. Vogel, and P. Hubner, *Reforming of Natural Gas - Hydrogen Generation for Small Scale Stationary Fuel Cell Systems*. *Journal of Power Sources*, **2002**. 105(2): p. 202-207.
25. Gallucci, F., et al., *Steam Reforming of Methane in a Membrane Reactor: An Industrial Case Study*. *Industrial & Engineering Chemistry Research*, **2006**. 45(9): p. 2994-3000.
26. Hohn, K.L. and L.D. Schmidt, *Partial Oxidation of Methane to Syngas at High Space Velocities over Rh-Coated Spheres*. *Applied Catalysis A: General*, **2001**. 211(1): p. 53-68.
27. Adams, T.A. and P.I. Barton, *Combining Coal Gasification and Natural Gas Reforming for Efficient Polygeneration*. *Fuel Processing Technology*, **2011**. 92(3): p. 639-655.
28. Winter, C.J., *Hydrogen Energy - Abundant, Efficient, Clean: A Debate over the Energy-System-of-Change*. *International Journal of Hydrogen Energy*, **2009**. 34(14): p. S1-S52.
29. Werner, H.A.F. and R. Bauer, *Hydrogen Production by Water Photolysis Using Nitrilotriacetic Acid as Electron Donor*. *Journal of Photochemistry and Photobiology a-Chemistry*, **1996**. 97(3): p. 171-173.
30. Grigoriev, S.A., V.I. Porembsky, and V.N. Fateev, *Pure Hydrogen Production by Pem Electrolysis for Hydrogen Energy*. *International Journal of Hydrogen Energy*, **2006**. 31(2): p. 171-175.
31. Gibson, T.L. and N.A. Kelly, *Predicting Efficiency of Solar Powered Hydrogen Generation Using Photovoltaic-Electrolysis Devices*. *International Journal of Hydrogen Energy*, **2010**. 35(3): p. 900-911.
32. Gibson, T.L. and N.A. Kelly, *Optimization of Solar Powered Hydrogen Production Using Photovoltaic Electrolysis Devices*. *International Journal of Hydrogen Energy*, **2008**. 33(21): p. 5931-5940.
33. Gokcek, M., *Hydrogen Generation from Small-Scale Wind-Powered Electrolysis System in Different Power Matching Modes*. *International Journal of Hydrogen Energy*, **2010**. 35(19): p. 10050-10059.
34. Mantz, R.J. and H. De Battista, *Hydrogen Production from Idle Generation Capacity of Wind Turbines*. *International Journal of Hydrogen Energy*, **2008**. 33(16): p. 4291-4300.
35. Balat, H. and E. Kirtay, *Hydrogen from Biomass - Present Scenario and Future Prospects*. *International Journal of Hydrogen Energy*, **2010**. 35(14): p. 7416-7426.

36. Turner, J., et al., *Renewable Hydrogen Production*. International Journal of Energy Research, **2008**. 32(5): p. 379-407.
37. Sørensen, B., *Chapter 2 - Hydrogen*, in *Hydrogen and Fuel Cells*. **2005**, Academic Press: Burlington. p. 5-111.
38. Liso, V., et al., *Performance Comparison between Partial Oxidation and Methane Steam Reforming Processes for Solid Oxide Fuel Cell (Sofc) Micro Combined Heat and Power (Chp) System*. Energy, **2011**. 36(7): p. 4216-4226.
39. Dupont, V., et al., *Production of Hydrogen by Unmixed Steam Reforming of Methane*. Chemical Engineering Science, **2008**. 63(11): p. 2966-2979.
40. Holladay, J.D., et al., *An Overview of Hydrogen Production Technologies*. Catalysis Today, **2009**. 139(4): p. 244-260.
41. Ersöz, A., *Investigation of Hydrocarbon Reforming Processes for Micro-Cogeneration Systems*. International Journal of Hydrogen Energy, **2008**. 33(23): p. 7084-7094.
42. Genovese, J., Harg, K., Paster, M., Turner, J., *Current (2009) State-of-the-Art Hydrogen Production Cost Estimate Using Water Electrolysis*, U.S.D.o.E.H. Program, Editor **2009**, NREL: Colorado.
43. D'Andrea, T., P. Henshaw, and D.S.K. Ting, *The Addition of Hydrogen to a Gasoline-Fuelled Si Engine*. International Journal of Hydrogen Energy, **2004**. 29(14): p. 1541-1552.
44. Ma, F.H., et al., *Experimental Study on Thermal Efficiency and Emission Characteristics of a Lean Burn Hydrogen Enriched Natural Gas Engine*. International Journal of Hydrogen Energy, **2007**. 32(18): p. 5067-5075.
45. Ma, F.H., et al., *Influence of Different Volume Percent Hydrogen/Natural Gas Mixtures on Idle Performance of a Cng Engine*. Energy & Fuels, **2008**. 22(3): p. 1880-1887.
46. Ma, F.H., et al., *Performance and Emission Characteristics of a Turbocharged Cng Engine Fueled by Hydrogen-Enriched Compressed Natural Gas with High Hydrogen Ratio*. International Journal of Hydrogen Energy, **2010**. 35(12): p. 6438-6447.
47. Ji, C. and S. Wang, *Effect of Hydrogen Addition on the Idle Performance of a Spark Ignited Gasoline Engine at Stoichiometric Condition*. International Journal of Hydrogen Energy, **2009**. 34(8): p. 3546-3556.
48. Sáinz, D., et al., *Conversion of a Gasoline Engine-Generator Set to a Bi-Fuel (Hydrogen/Gasoline) Electronic Fuel-Injected Power Unit*. International Journal of Hydrogen Energy, **2011**. 36(21): p. 13781-13792.
49. Ji, C. and S. Wang, *Combustion and Emissions Performance of a Hybrid Hydrogen-Gasoline Engine at Idle and Lean Conditions*. International Journal of Hydrogen Energy, **2010**. 35(1): p. 346-355.
50. Verhelst, S. and R. Sierens, *A Quasi-Dimensional Model for the Power Cycle of a Hydrogen-Fuelled Ice*. International Journal of Hydrogen Energy, **2007**. 32(15): p. 3545-3554.
51. Verhelst, S., et al., *Increasing the Power Output of Hydrogen Internal Combustion Engines by Means of Supercharging and Exhaust Gas Recirculation*. International Journal of Hydrogen Energy, **2009**. 34(10): p. 4406-4412.
52. Szwaja, S., K.R. Bhandary, and J.D. Naber, *Comparisons of Hydrogen and Gasoline Combustion Knock in a Spark Ignition Engine*. International Journal of Hydrogen Energy, **2007**. 32(18): p. 5076-5087.
53. Bortnikov, L.N., *Combustion of a Gasoline-Hydrogen-Air Mixture in a Reciprocating Internal Combustion Engine Cylinder and Determining the*

Bibliography

- Optimum Gasoline-Hydrogen Ratio*. Combustion, Explosion, and Shock Waves, **2007**. 43(4): p. 378-383.
54. Wang, Q., et al., *Nature of Ti Species in the Li-Mg-N-H System for Hydrogen Storage: A Theoretical and Experimental Investigation*. Industrial & Engineering Chemistry Research, **2009**. 48(11): p. 5250-5254.
55. Parmuzina, A.V. and O.V. Kravchenko, *Activation of Aluminium Metal to Evolve Hydrogen from Water*. International Journal of Hydrogen Energy, **2008**. 33(12): p. 3073-3076.
56. Grosso, M., L. Biganzoli, and L. Rigamonti, *A Quantitative Estimate of Potential Aluminium Recovery from Incineration Bottom Ashes*. Resources, Conservation and Recycling, **2011**. 55(12): p. 1178-1184.
57. Vargel, C. and M.P. Schmidt, *Corrosion of Aluminium*. **2004**, Amsterdam ; Oxford: Elsevier.
58. Deltombe, E., Pourbaix, M., *The Electrochemical Behavior of Aluminum: Potential Ph Diagram of the System Al-H₂ at 25°C*. Corrosion, **1958**. 14: p. 496-500.
59. Belitskus, D., *Reaction of Aluminum with Sodium Hydroxide Solution as a Source of Hydrogen*. Journal of the Electrochemical Society, **1970**. 117(8): p. 1097-1099.
60. Wang, H.Z., et al., *Modeling of Parasitic Hydrogen Evolution Effects in an Aluminum-Air Cell*. Energy & Fuels, **2010**. 24: p. 3748-3753.
61. Petrovic, J. and G. Thomas, *Reaction of Aluminum with Water to Produce Hydrogen*, **2008**.
62. Grosjean, M.H., et al., *Hydrogen Production Via Hydrolysis Reaction from Ball-Milled Mg-Based Materials*. International Journal of Hydrogen Energy, **2006**. 31(1): p. 109-119.
63. Grosjean, M.H. and L. Roue, *Hydrolysis of Mg-Salt and MgH₂-Salt Mixtures Prepared by Ball Milling for Hydrogen Production*. Journal of Alloys and Compounds, **2006**. 416(1-2): p. 296-302.
64. Uehara, K., H. Takeshita, and H. Kotaka, *Hydrogen Gas Generation in the Wet Cutting of Aluminum and Its Alloys*. Journal of Materials Processing Technology, **2002**. 127(2): p. 174-177.
65. Ilyin, A.P., et al., *Reactionary Ability of Aluminum Ultrafine Powders in Various Oxidation Processes*. Korus 2000: 4th Korea-Russia International Symposium on Science and Technology, Pt 3, Proceedings, **2000**: p. 299-304.
66. Koroglu, S., et al., *Influence of Contact Resistance on Shielding Efficiency of Shielding Gutters for High-Voltage Cables*. Iet Electric Power Applications, **2011**. 5(9): p. 715-720.
67. Leighton, T.G., *The Acoustic Bubble*. **1994**.
68. Young, F.R., *Cavitation*. **1999**, London: Imperial College Press.
69. Lauterborn, W., *Cavitation and Inhomogeneities in Underwater Acoustics: Proceedings of the First International Conference, Göttingen, Fed. Rep. Of Germany, July 9-11, 1979*. **1980**: Springer-Verlag.
70. Birkhoff, G. and E.H. Zarantonello, *Jets, Wakes, and Cavities*. **1957**: Academic Press.
71. Gurevich, M.I., *The Theory of Jets in an Ideal Fluid*. Naval Engineers Journal, **1967**. 79(4): p. 681-682.
72. Mørch, K.A., *On the Collapse of Cavity Clusters in Flow Cavitation*, in *Cavitation and Inhomogeneities in Underwater Acoustics*, W. Lauterborn, Editor. **1980**, Springer Berlin Heidelberg. p. 95-100.

73. Lauterborn, W. and H. Bolle, *Experimental Investigations of Cavitation-Bubble Collapse in Neighborhood of a Solid Boundary*. Journal of Fluid Mechanics, **1975**. 72(Nov25): p. 391-&.
74. Vogel, A., W. Lauterborn, and R. Timm, *Optical and Acoustic Investigations of the Dynamics of Laser-Produced Cavitation Bubbles near a Solid Boundary*. Journal of Fluid Mechanics, **1989**. 206: p. 299-338.
75. Ward, B. and D.C. Emmony, *Conservation of Energy in the Oscillations of Laser-Induced Cavitation Bubbles*. Journal of the Acoustical Society of America, **1990**. 88(1): p. 434-441.
76. Shah, Y.T., A.B. Pandit, and V.S. Moholkar, *Cavitation Reaction Engineering*. **1999**, New York ; London: Kluwer Academic.
77. Ellis, A.T. and C.I.O.T.P.H. LAB., *Parameters Affecting Cavitation and Some New Methods for Their Study: Final Report*. **1965**: Hydrodynamics Laboratory, Kárm á Laboratory of Fluid Mechanics and Jet Propulsion, California Institute of Technology.
78. Kling, C.L., *A High Speed Photographic Study of Cavitation Bubble Collapse*. **1970**, University of Michigan.
79. Blake, J.R. and D.C. Gibson, *Cavitation Bubbles near Boundaries*. Annual Review of Fluid Mechanics, **1987**. 19(1): p. 99-123.
80. Neppiras, E.A., *Acoustic Cavitation*. Physics Reports-Review Section of Physics Letters, **1980**. 61(3): p. 159-251.
81. Blake, F.G., *The Onset of Cavitation in Liquids*. Acoustics Res. Lab., Harvard Univ., Tech Memo. No.12, **1949**.
82. Vian, C.J.B., *A Comparison of Measurement Techniques for Acoustic Cavitation*, in *School of chemistry***2007**, University of Southampton: Southampton. p. 278.
83. Rayleigh, L., *Viii. On the Pressure Developed in a Liquid During the Collapse of a Spherical Cavity*. Philosophical Magazine Series 6, **1917**. 34(200): p. 94-98.
84. Noltingk, B.E. and E.A. Neppiras, *Cavitation Produced by Ultrasonics*. Proceedings of the Physical Society. Section B, **1950**. 63(9): p. 674.
85. Apfel, R.E., *Acoustic Cavitation Prediction*. Journal of the Acoustical Society of America, **1981**. 69(6): p. 1624-1633.
86. Flynn, H.G., *Cavitation Dynamics .1. Mathematical Formulation*. Journal of the Acoustical Society of America, **1975**. 57(6): p. 1379-1396.
87. Flynn, H.G., *Cavitation Dynamics .2. Free Pulsations and Models for Cavitation Bubbles*. Journal of the Acoustical Society of America, **1975**. 58(6): p. 1160-1170.
88. Holland, C.K. and R.E. Apfel, IEEE Trans. Ultrason. Ferroelect. Frequency Control, **1989**. 36: p. 204.
89. Suslick, K.S., D.A. Hammerton, and R.E. Cline, *Sonochemical Hot Spot*. Journal of the American Chemical Society, **1986**. 108(18): p. 5641-5642.
90. Šponer, J., *Theoretical Estimation of the Cavitation Threshold for Very Short Pulses of Ultrasound*. Ultrasonics, **1991**. 29(5): p. 376-380.
91. Hanumanthu, J.D.L.R., *A Study of Cluster Cavitation Erosion Using Electrochemical, Physical and High-Speed Imaging Techniques*, in *School of Chemistry* **2012**, University of Southampton: Southampton. p. 304.
92. Power, J.F., *Electrochemical, Photographic, Luminescent and Acoustic Charaterisation of Cavitaion*, in *Department of Chemistry* **2003**, University of Southampton.
93. Philipp, A. and W. Lauterborn, *Cavitation Erosion by Single Laser-Produced Bubbles*. Journal of Fluid Mechanics, **1998**. 361: p. 75-116.

Bibliography

94. Frenzel, H. and H. Schultes, *Luminescenz Im Ultraschallbeschickten Wasser (Luminescence in the Ultrasound-Fed Water)*. Z. Phys. Chem. Abt. B, **1934**. 27: p. 421-424.
95. Putterman, S.J. and K.R. Weninger, *Sonoluminescence: How Bubbles Turn Sound into Light*. Annual Review of Fluid Mechanics, **2000**. 32: p. 445-+.
96. Weissler, A., *Formation of Hydrogen Peroxide by Ultrasonic Waves: Free Radicals*. Journal of the American Chemical Society, **1959**. 81(5): p. 1077-1081.
97. Henglein, A., *Chemical Effects of Continuous and Pulsed Ultrasound in Aqueous Solutions*. Ultrason Sonochem, **1995**. 2(2): p. S115-S121.
98. Hansson, I. and K.A. Mørch, *The Dynamics of Cavity Clusters in Ultrasonic (Vibratory) Cavitation Erosion*. Journal of Applied Physics, **1980**. 51(9): p. 4651-4658.
99. Riddei, V. and G. Roch, *Cavitation Erosion - Survey of Literature 1940-1970*. Wear, **1973**. 23(1): p. 133-136.
100. Preece, C.M., *Cavitation Erosion*. Jom-Journal of Metals, **1975**. 27(12): p. A29-A29.
101. Philipp, A. and W. Lauterborn, *Damage of Solid Surfaces by Single Laser-Produced Cavitation Bubbles*. Acustica, **1997**. 83(2): p. 223-227.
102. Hansson, I. and K.A. Mørch, *Initial-Stage of Cavitation Erosion on Aluminum in Water-Flow*. Journal of Physics D-Applied Physics, **1978**. 11(2): p. 147-&.
103. Vyas, B. and C.M. Preece, *Stress Produced in a Solid by Cavitation*. Journal of Applied Physics, **1976**. 47(12): p. 5133-5138.
104. Werner, L. and K. Thomas, *Physics of Bubble Oscillations*. Reports on Progress in Physics, **2010**. 73(10): p. 106501.
105. Kanthale, P.M., et al., *Cavity Cluster Approach for Quantification of Cavitation Intensity in Sonochemical Reactors*. Ultrason Sonochem, **2003**. 10(4-5): p. 181-189.
106. Krefting, D., R. Mettin, and W. Lauterborn, *High-Speed Observation of Acoustic Cavitation Erosion in Multibubble Systems*. Ultrason Sonochem, **2004**. 11(3-4): p. 119-123.
107. Kanthale, P.M., et al., *Dynamics of Cavitation Bubbles and Design of a Hydrodynamic Cavitation Reactor: Cluster Approach*. Ultrason Sonochem, **2005**. 12(6): p. 441-452.
108. Akhatov, I., U. Parlitz, and W. Lauterborn, *Pattern-Formation in Acoustic Cavitation*. Journal of the Acoustical Society of America, **1994**. 96(6): p. 3627-3635.
109. Akhatov, I., U. Parlitz, and W. Lauterborn, *Towards a Theory of Self-Organization Phenomena in Bubble-Liquid Mixtures*. Physical Review E, **1996**. 54(5): p. 4990-5003.
110. Doinikov, A.A., *Mathematical Model for Collective Bubble Dynamics in Strong Ultrasound Fields*. Journal of the Acoustical Society of America, **2004**. 116(2): p. 821-827.
111. Luther, S., et al., *Observation of Acoustic Cavitation Bubbles at 2250 Frames Per Second*. Ultrason Sonochem, **2001**. 8(3): p. 159-162.
112. Mettin, R., et al., *Acoustic Cavitation Structures and Simulations by a Particle Model*. Ultrason Sonochem, **1999**. 6(1-2): p. 25-29.
113. Mettin, R., C.D. Ohl, and W. Lauterborn, *Particle Approach to Structure Formation in Acoustic Cavitation*. Sonochemistry and Sonoluminescence, **1999**. 524: p. 139-144.
114. Parlitz, U., et al., *Structure Formation in Cavitation Bubble Fields*. Chaos Solitons & Fractals, **1995**. 5(10): p. 1881-1891.

115. Dubus, B., A. Moussatov, and C. Granger, *Cone-Like Bubble Formation in Ultrasonic Cavitation Field*. Ultrason Sonochem, **2003**. 10(4-5): p. 191-195.
116. Lauterborn, W. and T. Kurz, *Physics of Bubble Oscillations*. Reports on Progress in Physics, **2010**. 73(10).
117. Malykh, N.V. and G.N. Sankin, *Stabilization and Acoustic Spectra of a Cavitation Cluster in an Ultrasonic Spherical Cavity*. Technical Physics, **2010**. 55(1): p. 92-97.
118. Doinikov, A.A., *Bubble and Particle Dynamics in Acoustic Fields : Modern Trends and Applications*. **2005**, Kerala, India: Research Signpost. 338 p.
119. Pelekasis, N.A., et al., *Secondary Bjerknes Forces between Two Bubbles and the Phenomenon of Acoustic Streamers*. Journal of Fluid Mechanics, **2004**. 500: p. 313-347.
120. Crum, L.A., *Bjerknes Forces on Bubbles in a Stationary Sound Field*. Journal of the Acoustical Society of America, **1975**. 57(6): p. 1363-1370.
121. Leighton, T.G., A.J. Walton, and M.J.W. Pickworth, *Primary Bjerknes Forces*. European Journal of Physics, **1990**. 11(1): p. 47.
122. Bjerknes, V., *Fields of Force: Supplementary Lectures, Applications to Meteorology*. **1906**: Columbia University Press.
123. Doinikov, A.A., *Dissipative Effects on Bjerknes Forces between Two Bubbles*. Journal of the Acoustical Society of America, **1997**. 102(2): p. 747-751.
124. Hansson, I., V. Kedrinskii, and K.A. Morch, *On the Dynamics of Cavity Clusters*. Journal of Physics D-Applied Physics, **1982**. 15(9): p. 1725-1734.
125. Klima, J. and C. Bernard, *Sonoassisted Electrooxidative Polymerisation of Salicylic Acid: Role of Acoustic Streaming and Microjetting*. Journal of Electroanalytical Chemistry, **1999**. 462(2): p. 181-186.
126. Macounova, K., et al., *Ultrasound-Assisted Anodic Oxidation of Diuron*. Journal of Electroanalytical Chemistry, **1998**. 457(1-2): p. 141-147.
127. Davis, J., et al., *Electrochemical Detection of Nitrate at a Copper Modified Electrode under the Influence of Ultrasound*. Electroanalysis, **2000**. 12(17): p. 1363-1367.
128. Hardcastle, J.L. and R.G. Compton, *The Electroanalytical Detection and Determination of Copper in Heavily Passivating Media: Ultrasonically Enhanced Solvent Extraction by N-Benzoyl-N-Phenyl-Hydroxylamine in Ethyl Acetate Coupled with Electrochemical Detection by Sono-Square Wave Stripping Voltammetry Analysis*. Analyst, **2001**. 126(11): p. 2025-2031.
129. Vian, C.J., P.R. Birkin, and T.G. Leighton, *Opto-Isolation of Electrochemical Systems in Cavitation Environments*. Anal Chem, **2009**. 81(12): p. 5064-9.
130. Birkin, P.R., D.G. Offen, and T.G. Leighton, *The Study of Surface Processes under Electrochemical Control in the Presence of Inertial Cavitation*. Wear, **2005**. 258(1-4): p. 623-628.
131. Offen, D., *Acoustoelectrochemical Characterisation of Cavitation and Its Use in the Study of Surface Processes*, in *School of Chemistry 2006*, University of Southampton: Southampton.
132. Vian, C.J.B., P.R. Birkin, and T.G. Leighton, *Opto-Isolation of Electrochemical Systems in Cavitation Environments*. Anal Chem, **2009**. 81(12): p. 5064-5069.
133. Birkin, P.R., D.G. Offen, and T.G. Leighton, *Electrochemical Measurements of the Effects of Inertial Acoustic Cavitation by Means of*

Bibliography

- a Novel Dual Microelectrode*. Electrochemistry Communications, **2004**. 6(11): p. 1174-1179.
134. Birkin, P.R., D.G. Offin, and T.G. Leighton, *Experimental and Theoretical Characterisation of Sonochemical Cells. Part 2: Cell Disruptors (Ultrasonic Horns) and Cavity Cluster Collapse*. Phys Chem Chem Phys, **2005**. 7(3): p. 530-7.
135. Birkin, P.R., et al., *Cavitation, Shock Waves and the Invasive Nature of Sonoelectrochemistry*. Journal of Physical Chemistry B, **2005**. 109(35): p. 16997-7005.
136. Vian, C., et al. *Using Surface Erosion of an Electrode as a Method to Map and Characterise Cavitation*. in *Proceedings of the Institute of Acoustics*. **2006**.
137. Griffing, V., *Theoretical Explanation of the Chemical Effects of Ultrasonics*. The Journal of Chemical Physics, **1950**. 18(7): p. 997-998.
138. Jarman, P., *Sonoluminescence: A Discussion*. The Journal of the Acoustical Society of America, **1960**. 32(11): p. 1459-1462.
139. Vaughan, P.W. and S. Leeman, *Some Comments on Mechanisms of Sonoluminescence*. Acustica, **1986**. 59(4): p. 279-281.
140. Margulis, M., *Investigation of Electrical Phenomena Connected with Cavitation. li. On Theory of Appearance of Sonoluminescence and Sonochemical Reactions*. Russ. J. Phys. Chem, **1984**. 58: p. 1450.
141. Crum, L.A. and D.F. Gaitan, *Sonoluminescence*. 14th International Congress on Acoustics, Proceedings, Vols 1-4, **1992**: p. 433-434.
142. Gaitan, D.F., et al., *Sonoluminescence and Bubble Dynamics for a Single, Stable, Cavitation Bubble*. Journal of the Acoustical Society of America, **1992**. 91(6): p. 3166-3183.
143. McMurray, H.N. and B.P. Wilson, *Mechanistic and Spatial Study of Ultrasonically Induced Luminol Chemiluminescence*. Journal of Physical Chemistry A, **1999**. 103(20): p. 3955-3962.
144. Merenyi, G. and J.S. Lind, *Role of a Peroxide Intermediate in the Chemiluminescence of Luminol - a Mechanistic Study*. Journal of the American Chemical Society, **1980**. 102(18): p. 5830-5835.
145. Birkin, P.R., et al., *A 1 Khz Resolution Frequency Study of a Variety of Sonochemical Processes*. Physical Chemistry Chemical Physics, **2003**. 5(19): p. 4170-4174.
146. Birkin, P.R., et al., *Experimental and Theoretical Characterization of Sonochemical Cells. Part 1. Cylindrical Reactors and Their Use to Calculate the Speed of Sound in Aqueous Solutions*. Journal of Physical Chemistry A, **2003**. 107(2): p. 306-320.
147. Hodnett, M. and B. Zeqiri, *A Strategy for the Development and Standardisation of Measurement Methods for High Power/Cavitating Ultrasonic Fields: Review of High Power Field Measurement Techniques*. Ultrason Sonochem, **1997**. 4(4): p. 273-288.
148. Zeqiri, B., M. Hodnett, and T.G. Leighton, *A Strategy for the Development and Standardisation of Measurement Methods for High Power/Cavitating Ultrasonic Fields - Final Project Report*, in *NPL Report CIRA(EXT)0161997*, National Physical Laboratory.
149. Gelat, P., *Establishing a Reference Ultrasonic Cleaning Vessel: Supporting Infrastructure and Early Measurements*. **2000**: National Physical Laboratory.
150. Hodnett, M., M.J. Choi, and B. Zeqiri, *Towards a Reference Ultrasonic Cavitation Vessel. Part 1: Preliminary Investigation of the Acoustic Field*

- Distribution in a 25 Khz Cylindrical Cell*. Ultrason Sonochem, **2007**. 14(1): p. 29-40.
151. Hodnett, M. and B. Zeqiri, *Toward a Reference Ultrasonic Cavitation Vessel: Part 2 - Investigating the Spatial Variation and Acoustic Pressure Threshold of Inertial Cavitation in a 25 Khz Ultrasound Field*. Ieee Transactions on Ultrasonics Ferroelectrics and Frequency Control, **2008**. 55(8): p. 1809-1822.
 152. Hodnett, M., Zeqiri B., Lee, N., Gelat, P. N., *Report on the Feasibility of Establishing a Reference Cavitating Medium : Final Project Report*. **2001**: National Physical Laboratory.Great Britain, Centre for Mechanical and Acoustical Metrology.
 153. Leighton, T.G., et al., *Characterisation of Measures of Reference Acoustic Cavitation (Comorac): An Experimental Feasibility Trial*, in *Bubble and Particle Dynamics in Acoustic Fields: Modern Trends and Applications*, A.A. Doinikov, Editor. **2005**, Research Signpost, pp. 37-94.
 154. Weissler, A. *A Chemical Method for Measuring Relative Amounts of Cavitation in an Ultrasonic Cleaner*. in *1962 IRE National Convention*. **1962**.
 155. Birkin, P.R., et al., *Cathodic Electrochemical Detection of Sonochemical Radical Products*. Anal Chem, **2002**. 74(11): p. 2584-90.
 156. Fricke, H. and E.J. Hart, *Radiation Dosimetry 2nd Edition*. Vol. 2 - Instrumentation. **1966**, New York: Academic Press.
 157. Price, G.J. and E.J. Lenz, *The Use of Dosimeters to Measure Radical Production in Aqueous Sonochemical Systems*. Ultrasonics, **1993**. 31(6): p. 451-456.
 158. Lorimer, J.P., et al., *Effect of Ultrasound on the Degradation of Aqueous Native Dextran*. Ultrason Sonochem, **1995**. 2(1): p. S55-S57.
 159. Crawford, A.E., *The Measurement of Cavitation*. Ultrasonics, **1964**. 2(3): p. 120-123.
 160. Zeqiri, B., et al., *A Novel Sensor for Monitoring Acoustic Cavitation. Part I: Concept, Theory, and Prototype Development*. Ieee Transactions on Ultrasonics Ferroelectrics and Frequency Control, **2003**. 50(10): p. 1342-1350.
 161. Zeqiri, B., et al., *A Novel Sensor for Monitoring Acoustic Cavitation. Part li: Prototype Performance Evaluation*. Ieee Transactions on Ultrasonics Ferroelectrics and Frequency Control, **2003**. 50(10): p. 1351-1362.
 162. Coleman, A.J., et al., *Acoustic Emission and Sonoluminescence Due to Cavitation at the Beam Focus of an Electrohydraulic Shock Wave Lithotripter*. Ultrasound in Medicine and Biology, **1992**. 18(3): p. 267-81.
 163. Coleman, A.J., et al., *The Spatial Distribution of Cavitation Induced Acoustic Emission, Sonoluminescence and Cell Lysis in the Field of a Shock Wave Lithotripter*. Phys Med Biol, **1993**. 38(11): p. 1545-60.
 164. Kumar, A., P.R. Gogate, and A.B. Pandit, *Mapping the Efficacy of New Designs for Large Scale Sonochemical Reactors*. Ultrason Sonochem, **2007**. 14(5): p. 538-44.
 165. Memoli, G., et al., *Characterisation and Improvement of a Reference Cylindrical Sonoreactor*. Ultrason Sonochem, **2012**. 19(4): p. 939-952.
 166. Wang, L., et al., *Characterisation of a Multi-Frequency Cavitation Vessel*. International Symposium on Ultrasound in the Control of Industrial Processes (Ucip 2012), **2012**. 42.
 167. Vishay, *Designing Linear Amplifiers Using the I1300 Optocoupler*, in *Vishay semiconductors***2012**, www.vishay.com.

Bibliography

168. Alphasense, *Co-Bf Carbon Monoxide Sensor Technical Specifications*, **2011**.
169. Offin, D.G., P.R. Birkin, and T.G. Leighton, *An Electrochemical and High-Speed Imaging Study of Micropore Decontamination by Acoustic Bubble Entrapment*. *Physical Chemistry Chemical Physics*, **2014**. 16(10): p. 4982-4989.
170. Birkin, P.R., Leighton, T. G. , Offin, D. G. , Vian, J. B. . *Observations of Bubble Clusters within Different Cavitation Environments – Electrochemistry, Acoustics and Imaging Studies*. in *Proceedings of 20th International Congress on Acoustics, ICA 2010*. **2010**. Sydney, Australia.
171. Hodnett, M., R. Chow, and B. Zeqiri, *High-Frequency Acoustic Emissions Generated by a 20 Khz Sonochemical Horn Processor Detected Using a Novel Broadband Acoustic Sensor: A Preliminary Study*. *Ultrason Sonochem*, **2004**. 11(6): p. 441-454.
172. Birkin, P.R., et al., *Electrochemical, Luminescent and Photographic Characterisation of Cavitation*. *Ultrason Sonochem*, **2003**. 10(4-5): p. 203-208.
173. Liu, H.L. and C.M. Hsieh, *Single-Transducer Dual-Frequency Ultrasound Generation to Enhance Acoustic Cavitation*. *Ultrason Sonochem*, **2009**. 16(3): p. 431-438.
174. Zeqiri, B., M. Hodnett, and A.J. Carroll, *Studies of a Novel Sensor for Assessing the Spatial Distribution of Cavitation Activity within Ultrasonic Cleaning Vessels*. *Ultrasonics*, **2006**. 44(1): p. 73-82.
175. Birkin, P.R., E. Eweka, and J.R. Owen, *The Effect of Ultrasound on Lithium Surfaces in Propylene Carbonate*. *Journal of Power Sources*, **1999**. 81: p. 833-837.
176. Birkin, P.R., et al., *Multiple Observations of Cavitation Cluster Dynamics Close to an Ultrasonic Horn Tip*. *Journal of the Acoustical Society of America*, **2011**. 130(5): p. 3379-3388.
177. Vian, C.J.B., P.R. Birkin, and T.C. Leighton, *Cluster Collapse in a Cylindrical Cell: Correlating Multibubble Sonoluminescence, Acoustic Pressure, and Erosion*. *Journal of Physical Chemistry C*, **2010**. 114(39): p. 16416-16425.
178. Suslick, K.S., M.M. Mdleleni, and J.T. Ries, *Chemistry Induced by Hydrodynamic Cavitation*. *Journal of the American Chemical Society*, **1997**. 119(39): p. 9303-9304.
179. Suslick, K.S., S.J. Doktycz, and E.B. Flint, *On the Origin of Sonoluminescence and Sonochemistry*. *Ultrasonics*, **1990**. 28(5): p. 280-290.
180. Suslick, K.S. and Y.T. Didenko, *The Energy Efficiency of Formation of Photons, Radicals and Ions During Single-Bubble Cavitation*. *Nature*, **2002**. 418(6896): p. 394-397.
181. Flint, E.B. and K.S. Suslick, *The Temperature of Cavitation*. *Science*, **1991**. 253(5026): p. 1397-1399.
182. Flannigan, D.J. and K.S. Suslick, *Plasma Formation and Temperature Measurement During Single-Bubble Cavitation*. *Nature*, **2005**. 434(7029): p. 52-55.
183. Hecht, F., P.J. Mucha, and G. Turk, *Virtual Rheoscopic Fluids*. *Ieee Transactions on Visualization and Computer Graphics*, **2010**. 16(1): p. 147-160.
184. Rhee, H.S., J.R. Koseff, and R.L. Street, *Flow Visualization of a Recirculating Flow by Rheoscopic Liquid and Liquid-Crystal Techniques*. *Experiments in Fluids*, **1984**. 2(2): p. 57-64.

185. Dominguez - Lerma, M.A., G. Ahlers, and D.S. Cannell, *Effects of Kalliroscope Flow Visualization Particles on Rotating Couette-Taylor Flow*. Physics of Fluids (1958-1988), **1985**. 28(4): p. 1204-1206.
186. Susumu, G. and K. Shigeo, *Turbulence Visualization Using Reflective Flakes*. Journal of Physics: Conference Series, **2011**. 318(5): p. 052030.
187. King, L.V., *On the Acoustic Radiation Pressure on Spheres*. Proceedings of the Royal Society of London. Series A, Mathematical and Physical Sciences, **1934**. 147(861): p. 212-240.
188. Vandenstein, L., *Schmitt Trigger with Voltage-Controlled Trigger Levels*. Electronic Engineering, **1975**. 47(566): p. 21-&.
189. Settles, G.S., *Schlieren and Shadowgraph Techniques: Visualizing Phenomena in Transparent Media*. **2001**: Springer.
190. Ian. *Schlieren Photography - Seeing Air*. **2012** 26.09.12]; Available from: <http://www.ian.org/Schlieren/>.
191. PhotoJoJo. *Schlieren Photography: How to Photograph the Invisible*. **2012** 26.09.12]; Available from: <http://content.photojojo.com/guides/schlieren-photography-guide/>.
192. Hansen, G.M., *Mie Scattering as a Technique for the Sizing of Air Bubbles*. The Journal of the Acoustical Society of America, **1984**. 76(S1): p. S31-S31.
193. Chouhan, N. and R.-S. Liu, *Electrochemical Technologies for Energy Storage and Conversion*, in *Electrochemical Technologies for Energy Storage and Conversion*. **2011**, Wiley-VCH Verlag GmbH & Co. KGaA. p. 1-43.
194. Millet, P., et al., *Pem Water Electrolyzers: From Electrocatalysis to Stack Development*. International Journal of Hydrogen Energy, **2010**. 35(10): p. 5043-5052.
195. Rosa, V.M., M.B.F. Santos, and E.P. Dasilva, *New Materials for Water Electrolysis Diaphragms*. International Journal of Hydrogen Energy, **1995**. 20(9): p. 697-700.
196. Ursua, A., L.M. Gandia, and P. Sanchis, *Hydrogen Production from Water Electrolysis: Current Status and Future Trends*. Proceedings of the Ieee, **2012**. 100(2): p. 410-426.
197. Myland, J.C. and K.B. Oldham, *Uncompensated Resistance. 1. The Effect of Cell Geometry*. Anal Chem, **2000**. 72(17): p. 3972-80.
198. Minnaert, M., *On Musical Air-Bubbles and the Sounds of Running Water*. Phil. Mag, **1933**. 16: p. 235-248.
199. Leighton, T.G., et al., *Studies of the Cavitation Effects of Clinical Ultrasound by Sonoluminescence: 1. Correlation of Sonoluminescence with the Standing Wave Pattern in an Acoustic Field Produced by a Therapeutic Unit*. Phys Med Biol, **1988**. 33(11): p. 1239.
200. De La Rue, R.E. and C.W. Tobias, *On the Conductivity of Dispersions*. Journal of the Electrochemical Society, **1959**. 106(9): p. 827-833.
201. Bruggeman, D.A.G., *Berechnung Verschiedener Physikalischer Konstanten Von Heterogenen Substanzen. I. Dielektrizitätskonstanten Und Leitfähigkeiten Der Mischkörper Aus Isotropen Substanzen*. Annalen der Physik, **1935**. 416(8): p. 665-679.
202. McCleskey, R.B., *Electrical Conductivity of Electrolytes Found in Natural Waters from (5 to 90) °C*. Journal of Chemical & Engineering Data, **2011**. 56(2): p. 317-327.
203. Grulke, D.C., N.A. Marsh, and B.A. Hills, *Experimental Air-Embolism - Measurement of Microbubbles Using Coulter Counter*. British Journal of Experimental Pathology, **1973**. 54(6): p. 684-&.

Bibliography

204. Feshitan, J.A., et al., *Microbubble Size Isolation by Differential Centrifugation*. Journal of Colloid and Interface Science, **2009**. 329(2): p. 316-324.
205. Sennoga, C.A., et al., *Evaluation of Methods for Sizing and Counting of Ultrasound Contrast Agents*. Ultrasound in Medicine and Biology, **2012**. 38(5): p. 834-845.
206. Weller, G.E.R., et al., *Targeted Ultrasound Contrast Agents: In Vitro Assessment of Endothelial Dysfunction and Multi-Targeting to Icam-1 and Sialyl Lewis*. Biotechnology and Bioengineering, **2005**. 92(6): p. 780-788.
207. Rychak, J.J., et al., *Deformable Gas-Filled Microbubbles Targeted to P-Selectin*. Journal of Controlled Release, **2006**. 114(3): p. 288-299.
208. Graham, M.D., *The Coulter Principle: Foundation of an Industry*. Journal of the Association for Laboratory Automation, **2003**. 8(6): p. 72-81.
209. Kubitschek, H.E., *Electronic Counting and Sizing of Bacteria*. Nature, **1958**. 182(4630): p. 234-235.
210. Bull, B.S., *Citation Classic - Platelet Counts with the Coulter-Counter*. Current Contents/Clinical Practice, **1980**(41): p. 14-14.
211. Klivanov, A.L., et al., *Detection of Individual Microbubbles of Ultrasound Contrast Agents: Imaging of Free-Floating and Targeted Bubbles*. Investigative Radiology, **2004**. 39(3): p. 187-95.
212. Allen, T., *Particle Size Measurement*. **1975**: Chapman and Hall.
213. Stanley-Wood, N. and R.W. Lines, *Particle Size Analysis*. **1992**: Royal Society of Chemistry.
214. Grover, N.B., et al., *Electrical Sizing of Particles in Suspensions. I. Theory*. Biophysical Journal, **1969**. 9(11): p. 1398-414.
215. Grover, N.B., et al., *Electrical Sizing of Particles in Suspensions. II. Experiments with Rigid Spheres*. Biophysical Journal, **1969**. 9(11): p. 1415-25.
216. Adams, R.B. and E.C. Gregg, *Pulse Shapes from Particles Traversing Coulter Orifice Fields*. Phys Med Biol, **1972**. 17(6): p. 830-&.
217. Berg, R.H., *Particle Size Measurement*. American Society for Testing Materials, **1958**. 234.
218. Needham, T.E., *Parenteral Quality Control: Sterility, Pyrogen, Particulate, and Package Integrity Testing*. By Michael J. Akers. Marcel Dekker, Inc., 270 Madison Avenue, New York, Ny 10016. 1985. 272pp. 16 x 23.5 Cm. \$55.00. Journal of Pharmaceutical Sciences, **1986**. 75(1): p. 102-103.
219. Edmundson, I.C., *Coincidence Error in Coulter Counter Particle Size Analysis*. Nature, **1966**. 212(5069): p. 1450-1452.
220. Maxwell, J.C. and J.J. Thompson, *A Treatise on Electricity and Magnetism*. Clarendon Press Series. **1904**, Oxford: Clarendon Press. 2 v.
221. Strutt, J.W., *On the Influence of Obstacles Arranged in Rectangular Order Upon the Properties of a Medium*. Scientific Papers. **2009**.
222. Deblois, R.W. and C.P. Bean, *Counting and Sizing of Submicron Particles by Resistive Pulse Technique*. Review of Scientific Instruments, **1970**. 41(7): p. 909-&.
223. Smythe, W.R., *Flow around a Spheroid in a Circular Tube*. Physics of Fluids (1958-1988), **1964**. 7(5): p. 633-638.
224. Anderson, J.L. and J.A. Quinn, *Relationship between Particle Size and Signal in Coulter-Type Counters*. Review of Scientific Instruments, **1971**. 42(8): p. 1257-&.
225. Smythe, W.R., *Flow around a Sphere in a Circular Tube*. Physics of Fluids (1958-1988), **1961**. 4(6): p. 756-759.

- 226. Anderson, J.L. and J.A. Quinn, *The Relationship between Particle Size and Signal in Coulter - Type Counters*. Review of Scientific Instruments, **1971**. 42(8): p. 1257-1258.
- 227. Deblois, R.W., C.P. Bean, and R.K.A. Wesley, *Electrokinetic Measurements with Submicron Particles and Pores by Resistive Pulse Technique*. Journal of Colloid and Interface Science, **1977**. 61(2): p. 323-335.
- 228. Thom, R., A. Hampe, and G. Sauerbrey, *Die Elektronische Volumenbestimmung Von Blutkörperchen Und Ihre Fehlerquellen*. Zeitschrift für die gesamte experimentelle Medizin einschließlich experimentelle Chirurgie, **1969**. 151(4): p. 331-349.
- 229. Poiseuille, *Recherches Expérimentales Sur Le Mouvement Des Liquides Dans Les Tubes De Très-Petits Diamètres*. **1846**, Paris.
- 230. Lide, D.R., *Crc Handbook of Chemistry and Physics, 85th Edition*. **2004**: Taylor & Francis.